Internal waves in fluid flows. Possible coexistence with turbulence

FEDERICO FRATERNALE

Internal waves in fluid flows. Possible coexistence with turbulence

ScuDo

Scuola di Dottorato ~ Doctoral School

WHAT YOU ARE, TAKES YOU FAR

Doctoral Dissertation

Doctoral Program in Aerospace Engineering (29^{th} cycle)

Internal waves in fluid flows. Possible coexistence with turbulence

By

Federico Fraternale

Supervisor:
Prof. Daniela Tordella

Doctoral Examination Committee:
Prof. Nathaniel S. Barlow, Rochester Institute of Technology (referee)
Prof. Luca Sorriso Valvo, Università della Calabria (referee)
Prof. Silvano Massaglia, Università di Torino
Prof. Nikolai Pogorelov, University of Alabama
Prof. Luigi Preziosi, Politecnico di Torino
Dr. John D. Richardson, Massachusetts Institute of Technology
Prof. Lamberto Rondoni, Politecnico di Torino

Politecnico di Torino
26 October 2017

Alle persone che amo.

DECLARATION

I hereby declare that the contents and organization of this dissertation constitute my own original work and do not compromise in any way the rights of third parties, including those relating to the security of personal data.

Torino, 26 October 2017

Federico Fraternale

* This dissertation is presented in partial fulfillment of the requirements for **Ph.D. degree** in the Graduate School of Politecnico di Torino (ScuDo).

ABSTRACT

Waves in fluid flows represents the underlying theme of this research work. Wave interactions in fluid flows are part of multidisciplinary physics. It is known that many ideas and phenomena recur in such apparently diverse fields, as solar physics, meteorology, oceanography, aeronautical and hydraulic engineering, optics, and population dynamics. In extreme synthesis, waves in fluids include, on the one hand, surface and internal waves, their evolution, interaction and associated wave-driven mean flows; on the other hand, phenomena related to nonlinear hydrodynamic stability and, in particular, those leading to the onset of turbulence. Close similarities and key differences exist between these two classes of phenomena.

In the hope to get hints on aspects of a potential overall vision, this study considers two different systems located at the opposite limits of the range of existing physical fluid flow situations: first, sheared parallel continuum flows - perfect incompressibility and charge neutrality - second, the solar wind - extreme rarefaction and electrical conductivity. Therefore, the activity carried out during the doctoral period consists of two parts. The first is focused on the propagation properties of small internal waves in parallel flows. This work was partly carried out in the framework of a MISTI-Seeds MITOR project proposed by Prof. D. Tordella (PoliTo) and Prof. G. Staffilani (MIT) on the long term interaction in fluid flows[1]. The second part regards the analysis of solar-wind fluctuations from in situ measurements by the Voyagers spacecrafts at the edge of the heliosphere. This work was supported by a second MISTI-Seeds MITOR project, proposed by D. Tordella (PoliTo), J. D. Richardson (MIT, Kavli Institute), with the collaboration of M. Opher (BU)[2,3].

1 MISTI-Seeds MITOR project “Long-term interaction in fluid systems" 2009-2012

2 MISTI-Seeds MITOR project “Laboratory simulation of planet-solar wind and interstellar medium/heliosphere interactions" 2012-2015

3 MISTI-Seeds MITOR project “Spectral analysis of the solar wind beyond the termination shock - interstellar medium/heliosphere interactions" 2015-2016

ACKNOWLEDGMENTS

I would like to thank my supervisor Prof. Daniela Tordella for her teachings, for providing me the opportunity to be part of this group and for her trust in me.

I am grateful to Dr. John D. Richardson for offering me the possibility to do research on solar wind, a totally new topic to me in 2013 when my PhD started.

I wish to thank Prof. John W. Belcher for giving me chance to work as a visitor at the MIT Kavli Institute for Astrophysics and Space Research in 2015 and for supporting, together with John Richardson, my application for a post-doctoral study period.

I acknowledge Prof. Gigliola Staffilani at the Mathematics Department at MIT, for her collaboration on hydrodynamic stability topics and her five-year support.

I thank Prof. Merav Opher for her collaboration on my research on solar wind topics, Prof. Enrico Magli and Dr. Sophie M. Fosson for their collaboration on data analysis.

I acknowledge the "Progetto MITOR" for providing financial support to my research. The Department of Control and Computer Engineering is acknowledged for providing computational resources at HPC@POLITO

I am grateful to a number of people I had the pleasure to work with:
I thank my colleagues from our research group "Philofluid": Francesca De Santi, Luca Gallana, and Michele Iovieno. I thank all the visiting students and the Master's students who worked with me: Mathieu Catchirayer (ENSTA ParisTech), Rachel Morgan (MIT), Ma Rubing (Beihang University), Kushan Tyagi (MIT), Loris Domenicale (Polito), Gabriele Nastro (Polito).

I express my gratitude to Daniela Foravalle, for her precious help and friendship.

I want to express my gratitude to my friends and colleagues Costantino Sardu and Stefano Valvano, for the time spent together during the last four years, and to all my other friends.

A special thank goes to Chiara.

The greatest acknowledgments are for my parents, my sister Valeria and my whole family.

CONTENTS

LIST OF FIGURES

LIST OF TABLES

PREFACE

Wave dynamics is at the basis of information transport in the broadest sense. Fluid waves can transport mass and energy, transmit forces and modify the system stability. Consequently, this subject links various physical contexts.

This doctoral research focuses on two multi-scale systems at opposite limits of the physics of fluids - incompressible continuum and collisionless magnetized plasma - and has internal wave motion as a common thread. The first topic of the thesis (Part 1) regards linear transient wave dynamics, which is governed by the perturbation theory of the Navier-Stokes equations in classical continuum mechanics. One aim of the research was to investigate the propagation properties of internal waves in sheared parallel flows during the transient evolution. We showed the possibility of dispersive and nondispersive components coexisting in the system and found that at a fixed value of the control parameter the transition between the two behaviors is ruled by specific wavenumber thresholds (§1.4, §2.3, figure 12). We then considered wave packets and highlighted how the above propagation characteristics can explain their morphology as well as some features which include nonlinear coupling which are fully expressed when the flow undergoes transition to turbulence (§2.4, §2.5). Another important aspect of wave dynamics is the transient wave amplitude, which is also crucial for the potential onset of the nonlinear coupling. In this regard, in place of the commonly observed wave kinetic energy we considered the perturbation enstrophy (the size of vorticity). In two-dimensions, we looked for the lower bound for transient growth of the integral enstrophy. This bound is closer to the region of the parameter space where nonlinear coupling can be expected than the bound computed in terms of perturbation kinetic energy(§3.4).

The second topic (Part 2) concerns the heliospheric fluctuations of the solar-wind, particularly those of the collisionless plasma present in the outermost region of the heliosphere. This region has been lately explored by the two Voyager spacecrafts, which measure *in loco* plasma velocity, magnetic field and energetic particle fluxes. Such plasma measurements would not be available without the work of Bruno Rossi, who was one of first researchers hypothesizing the existence of cosmic rays since the thirties [1,2]. In the fifties, he launched the idea of measuring cosmic rays with a spacecraft and, while at MIT, designed the Faraday cup which is still collecting unique plasma data at the edge of the heliosphere as far as 20 billions kilometers from Earth. This section of the thesis

1 B. Rossi. *Nature* 125 (1930)
2 B. Rossi. *Phys. Rev.* 45 (1932)

presents an experimental-data analysis on fluctuations of both the magnetic field and the plasma in the outer heliosphere.

At the time of Bruno Rossi's pioneering studies on cosmic rays, fluid motions of charged particles were also found to permeate the interplanetary space. The discovery of solar wind by Eugene Parker in 1958 [3] followed earlier studies by Sydney Chapman, as well as Ludwig Biermann's observations of comet tails in 1951. Hannes Alfvén in 1942[4] proved the existence of magnetohydrodynamic waves, which contributed to his Nobel Prize in Physics in 1971. Small-scale Alfvén waves were first detected in solar wind by John. W. Belcher in 1975[5]. The possibility to explore space via spacecraft, such as the Voyagers, led the way to intense research on collisionless plasmas and astrophysical turbulence. The huge separation of scales present in our heliosphere makes the latter a perfect laboratory to study the nature of multi-scale fluctuations, from the hydrodynamic scales to the kinetic ones.

With the aim of characterizing the multiscale nature of the wind fluctuations and possibly discriminating different physical processes, this work provides for the heliosheath the first broadband power spectra [4,5, in Part 2] over a frequency range of more than five decades (Chapter 5), that is from $f \approx 10^{-7}$ Hz (larger scales than the energy-injection scale) to 0.02 Hz, (beginning of the kinetic regime).

This was possible by fitting to this application six procedures for spectral estimation of highly gapped datasets. These procedure where inferred from different contexts, from astrophysics to telecommunication (the *compressed sensing* estimation was tested for the first time on turbulent data).

Since Alfvén's study, solar-wind has been supposed to be the ideal playground for the development of a kind of "turbulence" made of weakly interacting Alfvén wave packets (*wave turbulence*). However, very few specific observations of wave packets are available to date, due to the well known difficulty in discriminating them from turbulent structures. On the basis of spectra we obtained, we suggest that the heliosheath spectra are consistent with the coexistence of both strong turbulence and weak Alfvénic turbulence (§5.4). Furthermore, we highlight that special attention has to be paid to the interpretation of spectral slopes, since very close values may be associated with quite different physical processes.

Shear MHD Alfvén waves are typically considered nondispersive by the classical theory. In this theory, perturbation waves are considered merged in an average uniform field. However, it is not excluded that shear Alfvén waves can disperse, if the model includes other effects such as finite giroradius, viscosity/resistivity, or the presence of

3 E. N. Parker. *Astrophys. J.* 128 (1958)
4 H. Alfvén. *Nature* 150 (1942)
5 J. W. Belcher and C. V. Solodyna. *J. Geophys. Res* 80 (1975)

multiple fluids[6]. In addition we hypothesize that the presence of gradients of velocity and magnetic fields could considerably modify the dispersion properties in analogy to what we observed in the hydrodynamic context of waves in sheared fluid flows (see §4.6). As a consequence, threshold wavenumbers and coexistence of dispersive and nondispersive behavior may exist in magnetohydrodynamics as well as in hydrodynamics. Such a situation might be expected in the solar-wind system, where the folded-structure of the heliospheric current sheet determines magnetic sectors of opposite polarity. Together with analysis of transient energy growth, this may shed light on the mechanisms underlying the transport properties in the heliosheath, and on the observed scales of energy-injection for turbulent fluctuations.

Analysis of dispersion and non-normal growth for large-scale Alfvén waves due to magnetic shear is therefore proposed as a future line of research.

6 Zank et al. *ApJ* (2014)

Part I

Internal waves in sheared flows

PART 1 SUMMARY

The first part of the dissertation regards linear internal wave perturbation dynamics inside near-parallel incompressible flows such as plane Couette (PCF), plane Poiseuille (PPF), and the wake flows. The key aspects considered by this research are: (i) phase velocity temporal evolution; (ii) dispersion/non-dispersion properties and their relation to the morphology of linear wave packets. (iii) intermediate self-similarity; (iv) lower bound on the transient growth of the enstrophy perturbation.

In regard to point (i) above, we showed that for early and intermediate time, the phase velocity experiences clearly defined oscillations, which were observed for the first time in an explorative analysis of traveling perturbations in the two-dimensional wake flow, see figure 4 in [118]. The time scale associated with these wave accelerations/decelerations was found to be inversely proportional to the width of the eigenvalue spectrum of the governing equations. Moreover, the phase speed temporal evolution shows rapid variations in the intermediate term, which are symptoms of a rapid change of the perturbation distribution along the cross-stream direction. (ii) At any given Reynolds number, a new wavenumber threshold (k_d) was observed to affect the wave propagation characteristics. This threshold separates the dispersive ($k < k_d$) from the non-dispersive ($k > k_d$) solutions in the long term. The dispersive solutions are slow modes which belong to the left branch of the Orr-Sommerfeld eigenvalues spectrum. In this case, the perturbation has high vorticity in the high-shear region of the basic flow. In contrast, the non-dispersive modes are fast and belong to the right branch of the eigenvalues spectrum, where the phase velocity is almost equal to the basic flow speed. In this case, the perturbation vorticity is primarily located where the main flow has a low shear. Furthermore, evidence of self-similarity in the intermediate term was provided. This piece of work has been published in *Physical Review E*, 2016 [1] and promoted by several press releases [7]. Here, the reader can find any details in Chapter 1.

Point (iii) regards wave packets propagation in the plane Poiseuille flow. By assembling wave packets, it was possible to relate their morphology to the dispersion properties of the wave components inside the packet. In particular, the spot fast-moving front appears to be associated with the non-dispersive components ($k > k_d$). This can clarify the physical mechanisms determining the arrow-shaped morphology of spots and the

7 *AlphaGalileo*: `http://www.alphagalileo.org/ViewItem.aspx?ItemId=162474&CultureCode=en`
PhysOrg: `http://phys.org/news/2016-03-mechanisms-fluids.html`
PoliTo: `http://www.politocomunica.polito.it/press_room/comunicati/2016/le_onde_nei_fluidi_svelati_i_meccanismi_che_le_regolano%C3%A2%C2%80%C2%8B`

spatial spreading rates, a issue still debated in the literature (see Henningson, Johansson and Alfredsson, *J. Eng. Math.*, 1994, and Lemoult *et al.*, *Eur. Phys. J. E*, 2014). Note that this dynamics is also present in the formation of puffs in pipes (Duguet, Willis, and Kerswell, *J. Fluid Mech.*, 2010, and Manneville *Mech. Eng. Reviews*, 2016). As a consequence, we built a propagation scheme which is based on the group velocity directional distribution. It represents correctly the front, the leading edge and the spanwise tips of a linear spot. Moreover, by further examining the dispersion relation over a wide range of wave numbers ($k \in [10^{-2}, 10]$) and Reynolds numbers ($Re \in [10, 10^5]$) we observed the existence of niches of non-dispersion nested in regions of quite intense dispersion in the low-wavenumber part of the stability map. These topics will be be the subject of Chapter 2, and a publication is currently in preparation [4].

Point (iv) considers the wave enstrophy. No investigations on the enstrophy growth of linear wavy perturbations have been done since the thirties, when J. L. Synge raised the attention on the important role played by the vorticity field. The obstacle is represented by the boundary conditions which are not known a priori for the vorticity, and as a consequence for the enstrophy. In spite of this, Synge developed a procedure to overcome this difficulty, remaining inside the framework of the modal analysis (see Synge, *P. Lond. Math. Soc*, 1936, Synge, *Semicentenn. Publ. Amer. Math. Soc.*, 1938 and Synge, *Proc. Fifth. Intern. Congress of Appl. Mechanics*, 1938). By extrapolating Synge's ideas to the non-modal analysis (the initial value problem), we determined the lowest Reynolds number $Re_\Omega(k)$ allowing the transient growth of the 2D perturbation's enstrophy. We observed that this bound is less restrictive than that for the perturbation kinetic energy (see Orr, *Proc. R. Irish Acad* 1907 for 2D, and Joseph & Carmi, *Q. Appl. Math.*, 1969 for 3D). In particular, the smallest value is $Re^*_\Omega = 56.5$ for the PCF and 155 for PPF. Details can be found in Chapter 3 and in ref. [3] (under review, extended version available on ArXiv).

This work was partly carried out in the framework of a MISTI-Seeds MITOR project proposed by Prof. D. Tordella (PoliTo) and Prof. G. Staffilani (MIT) on the long term interaction in fluid flows[8].

8 MISTI-Seeds MITOR project "Long-term interaction in fluid systems" 2009-2012

1

LINEAR WAVES IN SHEARED FLOWS: A DISPERSIVE-TO-NONDISPERSIVE TRANSITION AND PHASE VELOCITY TRANSIENTS

The first chapter of this dissertation is concerned with the transient life of linear three-dimensional hydrodynamic waves traveling in sheared flows. The majority of results and methods presented here have been recently published in *Physical Review E* in 2016 [40]. Francesca De Santi is coauthor of that work, which overlapped in part with her research topics. Part of the following material can be inevitably found in our publication[1]. These analyses have been previously presented at the European Turbulence Conference in 2015 [7], and at the 68th Annual Meeting of the APS (DFD) [6].

1.1 **Summary**

In this study we analyzed the phase and group velocity of viscous, incompressible, three-dimensional linear waves, traveling in two archetypal sheared flows, namely the plane Poiseuille and the wake flows. The analysis were carried out by setting a large interval for the wavenumber, at a given value of the flow control parameter (the Reynolds number). Evidence is given about the presence of both a dispersive and nondispersive long-term behavior which is related to long and short wavelengths, respectively. By solving the Orr-Sommerfeld/Squire eigenvalue problem and by focusing on the least-stable mode, we showed that a specific wavenumber threshold (k_d) is the discriminant of such dual nature. In fact, for large wavelengths the least-damped eigenmode belongs to the tip of the left branch of the spectrum and behaves dispersively. Conversely, waves shorter than the threshold travel without dispersion. In this case, the dominant wave belongs to the right branch of the spectrum and travels with the basic flow speed. The Reynolds number was chosen in the ranges 20-100, 1000-8000 for the wake and channel flow, respectively.

The transient life of these hydrodynamic waves was then considered, with a focus on the temporal evolution of the phase speed in the early, intermediate and far terms. We investigated the origin of frequency oscillations and jumps which have been observed in a previous study [118] and at the publication time were still missing an explanation.

1 In agreement to the policy of the American Physical Society

An explanation was then delineated in the framework of my doctoral studies and published in 2016 [40], see §1.5. Eventually, we showed that the features of wave transients are highly affected by the dispersive-to-nondispersive wavenumber threshold introduced above. Furthermore, evidence of intermediate near-similarity was given for the perturbation field. It was shown that the temporal evolution is featured by a three-part structure, with an early, an intermediate and an asymptotic stage. This was possible by a careful investigation of the shape of the initial velocity perturbations.

1.2 **Introduction**

The relationship between the oscillation frequency ω and the wavenumber vector $\mathbf{k}$ - which is known as the dispersion relation - is a fundamental relationship in all areas of wave physics. Simply stated, the dispersion relation is the function $\omega(k)$. The ratio ω/k is the propagation speed c of the single wave, known as the phase velocity. In the simplest case of phase velocity independent of the wavenumber, the dispersion relation is simply $\omega(k) = ck$. As will be clarified in the following and in Chapter 2, this case is *nondispersive*. Intuitively, each component of a nondispersive wave packet propagates with the same speed, leaving the packet unmodified during its temporal evolution. However, this is not always the case. An example of *dispersion* is given by the propagation of light in a dielectric medium, where the index of refraction depends upon the wavelength. Another example is provided by the propagation of gravity waves in deep water. The last field is analogous with the results we present in the hydrodynamic context of viscous incompressible linear waves in sheared flows (no gravity effects), an objective of this dissertation (see §1.4).

In the hydrodynamic context of viscous incompressible flows, the motion of linear waves is governed by the well known Orr-Sommerfeld (OS) and Squire equations, that can be written in various ways. In particular, in the present study the wall-normal velocity/vorticity formulation is used (see §1.3). The modal OS equation is homogeneous and drives the Squire equation for the wall-normal vorticity. It yields a set of complex eigenvalues $\sigma = \sigma_\mathrm{r} + i\sigma_\mathrm{i}$, which depend on the Reynolds number and on the wavenumber. The associated modes were found to be non-orthogonal, a fact which is at the basis of the transient algebraic growth of perturbations kinetic energy [109, 130]. For confined flows, the Orr-Sommerfeld spectrum consists of an infinite number of discrete eigenvalues and it is complete [41]. For unbounded flows instead, only a finite number of discrete eigenvalues exists and thus a continuum of modes must exist, as shown by Grosch and Salwen [61] and Salwen and Grosh [116]. A dispersion relation can therefore be traced for each mode. The least-stable mode (LSM) eventually prevails in the long term. Temporal stability analyses have been usually focused on the range of wavenumbers where the maximum temporal growth rate σ_i is positive and in general the information on the

relation $\sigma_i(k)$ is more abundant with respect to the corresponding $\sigma_r(k) = \omega(k)$ [62, 61, 63, 33, 36, 120].

Spectral theory of hydrodynamic waves in neutral fluids has been developed to a high degree of sophistication, with intricate analytical tools supplemented by accurate multi-dimensional computational methods [130, 109, 73, 98, 129]. Nevertheless, unresolved key issues in this classical problem can be still identified. The present chapter focuses on the following points:

(i) The frequency (and by extension the phase velocity) of a wavy perturbation, with a fixed wavelength and at a chosen Reynolds number, varies considerably during a typical transient response. In particular, *periodic variations* and *abrupt jumps* have been observed by our group, see references [118, 119]. An explanation was still missing. Recently [40], we provided an explanation by relating these phenomena to the structure of the eigenvalue spectrum. Here, we also exploit this knowledge to reason on the physical phenomenology of wave packet propagation.

(ii) The complicated branched structure of the eigenvalues spectra is well known. However some aspects have not been fully examined yet: what are the necessary conditions to observe dominant dispersive (or non-dispersive) modes? Is there a discriminant wavelength between the two behaviors, and why? How could this affect the wave transient evolution?

(iii) Is intermediate self-similarity of perturbation profiles possible inside transients?

In the first instance we analysed the dispersion relationship of the least stable OS mode, for a wide range of wavenumbers, that is $k \in [0.2, 20]$. This interval extends from below to well above the eventual instability range. We considered two classical incompressible sheared flows, the plane Poiseuille flow and wake flow. The analysis was carried out by setting the Reynolds number in the range $1000 - 8000$ for the channel flows, and in the range $20 - 100$ for the wake. The aim was to highlight possible variations of the dispersion features for different wavenumbers. In fact, we observed the existence of a wavenumber threshold (k_d, in the following) separating waves which propagate dispersively from those which propagate in a non-dispersive way. While of interest for the study of wave packets (subject of Chapter 2), we show that the existence of this dispersive/non-dispersive transition can also affect the transient dynamics of single traveling waves.

It should be mentioned that these topics can be of great interest in magnetohydrodynamics, where dispersive effect for the large-scale shear Alfvén wave are not considered possible by the classical theory but may arise in the case of strong gradients of the magnetic and velocity fields (a situation of interest for both astrophysical and laboratory plasmas). Moreover, applications of the nonmodal theory in this field are much more recent [25] and still limited to the kinetic regime (see the discussion in §4.6).

In this chapter, the temporal evolution between the early transient and the asymptotic state is considered in details. It is observed that under certain conditions - which we determine and classify - the evolution can be characterized by phase velocity jumps. This implies that the perturbation may experience acceleration or deceleration during its life. This behavior was found to depend firstly on if the perturbation's wavelength is smaller or greater with respect to the dispersive/non-dispersive threshold introduced above, and secondly on the location of the initial disturbance's vorticity peak.

1.3 **Physical problem and mathematical formulation**

Two typical sheared flows are considered: the plane Poiseuille flow (PPF), an archetype of bounded flows, and the plane bluff-body wake, one of the few unbounded-flow archetypes. A Cartesian coordinate system is adopted, with origin located at the channel mid plane in the first case and at the bluff-body location in the wake case. The x, y, z axis are oriented in the streamwise, cross-shear and spanwise directions, respectively (see figure 1). After introducing arbitrary small perturbations, the linearized, viscous, incompressible Navier-Stokes and continuity equations in non-dimensional form read

$$\partial_x \widetilde{u} + \partial_y \widetilde{v} + \partial_z \widetilde{w} = 0 \tag{1}$$

$$\partial_t \widetilde{u} + U\partial_x \widetilde{u} + \widetilde{v}U' + \partial_x \widetilde{p} = \frac{1}{Re}\nabla^2 \widetilde{u} \tag{2}$$

$$\partial_t \widetilde{v} + U\partial_x \widetilde{v} + \partial_y \widetilde{p} = \frac{1}{Re}\nabla^2 \widetilde{v} \tag{3}$$

$$\partial_t \widetilde{w} + U\partial_x \widetilde{w} + \partial_z \widetilde{p} = \frac{1}{Re}\nabla^2 \widetilde{w} \tag{4}$$

where $(U(y),0,0)$ is the unperturbed basic state ($\widetilde{u}(x,y,z,t)$, $\widetilde{v}(x,y,z,t)$, $\widetilde{w}(x,y,z,t)$) and $\widetilde{p}(x,y,z,t)$ are the components of the perturbation velocity and pressure, respectively. The domain is $-\infty < x, z < \infty$, $-1 < y < 1$ for the channel flow, and $0 < x < \infty$, $-\infty < z < \infty$, $-\infty < y < \infty$ for the wake. No-slip boundary conditions for the channel flow imply vanishing perturbation velocity at the walls, $\widetilde{u} = \widetilde{v} = \widetilde{w} = 0$ as $y = \pm 1$, while decaying disturbances are considered for the wake flow, which is unbounded also in the cross-flow direction, so that $\widetilde{u}, \widetilde{v}, \widetilde{w} \to 0$ as $y \to \infty$.

The channel half-width h, and the body diameter D are considered as reference external length scales. The reference velocity for the channel flow is the centerline velocity U_{CL}, while in the wake case the free-stream velocity U_f is considered. The reference time is the convective one. Consequently, the flow control parameter is the Reynolds number, defined as $Re = U_{CL}h/\nu$, for the channel flow, and $Re = U_f D/\nu$ for the wake flow, where ν is the kinematic viscosity. The channel basic flow is represented by the plane Poiseuille solution

$$U(y) = 1 - y^2. \tag{5}$$

As an expression of the wake flow, we use the first two orders of the Navier–Stokes solution described in [14, 127] and reported below:

$$U(y; x_0, Re) = C_0 - \frac{1}{\sqrt{x_0}} C_1 e^{-Re\ y^2/(4x_0)}, \tag{6}$$

where $C_0 = 1$ and $C_1 = 1.22 + 0.000067Re^2$ and x_0 is a streamwise location. The two-dimensional laminar wake is a spatially evolving free flow. Leaving aside the near field, which is highly non-parallel since it hosts the two symmetric counter-circulating vortices in the separation region, the intermediate and long term wake is a near-parallel flow. The wake slowly becomes thicker according to a law which, at first order, scales as $(x/Re)^{0.5}$. As a representation of this steady sub-critical flow, we consider the previously mentioned asymptotic expansion in inverse powers of x (valid in the range of Reynolds numbers $[20, 100]$) which was also used in convective instability intermediate-asymptotics analysis [15, 128, 119]. In particular, we consider the intermediate/far field, well represented by streamwise sections located in the interval $x \in [5, \infty]$. In the present study indeed, the wake basic flow is frozen at three longitudinal stations placed at $x_0 = 10, 20, 50$. In so doing, the basic flow is parametrized with x_0 and the Reynolds number. It is thus homogeneous in x and z. The momentum equations 2-4 can be expressed in terms of the velocity-vorticity formulation:

$$\big[(\partial_t + U\partial_x)\nabla^2 - U''\partial_x - \frac{1}{Re}\nabla^4\big]\widetilde{v} = 0 \tag{7}$$

$$\big[\partial_t + U\partial_x - \frac{1}{Re}\nabla^2\big]\widetilde{\omega}_y = -U'\partial_z\widetilde{v} \tag{8}$$

$$\widetilde{\omega}_y = \partial_z\widetilde{u} - \partial_x\widetilde{w}. \tag{9}$$

Eqs. (7,8,9) are solved by means of a combined Fourier–Fourier (channel) and Laplace–Fourier (wake) transform in the plane normal to the basic flow profile. The transformation of a generic quantity $\tilde{q}(x, y, z, t)$ reads:

$$\widehat{q}(y, t; \alpha, \beta) = \int_{-\infty}^{+\infty} \int_{0,-\infty}^{+\infty} \widetilde{q}(x, y, z, t) e^{-i\alpha x - i\beta z}\, \mathrm{d}x, \mathrm{d}z \tag{10}$$

where α and β are the streamwise and spanwise wavenumbers, respectively. Our analysis only considers real wavenumbers. However, for the wake flow the formulation allows one to take into account spatially evolving waves. In the channel case this would lead to unphysical results (infinite energy) due to the unboundedness of the independent spatial variable $x$and $z$which take values in $(-\infty,\infty)$ (damping factor in the positive half domain becomes an amplification factor in the other half domain, which leads to infinite energy). The wavenumber modulus is $k = \sqrt{\alpha^2 + \beta^2}$ and the wave angle with

Table 1: Initial conditions imposed on the velocity, $\widehat{v}_0 = \widehat{v}(0, y)$. For the channel flow they are named SC/AC: symmetric/ antisymmetric and central. SW/AW: symmetric/antisymmetric and wall-located (the initial condition has large variations close to the channel walls). For the wake flow, SI/AI: symmetric/antisymmetric and inside-wake. SO/AO: symmetric/antisymmetric and out-of-wake (see figure 5).

I.C.	Wake flow	Channel flow
SI/SC	$\widehat{v}_0 = e^{-y^2}\cos(y)$	$\widehat{v}_0 = e^{-\frac{y^2}{0.01}}\cos(3y)$
AI/AC	$\widehat{v}_0 = e^{-y^2}\sin(y)$	$\widehat{v}_0 = e^{-\frac{y^2}{0.01}}\sin(3y)$
SO/SW	$\widehat{v}_0 = e^{-(y-10)^2} + e^{-(y+10)^2}$	$\widehat{v}_0 = (1-y^2)^2$
AO/AW	$\widehat{v}_0 = e^{-(y-10)^2} - e^{-(y+10)^2}$	$\widehat{v}_0 = y(1-y^2)^2$

respect to the basic flow is $\phi = \tan^{-1}(\beta/\alpha)$, see figure 1. The governing equations in the wavenumber space are thus formulated:

$$\left[\left(\partial_t + i\alpha U\right)\left(\partial_y^2 - k^2\right) - i\alpha U'' - \frac{1}{Re}\left(\partial_y^2 - k^2\right)^2\right]\widehat{v} = 0 \tag{11}$$

$$\left[\left(\partial_t + i\alpha U\right) - \frac{1}{Re}\left(\partial_y^2 - k^2\right)\right]\widehat{\omega}_y = -i\beta U'\widehat{v}. \tag{12}$$

The streamwise and the spanwise velocity components can be recovered *a posteriori* from $\widehat{v}$ and $\widehat{\omega}_y$. The following expressions come from the continuity equation and from the definition of wall-normal vorticity:

$$\widehat{u} = \frac{i}{k^2}\left(\alpha\frac{\partial\widehat{v}}{\partial y} - \beta\widehat{\omega}_y\right) \tag{13}$$

$$\widehat{w} = \frac{i}{k^2}\left(\beta\frac{\partial\widehat{v}}{\partial y} + \alpha\widehat{\omega}_y\right), \tag{14}$$

The boundary conditions associated with the system 11-12 for the channel flow are

$$\widehat{v}(\pm 1, t) = \partial_y\widehat{v}(\pm 1, t) = \widehat{\omega}_y(\pm 1, t) = 0, \tag{15}$$

while in the wake case we consider finite-energy harmonic velocity as $|y| \to \infty$, and vanishing vorticity in the free-stream, see also [61] and [118]:

$$\partial_y^2\widehat{v} = k^2\widehat{v}, \quad \widehat{\omega}_y = 0 \qquad y \to \pm\infty, \forall t. \tag{16}$$

The initial conditions are given in table 1, and shown in figure 5, §1.5.

The eigenvalues $\sigma = \sigma_r + i\sigma_i$ and the eigenfunctions associated with the system 11-12 are computed by means of three different methods: a 5^{th}-order Galerkin method based on Chandrasekhar functions expansion (see [48], and Appendix A), a finite difference 4^{th}-order scheme, [117], and a hybrid spectral collocation method based on

Chebyshev polynomials [120]. A comparison of this techniques and the details of the first method are given in Appendix A, see figure 81.

Two different numerical methods[2] are used to solve the initial value problem: (i) the method of lines, based on finite difference spatial discretization and a Runge-Kutta (2,3) temporal integration scheme, and (ii) the 5^{th}-order Galërkin method based on the Chandrasekhar functions expansion cited above. The results obtained by the two approaches are in agreement.
The computational domain is $[-y_f, y_f]$. For channel flows $y_f = 1$, while for the wake flow y_f is defined so that the numerical solution be insensitive to further extensions of the computational domain size ($y_f = 20$ for short waves and y_f up to 100 for long waves). The solution computed by the initial-value formulation at long enough time shows agreement with the behavior predicted by the modal analysis.

In order to measure the growth of perturbations, a specific norm has to be chosen. We define the integral kinetic energy density as

$$e(t;\alpha,\beta) = \frac{1}{4y_f}\int_{-y_f}^{+y_f} (|\widehat{u}|^2 + |\widehat{v}|^2 + |\widehat{w}|^2)\,\mathrm{d}y. \tag{17}$$

Then the amplification factor G, is introduced as the kinetic energy density normalized with respect to its initial value,

$$G(t;\alpha,\beta) = e(t;\alpha,\beta)/e(t=0;\alpha,\beta). \tag{18}$$

Since the temporal asymptotic behavior of the linear perturbations is exponential, the temporal growth rate r is defined [36] as

$$r(t;\alpha,\beta) = log(G)/(2t). \tag{19}$$

The temporal evolution of the perturbation's integral kinetic energy is given by the Reynolds-Orr equation; in wavenumber space it reads

$$\begin{aligned}\frac{\mathrm{d}e}{\mathrm{d}t} = \quad & \frac{1}{k^2}\Im\int U'\left(\alpha\bar{v}\partial_y\widehat{v} - \beta\bar{v}\widehat{\omega}_y\right)\,\mathrm{d}y \\ - \quad & \frac{1}{Re\ k^2}\int\Big(|\partial_y^2\widehat{v}|^2 + 2k^2|\partial_y\widehat{v}|^2 + k^4|\widehat{v}|^2 \\ + \quad & |\partial_y\widehat{\omega}_y| + k^2|\widehat{\omega}_y|^2\Big)\,\mathrm{d}y,\end{aligned} \tag{20}$$

where the bar indicates the complex-conjugate and $\Im$ is the imaginary part. While the dissipative term is always negative, the convective term has undetermined sign and can

2 Our codes are open source, distributed under the GNU General Public License. Find the software and related manuals at the *Philofluid* website `http://areeweb.polito.it/ricerca/philofluid/software.html`

be responsible for kinetic energy growth. The same equation in the physical space is written:

$$\frac{\mathrm{d}E}{\mathrm{d}t} = \underbrace{-\int \frac{\mathrm{d}U}{\mathrm{d}y}\widetilde{u}\widetilde{v}\,\mathrm{d}\mathcal{V}}_{Production} \underbrace{-\frac{1}{Re}\int |\nabla\widetilde{u}|^2 + |\nabla\widetilde{v}|^2 + |\nabla\widetilde{w}|^2\,\mathrm{d}\mathcal{V}}_{Dissipation}, \tag{21}$$

where $\mathcal{V}$ is an arbitrary three-dimensional domain. An important consideration is that nonlinear terms of the momentum equation drop out of the above equation due to integration over the volume. As a consequence, the growth rate of the disturbance is independent on its initial amplitude, which means that kinetic energy growth is uniquely governed by linear mechanisms [71]. From this equation it is possible, by means of the variational method, to obtain conditions for flow *monotonic stability*, see Appendix B.

The (time-dependent) frequency of the perturbation ω is defined as the temporal derivative of the unwrapped wave phase $\theta(y,t;\alpha,\beta)$, at a specific spatial point along the y direction. The wrapped phase,

$$\theta_w(y,t;\alpha,\beta) = \arg\,\widehat{v}(y,t;\alpha,\beta), \tag{22}$$

is a discontinuous function of t defined in $[-\pi,+\pi]$, while the unwrapped phase θ is a continuous function obtained by introducing a sequence of 2π shifts on the phase values in correspondence to the periodical discontinuities. In the case of the wake we compute the frequency at a reference transversal observation point $y_0 = 1$ or $y_0 = 5$, and in the case of the channel flow at $y_0 = 0.5$. The frequency [118] is thus

$$\omega(t;y_0,\alpha,\beta) = |d\theta(t;y_0,\alpha,\beta)|/\,\mathrm{d}t. \tag{23}$$

The phase velocity is defined as

$$\boldsymbol{c} = (\omega/k)\mathbf{e_k}, \tag{24}$$

where $\mathbf{e_k} = \cos(\phi)\mathbf{e_1} + \sin(\phi)\mathbf{e_3}$ is the unit vector in the direction of $\mathbf{k}$.

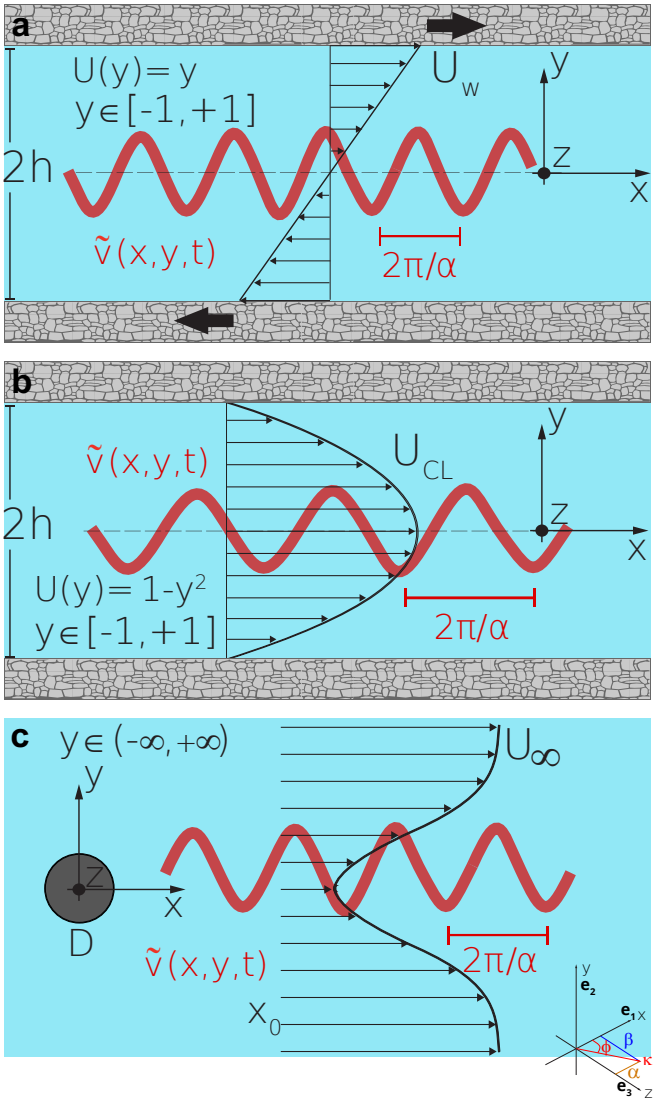

Figure 1: Sketch of basic flows, reference systems and reference quantities. A Cartesian reference frame is adopted, with unit vectors $\mathbf{e_1}$, $\mathbf{e_2}$, $\mathbf{e_3}$ in the x (streamwise), y (normal), z (spanwise) directions, respectively. The basic flow profiles are qualitatively represented in black with arrows. $\mathbf{k} = \alpha\mathbf{e_1} + \beta\mathbf{e_3}$ is the wavenumber vector, ϕ is the wave angle with respect to the basic flow $\mathbf{U} = U(y)\mathbf{e_1}$. In the physical domain, x is unbounded for the channel flows and positive for the wake flow. However, due to the adoption of the frozen-flow approximation, also the wake flow is unbounded. The spanwise coordinate z is unbounded for all flows. **(a)** Plane Couette flow (PCF), a flow driven by two sliding walls. The reference length is the channel half-heigth h, the reference velocity is the wall speed U_w. The Reynolds number is $Re = U_w h/\nu$, where ν is the kinematic viscosity. **(b)** Plane Poiseuille flow (PPF), a flow between two fixed walls, driven by the pressure gradient. The reference length is again the channel half-height h, the reference velocity is the centerline velocity U_{CL}. Thus the Reynolds number is $Re = U_{CL} h/\nu$. **(c)** Wake flow. The reference length is the cylinder diameter D, the reference speed is U_∞. The red oscillation represents a generic perturbation with streamwise wavenumber α. Part of this figure will be used in [49].

1.4 Dispersive to non-dispersive transition in the long term

The focus of this section is on the long-term temporal behavior of small-amplitude traveling waves, and on the relation between the frequency of the least stable eigenvalue and its wavenumber. The wavenumber is within the range $k \in [0.2, 20]$, which was numerically discretized with a small step, $\Delta k = 0.005$. This allowed an accurate computation of phase and group velocity diagrams in order to highlight a transition from dispersive to non-dispersive behavior.

This transition proves to be important to understand the temporal evolution of general arbitrary initial perturbations, which is the object of the next sections. The results here presented in tables 2 and 3 and in figure 4 have been compared with literature data obtained by means of different methods of investigation, in particular laboratory experiments, modal and initial-value problem analysis.

Figure 4 (**a, b**) shows the dependence of the phase velocity c on the polar wavenumber k. In both the flows we observed the existence of a threshold wavenumber that we named k_d where a step variation of the phase velocity occurs. For $k > k_d$ the phase velocity is approximately constant and is nearly equal to the group velocity $v_\mathrm{g} = \mathrm{d}\omega/\,\mathrm{d}k$, a fact which highlights a non-dispersive behavior. For $k < k_d$ instead, c depends on k and hence behavior is dispersive. These concepts will be more extensively covered in the next chapter, focused on wave packets, see 2.2.

In other words, inside the range of wavenumbers that can be hosted in the system, there is a threshold above which the least stable mode is always on the tip of the right branch (*P-branch*) of the eigenvalue spectrum (about the branched structure of the eigenvalue spectrum, see figure 2, figure 6 (**d**, **h**), or references [94, 120, 36]). In this case, the frequency of the least stable mode increases proportionally to the wavenumber, which yields non-dispersion. Vice-versa, below this threshold the least stable mode is located on the tip of the left branch (*A-branch*). By varying the wavenumber one sees that this least-stable mode does not vary proportionally to the wavenumber, which yields dispersion. In terms of phase and group velocity, this threshold yields a sharp transition since the tips of the left and right branches of the eigenvalue spectrum have substantially different frequencies, see again figure 6, panels (**d**,**h**).

A question naturally arises: why does the set of least-damped waves become non-dispersive above a specific k?

In this regard, by looking at the Orr-Sommerfeld solutions in both the case of wave dispersion and nondispersion, we highlighted few features common to both flows, which are summarized in the following. As already shown, it can be observed that when $k < k_\mathrm{d}$ the least-stable OS eigenvalue is located on the tip of the left branch of the eigenvalues spectrum. The related velocity eigenfunction is a *shear mode*: the largest perturbation

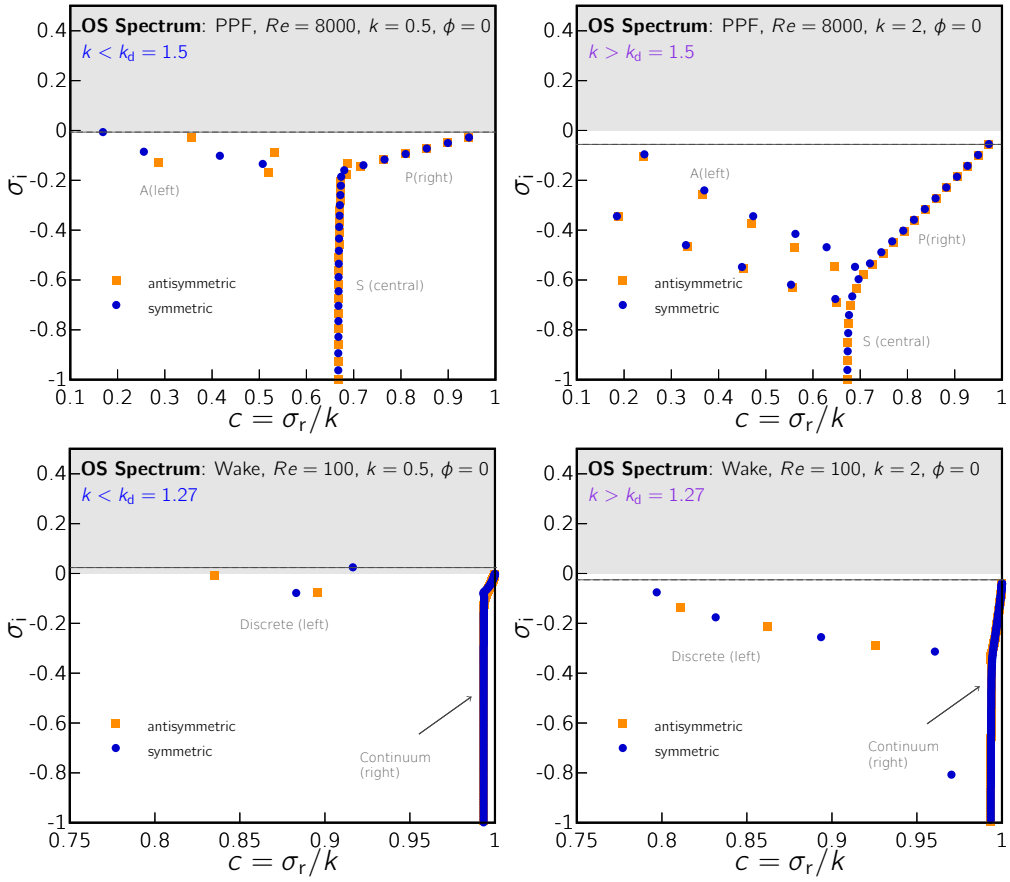

Figure 2: The Orr-Sommerfeld eigenvalues spectrum of the plane Poiseuille and wake flows. The figure shows the structure of the Orr-Somemerfeld eigenvalues spectrum for the wall-normal perturbation velocity $\hat{v}$, when $k < k_d$ (left panels) or when $k > k_d$ (right panels). Note the location of the least-damped mode, which is highlighted with a dashed line. Top panels show the plane Poiseuille case, while bottom panels show the wake flow case. The three branches of the PPF spectrum have been labeled *A-, P-, S-branch* by Mack in 1976 [94]. In the case of unbounded sheared flows, such as the wake flow, both a continuous spectrum and a discrete one exist.

variations ($\partial_y \hat{v}$) are located where the basic flow vorticity $\mathrm{d}U/\mathrm{d}y$ is high (in the shear region). This region is located close to the walls for the plane Poiseuille flow, while it is close to the inflection points in the wake flow. We refer to these perturbations as *wall modes* for channel flow, and *in-wake modes* for the wake. Vice-versa, when $k > k_d$ the least-stable eigenvalue is located on the tip of the right branch and the dominant perturbation is an *external mode*: in this case the perturbation varies rapidly where the basic flow vorticity is low (out of the high-shear region). In synthesis, in any case,

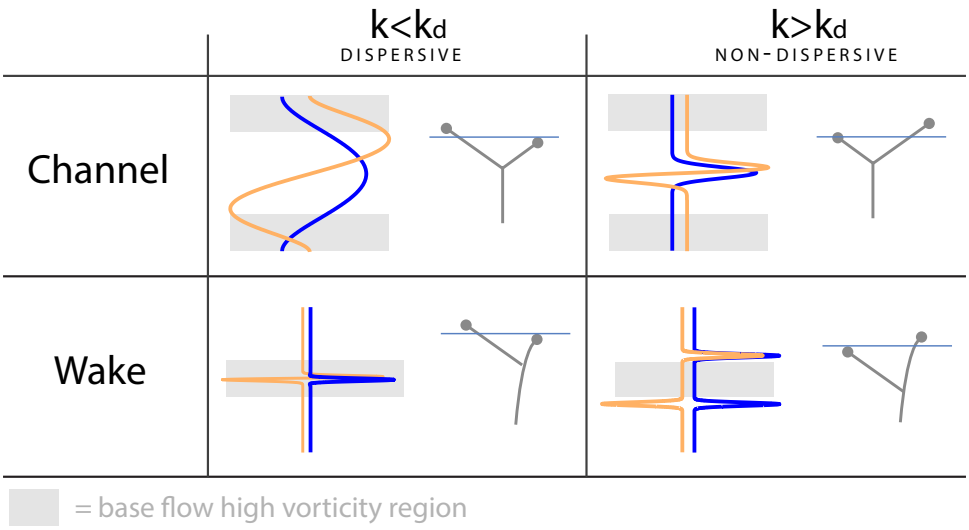

Figure 3: Qualitative representation of the shape of the least-stable mode for k above and below the threshold value. The figure qualitatively represents the shape of the least-damped mode when the wavenumber is below (left) or above (right) the dispersive-to-nondispersive transition value k_d. The figure also shows, for each case, the structure of the eigenvalues spectrum (σ_r vs σ_i). Here, the purpose of the horizontal bar is to highlight which branch is dominant; it is reminded that the right branch never contains unstable eigenvalues. Notice the reciprocal location of the perturbation's high-variations and the basic flow high vorticity.

when the wavelength of a perturbation is short enough ($k > k_\mathrm{d}$) the dominant mode variation $\partial_y \widehat{v}$ is confined in a region of low basic-flow vorticity. Here it is interesting to note that the dispersion relation of the least-damped modes is similar to the dispersion relation for a uniform basic flow, where only the continuum spectrum exists and the wave propagation is convective and non-dispersive, $c = U$ (this can be analytically derived, see [120, §3.2]). In this case, we refer to such solution as *central modes* for the Poiseuille flow, and *out-of-wake modes* for the wake flow.

Coming back to the comparison with data in the literature, one can see that the agreement between laboratory data as well as numerical modal analysis and our work is very good. In particular, as regards PPF, we observe a good agreement with the works of Grosh & Salwen 1968 [62], Ito 1974 [78], Nishioka et al. 1975 [99], and Asai & Floryan 2006 [8] (see panel (**a**) of figure 4). Grosh & Salwen give the least stable eigenvalues in the range $\alpha \in [1-2.4]$, $\phi = 0$ and $Re \in [5-25000]$ (under our normalization). Asai & Floryan investigated experimentally the effects of wall corrugation on the stability of wall-bounded shear flows and found a good agreement with the Orr-Sommerfeld theory coupled to roughness in the form of a single Fourier harmonic and in the form

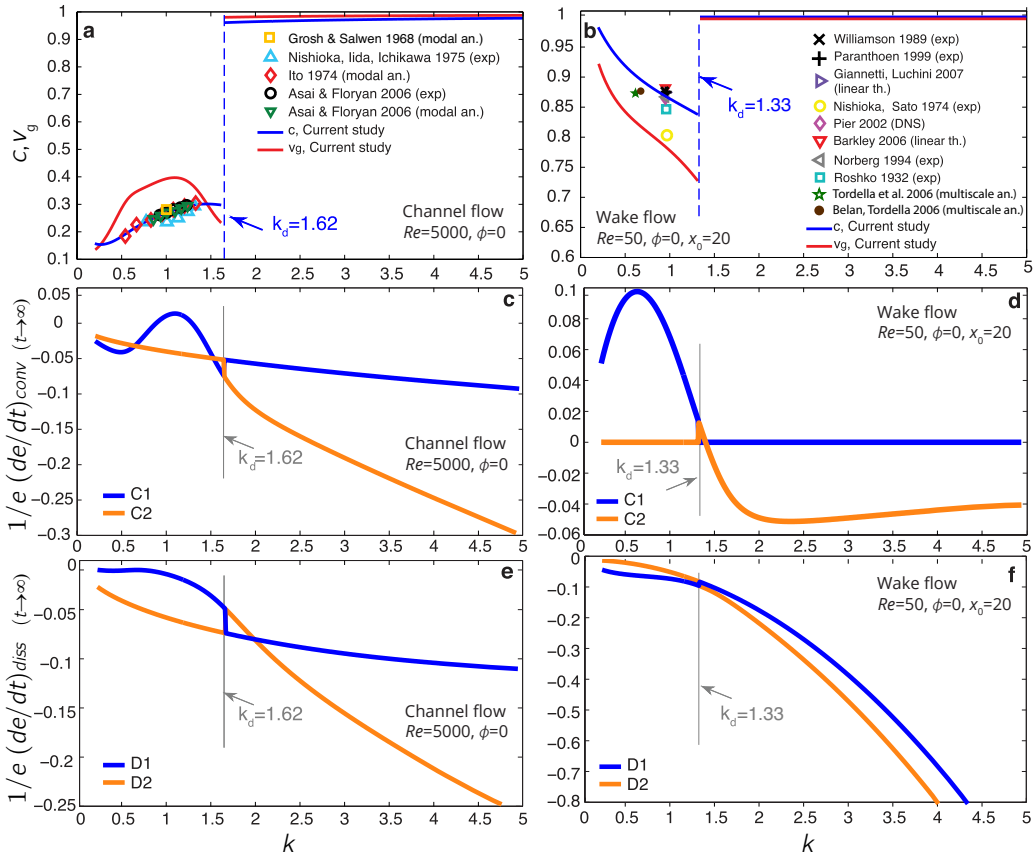

Figure 4: Dispersion relations for longitudinal waves ($\phi = 0$) in the plane Poiseuille and the wake flow. Results from modal analysis of the least-damped modes are shown. **(a,b)** Phase (blue) and group (red) velocity as a function of the wavenumber and comparison with other studies. The wavenumber range $[0.2, 5]$ is discretized with $\Delta k = 0.005$. k_d indicates the threshold value that separates dispersive from non-dispersive waves. **(a)** Channel flow at $Re = 5000$, and comparison with other studies, see Grosh & Salwen 1968 [62], Ito 1974 [78], Nishioka *et al.* 1975 [99], Asai & Florian 2006 [8]. **(b)** Wake flow, $Re = 50$ and $x_0 = 20$. Here $k_\mathrm{d} = 1.32$. Comparison with the phase velocity values found by Roshko 1974 [114], Nihsioka & Sato 1974 [100], Williamson 1989 [138], Norberg 1994 [101], Paranthoën *et al.* 1999 [106], Pier 2002 [107], Barkley 2006 [10], Belan & Tordella 2006 [15], Tordella *et al.* 2006 [128], Giannetti & Luchini 2007 [60]. Wherever not available, the wavelength was set equal to the mean of the values measured by Paranthoën et al. ($\lambda = 7D$) and Williamson ($\lambda = 7.15D$). **(c-f)** Convective and dissipative terms of energy rate (25) for the two least-stable modes of the left and right branch of the OS spectrum. Blue curves represent the least-damped solution. Figure published in [40].

of spanwise grooves with rectangular and triangular shapes [47].

For the wake flow, it should be observed that in literature data are mostly focused

on the value of the shedding frequency. Our references include the works by Roshko 1954 [114], Nishioka & Sato 1974 [100], Williamson 1989 [138], Norberg 1994 [101], Paranthöen *et al.* 1999 [106], Pier 2002 [107], Barkley 2006 [10], Belan & Tordella 2006 [15], Tordella *et al.* 2006 [128], and Giannetti & Luchini 2007 [60]. The agreement is good also in this case. Indeed, the relative error with respect to the measurements by Williamson and Paranthöen *et al.* is about 3.3%. We would like to remind the reader that wake data in the literature typically provide information on the vortex-shedding frequency but barely give information about the wavenumber of the shedding. Thus for the cited works, in the case of lack of wavenumber data, we chose to assign to the reported frequency values the average wavenumber among the measurements currently available at $Re = 50$, that is Williamson [138] and Paranthöen [106]. Hence, apart form the two points provided by from near-parallel multiple-scale convective analysis [15, 128], all the points in figure 4 have been traced at the same wavenumber.

The threshold k_d is a function of the Reynolds number and the wave angle, as can be inferred from tables 2 and 3. For the wake flow, which is weakly evolving in the streamwise direction, it is also a function of the streamwise location x_0. In particular, for the channel flow, values of k_d have been computed in the range $Re \in [1000, 8000]$ and $\phi \in [0, \pi/3]$. We observe that k_d decreases as the wave angle and increases as the Reynolds number. The trend $k_\mathrm{d}(Re)$ is reversed for the wake flow, see table 3 where the range $Re \in [20, 100]$ was considered, being the range of validity of the basic flow expression. Here the dependence on the location x_0 is also shown for ($x_0 = [10, 20, 50]$), in particular k_d decreases with x_0. Considering that the computed values of nondimensional k_d are of order unity, one could in the first instance roughly observe that the system becomes nondispersive when the wavelength exceeds the size of the system (the channel height and the bluff body diameter). However this is not totally correct, as we put in evidence that k_d varies with the control parameters so it does not depend only on the system size.

In the case of the plane Poiseuille flow, the range of the dispersive wavenumbers narrows as Re increases (see also figure 13 in §2.3). For the wake flow, the opposite occurs. This may not be intuitive but one can consider that with increasing Re, even if the wake becomes narrower, the shear intensity increases and the range of dispersive waves broadens. On the contrary, the wake becomes weaker and closer to uniformity as x_0 increase, and the range of non-dispersive waves increase. This supports the idea that the intensity and distribution of the basic vorticity plays a key role in the dispersion, even though further investigations are needed to understand the nature of the discriminant wavelength.

A parallel with surface gravity water waves

A parallel is proposed with the fluid system which is probably most known to all readers: the system of linear surface gravity waves in incompressible flows (see, for instance [137]). In that context, the dispersion relation can be analytically obtained under a set of simplifying hypothesis, by looking for an exponential mode along the vertical coordinate z. The dispersion relation is $\omega = \pm\sqrt{gk\tanh(kH)}$ ($k = 2\pi/\lambda$ dimensional wavenumber, H water depth, g gravitational acceleration). Two limiting cases are observed, the (i) *deep-water waves* ($\lambda/H \ll 1$): here $\omega = \pm\sqrt{gk}$, $c = \pm\sqrt{g/k} = 2v_g$, which are dispersive; (ii) the *shallow-water waves* ($\lambda/H \gg 1$), which travel in a non-dispersive way since $\omega = \pm\sqrt{gk^2H}$, $c = v_g = \pm\sqrt{gH}$.
It can be noticed that, analogously to our system of internal waves in sheared flows, also here two limiting behaviors in terms of dispersion are observed to occur according to the wavelength value with respect to a typical length scale ($2\pi/k_d$ in our case, H in the gravity wave case). However, it is interesting to observe that the occurrence of dispersion/non-dispersion for gravity waves is opposite with respect to the system of internal waves in sheared flows. That is, for surface gravity waves, fast long waves **do not** disperse while slow short ones do.
The system of internal waves in sheared flows has become less popular to both the general public - for the lack of everyday experience - and to specialists for the difficulty of doing noise-free experiments and the scarcity of analytical results. The spectral structure is nonetheless quite complicated due to the concomitant presence of infinite wave-modes having different dispersion properties and damping rates. Understanding the nature of such a structure and the reasons for exchange of least-damped modes at specific wavelength thresholds is a challenging issue.

Table 2: Values of the dispersive/non-dispersive regime threshold wavenumber k_d for the plane Poiseuille flow, at various Reynolds numbers and wave angles. The uncertainty on k_d due to the numerical discretization is ± 0.005.

	Channel flow			
Re	$\phi = 0$	$\phi = \pi/6$	$\phi = \pi/4$	$\phi = \pi/3$
1000	2.071	2.111	2.168	2.256
2000	1.883	1.922	1.979	2.073
3000	1.764	1.803	1.866	1.960
4000	1.686	1.725	1.784	1.878
5000	1.623	1.662	1.721	1.815
6000	1.576	1.615	1.670	1.765
7000	1.536	1.568	1.627	1.720
8000	1.497	1.536	1.589	1.682

Table 3: Computed values of the dispersive/non-dispersive regime threshold k_d (the uncertainty is ± 0.005) for the wake flow, at various Reynolds numbers, wave angles and streamwise locations x_0.

		$x_0 = 10$		
Re	$\phi = 0$	$\phi = \pi/6$	$\phi = \pi/4$	$\phi = \pi/3$
20	1.073	1.032	0.977	0.868
30	1.373	1.333	1.276	1.154
40	1.636	1.598	1.534	1.407
50	1.875	1.835	1.772	1.640
60	2.091	2.052	1.989	1.862
70	2.293	2.253	2.195	2.068
80	2.485	2.448	2.390	2.264
90	2.663	2.628	2.575	2.453
100	2.837	2.802	2.749	2.633
		$x_0 = 20$		
Re	$\phi = 0$	$\phi = \pi/6$	$\phi = \pi/4$	$\phi = \pi/3$
20	0.758	0.735	0.696	0.617
30	0.974	0.946	0.903	0.817
40	1.158	1.131	1.087	0.997
50	1.326	1.298	1.251	1.161
60	1.478	1.451	1.408	1.318
70	1.623	1.596	1.553	1.463
80	1.756	1.733	1.689	1.604
90	1.885	1.858	1.819	1.737
100	2.001	1.983	1.944	1.862
		$x_0 = 50$		
Re	$\phi = 0$	$\phi = \pi/6$	$\phi = \pi/4$	$\phi = \pi/3$
20	0.482	0.461	0.441	0.401
30	0.615	0.593	0.573	0.522
40	0.732	0.714	0.684	0.633
50	0.840	0.815	0.795	0.734
60	0.935	0.916	0.886	0.835
70	1.026	1.007	0.977	0.926
80	1.112	1.088	1.068	1.007
90	1.189	1.169	1.148	1.098
100	1.267	1.249	1.229	1.179

Now we consider the integral kinetic energy equation for 2D disturbances,

$$\frac{\mathrm{d}e}{\mathrm{d}t} = \underbrace{\frac{1}{k^2}\Im\int U'\left(\alpha\bar{v}\partial_y\widehat{v}\right)\,\mathrm{d}y}_{Convection/Production}$$
$$\underbrace{-\frac{1}{Re\,k^2}\int\left(|\partial_y^2\widehat{v}|^2+2k^2|\partial_y\widehat{v}|^2+k^4|\widehat{v}|^2\right)\mathrm{d}y}_{Dissipation}, \tag{25}$$

and compare the convective and dissipative terms for the least-damped modes located at the tip of the left and right branches of the spectrum respectively, see panels (**c**,**d**,**e**,**f**) of figure 4. For simplicity, we have considered only symmetric modes but it can be shown that the results do not change when antisymmetric modes are considered. In figure 4, the labels $C1$ and $D1$ indicate the contribution to the temporal rate of normalized kinetic energy of convective and dissipative terms (equation 25) respectively, for the least-stable mode. The curves $C2$ and $D2$ instead stand for the contribution given by the second-last mode. When $k > k_\mathrm{d}$, it belongs to the P-family of eigensolutions for PPF, and to the continuous branch for the wake.
An exchange of modes occurs as k_d is approached. Beyond, the wave-amplitude is always damped, but the behavior is pretty much convective and very weakly dependent on the wavenumber, especially in the wake case.

Cases of mode-exchange for shear or stratified flows with complex dispersion relations have been reported by other authors (see, for instance, [116, 115] for the Poiseuille pipe flow and [64] for the stratified Couette flow). For a review, see [33], sections 2.2 and 2.6. It should be noted that the mode exchange observed here for the plane channel flow went mostly unnoticed or disregarded up to now. Possibly, because it takes place in the asymptotically stable region above the neutral curve of the k-Re stability map. Such a region of the parameters space it not of great interest if the focus is on exponential instability. However, as shown in Chapter 3 (see figure 37) large kinetic energy and vorticity algebraic growth can occur at these wavenumbers.

The following sections are focused on the wave transient evolution. It is indeed interesting to understand how (and if) the global, intrinsic properties highlighted above affect the transient. Special attention is kept on the phase velocity and on near-similar solutions.

1.5 The transient dynamics of the phase velocity

Several works dedicated to sheared flows have shown the importance of the early-term dynamics, that in principle can lead to large transient perturbation growth long before the exponential mode becomes dominant [35, 24, 72, 73, 92, 90, 18]. Transient dynam-

ics offers a variety of different behaviors and phenomena which are not easy to predict *a priori*. It is interesting to note that these phenomena develop in the context of the linear dynamics, where interaction among different scales (and even self-interaction) is absent. Today, there is clear evidence that some features of such linear dynamics are retained in turbulent flows and play an important role in turbulence-generation mechanisms, as very recently highlighted by Jimenez in 2013 [80], Brandt in 2013 [21] and Meseguer&Trefethen [98], 2003. Transient wave dynamics has been typically analyzed in terms of energy amplification, while less attention has been given to the phase velocity evolution. However, the analysis of the phase speed temporal evolution provides insights towards the understanding of why and how different time scales show up inside the transient (see figures 6-10 below). Moreover, the sequence of different transient phases leading to the final asymptote can be better observed through the phase speed rather than through the kinetic energy amplification factor.

In the context of the velocity-vorticity formulation, proper initial conditions on $\widehat{v}$ and $\widehat{\omega}_y$ have to be associated with the system 11-12. Notice that the OS equation 11 is homogeneous and its solutions drives the solution of the Squire equation 12 for $\widehat{\omega}_y$. The initial vorticity $\widehat{\omega}_y(0, y)$ was set to zero for all the simulations here performed, in order to observe the net contribution of three-dimensionality on the wall-normal vorticity amplification and temporal evolution, as in [118]. In fact, due to the equations coupling, both Orr-Sommerfeld and Squire modes are excited by an initial condition with $\widehat{\omega}_y = 0$. As shown in ref. [71], the disturbance will experience a short-term transient algebraic growth of the normal vorticity (*lift-up effect*), much larger than the normal velocity growth. Since the particular solution of the Squire's equation is much larger than the normal velocity, such effect is observed even for moderate initial normal vorticity (see also the formal solution in Eq. 2.113, 2.114 in [120]). When $\widehat{\omega}_y = 0$, the growth is maximum, and nonzero initial vorticity does not contribute to optimal disturbances (those leading to the maximum transient growth) as shown by Criminale et al. [37] and Criminale, Jackson, and Joslin [36]. When non-zero normal vorticity is included in the initial conditions, the transient growth is typically diminished, as shown by Lassaigne, Joslin, and Criminale [90].

About the transversal velocity, we considered four different initial conditions, $\widehat{v}(0, y)$, selected on the basis of their parity the location of the perturbation with respect to the higher or lower vorticity region in the basic flow. To be more specific, the important physical aspect is whether or not the initial condition has quick momentum variations ($\partial_y \widehat{v}$) inside the basic flow high-shear region.
For a fixed wavenumber and Reynolds number, the combination of these two attributes produces a different level of excitation of the least stable subset of eigenvalues in both the left and the right branch of the spectrum (spectra are shown in figure 2 and in panels (**d**,**h**) in figure 6).

Table 1 reports the expressions of the initial perturbations we selected. They are also shown in figure 5. The initial conditions for the wake flow are named, in the following, SI, AI, SO, AO (S=symmetric, A=antisymmetric, I=inside-wake, O=out-of-wake). For the plane Poiseuille flow, we labeled them as SC, AC , SW, AW (C=central, W=wall). We recall that the for the channel flow the high shear region is located near the wall while for the wake flow it is located in the central region of the open domain that computationally is typically from 20 to 100 times larger than the basic flow.

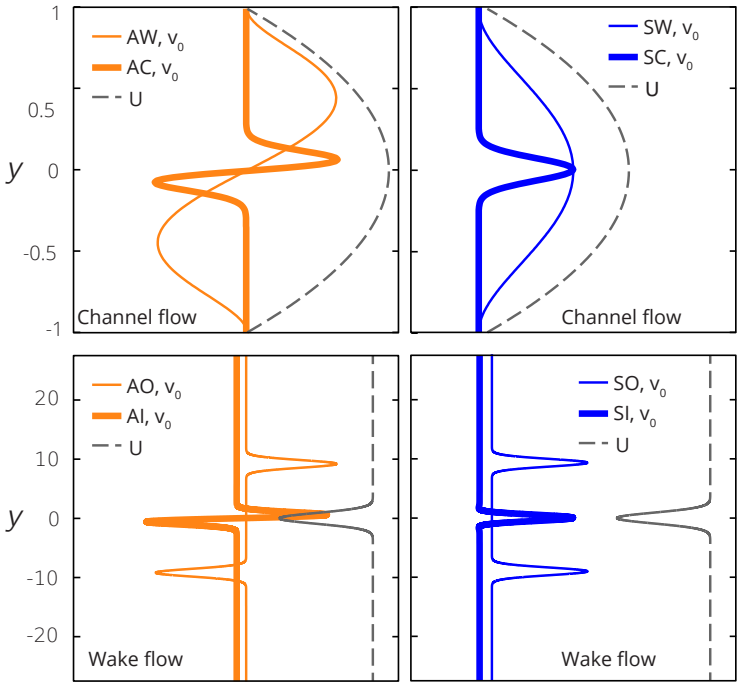

Figure 5: Initial wall-normal velocity $\widehat{\mathbf{v}}_0$ and basic flows. The amplitudes have been scaled for clarity. *Top*: plane Poiseuille flow. *Bottom*: wake flow. Blue curves represent symmetric disturbances (right panels), while the antisymmetric are in orange (left panels). Thick lines indicate central initial disturbances, thin curves represent the lateral ones. The mathematical expressions of such initial conditions are reported in table 1. Figure published in [40].

The transient dynamics for few case studies is shown in figure 6, where the evolution of three-dimensional waves is presented in terms of the amplification factor G, the phase speed c, and the growth rate r. In these cases, the wavenumber is below the threshold discussed in 1.4, $k < k_{\mathrm{d}}$. In fact, the trends for small wave numbers could be more easily observable in the laboratory. However the qualitative behavior of perturbations with wavenumber larger than k_{d} is discussed in the summary figure 11. Amplification factors and temporal growth rates are presented in panels (**b**,**c**,**f**,**g**) of figure 6. In the

wake case, initial perturbations of the type SI and AO yield to a brief early transient followed by the temporal asymptotic exponential behavior, which is reached after few time scales. In contrast, the dynamics arising from the other kind of initial disturbances - AI (antisymmetric and localized inside the wake) and SO (symmetric and external to the wake shear) - is featured by abrupt jumps of the phase speed, which can occur quite far along within the transient (panel **e**). These shifts represent wave accelerations (AI) or decelerations (SO) and lead to the final long-term state, which may be reached only after several convective time scales. Therefore, intermediate-term solutions might be expected to manifest in these cases. The physical meaning of the jumps will be clarified in the following.
The same features are observed in the case of the plane Poiseuille flow. However, here the role of the initial conditions is reversed: AC and SW reach the asymptotic exponential trend shortly after few time scales. SC and AW instead experience long transients with phase velocity jumps (panel **a**). Similarly to the wake case, the symmetric perturbation slows down while the antisymmetric one increase its phase speed.

The described dynamics can be brought back to the structure of the Orr-Sommerfeld spectra and the related modes. Indeed, it is known that for PPF the eigensolutions corresponding to left-branch eigenvalues (A-branch) are slow ($c < \frac{2}{3}$) wall-modes while those in the right branch (P-branch) are fast ($\frac{2}{3} < c < 1$) central modes. On the other hand, the spectrum of the wake flow (and of unbounded flows, in general) is composed by a discrete set of slow inside-wake modes, and a continuous branch of fast ($c = 1$) modes traveling in the nearly uniform region outside the wake. All branches contain both symmetric and antisymmetric functions, see panels (**d**,**h**) of figure 6. The dominant antisymmetric OS mode is usually located at the tip of the right branch, while the dominant symmetric one belongs to the left branch. This one is the only mode which can be unstable, and for $\phi = 0$ it is known as the *Tollmien-Schlichting wave*.

An additional time scale is observed: the periodicity T_c, related to the temporal modulation of the phase speed during the early and intermediate terms, see figure 6 (**b**,**f**). It was already reported in ref. [118], but an explanation was still missing. In this study, we found that this oscillation is related to the real-axis width of the eigenvalue spectrum. In particular the period is inversely proportional to the range of frequencies contained in the spectrum, that is $T_c = 2\pi/[\sigma_{r_{max}} - \sigma_{r_{min}}]$.

It is clear that in the linear framework purely symmetric and antisymmetric perturbations do not reach the same temporal asymptote. As recalled above, symmetric disturbances are always less or equally stable than the antisymmetric. This means that if a general asymmetric initial condition - made of both a symmetric and an antisymmetric part - is considered, in the long-term the symmetric component will always prevail.
Of course, in laboratory experiments (and numerical as well, unless special attention is paid) it is impossible to assume exact symmetry, since residual noise cannot be totally

suppressed. As a consequence, the phase velocity that can be eventually observed is that given by the symmetric part of the initial condition. In an attempt to mimic what would be observed in the laboratory, a mixed initial condition with prevailing antisymmetric component was built by adding to AI and AO a small white noise $O(10^{-7})$. The evolution of such a disturbance is shown in figure 7: after an early transient, the wave experiences acceleration (as happened to AI and AO, see figure 6) and retains the antisymmetric profile until the symmetric part becomes eventually dominant. The temporal asymptote is eventually reached ($t \approx 3000$) and it is announced by a second phase velocity jump to a lower speed. In air ($\nu = 1.4 \cdot 10^{-5} m^2 s^{-1}$) if the cylinder diameter were 1 cm, the second jump would occur after about 180 seconds.

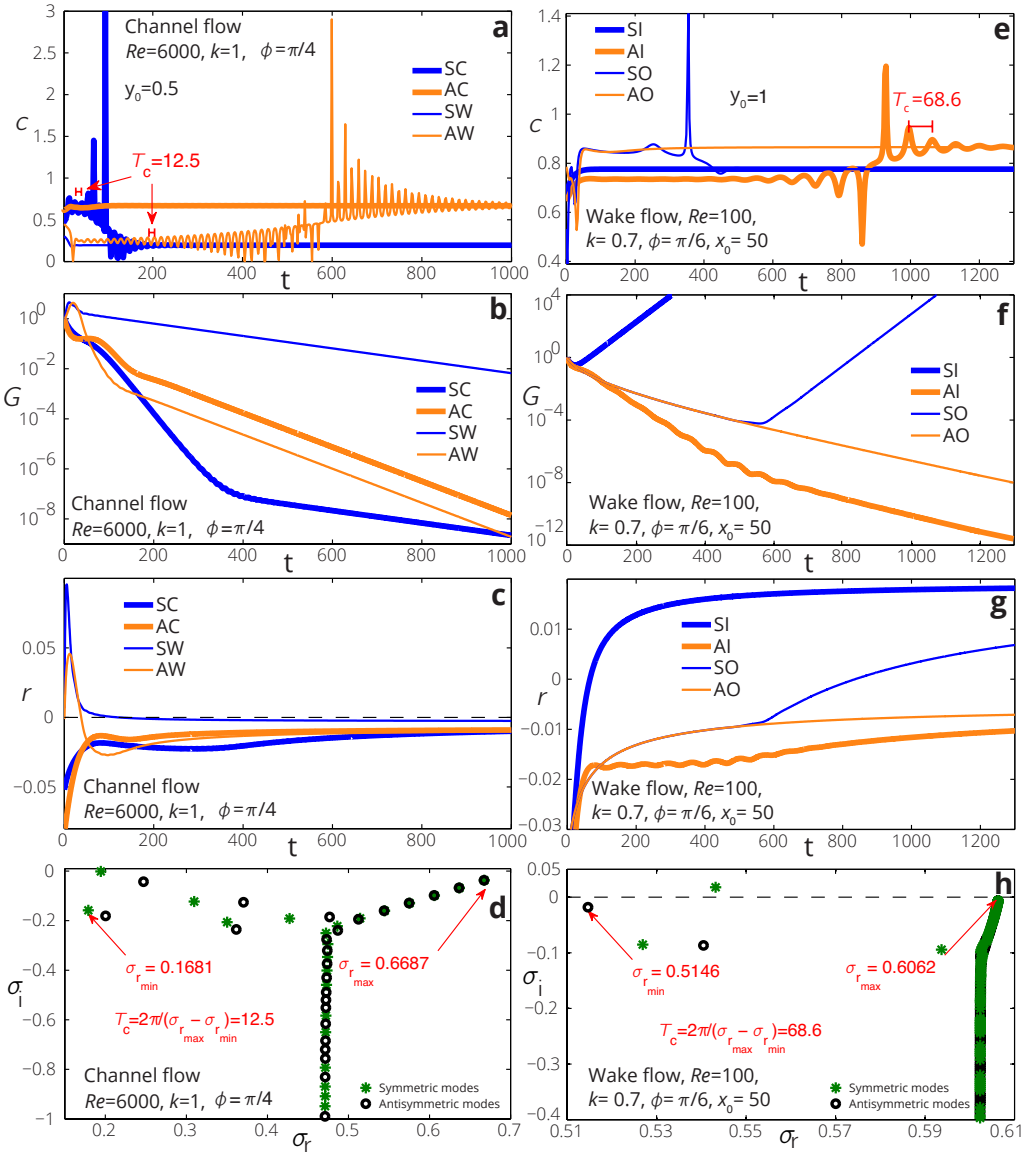

Figure 6: Temporal evolution of perturbations in terms of the phase velocity c **(a,e)**, the amplification factor G **(b,f)**, and the temporal growth rate r (panels **c**,**g**), for initial conditions of figure 5. The Orr-Sommerfeld eigenvalues spectra are shown in panels **(d, h)**. *Left*: PPF at $Re = 6000$, $\phi = \pi/4$ and $k = 1$. *Right* : wake flow at $Re = 100$, $\phi = \pi/6$ and $k = 0.7$. The phase velocity is computed at $y_0 = 0.5$ for the channel and at $y_0 = 1$ for the wake flow. The time scale T_c, see **(a)** and **(e)**, indicates the oscillation period of phase velocity fluctuations observed in the early/intermediate term. We show that T_c is determined by the spectral frequency width by $T_c = 2\pi/[\sigma_{r_{max}} - \sigma_{r_{min}}]$, see panels **(d)** and **(h)**. Figure published in [40].

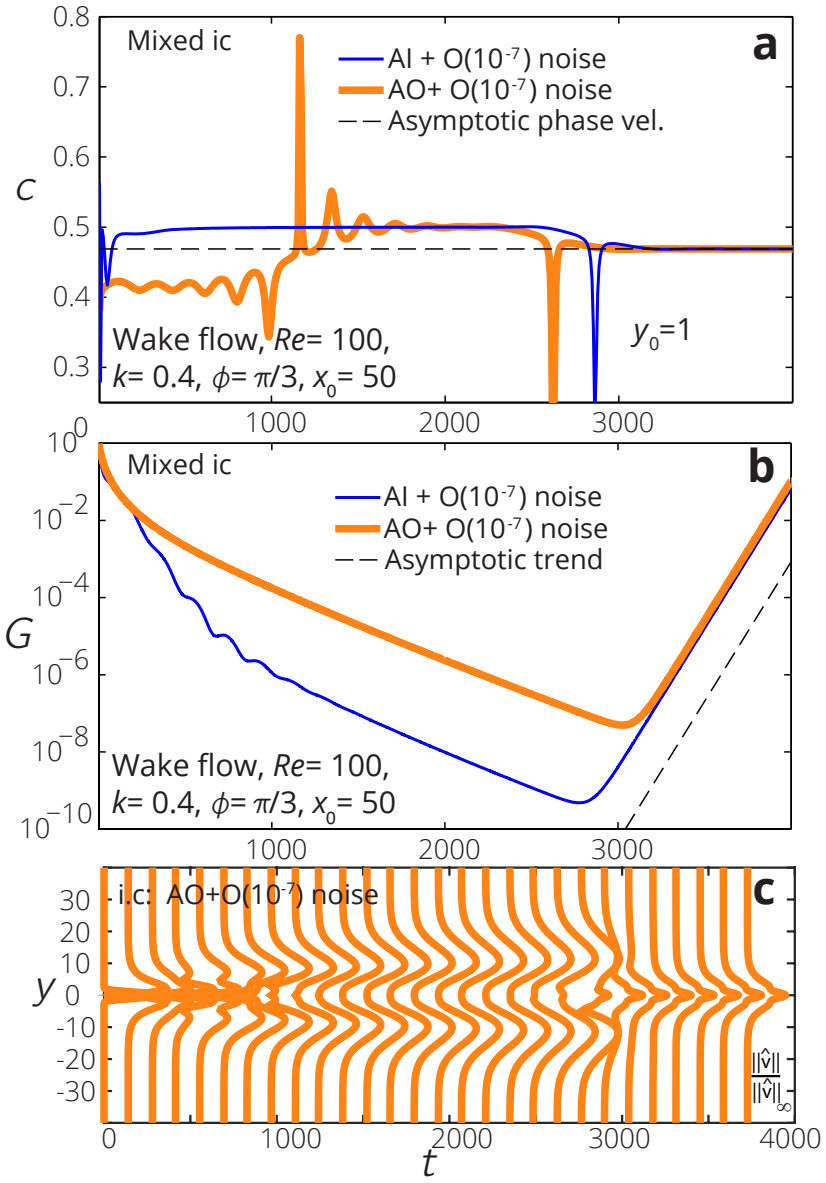

Figure 7: Dynamics of noisy antisymmetric initial conditions in the wake flow at $Re = 100$, $k = 0.4$, $\phi = \pi/3$ and $x_0 = 50$. A small uniform random noise of magnitude $O(10^{-7})$ was added to the initial disturbances Al and AO, with the aim to represent the evolution of a general perturbation. **(a)** Phase speed. **(b)** Kinetic energy growth rate. The dashed line represents the asymptotic trend obtained from a modal analysis. **(c)** Temporal evolution of the velocity profile modulus for the noisy AO initial condition. Profiles are normalized to their peak value at each time instant. Figure published in [40].

1.6 **Near-similarity of wavy perturbations**

The observations of frequency jumps yielded an interesting result: the perturbation temporal evolution has a three-part structure, with an early stage, an intermediate stage and an asymptotic stage.

The dynamics of the phase speed discussed in the section above suggests the possibility for a multi-stage structure (early/intermediate/far transient) of the perturbation evolution. The nature of the phase speed shifts presented previously can be better understood if the temporal evolution of the perturbation's velocity transversal profile is considered. In figures 9 and 10 we show the modulus $|\widehat{v}|$, normalized to its instantaneous peak value.

During the early term, the perturbation is mostly affected by the fine details of the initial state. During the intermediate stage the perturbation evolves almost exponentially, as can be observed from the almost constant growth rate in figure 6 (**b**, **g**), or from the amplification factor in figure 7 (**b**). In this temporal term, the phase velocity stabilizes to a constant value, the transverse velocity profiles maintain a near self-similar nature in time and the growth factor changes very slowly. Notice that even though this stage may resemble the asymptote, actually the perturbation's shape may differ quite from the asymptotic form, and last for many (even hundreds) time scales. The establishment of self-similarity can be recognized by the constancy of the wave propagation speed. This can be observed from figures 7 (**c**), 9 (**b**,**c**) and 10 (**b**,**c**). The intermediate term can be in general considered extinguished only when both the frequency and the temporal growth rate become constant.

In figures 9 and 10, we present the cases of $Re = 100$, $x_0 = 50$, $k = 0.7$, $\phi = \pi/6$ with SO and AI initial conditions for the wake flow and $Re = 6000$, $k = 1$, $\phi = \pi/4$ with SC and AW initial perturbations for the plane Poiseuille flow. Panels (**b**,**c**) show the velocity profiles normalized to the instantaneous peak value, $|\widehat{v}|/\|\widehat{v}\|_\infty$. Phase velocity variations are associated with changes of the perturbation profile. The jumps are symptom of a transition from an old state to a new state, and the phase speed oscillations are due to the interchange of different coexisting modes which at a certain time instant can have the same energy level but different frequency. Such transitions represent periods of "adjustment" for the solution.

In the case of the wake flow, a perturbation spreading along the cross-shear coordinate y was also observed. However, it is noteworthy that lateral diffusion occurs only under certain conditions, which we summarized in figure 11. The wake perturbation's width was found to scale with time as a power law t^p. Note that non-integer power law exponents have also been recently observed by King et al. [82] for algebraically growing wave packets in the context of planar liquid sheets. In the simulations of figure 10, $p \approx 0.42$. We investigated the possible values of the power law exponent p as a function

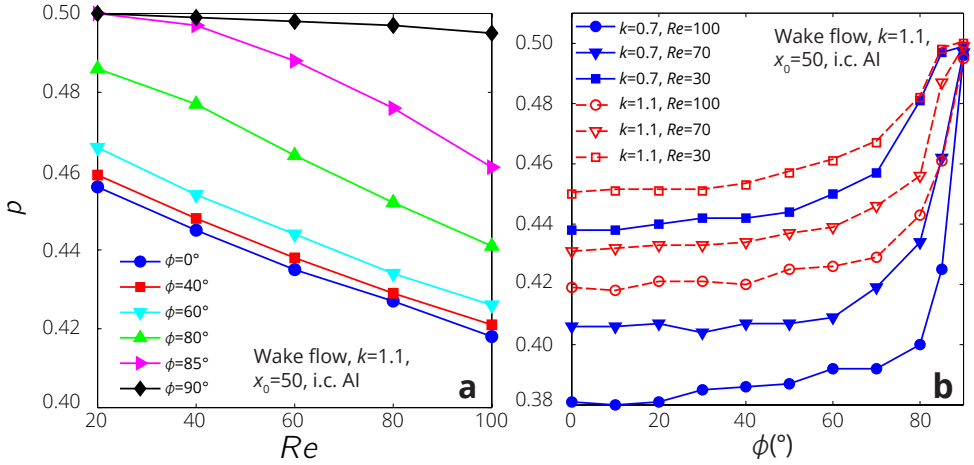

Figure 8: Scaling exponent p for the temporal evolution of the wake perturbation width in the intermediate term at $x_0 = 50$ and with Al initial condition. **(a)** The exponent dependence on the Reynold number is shown for few values of the wave angle in the range $[0, \pi/2]$. **(b)** The dependence on the wave angle is shown for $Re = \{30, 70, 100\}$ and $k = \{0.7, 1.1\}$. Figure published in [40].

of the system parameters, that is the wavenumber, the wave angle and the Reynolds number. Results are shown in figure 8. One can observe that the exponent decreases as the Reynolds number and increases as the wave obliquity and the polar wavenumber. For very low values of the Reynolds number, when the inertial effects become very little, the exponent is expected to take the diffusive value 0.5. Note that $Re \approx 20$ is the smallest reliable value for which the wake flow can be represented in terms of a matched asymptotic expansions solution, valid in both the spatial intermediate and far field, see [127] for major details on the wake basic flow computation. The dependence on the obliquity angle is weak at low angles, while the diffusive scaling $t^{0.5}$ occurs for perturbations orthogonal to the basic flow ($\phi = \pi/2$) since in this case the convective transport does not matter (Eqs. 11-12). Moreover, as expected, we observe that short waves present a more diffusive behavior than the long ones, see the panel (**b**) in figure 8.

Figure 11 summarizes the different kinds of the phase velocity transient, for various combinations of wavenumber and type of initial condition. In particular, the transient behavior depends on if the wavenumber is above or below the threshold k_d. The diagram distinguishes the cases where the perturbation experiences acceleration or deceleration through a phase speed jump, and also shows the perturbation shape in the long term.

The wake case offers other interesting considerations. We can observe from figure 10 that a perturbation initially located inside the wake (AI) can eventually "escape" from the high-shear region (panel **c**). More generally, this always happen (for any initial disturbance) for short waves with $k > k_{\mathrm{d}}$, as shown in figure 11. If the wavelength is bigger than the threshold ($k < k_{\mathrm{d}}$), this situation only occurs for purely antisymmetric perturbations, which cannot be observed in nature. Therefore, we can say that general low-wavenumber perturbations will always stay inside the wake flow in the long-term as occurs for the noisy perturbation in figure 7. Note that this is true also for perturbations initially located outside the shear, as observed for SO in panel (**b**) of figure 10. Here, oppositely to the case AI in panel (**c**), the disturbance seem to be "captured" by the wake, as soon as it starts interacting with the shear region of the basic flow (at about $t = 600$). Such transitions are highlighted by the phase velocity jumps. This results might be of interest for readers in the research area of the so called *receptivity*, dealing with the influence of external repetitive free-stream disturbances on the stability of wakes, jets, or boundary layers.

It should be also noticed that the time instant when the frequency/phase velocity jumps are observed can be distant from the beginning time, and for this reason it could be observed in the laboratory. For instance, in the wake case at $Re = 100$ and AI initial condition (see panel (**e**) in figure 6), if the cylinder size is $D = 2\ cm$, the jump is detected after nearly 4 minutes if the fluid is air, and after about 50 minutes if the fluid considered is water. In the case of Poiseuille motion, $Re = 6000$ and SC initial disturbance (figure 6 **a**), if we consider a channel half-width of $h = 15$ cm, the jump is found after 25 sec if the fluid is air, and after nearly 6 minutes in water.

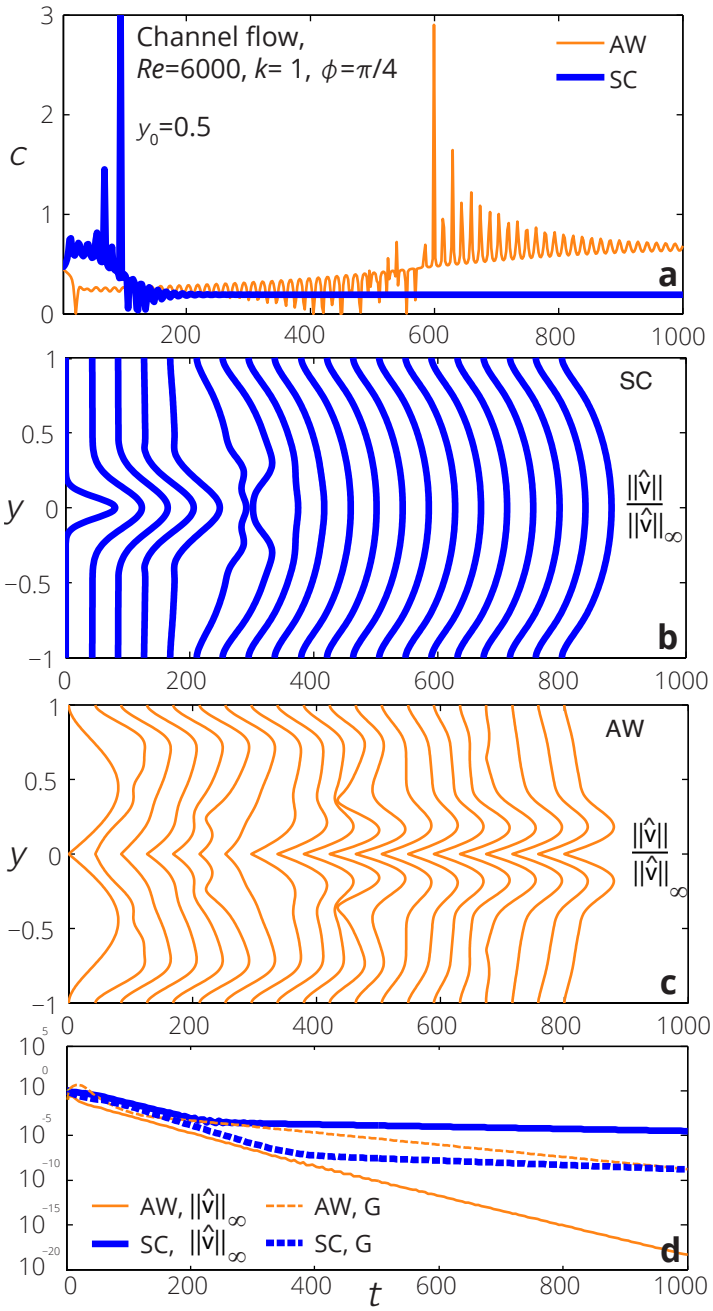

Figure 9: Perturbation evolution in the plane Poiseuille flow. $Re = 6000$, $k = 1$, $\phi = \pi/4$, initial disturbance AW (orange, thin lines) and SC (blue, thick lines). **(a)** Temporal evolution of the phase velocity, measured at $y_0 = 0.5$. A jump is observed at $t \approx 100$ for SC and at $t \approx 600$ for AW. **(b)** Temporal evolution of the wall-normal velocity profiles for the SC initial condition. The velocity is normalized to the instantaneous peak value. **(c)** Evolution of the normalized velocity profiles for the case AW. **(d)** Temporal evolution of the amplification factor G and of the amplitude of the wall-normal velocity, $\|\hat{v}\|_\infty$. Figure partially published in [40].

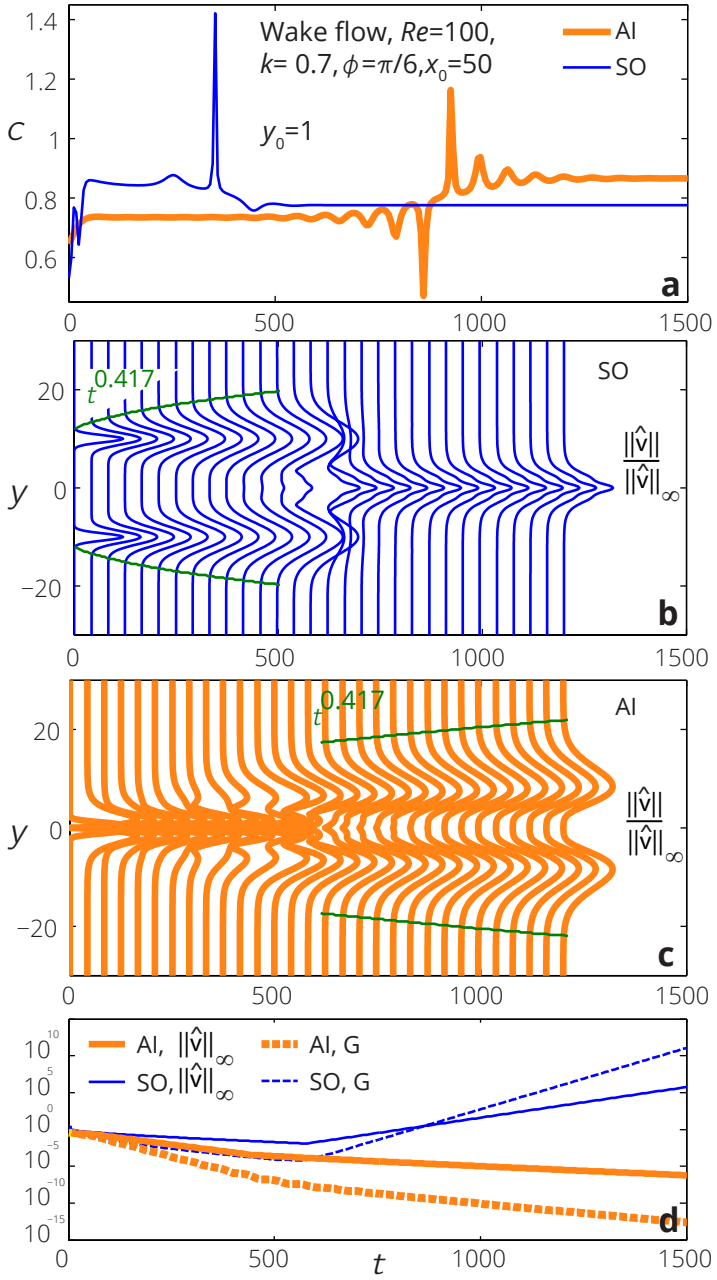

Figure 10: Perturbation evolution in the wake flow. $Re = 100$, $k = 0.7$, $\phi = \pi/6$, $x_0 = 50$, initial conditions AI (orange, thick lines) and SO (blue, thin lines). **(a)** Phase speed, measured at $y_0 = 1$. A jump is observed at $t \approx 400$ for SO and at $t \approx 800$ for AI. **(b)** Evolution of the wall-normal normalized velocity profiles for the initial condition SO. **(c)** Evolution of the normalized velocity profiles for AI. Note the presence of time intervals where the solution expands in the cross-shear direction (see also figure 11) . It is also interesting to note that the rapid transition happens when the perturbation reaches the wake from the outer region (SO), or when it exits the wake region (AI). The perturbation width here follows a power law t^p, $p \approx 0.42$. **(d)** Temporal evolution of the amplification factor G and of the amplitude of the wall-normal velocity, $\|\hat{v}\|_\infty$. Figure partially published in [40].

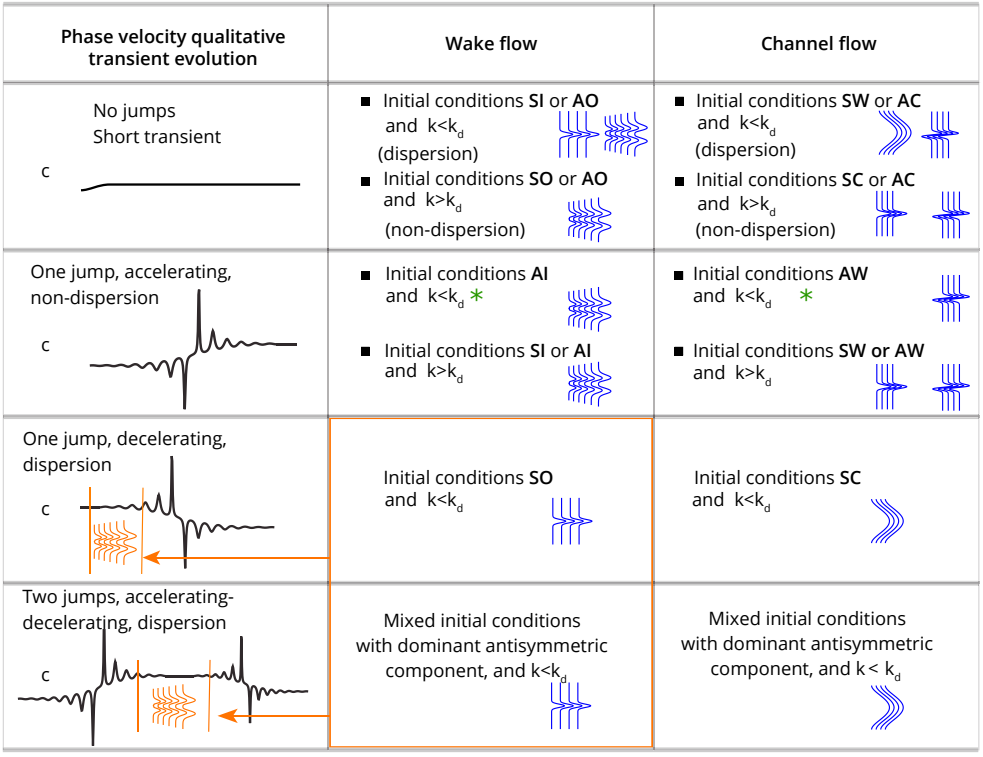

Figure 11: Qualitative scheme for the perturbation phase velocity transients. *Left column*: type of transient; the black lines represent qualitatively the phase velocity evolution over time. Orange symbols indicate the presence of intermediate self-similar perturbation profiles for the wake. *Mid column*: wake flow. Each cell shows the conditions leading to the corresponding kind of transient (indicated in the left column), in terms of initial condition type (SI=symmetric in-wake, AI=antisymmetric in wake, SO=symmetric out-of-wake, AO=antisymmetric out-of-wake) and the wavenumber, specifically $k < k_\mathrm{d}$ or $k > k_\mathrm{d}$. *Right column*: Poiseuille flow (SC=symmetric central, AC=antisymmetric central, SW=symmetric lateral, AW = antisymmetric lateral). With the blue symbols we represent, for each case, the long-term shape of the disturbance (the least-stable solution at the temporal asymptote). The green star is a reminder that, even for $k < k_\mathrm{d}$, the least-damped antisymmetric mode is located in the right branch of the spectrum and it is non-dispersive. Figure published in [40].

1.7 **Final remarks**

The first chapter of this dissertation was aimed at shedding light on few aspects of the transient dynamics of internal linear waves in parallel/near-parallel flows, which have been poorly investigated in the literature on hydrodynamic stability of sheared, incompressible, viscous flows. The focus was on wave propagation properties and in particular we investigated the possibility for the system to behave both in a dispersive and a non-dispersive manner. Though the spectral structure of the governing Orr-Sommerfeld/Squire equations has been long been known, the conditions for which dispersive - or nondispersive - modes are dominant have not been considered in detail. Here, we stressed the impact of such conditions on the transient behavior of single wavy perturbations. In fact, for the plane Poiseuille and wake flows, we observed the existence of a threshold k_d that splits the range of wavenumbers where least-damped solutions would yield dispersion (when wave packets are considered) from the range where they would yield non-dispersion.

The abrupt transition between the two behaviors is related to the fact that for $k < k_d$ the least damped OS eigenvalue is located at the tip of the left branch of the spectrum, while for $k > k_d$, it belongs to tip of the right branch. Non-dispersion is mostly related to a convective wave propagation ($c \sim 1$). For both the flows, dispersive waves are featured by velocity profiles (in the y cross-shear direction) which vary rapidly in correspondence to the basic flow high-vorticity region. The opposite is true for non-dispersive waves.

The transition in the asymptotic dispersion relation helped to understand some features of the transient dynamics. Different kinds of wave transients have been identified and then classified in the following four categories:

1. short transients where the phase speed reaches its long-term solution smoothly (no jumps)
2. long transients where the wave experience an abrupt acceleration (one phase speed jump)
3. long transient where the wave experience an abrupt slow-down (one phase speed jump)
4. long transients where more than one phase speed jumps occur in the transient.

By considering four initial perturbations with (i) different parity and (ii) different vorticity distribution along the y-direction, we investigated the conditions necessary to observe each of the above types of transient dynamics. In this regard, a key factor is the wavenumber value with respect to the threshold k_d.

We showed that within the transient evolution three stages can typically be observed. An *early transient*, heavily dependent on the fine details of the initial condition; an

intermediate transient where the perturbation evolve almost exponentially for many time scales, but the final state is not yet reached; the *far transient*, that is the asymptotic state. In the wake flow, our simulations highlight a growth of the perturbation profiles in the cross-shear direction, which follows a temporal power-law scaling where the exponent varies not only with the Reynolds number, but also with the wavelength and wave-angle.

In the following chapter, the dispersion properties of channel flows will be further investigated. Therefore, the analysis will no longer consider single traveling waves, but linear wave packets containing a high number of wave components. An anticipation of the scenario one may expect is given in figure 1.2. These picture has been published by several press-releases (see, among others[3] AplhaGalileo, PhysOrg, PoliTo news) which promoted the results shown in this chapter to the public.

3 https://aps.altmetric.com/details/6209937/news

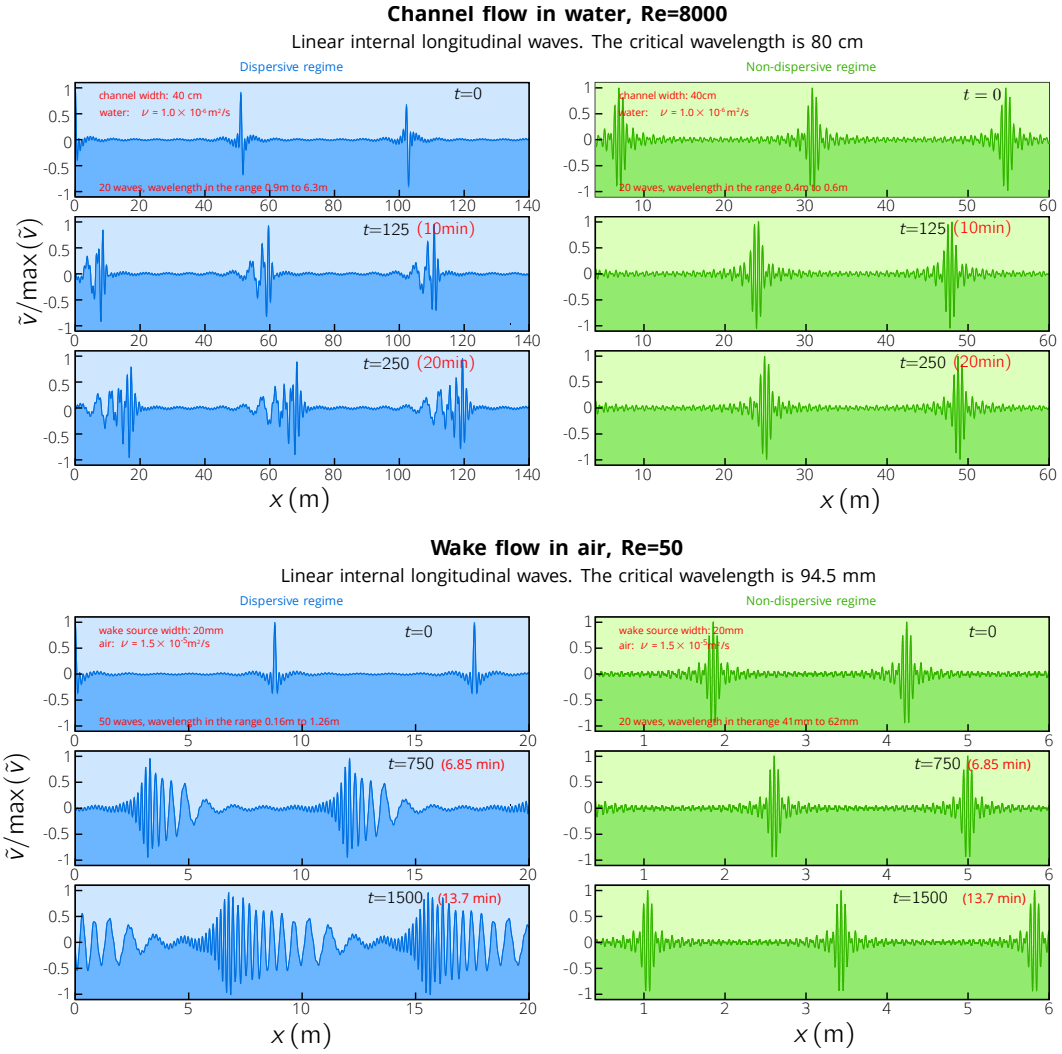

Figure 12: The dual nature of the wave packet's propagation. The dispersion properties for wavenumbers below (left pictures, dispersive regime) and above (right pictures, non-dispersive regime) the threshold k_d have been highlighted by building two wave packets for both the channel and the wake flow. *Left*: dispersive cases, the packets are made of 50 wave components with the wavenumber below the threshold k_d. *Right*: non-dispersive case, here the packets contain 20 waves with wavenumber larger than the threshold. These figures report the values for the following dimensional cases: channel water flow, $h = 0.4$ m, $Re = 8000$; wake air flow, $D = 2$ cm, $Re = 50$. Part of this figure has been promoted by some press releases: *AlphaGalileo*[a]; *PhysOrg*[b]; *PoliTo*[c].

a http://www.alphagalileo.org/ViewItem.aspx?ItemId=162474&CultureCode=en
b http://phys.org/news/2016-03-mechanisms-fluids.html
c http://www.politocomunica.polito.it/press_room/comunicati/2016/

2

LINEAR WAVE PACKETS IN SHEARED FLOWS

After the discussion in Chapter 1 on peculiar aspects of the transient evolution of the phase speed of single waves from the early to the long temporal term, the present chapter is focused on wave packets containing a broad range of wavenumbers. A publication on these subject is being prepared [4], and results will be presented at the 70th APS DFD (2017). Gabriele Nastro is coauthor, for the contribution given during his M. S. thesis preparation.

2.1 **Summary**

We further investigated the capacity of the parallel-flow motion to host both dispersive and non-dispersive small perturbation waves under fixed flow conditions. Although it is known that long perturbation waves may slowly disperse [38, 54, 56], this scenario is not yet complete.

Recalling the results of Chapter 1, by computing the exact dispersion relation for perturbations observed in their long-term temporal asymptote, we showed that dispersion does not occur for all wave numbers and in the whole range of Reynolds numbers. For instance, for a fixed value of Re, waves with length shorter than a certain value were found to propagate in a non-dispersive way.

The present study extends that analysis and focuses on the impact of those findings on three-dimensional localized disturbances, or wave packets. By finely tuning the wavenumber and Reynolds number resolution, we explored the stability map in the limit of long waves (§2.3). We discovered the existence of three subregions in the wavenumber-Reynolds number parameters space, having different dispersion features than their surroundings. In particular, these regions look like niches tilted by 45° in the log-log space, which are nested in the dispersive, low-wavenumber, part of the map. The first one is observed at $Re > 546$ and $k < 0.28$, and shows propagation speed higher than the surroundings, associated with a very mild dispersion. The second one is observed for $Re > 9770$ and $k < 0.13$, and highlights again a propagation speed larger than the surroundings which is now associated with an enhanced dispersion. The last one is observed for $Re > 29840$ and $k < 0.35$, and contains non-dispersive waves which propagate with the convective speed of the basic flow.

By assembling two and three-dimensional wave packets (§2.4), it was then possible to relate their morphology to the propagation properties of the wave components inside the packet. In particular, the front of the linear spot [86] - also present in pipe puffs (see refs. [43, 95]) - appears associated with the non-dispersive wave components. This helps to elucidate the physical mechanisms determining the spot arrow-shape and spatial spreading of the spot, an aspect still missing in the literature (see refs. [75, 91]). With the help of a propagation representation, based on the directional distribution of the computed asymptotic group velocity, we can qualitatively reconstruct the features of the spot.

2.2 **Theoretical bases for linear dispersive waves**

In this section, the basic theory and mathematical tools are exposed, regarding a wide class of wave solutions that have been generally referred to as *dispersive*. Intuitively, a wave packet disperses in space as it evolve in time if its components, having different wavenumbers, travel with different phase speeds. Although this terminology finds origins in the type of the solutions, rather than the type of governing equations, we can talk about *dispersive equations*: well-known examples of linear and nonlinear dispersive partial differential equations are the *Airy equation*, the *Euler-Bernoulli beam equation*, the *Klein-Gordon equation*, the *Schrödinger equation*, the *Korteweg - de Vries equation* and the *Boussinesq equation*, find further information in references [30, 42].

The focus of this dissertation is on the solutions of the *Navier-Stokes equations*, linearized for small perturbations of a laminar state. We consider the wall-normal velocity/vorticity formulation known as the Orr-Sommerfeld/Squire initial-value problem, introduced in §1.3. In Chapter 1, by considering single wave perturbations, it was shown that parallel flows can host both dispersive and non-dispersive wave solutions, under fixed values of the flow control parameter, Re. This "double nature" have been related to the basic flow spatial variations (so, its vorticity). The reader is reminded that the basic flow $U(y)$ appears in the equations as a space-dependent coefficient, and that only for a uniform flow the dispersion relation can be computed analytically (in this case it is purely non-dispersive).

In this chapter, we will discuss the effects of the coexistence of dispersive and non-dispersive wave solutions on the dynamics of linear localized perturbations (wave packets), built by superposition of a high number of waves. This work has been done for the plane Poiseuille flow, as a representative example of sheared flow with nonuniform vorticity. However, there are indications to retain that the phenomenology described is a common feature of sheared flows (in Chapter 1, for instance, results have been presented for the wake flow as an example of unbounded flow). The plane Couette flow is an exception in that it leads to dispersion at all wavenumbers with only a smooth ten-

dency to non-dispersion in the short-wave and high-Re limit [48]. In this case however, a Reynolds number lower bound for wave propagation exists [51]. In §2.3 we show asymptotic dispersion relations maps in the $k - Re$ parameters space, for the least-stable mode of both the plane Poiseuille and Couette flows. The following sections will then be focused on the numerical simulations of two and three-dimensional wave packets, whose morphology is discussed in reference to the dispersion property of the flow.

Definition of dispersive waves

Considering the long-term, wave solutions of linear constant-coefficient partial differential equations can be sought in the form of superposition of normal modes

$$q(\mathbf{x}, t) = \hat{q}\ e^{i\mathbf{k}\cdot\mathbf{x} - i\sigma t}. \tag{26}$$

The eigenvalue σ, and the vector wavenumber $\mathbf{k}$, can be complex. They have to satisfy the *dispersion relation*:

$$D(\sigma, \mathbf{k}) = 0, \tag{27}$$

which may be solved explicitly to get the angular frequency $\omega(\mathbf{k})$, i.e. the real part of σ, as a function of the wavenumber. The imaginary part of σ represents the temporal growth/decay rate of the wave amplitude, while the imaginary part of the wavenumber takes into account for spatial growth/decay. According to Whitham [135, Chap. 11], a linear system is said to be dispersive if

$$\det\left(\frac{\partial^2 \omega}{\partial k_i \partial k_j}\right) \not\equiv 0. \tag{28}$$

Reminding that the phase velocity is $\mathbf{c} = (\omega(\mathbf{k})/k)\mathbf{e}_k$, and the group velocity is $\mathbf{v}_g = \boldsymbol{\nabla}\omega$, the above definition states that the system is dispersive if the phase speed varies with the wavenumber. Instead, non-dispersion is observed when $\mathbf{c} = \mathbf{v}_g$. Note, however, that it is difficult to find a comprehensive definition, since dispersion is a property of the type of solutions rather than of the equation. For instance, think of the case of non-constant coefficients (inhomogeneous medium), or nonlinear systems for which 26 is not a solution.
A couple of other definitions have been borrowed from a talk by Prof. G. Staffilani (MIT Mathematics):
"an evolution partial differential equation is dispersive if, when no boundary conditions are imposed, its wave solutions spread out in space as they evolve in time".
"We say that an evolution equation (defined in $\mathbb{R}^n$) is dispersive if $\omega(\mathbf{k})/|\mathbf{k}| = g(\mathbf{k})$ is a real function such that $|g(\mathbf{k})| \to \infty$ as $|\mathbf{k}| \to \infty$" (more formal).

Considering for the sake of simplicity a real dispersion relation (that is, $\sigma(\mathbf{k}) = \omega(\mathbf{k})$) in $\mathbb{R}^n$, the wave packet can be formally represented by a Fourier integral:

$$q(\mathbf{x}, t) = \int_{-\infty}^{\infty} \hat{q}(\mathbf{k}) e^{i\mathbf{k}\cdot\mathbf{x} - i\omega(\mathbf{k})t} \, \mathrm{d}\mathbf{k}. \tag{29}$$

If the angular frequency is expanded in Taylor series around the wavenumber $\mathbf{k}_0$,

$$\omega(\mathbf{k}) = \omega(\mathbf{k_0}) + \boldsymbol{\nabla}\omega\Big|_{\mathbf{k_0}} \cdot (\mathbf{k} - \mathbf{k_0}) + (\mathbf{k} - \mathbf{k_0})^{\mathsf{T}} \mathbf{H}_\omega\Big|_{\mathbf{k_0}} (\mathbf{k} - \mathbf{k_0}) + O(\mathbf{k} - \mathbf{k_0})^3, \tag{30}$$

where $\mathbf{H}_\omega = \frac{\partial^2 \omega}{\partial k_i \partial k_j}$ is the Hessian. By truncating the series at the linear term, the integral becomes

$$q(\mathbf{x}, t) = e^{i\mathbf{k_0}\cdot\mathbf{x} - i\omega(\mathbf{k_0})t} \int_{-\infty}^{\infty} \hat{q}(\mathbf{k}) e^{i(\mathbf{k}-\mathbf{k_0})\cdot(\mathbf{x} - \boldsymbol{\nabla}\omega|_{\mathbf{k_0}} t)} \, \mathrm{d}\mathbf{k}, \tag{31}$$

where the first factor indicates a monochromatic wave moving with phase speed $\mathbf{c_0} = \omega(\mathbf{k_0})/|\mathbf{k_0}|$, while the second factor represents the wave packet envelope near $\mathbf{k_0}$, which moves with the group speed $\mathbf{v}_g = \boldsymbol{\nabla}\omega|_{\mathbf{k_0}}$. The above approximation helps to understand the role of group speed, but it is no longer useful to describe dispersion, which leads to a distortion of the initial envelope shape. Looking for the asymptotic form (large t with $\mathbf{x}/t$ of order unity), the *stationary phase approximation* method [see, e.g, 45] leads to the following expression:

$$q(\mathbf{x}, t) \approx \hat{q}(\boldsymbol{\kappa}) \Big(\frac{2\pi}{t}\Big)^{\frac{n}{2}} \sqrt{\frac{1}{|\det(\mathbf{H}_\omega(\boldsymbol{\kappa}))|}} e^{i(\boldsymbol{\kappa}\cdot\mathbf{x} - \omega(\boldsymbol{\kappa})t - \frac{\pi}{4}\mathrm{sign\ det}(\mathbf{H}_\omega))} \tag{32}$$

$$= A(\mathbf{x}, t) e^{i\chi(\mathbf{x}, t)}, \tag{33}$$

where n is the space dimension ($n = 2$ in our case of planar waves) and $\boldsymbol{\kappa}$ is the specific wavenumber such that the phase of the integral 29 is stationary

$$\boldsymbol{\kappa}: \quad \boldsymbol{\nabla}\theta(\boldsymbol{\kappa}) = \mathbf{x} - \boldsymbol{\nabla}\omega(\boldsymbol{\kappa})t = 0 \ \rightarrow \ \frac{\mathbf{x}}{t} = \mathbf{v}_g \tag{34}$$

It is reminded that the above formulas are derived from the stationary phase approximation, which can be applied if the imaginary part of the dispersion relation (σ_i) is zero. The $\frac{1}{2}$ exponent at the second and third factors in 32 is related to the first nonzero term in the expansion 30, which here is assumed to be the term including second derivatives. If one wants to take into account for temporal grow or decay rates of wave components ($\sigma_i \neq 0$), the more general *steepest-descent method* (also referred to as the *saddle-point method*) should be used [123, 16]. When a complex dispersion relation is considered, the phase is $\theta(\boldsymbol{\kappa}) = i\mathbf{x}\cdot\mathbf{x} - i\sigma(\boldsymbol{\kappa})t$, by the steepest descent method the contour is modified so that the periodic part of the integrand is constant and the exponential term is at a maximum, so that the condition 34 becomes (see [54]):

$$\boldsymbol{\kappa}: \quad \boldsymbol{\nabla}\theta(\boldsymbol{\kappa}) = \mathbf{x} - \boldsymbol{\nabla}\omega(\boldsymbol{\kappa})t = 0 \ \rightarrow \ \begin{cases} \frac{\mathbf{x}}{t} = \boldsymbol{\nabla}\sigma_{\mathrm{r}}(\boldsymbol{\kappa}) = \mathbf{v}_g \\ 0 = \boldsymbol{\nabla}\sigma_{\mathrm{i}}(\boldsymbol{\kappa}). \end{cases} \tag{35}$$

Physically, such asymptotic approximation has an interesting meaning, which motivates the procedure followed in section §2.5 to represent the long-term shape of linear spots in the plane Poiseuille flow. Where Eq. 34 or Eq. 35 have real solutions $\boldsymbol{\kappa}(\mathbf{x}, t)$, the disturbance is a wave packet having that specific wavenumber, space and time dependent, and the variable frequency $\omega(\boldsymbol{\kappa}(\mathbf{x}, t))$. In the case of complex σ, along wave rays the disturbance experience growth or damping given by the factor $\exp[\sigma_i(\boldsymbol{\kappa})t]$.
Moreover, it can be noted that if the medium is uniform the local wavenumber is constant along the characteristic line defined by Eq. 34, so the wavenumber information is propagated with the group velocity (and so does the frequency). In the general case of non-uniform and non-stationary medium, the dispersion relation depends explicitly on space and time, it should be written as

$$\omega = \omega(\boldsymbol{\kappa}, \mathbf{x}, t), \tag{36}$$

and the two following expressions can be derived from the wave crests continuity law [find the complete derivation in 135, §11.5]

$$\frac{D\mathbf{k}}{Dt} = \frac{\partial \mathbf{k}}{\partial t} + (\mathbf{v_g} \cdot \boldsymbol{\nabla}_k)\mathbf{k} = -\boldsymbol{\nabla}_{\boldsymbol{x}}\omega, \tag{37}$$

$$\frac{D\omega}{Dt} = \frac{\partial \omega}{\partial t} + (\mathbf{v_g} \cdot \boldsymbol{\nabla}_k)\omega = -\frac{\partial \omega}{\partial t}, \tag{38}$$

where $\boldsymbol{\nabla}_k = \partial/\partial k_i$ and $\boldsymbol{\nabla}_x = \partial/\partial x_i$. Such relations show that if the medium is not uniform nor stationary the characteristics are not straight lines. Moreover, it is interesting to observe that Eq. 37 and Eq. 38 are nonlinear in k and hyperbolic, even if the original problem is linear and generally not hyperbolic.
The group velocity is also the propagation speed of the wave packet energy density. If $\mathcal{E}$ and $\mathcal{F}$ are the energy density and flux respectively, for a conservative system

$$\frac{\partial \mathcal{E}}{\partial t} + \boldsymbol{\nabla} \cdot \mathcal{F} = 0. \tag{39}$$

This becomes

$$\frac{\partial \mathcal{E}}{\partial t} + \boldsymbol{\nabla} \cdot (\mathbf{v_g}\mathcal{E}) = 0, \tag{40}$$

meaning that the energy density changes, and the total energy contained within the group lines remains constant. In the wavenumber space instead, the spectral energy within a wavenumber range keeps constant, so the spectral density remains equal to the initial value. Note that the energy expression depends on the governing equation. The same behavior is followed by the squared amplitude A^2 and the *wave-action* $\mathcal{E}/\omega$ [for the complete theory, see 135, 136, 66].

2.3 Dispersion relation maps for the plane Poiseuille and Couette flows: phase velocity and group velocity

In the light of the results shown in Chapter 1, the analysis was extended over a wider range of Reynolds number and wavenumber. In the following, we present long-term dispersion relations maps of the wall-normal velocity perturbation for both the plane Poiseuille flow and the plane Couette flow.

Solutions to the Orr-Sommerfeld modal problem are well known. The first very accurate computations have been made available by Orszag in 1971 [104]. Earlier computations of the dispersion relation are due to Gallagher & Mercer in 1962 [51] for PCF, to Grosh & Salwen [62] and Mack [94] for PPF. The last authors also focused on the continuous spectrum, distinctive of unbounded flows [61, 116]. However, Reynolds wavenumber-Reynolds number maps concerning exact group velocity and dispersion are hard to find in the literature, especially for a wide range of Re and k. On the one hand, at the time of the first studies the computational resources required to trace such maps were simply not enough. Consequently, for studies about wave packets dynamics, this difficulty has often made it necessary to use the Squire's transformation; analytical approximations of the dispersion relation (expansion around points of maximum amplification [38] or, more suitably, about the saddle node of the integral 29 - with complex dispersion relation - as done by Gaster in several works [54, 59, 53, 55, 56]); algebraic model expansions, as done by Craik [31, 32]. On the other hand, the advent of computational resources after the 1980s shifted the focus on the newborn *non-modal* linear theory describing short-term transient algebraic growth [130] and nonlinear stability, by means of tools of analysis such as direct numerical simulations [105].

Here, the long-term dispersion relation is reconsidered, with the aim to highlight some features unexplored so far, which can be of help to explain the dynamics of small spots in sheared flows, as described in the following sections. The focus will be on the propagation properties, therefore the real part of the dispersion relation (asymptotic, that is for the least-damed mode) is taken for the analysis. Figure 13 shows the phase velocity (panels **a**, **b**), the group velocity (**c**, **d**) and the dispersion factor (**e**, **f**) for longitudinal waves ($\phi = 0$) in PPF (left) and PCF (right). These quantities refer to the temporal least-stable mode of the Orr-Sommerfeld equation 11 for the wall-normal velocity $\hat{v}$. The solutions have been computed by a 4th-order finite-difference scheme on uniform y-grid (700 points) implemented in the parallel MATLAB® environment (see [40] and figure 81 for a comparison with other numerical methods). Both the longitudinal wavenumber and the Reynolds number are uniformly distributed in the log-space, over a grid of 100×240 points respectively, with $k \in [0.01, 10]$ and $Re \in [10, 10^5]$. Computational resources were partially provided by HPC@POLITO, the project of Academic Computing within the Department of Control and Computer

Engineering at the Politecnico di Torino (`http://www.hpc.polito.it`).
The group velocity is computed from its definition ($\mathbf{v}_g(\mathbf{k_0}) = \boldsymbol{\nabla}\omega|_{\mathbf{k_0}}$) via the numerical derivative of the angular frequency ($\omega = \sigma_r$) over the wavenumber. A dispersion factor, indicative of the intensity of a wave packet's spreading rate, is then simply defined as the difference of the group and phase speeds $f_\mathrm{d} = \mathbf{v}_\mathrm{c} - \mathbf{c} = k(\mathrm{d}c/\,\mathrm{d}k)$. This is an index for the dispersion of a wave packet, as the spatial spreading rate is an increasing function of $|f_\mathrm{d}|$. In figure 13 (**e**,**f**), the sign of f_d is kept in order to retain information about if the packet, centered at a certain wavenumber, travels faster or slower with respect to the wave components contained in it.

The phase velocity map for the plane Poiseuille flow (figure 13 **a**) reveals interesting aspects. The dispersive-to-nondispersive threshold $k_\mathrm{d}(Re)$ (white curve) has been introduced in the previous chapter (see §1.4), where its role on the transient behavior for single waves was shown. Here, the dependence on Re becomes clear. Moreover, it was possible to observe that the sharp separation between fast nondispersive waves ($c \approx v_g \approx 1$ for $k > k_\mathrm{d}$) and slow dispersive waves ($k < k_\mathrm{d}$) ends up at about $Re \approx 88$ and $k \approx 2.5$ (wavelength almost equal to the channel width $2h$). Surprisingly, this value of Reynolds number is very close to the lower bound for perturbation kinetic energy growth. The curve Re_E for the energy and the curve Re for the enstrophy are reported in pink in all graphs, in order to give the complete picture. They will be the object of discussion in the next chapter. In particular, the lower bound for enstrophy growth is one of the original results of this dissertation. The region of the map close to this point is characterized by high level of dispersion as it is evident from panel (**e**) of figure 13.

The long waves also revealed unexpected features. The dispersive region below k_d, in fact, hosts three subregions where the dominant mode behaves differently than the least-stable mode in the surroundings. All these "niches" - as we called them for their narrowness - look tilted by $\pi/4$ in the log-log plot. This trend, $\partial/\partial(\log k) = \partial/\partial(\log Re) \rightarrow f = f(log(kRe))$, is recurrent in such maps at low wavenumbers, not only as regards the asymptotic phase velocity but also the transient growth of kinetic energy and enstrophy, see figure 37 in Chapter 3.
A common feature to all the three regions: excluding the instability region, they constitute the only part of the map where the leading mode (stable, in all cases) is *antisymmetric* (both the real and the imaginary part of $\hat{v}(y)$ are odd).

1. The first subregion is found for $Re > 545$ and $k < 0.28$. It is made of antisymmetric wall-modes (A-family, but close to S-family modes, according to the classification by Mack [94]) having intermediate phase speed ($c \approx 0.7$), pretty much equal to the group velocity, so dispersivity is low, and lower with respect to the surrounding part of the map.

2. The second subregion is found for $Re > 9770$ and $k < 0.13$, so it lies below the instability region. The identity of the eigenmodes is the same as in subregion 1, but these solutions travel with a lower phase speed ($c \approx 0.45$) which depends on the wavenumber, potentially leading to dispersion for wave packets containing this range of wavenumbers. In particular, the group speed ($v_g \approx 0.35$) is higher compared to the background region (see panel **c**) and it is smaller than the phase speed, see panel (**e**).

3. The third subregion is found for $Re > 29840$ and $k < 0.35$. In this case, the least-damped mode belongs to the right branch of the spectrum (P-family) and it is an antisymmetric, fast ($c \approx 1$), and central mode. Therefore, the behavior in this region is quite the same as in the non-dispersive part of the map at $k > k_d$.

Figure 13 also shows (in white) the *unconditional instability* region (where temporal asymptotic instability occurs, that is $\sigma_i > 0$), which begins at $Re_c = 5772.2$ and is located in the dispersive part of the graph just below k_d. In addition, the *monotonic stability* regions are shown for both the volume-averaged kinetic energy and enstrophy (pink curves). The reader will find definitions of such stability/instability regions in Chapter 3 which is focused on the transient growth of wave amplitude, see figure 33 in §3.2.

The dispersion relation map for the plane Couette flow differs quite considerably from the PPF one, see panels (**b**,**d**,**f**) of figure 13 (since the reference system is at the channel centerline, the eigenvalues spectrum is symmetric and centered at $c = 0$: there are always two least-damped solutions propagating in opposite directions. Figure 13 shows only the positive one). In this case there exists a threshold $k_p(Re)$ for non-propagation (white curve). This was first discovered by Gallagher&Mercer in 1962 [51], who observed that the three-branched symmetric eigenvalues spectrum, peculiar of the plane Couette flow, collapses to its central branch for wavenumbers below a certain value (all eigenvalues become purely imaginary, as a consequence the phase speed is zero). Analysis of wave transients for the Couette flow can be found in my MSc thesis [48]. The phase and group velocity are functions of $log(kRe)$, at least for $k < 1$, as can be noted from the contour lines. In contrast to the PPF case, no interchanges of leading modes are observed here, therefore an abrupt transition between dispersive and non-dispersive behavior does not exist. Dispersion is observed everywhere, with a smooth tendency to nondispersion as kRe increases. In general the dispersion is mild, but becomes intense close to the boundary curve $k_p(Re)$. A dispersion enhancement is also observed in a broad subregion below $Re \approx 100$.

What about the three three-dimensional case, that is the case of oblique waves ($\phi \neq 0$)?
Here, the dispersion relation of the least-damped mode can be deduced from the 2D case of figure 13. In fact, the Squire's transformation states that a 3D Orr-Sommerfeld

eigenmode at (k, Re) corresponds to a 2D eigenmode at the same wavenumber modulus and at a smaller Reynolds number, in particular $Re_{2D} = \frac{\alpha}{k} Re$, where $\alpha = k \cos\phi$ is the longitudinal component of the wavenumber. This means that the frequency for a 3D wave satisfies

$$\omega_{3D}(k, Re) = \omega_{2D}\left(k, \frac{\alpha}{k} Re\right),$$

leading directly to the following law for the modulus of the phase velocity (in the direction of the wavenumber vector):

$$c_{3D}(k, Re) = c_{2D}\left(k, \frac{\alpha}{k} Re\right) \cos\phi.$$

This means that the map structure remains the same but the map translates to the right, in the log-log plot (this of course does not apply to the energy and enstrophy curves Re_E, Re_Ω). Concurrently, as the wave angle increases, a decrease of both the phase velocity and the group velocity is observed, according to the above cosine law. Waves transversal to the basic flow direction ($\phi = \pi/2$) are indeed stationary. It should be noted that such law also describes the dispersion relation of shear Alfvén waves, see §4.6.

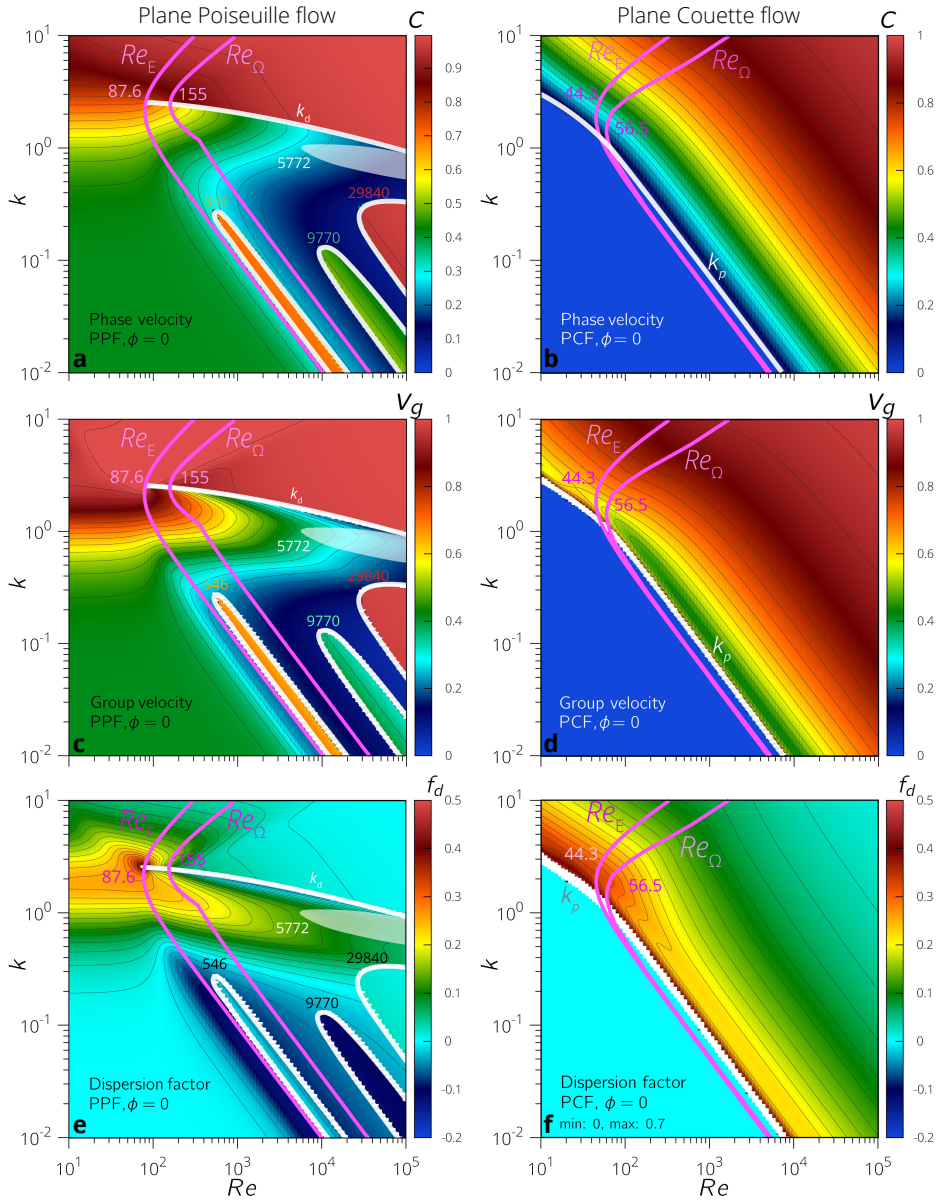

Figure 13: Long-term dispersion relation for the plane Poiseuille and Couette flows. The temporal asymptotic dispersion relations of the least-damped mode for PPF (left column) and PCF (right column) are shown for $Re \in [10, 10^5]$ and $k \in [10^{-2}, 10]$, for longitudinal waves ($\phi = 0$). These maps contain 100×240 (Re, k) simulations, uniformly distributed in the log-log space. **(a,b)** Phase velocity, c. The threshold k_d introduced in the Chapter 1 can be clearly observed here as a function of Re (white curve) for PPF. In the PCF case instead, a lower bound for wave propagation, k_p, is observed. The pink curves $Re_\mathrm{E}(k)$, $Re_\Omega(k)$, represent the lower bounds for kinetic energy and enstrophy transient growth, respectively. Moreover, three subregions are found for PPF, in the low-k part of the map, having different dispersion properties than the surroundings. In the text, we will denote them *subregion 1,2,3* (from left to right). **(c,d)** Group velocity, v_g. **(e,f)** Dispersion factor, $f_\mathrm{d} = v_\mathrm{g} - c$. In all maps, the asymptotic instability region is represented in white.

2.4 **Numerical simulations of linear wave packets in the plane Poiseuille flow**

The dynamics of wave packets internal to sheared flows has been of great interest since the pioneering experiments in pipe flows by Hagen in 1839 [65], by Poiseuille in 1840 [108], and later by Reynolds in 1883 [111]. In that occasion, the intermittent character of the transition was observed for the first time, and Reynolds named "flashes" the episodes of rapidly oscillating disturbances that he found to precede the development of turbulence. Since then, the laminar-to-turbulent transition has been one of the topics of major interest in fluid mechanics. The determination of the mechanisms at the onset of the transition is a challenging point of great importance for both the understanding of the general nature of turbulence and practical applications.
In particular, sheared parallel/near-parallel flows - both bounded, as the plane Poiseuille and Couette flows, and unbounded, as boundary layers, jets and wakes - undergo *subcritical* direct transition. The initial linear stage of the dynamics of localized perturbations is key in that it already displays features which are typical (and, in some cases, act as drivers) of the subsequent process of breakdown to turbulence. For a comprehensive and updated review of the instability and transitional processes we suggest the book by Yaglom [140].

In this section, the results of our linear numerical simulations of localized disturbances are shown and discussed for the two and three-dimensional case in the plane Poiseuille flow. This flow has been considered as a first case study due to the peculiar features of its dispersion relation, highlighted in §2.3 and in Chapter 1. Since the coexistence of dispersive and nondispersive wave components is an intrinsic property of several other shear flows as wakes, boundary layers and the pipe flow (see for instance [98]), it is possible to assume that the physical phenomenology described here may be general.

Numerical simulations have been performed via a MATLAB® software, built in order to compute localized wave packets of arbitrary initial shape. The processing core, dedicated to compute the temporal evolution of the single Fourier components, is based on a semi-analytical solution of the Orr-Sommerfeld and Squire initial-value problem via the Galërkin method. The full description can be found in the Supplementary Information of [40] and in Appendix A of this thesis. In the pre-processing, the base flow, the simulation parameters (the Reynolds number Re, the domain size L_x and L_z, the temporal and spatial discretization) and the initial conditions in the physical space are specified. A dedicated subroutine returns, by Fourier transform, the complex initial coefficients and the wavenumber components (α, β) which will be simulated. Eventually, the post-processing routine performs an inverse Fourier transform to compute the perturbation velocity and vorticity fields at selected points in space and time. Other post-processing routines are used to compute the wave packet center and the spreading rates, and to produce movies.

Noting that the plane Poiseuille flow is homogeneous in the x and z directions, the solution for any field quantity $\widetilde{q}$ of a general small perturbation is expressed as:

$$\widetilde{q}(x,y,z,t) = \Re\Big\{ \frac{1}{(2\pi)^2} \iint a_{\mathrm{q}}(t,y;\alpha,\beta) e^{i\alpha x + i\beta z}\, \mathrm{d}\alpha\, \mathrm{d}\beta \Big\}, \tag{41}$$

where $\Re$ stands for the real part. It is convenient to split the coefficient a_{q} in two factors

$$a_{\mathrm{q}}(t,y;\alpha,\beta) = \widehat{q}(t,y;\alpha,\beta)\widehat{f}(\alpha,\beta), \tag{42}$$

where $\widehat{q}$ is a single wave solution to the initial value problem 11 and $\widehat{f}$ is given by the initial spatial shape of the disturbance in the xz-plane. The initial coefficients result:

$$a^0_{\mathrm{q}}(y;\alpha,\beta) = \widehat{q}^0(y;\alpha,\beta)\widehat{f}(\alpha,\beta). \tag{43}$$

The velocity-vorticity formulation 11,12 requires the initial wall-normal velocity $\widehat{v}^0(y)$ and the initial wall-normal vorticity $\widehat{\omega}^0_y(y)$. The latter was set to zero, as discussed in §1.3. The cross-shear velocity $\widehat{v}^0(y)$ was instead chosen in order to guarantee a transient growth of the perturbation kinetic energy for any wavenumber included in the packet (the shape of $\widehat{v}^0(y)$ is shown in figure 36(**b**), in Chapter 3). Such initial condition was obtained from an optimization process which seeks the perturbation which maximizes the kinetic energy growth rate $1/E(\mathrm{d}E/\mathrm{d}t)$, at fixed values of k and Re.

A FORTRAN 90 code that I built based on the genetic optimization code PIKAIA [27, 28], proved to be versatile and adaptable to different problems faced within the context of this dissertation, from hydrodynamic stability to solar-wind spectral analyses. The optimization of the energy rate functional 1.4 occurs over the coefficients (acting as chromosomes, in the genetic optimization terminology) of the Chandrasekhar functions expansion 179. See Appendix B for an application of this software to find the monotonic stability region of the kinetic energy.
The initial condition $\widehat{v}^0(y)$ excites both symmetric and antisymmetric OS modes, it is smooth and has quite a 'simple' shape. The distribution in the xz plane was chosen to be Gaussian. This was done in order to represent a smooth, spatially-localized, perturbation ($= 0.1$) having a similar distribution to disturbances usually introduced in laboratory experiments (where dye is typically injected from a small hole in the wall [26, 85, 84]) or numerical experiments [71]:

$$f(x,z) = \frac{1}{\sqrt{2\pi}} e^{-[(x-x_0)^2+(z-z_0)^2]/2\gamma^2} \rightarrow \widehat{f}(\alpha,\beta) = \mathcal{F}\{f(x,z)\} \tag{44}$$

Operatively, the integral 41 is a discrete Fourier transform:

$$\widetilde{q}(x,y,z,t) = \Re\Big\{ \frac{1}{N_{\mathrm{x}} N_{\mathrm{z}}} \sum_{j=-\frac{N_{\mathrm{x}}}{2}}^{\frac{N_{\mathrm{x}}}{2}-1} \sum_{k=-\frac{N_{\mathrm{z}}}{2}}^{\frac{N_{\mathrm{z}}}{2}-1} a_{\mathrm{q}}(t,y;\alpha,\beta) e^{i\alpha_j x + i\beta_k z} \Big\}, \tag{45}$$

Table 4: Wave packets simulations parameters.

	2D linear	**2D** nonlinear	**3D** linear
$\mathbf{x_0}$	0	5	0
$\mathbf{z_0}$	-	-	0
γ	0.1	0.1	0.1
$\boldsymbol{Re}$	500, 1000	1000,6000	500,1000
$\boldsymbol{v}_{0\ max}$	-	$0.2U_{CL}$	-
$\mathbf{L_y}$	2	2	2
$\mathbf{N_y}$	100	129	100
$\mathbf{L_x}$	60	50	30
$\mathbf{L_z}$	-	0.1	64
$\mathbf{N_x}$	512	256	64
$\mathbf{N_z}$	-	8	64
$\mathbf{T_{max}}$	80	180	80
$\mathbf{\Delta t}$	0.3	0.01,0.03	0.3

where N_x and N_z are the number of grid points and $\alpha_j = \frac{2\pi j}{N_x \Delta x}$, $\beta_k = \frac{2\pi k}{N_z \Delta z}$ are the discrete streamwise and spanwise wavenumbers, respectively.

Table 4 summarizes the input parameters for the simulations presented in the following. These simulations include the 2D and 3D linear analyses described above, and two preliminary and demonstrative 2D nonlinear analysis performed via our DNS pseudospectral channel code [77]. The time step Δt does not affect the numerical stability of the linear simulations, as the numerical method is semi-analytic; the chosen value, 0.3, ensures good-quality movies (the highest frequencies in the packet are well resolved $\Delta t \approx \frac{T_{\min}}{5} \approx \frac{2\pi}{5 c_{\max} k_{\max}} \approx \frac{2\pi}{5 k_{\max}}$). For the DNS instead, a constant Runge-Kutta integration time $\Delta t = 10^{-4}$ is set for convergence. In this case the time is non-dimensionalized with the friction time $t_w = h/u_\tau$. It is reminded that the reference velocity for wall-units is defined as the *friction velocity* $u_\tau = \sqrt{\tau_w/\rho}$ (τ_w is the wall friction stress). In these units, the Reynolds number is $Re_\tau = u_\tau h/\nu$.

The wave packet center is computed for each squared field component (at a fixed distance from the wall $y_0 = -0.6$), for the averaged kinetic energy and for the averaged enstrophy. Using the following notations for the averaging operations over y, z and x:

$$\langle \widetilde{q} \rangle_{\mathrm{y}}(t,x,z) = \frac{1}{L_{\mathrm{y}}} \int \widetilde{q}\, \mathrm{d}y,$$
$$\langle \widetilde{q} \rangle_{\mathrm{z}}(t,x,y) = \frac{1}{L_{\mathrm{z}}} \int \widetilde{q}\, \mathrm{d}z,$$
$$\langle \widetilde{q} \rangle_{\mathrm{x}}(t,y,z) = \frac{1}{L_{\mathrm{x}}} \int \widetilde{q}\, \mathrm{d}x,$$

the wave packet center of a generic field component $\widetilde{q}$ is defined as

$$x_{\mathrm{G}}(t,y_0) = \frac{\int x \langle \widetilde{q}^2 \rangle_{\mathrm{z}}\, \mathrm{d}x}{\int \langle \widetilde{q}^2 \rangle_{\mathrm{z}}\, \mathrm{d}x}. \tag{46}$$

About the average kinetic energy $\langle E \rangle_y = \langle \widetilde{u}^2 + \widetilde{v}^2 + \widetilde{w}^2 \rangle_{\mathrm{y}}$, and enstrophy $\langle \Omega \rangle_y = \langle \omega_{\mathrm{x}}^2 + \omega_{\mathrm{y}}^2 + \widetilde{\omega}_{\mathrm{z}}^2 \rangle_{\mathrm{y}}$:

$$x_{\mathrm{G}}(t) = \frac{\int \langle \langle E \rangle_{\mathrm{y}} \rangle_{\mathrm{z}} x\, \mathrm{d}x}{\int \langle \langle E \rangle_{\mathrm{y}} \rangle_{\mathrm{z}}\, \mathrm{d}x} \qquad x_{\mathrm{G}}(t) = \frac{\int \langle \langle \Omega \rangle_{\mathrm{y}} \rangle_{\mathrm{z}} x\, \mathrm{d}x}{\int \langle \langle \Omega \rangle_{\mathrm{y}} \rangle_{\mathrm{z}}\, \mathrm{d}x}. \tag{47}$$

In order to compute correctly the packet center, especially at long times, we must overcome the periodicity problem. That is, as a consequence of the periodic boundary conditions in x and z, the perturbation moving from left to right exits the domain at right and enters at left, as it approaches the domain boundary. A post-processing subroutine has been dedicated to recognize this situation and to center the domain at the wave packet center. This is obtained through an iterative procedure using a moving-box.

The streamwise spreading is computed by looking for the portion of the domain containing 95% of the energy. The boundaries of this region are named $x_{2.5\%}$ and $x_{97.5\%}$ respectively, and are defined either as the locations of the 2.5^{th} and 97.5^{th} percentile of the z-averaged squared variable considered, or from the yz-averaged energy and enstrophy):

$$x_{2.5\%}(t) \quad \int_{-\infty}^{x_{2.5\%}} \langle \widetilde{q}^2 \rangle_{\mathrm{z}}\, \mathrm{d}x = 0.025 \int_{-\infty}^{\infty} \langle \widetilde{q}^2 \rangle_{\mathrm{z}}\, \mathrm{d}x, \tag{48}$$

$$x_{97.5\%}(t): \quad \int_{-\infty}^{x_{97.5\%}} \langle \widetilde{q}^2 \rangle_{\mathrm{z}}\, \mathrm{d}x = 0.97 \int_{-\infty}^{\infty} \langle \widetilde{q}^2 \rangle_{\mathrm{z}}\, \mathrm{d}x. \tag{49}$$

Analogously, the spanwise spreading and spreading half-angle are computed from the x-averaged squared variables:

$$z_{2.5\%}(t): \quad \int_{-\infty}^{z_{2.5\%}} \langle \widetilde{q}^2 \rangle_{\mathrm{x}}\, \mathrm{d}z = 0.025 \int_{-\infty}^{\infty} \langle \widetilde{q}^2 \rangle_{\mathrm{x}}\, \mathrm{d}z, \tag{50}$$

$$_{2.5\%} = tan^{-1}\left(\frac{z_{2.5\%}}{x_{\mathrm{G}}}\right). \tag{51}$$

2.4.1 *2D wave packets*

The two-dimensional case was firstly considered. The wave packet evolution in 2D is shown in figures 14 and 18 for $Re = 500$, and in figures 16 and 19 for $Re = 1000$ (see also the related movies, find the links in the figures caption). The basic flow is directed from left to right. These two values of Reynolds number were chosen as case studies since they are respectively below and above the *global stability* threshold of the plane Poiseuille flow ($Re_g \approx 840$, [97]), see §3.2. Moreover, these values are also above and below the first subregion - found for $Re > 546$ - in the dispersion relation map described in the previous section (figure 13). The wall-normal velocity perturbation $\widetilde{v}$ (figures 14,16) shows an algebraic, convective-instability scenario in the short/intermediate temporal term. The wave packet is featured by both dispersion and non-dispersion, it consists indeed of a *rear* part (or *trailing-edge*) moving much slower than the base flow centerline speed, $u_{rear} \approx 0.2U_{CL}$, and a fast *front* (or *leading-edge*, or *nose*) with propagation speed nearly equal to U_{CL}. The rear is dominated by long wavelengths (for instance, at $t = 30$ $\lambda_{rear} \approx 10$, $k_{rear} \approx 0.63$), while higher wavenumbers prevail in the front ($\lambda_{front} \approx 1.5$, $k_{front} \approx 4$). The disturbance center (see the black square in the figures) moves with a slightly smaller speed than $0.5U_{CL}$.
Such general structure is well known from experimental investigations on the bypass transition to turbulence, as referenced in the discussion below and in §2.4.2.

Form the spanwise vorticity distribution (figures 18 and 19) another interesting feature can be observed: the dynamics is associated with the generation of an intense streamwise shear layer, first observed in the 1980s in boundary layers by Breuer & Haritonidis [22], Breuer & Landahl [23], and in the plane Poiseuille flow by Klingmann [84] and Henningson, Lundbladh & Johansson [71] (see, for instance figure 6 in [84] and figure 3 in [71]). Similar structures are also peculiar of puffs in pipe flows, see for instance [139, 44, 9]. This shear layer has a characteristic Λ-shape heading downstream, made of two layers originating at the walls in the dispersive region of the packet and merging at the channel center, at the spot front. The physical mechanism leading to this structure is the *lift-up effect* described by Landahl in 1975 in a paper dedicated to wave breakdown leading to transition to turbulence [87]. Due to this effect, streamwise streaks of high and low perturbation velocity are generated as a consequence of vertical displacement of fluid particles by the wall-normal perturbation velocity. Although this mechanism - implied in the sustainment of wall-bounded turbulence - applies mostly to 3D perturbations, it is also present in the 2D case. Indeed, the mechanism is mainly linked to the "vortex tilting term" $i\beta U'\widehat{v}$ which appears at the right hand side of the Squire equation (12), but also to the U'' term in the Orr-Sommerfeld equation (11). Landahl discovered that the net generation of kinetic energy in the $\widetilde{u}$ perturbation leads, in the long term, to an elongated *permanent scar* convected downstream with the local basic flow speed. The term *permanent* refers to the much longer decay time experienced

by this streamwise perturbation, with respect to that of the wall-normal perturbation $\widetilde{v}$. For this region, such shear layer is not visible from the $\widetilde{v}$ component and it is usually observed from the streamwise velocity $\widetilde{u}$ or from the spanwise vorticity, as done in our study (figures 18, 19).

The situation described above is confirmed by our numerical simulations. In addition, we would like to stress that the separation between dispersive and "convective" parts of the initial disturbance can be framed within the viscous hydrodynamic linear wave theory both for the early transient evolution and for the asymptotic stage.

The observation of a wavenumber threshold k_{d} beyond which the non-dispersive $\widetilde{v}$ modes at the tip of the P-branch (or the continuous spectrum as shown in Chapter 1, figure 2, for the wake flow) are less damped than the dispersive A-family modes (both even and odd modes) is relevant to a better understanding of the described dynamics. The 2D spot front in terms of wall-normal velocity perturbation is highlighted in figures 15,17 for $Re = 500$ and $Re = 1000$, respectively. The short waves which constitute this part have their amplitude and y-derivative peaks located at the channel center, which translates into high vorticity at the spot nose. The broad rear part is made instead of a set of A-modes which at $t = 20$ already take the features of the symmetric least-stable one. Such modes have their amplitude maximum at the channel centerline but high cross-shear variations close to the wall, which explains the high vorticity at the walls and the generation of the shear layer.
The current state of our research does not allow us to deduce the influence of the wave components which belong to the subregion 1, shown in figure 13. In this regard, we are planning future investigations on longer channels, needed to catch those wavenumbers.

Two demonstrative nonlinear direct numerical simulations (DNS) have been performed at $Re = 1000$ and 6000, with an initial disturbance amplitude as high as 20% of the centerline speed, in order to show that the spot morphology arising from the linear analysis is persistent, very deep-seated in the nature of the plane Poiseuille flow (this applies as well to other shear flows). The results are shown in figures 20 and 21 for the same time instants shown in the preceding figures (see also the related movies). Apart from the amplitude, the initial condition is the exact same used for the linear simulations. The spot nose appears to be quickly ejected from the wave packet. Between the nose and the rear, a compact big-sized structure is found. It travels at an intermediate speed of about 0.77 U_{CL}, and can be clearly observed in the bottom panel of figures 20,21. It is not easy to identify it from figures 14, 16, but still exists in those linear simulations. This structure may be related to symmetric modes located close to central branch of the eigenvalues spectrum, having dispersion properties similar to those of subregion 1 in figure 13. About the trailing-edge, it is possible to note that the dispersion decreases as the Reynolds number increases, which is the reason why the intermediate structure is more visible in the case $Re = 6000$. This can be somehow guessed from panel (**e**)

of figure 13, as the discrepancy between the phase and group velocity reduces with Re for all the wavenumbers.

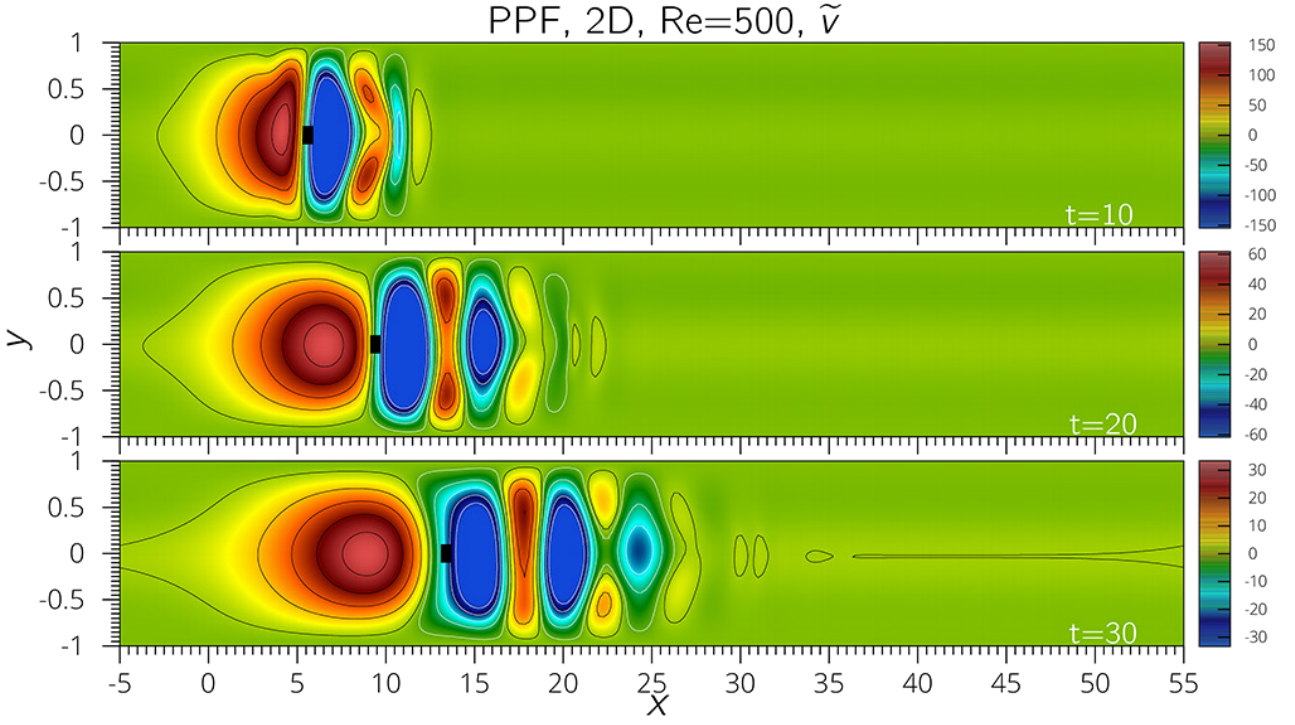

Figure 14: Linear 2D wave packet in plane Poiseuille flow at Re=500, wall-normal velocity perturbation. The disturbance velocity field $\widetilde{v}$ is shown at three time instants (top to bottom), $T = 10, 20, 30$ (all variables are non-dimensional, with the channel half-width h and the centerline speed U_{CL}). The initial perturbation is localized at $x_0 = 0$, the initial peak value is $\widetilde{v}_{\mathrm{max}}(t = 0) = 1530$, (irrelevant to the packet evolution, in the linear context). For each panel, five contour lines are traced, the first level is 0.05 $\widetilde{v}_{max}$ and the last one is 0.9 $\widetilde{v}_{max}$, where the peak value $\widetilde{v}_{max}$ can be inferred from the color bars. The simulation parameters are reported in table 4, the basic flow is from left to right. [External movie file: `movie_V_PPF2D_Re_500_V.avi`].

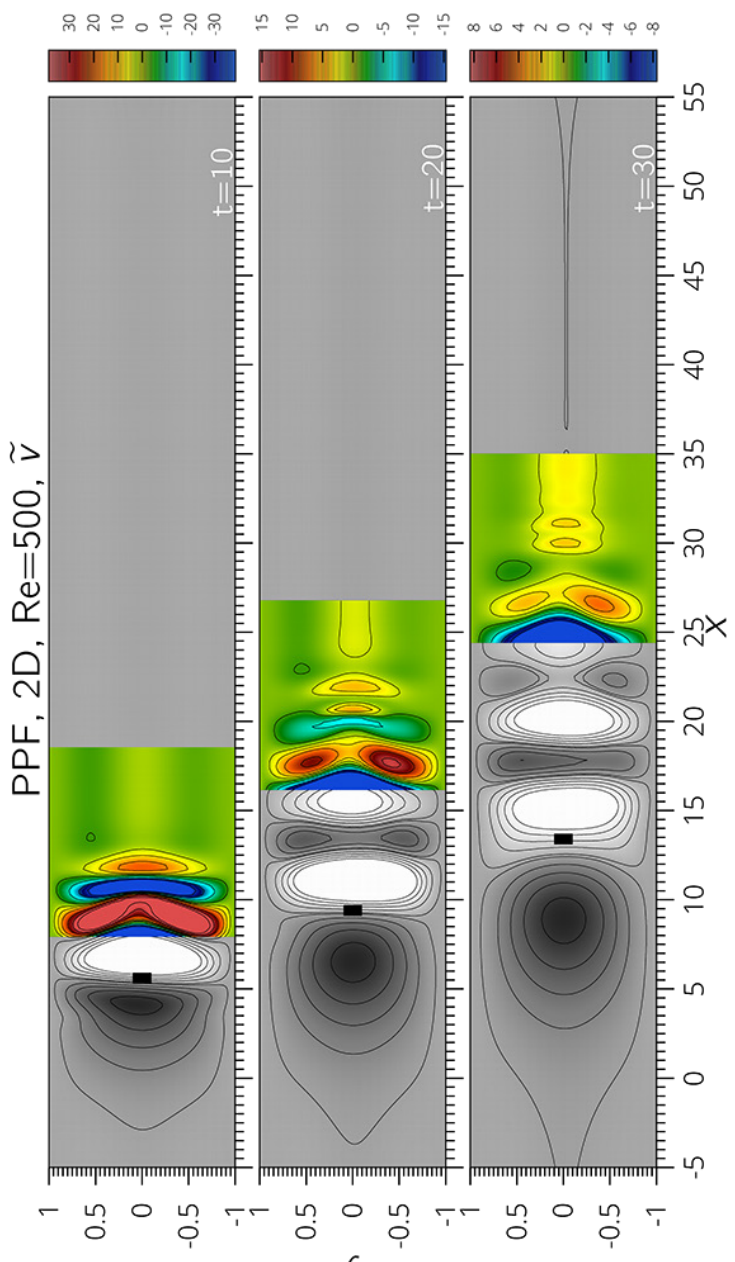

Figure 15: Focus on the non-dispersive front of a linear 2D wave packet in plane Poiseuille flow at Re=500, wall-normal velocity visualization. Figure 14 is here reproduced with a double color map in order to enhance the spot front, which is located at the channel center and propagates with the convective speed. For each panel, five contour lines are traced, the first level is 0.05 $\tilde{v}_{max}$ and the last one is 0.9 $\tilde{v}_{max}$, where here $\tilde{v}_{max}$ is the peak value in the enhanced region, which can be inferred from the color bars. For numerical values in the gray part of the figure, refer to figure 14 above.

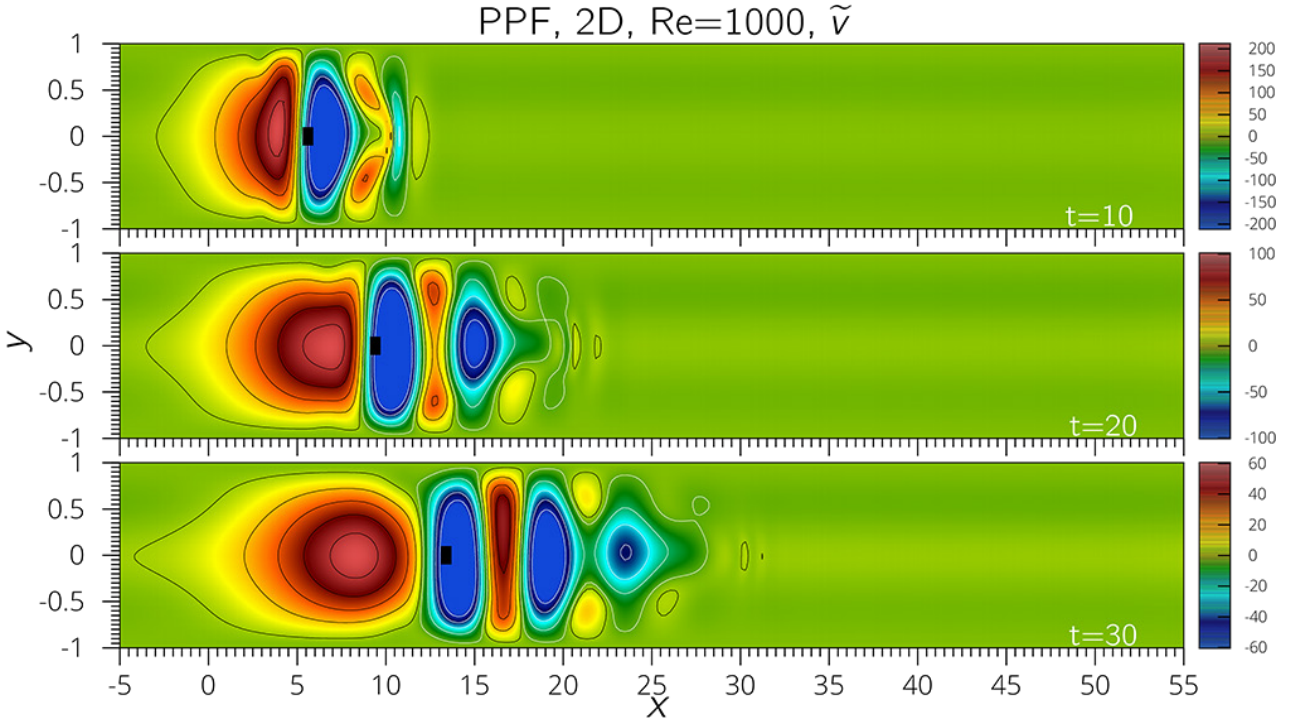

Figure 16: Linear 2D wave packet in plane Poiseuille flow at Re=1000, wall-normal velocity perturbation. The same initial perturbation of figure 14 is simulated at a higher Reynolds number, $Re = 1000$. This figure shows the $\widetilde{v}$ disturbance at $T = 10, 20, 30$ (top to bottom). The initial perturbation is localized at $x_0 = 0$, the initial peak value is $\widetilde{v}_{\max}(t = 0) = 1530$, (irrelevant to the packet evolution, in the linear context). For each panel, five contour lines are traced, the first level is 0.05 $\widetilde{v}_{max}$ and the last one is 0.9 $\widetilde{v}_{max}$, where the peak value $\widetilde{v}_{max}$ can be inferred from the color bars. [External movie file: `movie_V_PPF2D_Re_1000_V.avi`]

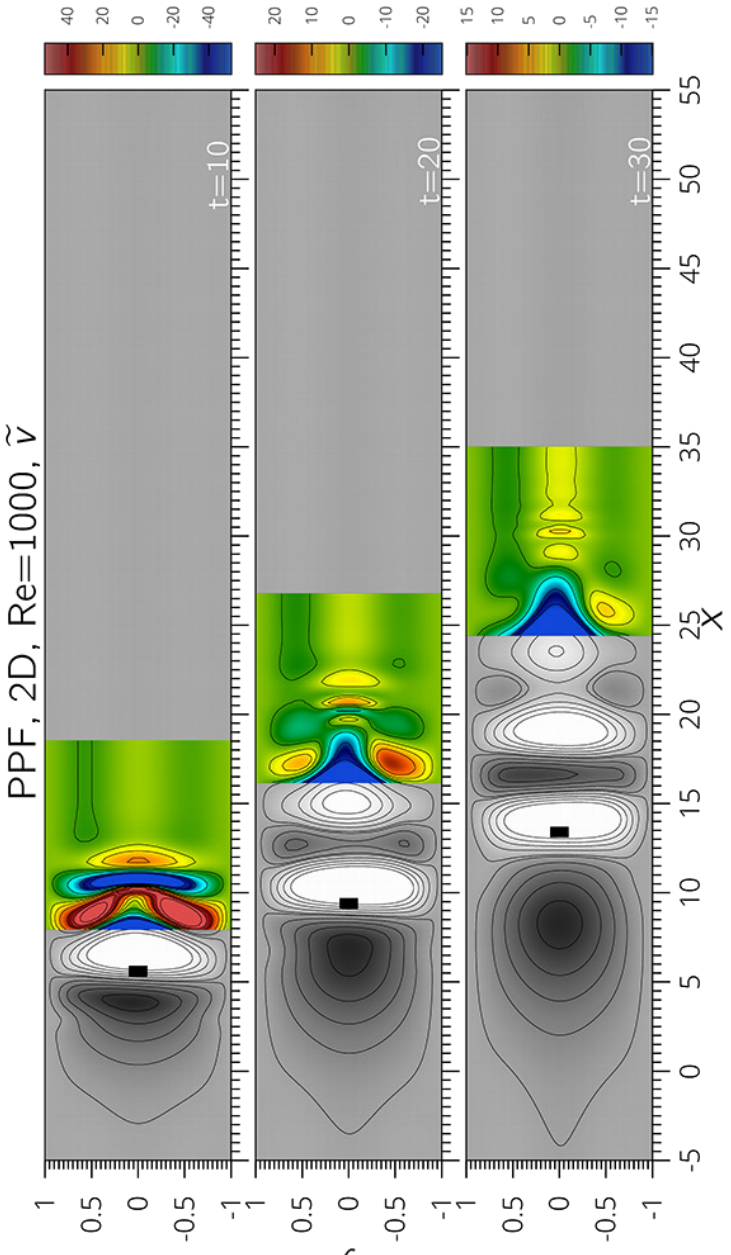

Figure 17: Focus on the non-dispersive front of a linear 2D wave packet in plane Poiseuille flow at Re=1000, wall-normal velocity visualization. Figure 16 is here reproduced with a double color map in order to enhance the spot front, which is located at the channel center and propagates with the convective speed. For each panel, five contour lines are traced, the first level is 0.05 $\tilde{v}_{max}$ and the last one is 0.9 $\tilde{v}_{max}$, where $\tilde{v}_{max}$ is the peak value in the enhanced region, which can be inferred from the color bars. For numerical values in the grey part of the figure, refer to figure 16 above.

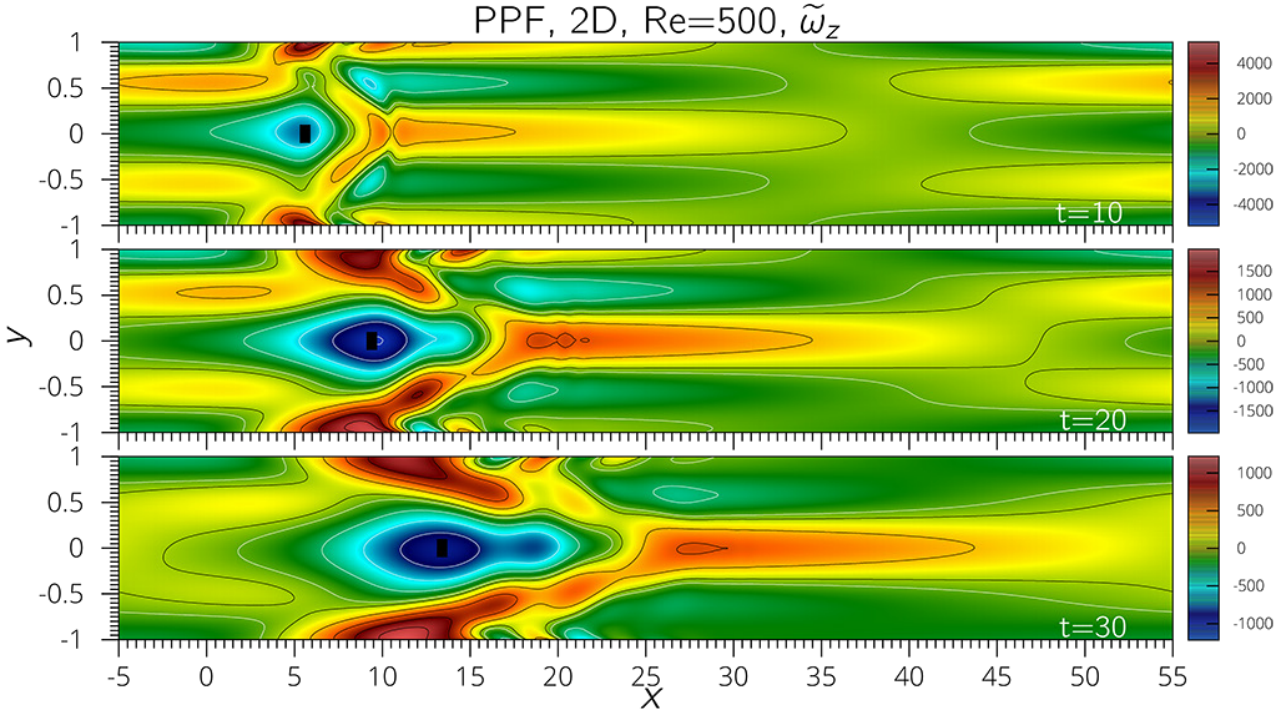

Figure 18: Linear 2D wave packet in plane Poiseuille flow at Re=500, vorticity visualization. The vorticity disturbance field $\widetilde{\omega}_z$ is shown for the same simulation of figure 14. The initial peak value in this case is about $\widetilde{\omega}_{y\ max}(t=0) = 12000$. For each panel, five contour lines are traced, the first level is 0.05 $\widetilde{\omega}_{y\ max}$ and the last one is 0.9 $\widetilde{\omega}_{y\ max}$, where the peak value $\widetilde{\omega}_{y\ max}$ can be inferred from the color bars. [External movie file: `movie_V_PPF2D_Re_500_OZ.avi`]

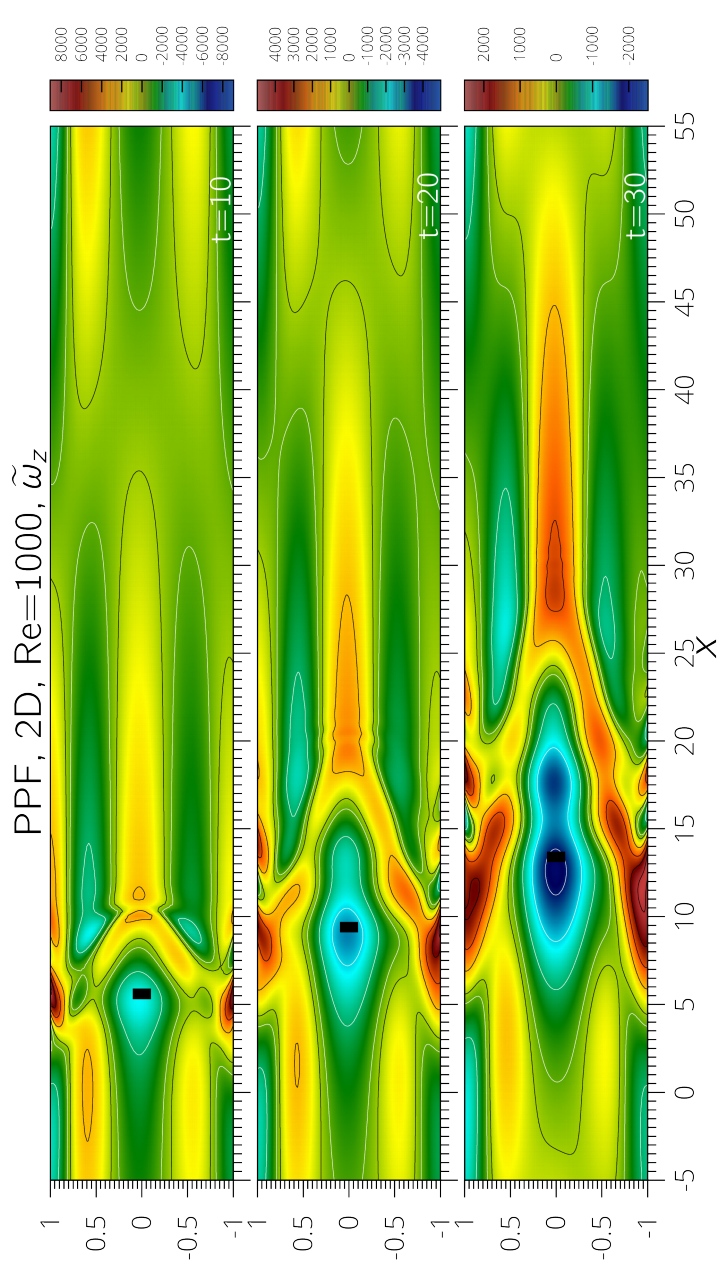

Figure 19: Linear 2D wave packet in plane Poiseuille flow at Re=1000, vorticity visualization. The vorticity disturbance field $\tilde{\omega}_z$ is shown for the same simulation of figure 16. The initial peak value in this case is about $\tilde{\omega}_{y\ max}(t=0) = 12000$. For each panel, five contour lines are traced, the first level is 0.05 $\tilde{\omega}_{y\ max}$ and the last one is 0.9 $\tilde{\omega}_{y\ max}$, where the peak value $\tilde{\omega}_{y\ max}$ can be inferred from the color bars. [External movie file: `movie_V_PPF2D_Re_1000_OZ.avi`]

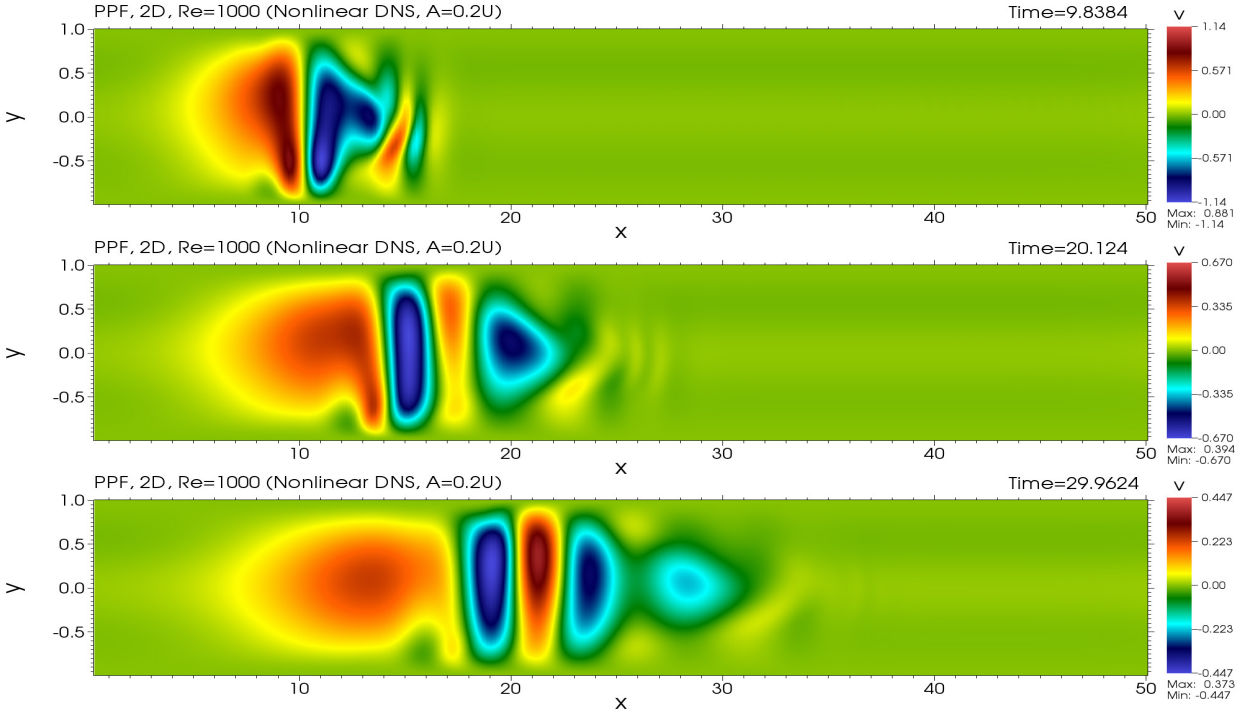

Figure 20: Nonlinear DNS of a 2D wave packet in plane Poiseuille flow at Re=1000 (Re_τ=44.7), wall-normal velocity visualization. The case study shown in the above figure 16 is here considered by taking account for nonlinear terms of the Navier-Stokes equations, via direct numerical simulation (parameters as in table 4). The panels show the wall-normal perturbation velocity (v/u_τ), that is, the values shown at the color bars are normalized with the friction velocity $u_\tau = \sqrt{\tau_w/\rho}$. Reminding that $Re_\tau = u_\tau h/\nu$, for the plane Poiseuille parabolic profile the following relations hold: $Re_{\mathrm{CL}} = 0.5 Re_\tau^2$, $(u/U_{\mathrm{CL}}) = 2(u/u_\tau)/Re_\tau$. The peak value at $t = 0$ for this simulation is $v/u_\tau = 3.95$, corresponding to $\widetilde{v} = v/U_{\mathrm{CL}} = 0.2$. [External movie file: `movie_dns_PPF2D_Re1000_A020_V.avi`]

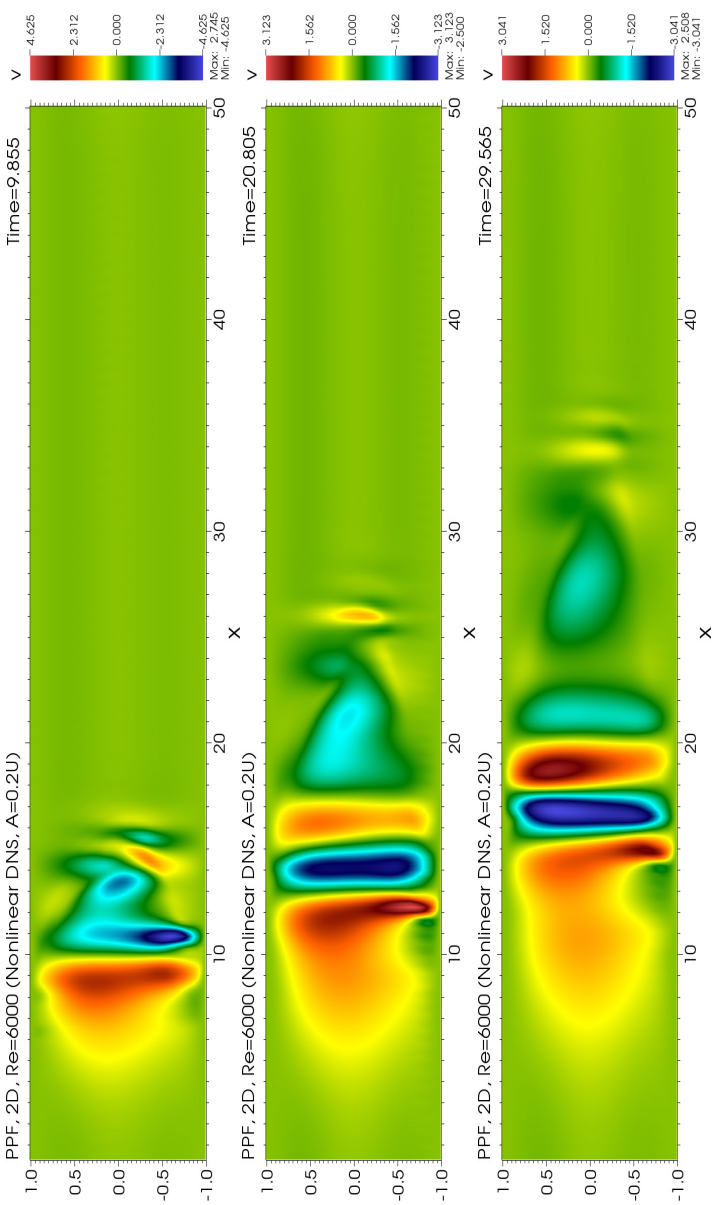

Figure 21: Nonlinear DNS of a 2D wave packet in plane Poiseuille flow at Re=6000 (Re_τ=109.5), wall-normal velocity visualization. Even in this simulation the initial maximum amplitude was set to 20% the centerline velocity. Note, compared to the case at $Re = 1000$, the more marked spacing between the spot leading edge and the rear part, due to the smaller dispersion of the latter (cfr. figure 13). An intermediate long-sized structure is clearly observed. [External movie file: `movie_dns_PPF2D_Re6000_A020_V.avi`]

2.4.2 *3D wave packets*

In this section, results of three-dimensional simulations of linear spots in the plane Poiseuille flow are given, in terms of (i) visualizations in the xz-plane of the perturbation velocity field (see figure 24), perturbation vorticity field (figure 25), y-averaged kinetic energy and enstrophy (figures 26, 27); (ii) propagation, longitudinal and lateral spreading and volume-averaged energy transient (figures 28, 29). Even for the three-dimensional localized perturbation, the transient temporal evolution is characterized by a slow dispersive part and a faster propagating front. The flow structure in the plane of the shear (the xy-plane, in our notation), which has been described in the previous section, is found even more so in the three-dimensional case, where tilted shear layers are generated by the lift-up effect (see the recent work by Brandt [2014, 21]) due to the presence of streamwise vorticity. The lift-up effect was found to be proportional to the wall-normal vorticity by Henningson [1988, 67]. As a consequence to this mechanism, which is particularly efficient for low streamwise wavenumbers (highly oblique waves), typical elongated streaks of high and low streamwise velocity arise at the spot leading-edge. Mathematically, such kinetic energy growth is due to cancellation effects among non-normal Orr-Sommerfeld and Squire modes, an *algebraic* instability process referred to as *non-modal growth*. For a complete review on non-modal stability theory, see Schmid [2007, 121]. It should be reminded that in the present context such algebraic instability occurs in the short/intermediate term. However, it has been shown [29] that algebraic instability can also occur in the long-time from the superposition of normal modes, see for instance the recent works in the field of hydrodynamics of thin planar liquid sheets [12, 11, 82].

The lift-up mechanism was first found to be responsible of the three-dimensional nature of the transition-to-turbulence process by secondary instability of longitudinal waves (cfr. the observations from the boundary-layer experiments by Klebanoff, Tidstrom & Sargent [1962 83], and the theoretical work by Landahl [1980 88]), reviewed by Herbert [1988 76] and Bayly [1988 13]. However, this process is also responsible for the growth of localized perturbations in sheared flows, which are of great interest in another scenario: the *subcritical* route to turbulence, also known as *bypass transition*. A process featured by the nucleation and growth of localized spots, which has been object of an enormous body of studies (up to this day), since their discovery from the experiments by Emmons [1951, 46], Riley [1985, 112], Carlson [1982, 26], Lundbladh & Johansson [1991, 93]. In fact, the thresholds for *global stability* (the limit below which perturbations of any initial shape and amplitude eventually decay over time) found from laboratory and numerical experiments still lack a thorough theoretical explanation (see Chapter 3 for a discussion about such threshold). Other features, not completely understood, concern the spreading rates, the spot morphology and the wave properties, which are the object of the present chapter.

The initial stage of the spatio-temporal evolution of a localized disturbances can be studied by means of a linear analysis. This is confirmed by the experiments, and justified by an important finding [1993, 71]. Quoting Henningson [1994, 75]: "The total energy of localized disturbance of arbitrary amplitude cannot grow without the existence of linear growth mechanism". Note, indeed, that the (not linearized!) Reynolds-Orr equation 21 for the total kinetic energy contains only linear terms in the energy.

The structure of turbulent spots in the plane Poiseuille flow was first described by Carlson [26] (see figure 3 in his paper) and subsequently confirmed by many other works, among which [5, 68, 74, 69, 85, 70, 84]. Recurrent features are the arrowhead shape marked by a fast nose, a leading-edge of quite oblique waves, spanwise wavy wingtips driving the spreading of the turbulent core, and streaks. The object of our work is to highlight the role of wave dispersion in the global morphology of linear spots, with a focus on the arrowhead shape and typical perturbation scales. This work may be of help to a better understanding of the transitional process.

The parameters of our simulations are shown in table 4. The arrowhead shape, which develops after an early transient lasting few time scales, is evident from any quantity considered and in particular from the wall-normal velocity perturbation. This is shown in figure 24, panels (**d**), (**e**), (**f**), for $Re = 1000$ (the morphology is qualitatively unchanged at $Re = 500$, see the movies in the figure caption). For this specific velocity component indeed, it is possible to plainly distinguish an outer part and an inner part, see figure 22. In the following, we will refer to the *outer region* as the wave packet spanwise tips, while the *inner region* comprises the spot center, the front and the leading edges.

Taking as a reference the case at $Re = 1000$ and $t = 30$, the tips appears as wavetrains having a typical wavelength $\lambda_{\text{tip}} \approx 4.2$ ($k_{\text{tip}} \approx 1.5$) and an angle between the wave vector and the undisturbed flow $\phi_{\text{tip}} \approx 35^\circ$. At the leading edge instead, we find more elongated and tilted waves with $\lambda_{\text{le}} \approx 1.89$ ($k_{\text{le}} \approx 3.32$) and $\phi_{\text{le}} \approx 71^\circ$. The inner part close to the spot core is featured by a modulation in both the streamwise and spanwise direction with intermediate length scales. Note that these packets not only represent with good agreement the initial stages of evolution localized perturbations (cfr. [84, figure 15]). Indeed, the typical waves found at the turbulent-laminar interface of developed turbulent spots have characteristics analogous to those observed the leading-edge of our wave packets (in particular, see table 1 in ref. [85]).

The streamwise and spanwise components of the velocity perturbation field show analogous wavelengths and wave angles. In this cases, the overall morphology presents a distinctive Λ-shape in the xz-plane, pointing downstream. The same features are shown by the vorticity field (see figure 25). Figures 28, 29 show the longitudinal and lateral spreadings (defined by the expressions 48,50,51), and the total energy as a function of time. The corresponding average spreading rates for the time interval $t \in [15, 35]$ are

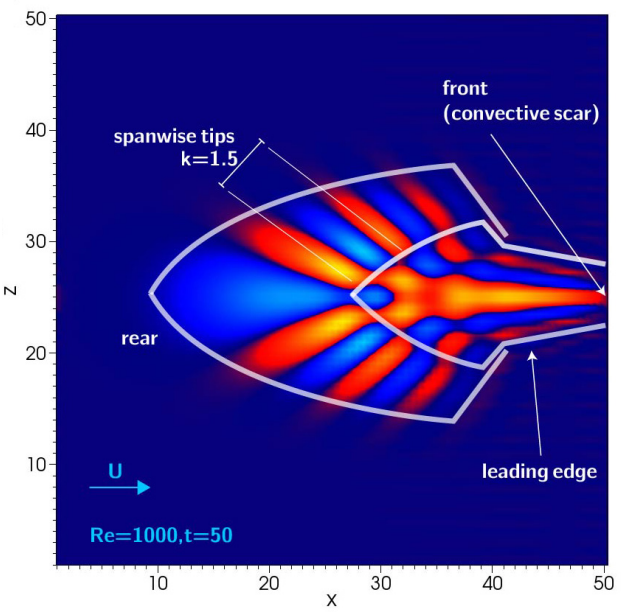

Figure 22: General features of 3D wave packets.

reported in tables 6 and 7. Note that after an early transient of about 10 time scales, this rates settle to nearly constant values.

The majority of literature works concerns the growth of turbulent spots (some are reported in table 5): in this context, turbulent fluctuations and linear waves coexist [26]. Even if the nonlinear stages of evolution are not the object of this dissertation, we compared the spreading of linear wave packets to those of developed turbulent spots. There is no doubt indeed on the role of waves in the fast spreading rates of turbulent

Table 5: Spreading rates (normalized with U_{CL}) of localized perturbations and turbulent spots form a few literature experiments on plane Poiseuille flow. These values mostly refer to the turbulent/laminar interface of developed spots.

	Re	$\dot{\mathbf{x}}_{\mathbf{G}}$	$\dot{\mathbf{x}}_{\text{rear}}$	$\dot{\mathbf{x}}_{\text{front}}$	$\dot{\mathbf{z}}$	$\psi_{\mathbf{turb}}$
Carlson *et al.* (1982)[26]	1000	0.5	0.33	0.6	-	8°
Alavyoon *et al.* (1986) [5]	1100-2200	-	0.62-0.52	0.75-0.8	-	6°-12°
Henningson & Alfredsson (1987) [68]	1200-3000	0.65	0.56	0.83	0.12	7°-15°
Klingmann & Alfredsson (1990) [85]	1600	0.65	0.55	0.7-0.85	0.09-0.2	8°
Henningson&Kim (1991) [70]	1500	0.64	0.55	0.70-0.8	0.08-0.12	8°-9°
Klingmann (1992) [84]	1600	0.65-0.7	0.55	0.82	0.06	6°-8°

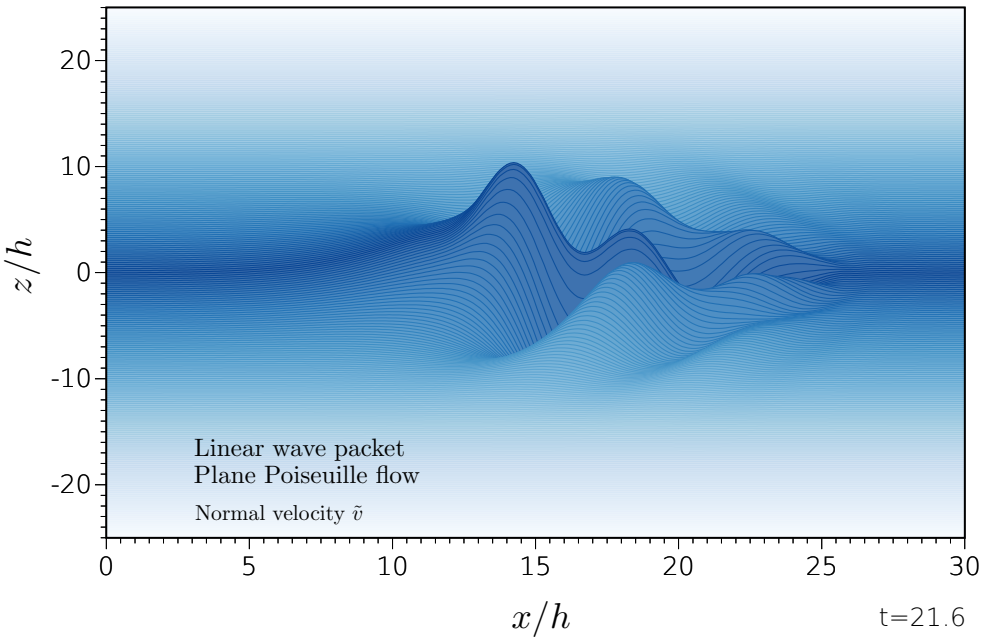

Figure 23: Pseudo-3D visualization of a linear wave packet in PPF at $Re = 1000$, perturbation wall-normal velocity component (see figure 24, panel **e**). The 3D effect is obtained by a simple superposition of 1D (x vs amplitude) plots, one per each value of z. [External movie file: `movie.avi`].

patches, and the underlying mechanisms are not fully understood. The spreading rates of the wave packets computed in the present work are reported in tables 6 and 7, while a review of spreading rates from literature experiments is shown in table 5. These values are in some cases explicitly stated by the authors, in other cases we extracted them from visualizations. Almost all of them regard the turbulent/laminar interfaces. It can be observed that the rear of the turbulent region correspond to the center of our linear spots, moving at a speed nearly equal to $0.5U_{CL}$. The turbulent spots front moves faster, with a speed about 0.7-0.8U_{CL}, almost equal to the values found for $\dot{x}_{97.5\%}$ of the linear spots. Actually, the very front propagates as fast as U_{CL}, it is laminar and represents the tip of the arrow-shaped patch, as discussed previously. The lateral spreading rates are similar as well: the values from experiments are in the range 0.06-0.12, while $\dot{z}_{2.5\%}$ is between 0.06 and 0.12 depending on the field component considered. Note that the spanwise location $z_{2.5\%}$ falls close to the boundary of the inner region introduced in the previous paragraphs (see 22). This multi-scale region corresponds to the turbulent area observed in the experiments. Moreover, we found that here wave-rays focus, as shown in the next section. The spreading half-angle (def. 51) is about 10°, if the kinetic energy or the enstrophy are considered for the computation. This value is close to the

Table 6: Spreading rates at $Re = 500$, time averages computed for $t \in [15, 35]$. The spreading rates of the field components are computed at a fixed distance from the wall, $y = -0.6$, while the kinetic energy and the enstrophy are y-averaged.

	$\widetilde{\mathbf{u}}$	$\widetilde{\mathbf{v}}$	$\widetilde{\mathbf{w}}$	$\langle \mathbf{E} \rangle_{\mathbf{y}}$	$\widetilde{\boldsymbol{\omega}}_{\mathbf{x}}$	$\widetilde{\boldsymbol{\omega}}_{\mathbf{y}}$	$\widetilde{\boldsymbol{\omega}}_{\mathbf{z}}$	$\langle \boldsymbol{\Omega} \rangle_{\mathbf{y}}$
$\dot{\mathbf{x}}_{\mathbf{G}}$	0.54	0.50	0.56	0.56	0.54	0.59	0.59	0.58
$\dot{\mathbf{x}}_{\mathbf{2.5\%}}$	0.33	0.27	0.41	0.36	0.42	0.43	0.43	0.38
$\dot{\mathbf{x}}_{\mathbf{97.5\%}}$	0.75	0.71	0.84	0.80	0.84	0.78	0.81	0.80
$\dot{\mathbf{z}}_{\mathbf{2.5\%}}$	0.08	0.12	0.10	0.06	0.08	0.06	0.08	0.05
$\psi_{\mathbf{2.5\%}}$	10.5°	16.1°	15.1°	10.2°	13.8°	9.43°	9.98°	10.2°

Table 7: Spreading rates at $Re = 1000$, time averages computed for $t \in [15, 30]$. The spreading rates of the field components are computed at a fixed distance from the wall $y = -0.6$, while the kinetic energy and the enstrophy are y-averaged.

	$\widetilde{\mathbf{u}}$	$\widetilde{\mathbf{v}}$	$\widetilde{\mathbf{w}}$	$\langle \mathbf{E} \rangle_{\mathbf{y}}$	$\widetilde{\boldsymbol{\omega}}_{\mathbf{x}}$	$\widetilde{\boldsymbol{\omega}}_{\mathbf{y}}$	$\widetilde{\boldsymbol{\omega}}_{\mathbf{z}}$	$\langle \boldsymbol{\Omega} \rangle_{\mathbf{y}}$
$\dot{\mathbf{x}}_{\mathbf{G}}$	0.51	0.45	0.50	0.54	0.50	0.57	0.56	0.56
$\dot{\mathbf{x}}_{\mathbf{2.5\%}}$	0.31	0.24	0.38	0.33	0.38	0.42	0.39	0.35
$\dot{\mathbf{x}}_{\mathbf{97.5\%}}$	0.74	0.65	0.79	0.80	0.82	0.73	0.79	0.82
$\dot{\mathbf{z}}_{\mathbf{2.5\%}}$	0.08	0.12	0.09	0.04	0.08	0.05	0.08	0.05
$\psi_{\mathbf{2.5\%}}$	10.4°	17.4°	15.3°	10.1°	14.1°	8.50°	9.92°	10.3°

one given by the streamwise velocity component, which indeed experiences the largest transient growth, as shown in panel (**e**) of figures 28,29. Regarding the enstrophy, the largest contribution is given by the spanwise vorticity. These values of the spreading half-angle are also observed for the turbulent region of developed spots (see table 5). The simulation at $Re = 1000$ shows an increase of kinetic energy and enstrophy by a factor > 2 with respect to the case at $Re = 500$. In the case at higher Reynolds number ($Re = 1000$), the streaky front appears more definite and more elongated. In fact, even if no great differences arise from the spreading rates, one can observe that at $Re = 1000$ the packet center and the rear are slower than at $Re = 500$, while the front moves faster. This yields to a more elongated arrow shape. This behavior was also observed and discussed in §2.4.1, for two-dimensional wave packets.

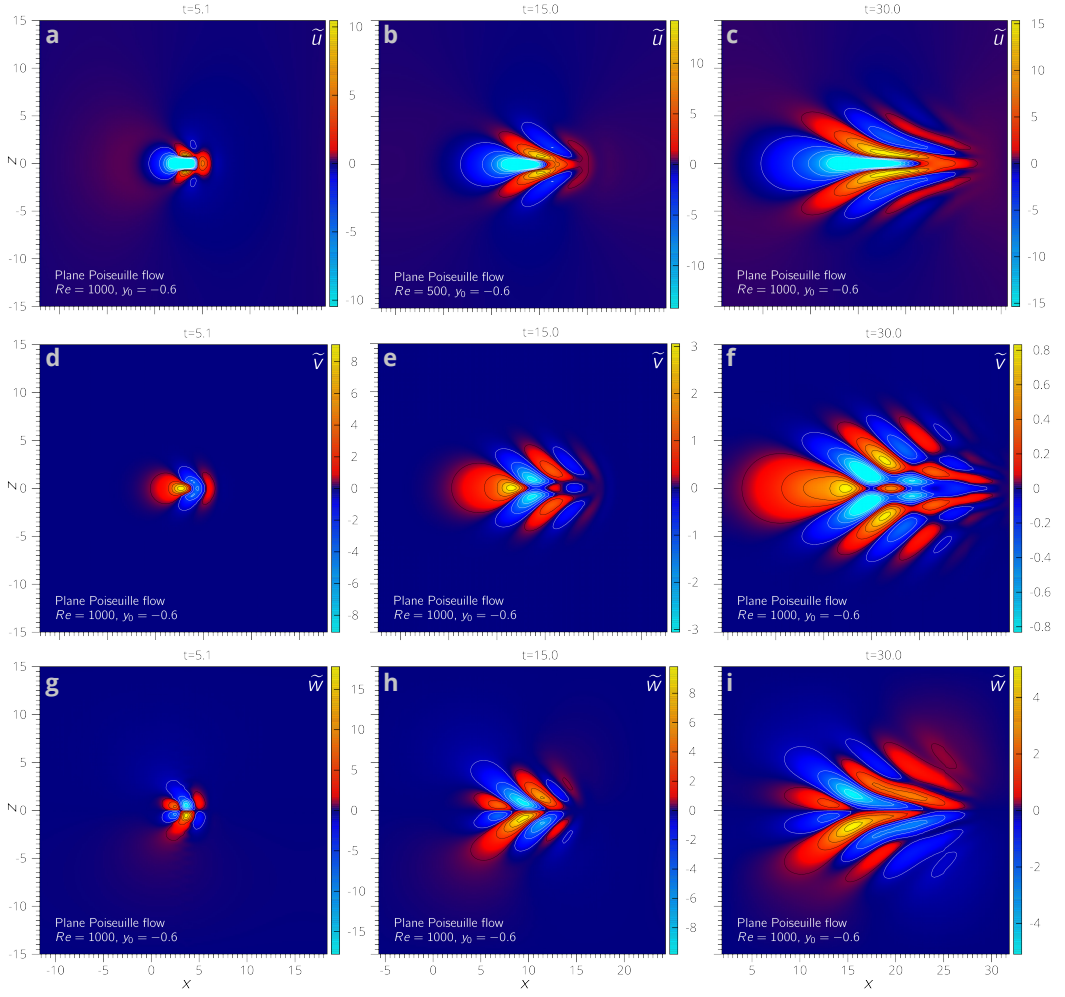

Figure 24: Linear 3D wave packet in plane Poiseuille flow at Re=1000, perturbation velocity visualization. The disturbance velocity field ($\widetilde{u}, \widetilde{v}, \widetilde{w}$, top to bottom) is shown at $T = 10, 20, 30$ (left to right) and at a fixed distance from the wall $y_0 = -0.6$. The initial perturbation is localized at $(x_0 = 0, z_0 = 0)$, the initial peak values are $\widetilde{u}_{\max}(t = 0) = 3.2$, $\widetilde{v}_{\max}(t = 0) = 19.8$, $\widetilde{w}_{\max}(t = 0) = 3.2$. Five contour lines are traced for both the negative (white lines) and the positive (black lines) part, the first level is $|0.05\ \widetilde{q}_{max}|$ and the last one is $|0.9\ \widetilde{q}_{max}|$, where the peak value $\widetilde{q}_{max}$ can be inferred from the color bars. [External movie files Re=1000: `movie_U_y06_PPF3D_Re1000_still.avi`, `movie_V_y06_PPF3D_Re1000_still.avi`, `movie_W_y06_PPF3D_Re1000_still.avi`]. [External movie files Re=500: `movie_U_y06_PPF3D_Re500_still.avi`, `movie_V_y06_PPF3D_Re500_still.avi`, `movie_W_y06_PPF3D_Re500_still.avi`].

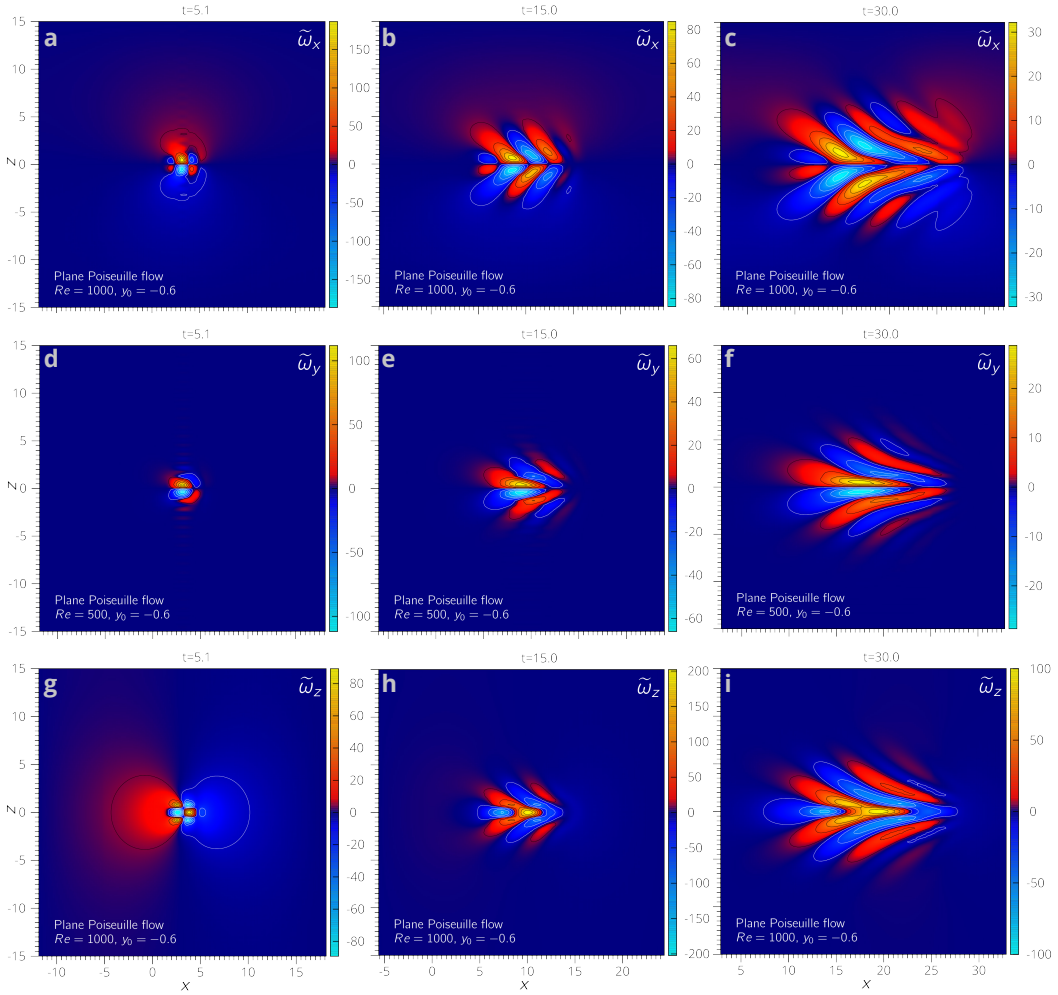

Figure 25: Linear 3D wave packet in plane Poiseuille flow at Re=1000, perturbation vorticity visualization. The disturbance vorticity field ($\widetilde{\omega}_x, \widetilde{\omega}_y, \widetilde{\omega}_z$, top to bottom) is shown at three time instants, $T = 10, 20, 30$ (left to right) and at a fixed distance from the wall $y_0 = -0.6$. The initial perturbation is localized at $(x_0 = 0, z_0 = 0)$ and the initial peak values are $\widetilde{\omega}_{x\ \max}(t = 0) = 103$, $\widetilde{\omega}_{y\ \max}(t = 0) = 0$, $\widetilde{\omega}_{z\ \max}(t = 0) = 101$. Contour lines and simulation parameters as in figure 24.
[External movie files Re=1000: `movie_OX_y06_PPF3D_Re1000_still.avi`, `movie_OY_y06_PPF3D_Re1000_still.avi`, `movie_OZ_y06_PPF3D_Re1000_still.avi`], [External movie files Re=500: `movie_OX_y06_PPF3D_Re500_still.avi`, `movie_OY_y06_PPF3D_Re500_still.avi`, `movie_OZ_y06_PPF3D_Re500_still.avi`]

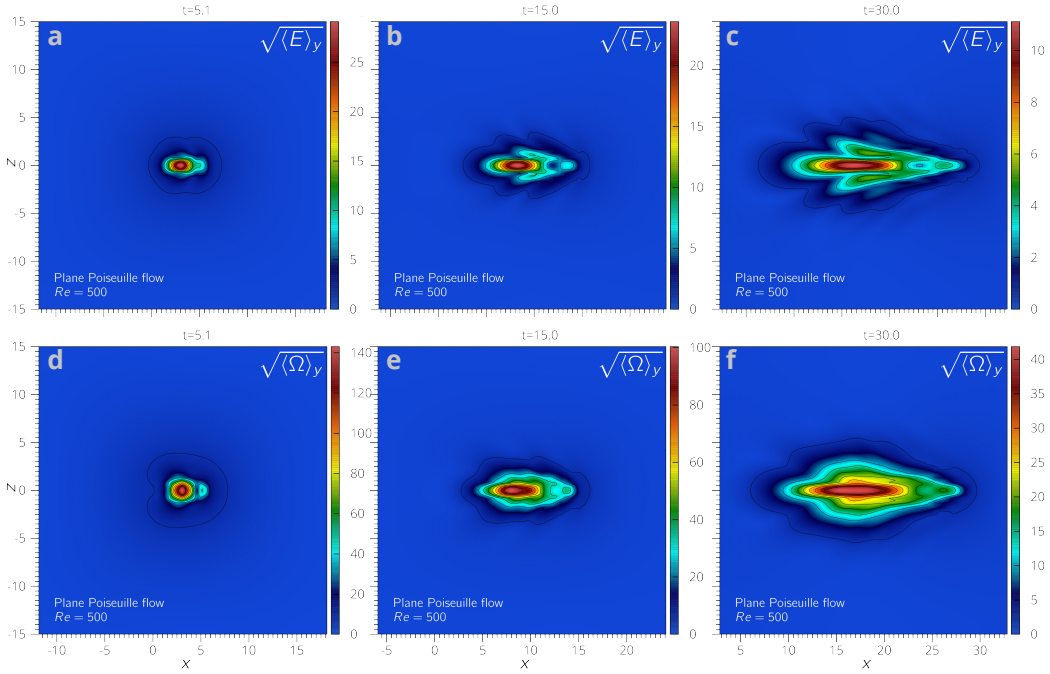

Figure 26: Linear 3D wave packet in plane Poiseuille flow at Re=500, kinetic energy and enstrophy visualization. The square root of the disturbance y-averaged kinetic energy (top panels) and enstrophy (bottom) are shown at $T = 10, 20, 30$ (left to right). The initial peak values are $\sqrt{\langle E\rangle_y}_{\max}(t = 0) = 18$, $\sqrt{\langle \Omega\rangle_y}_{\max}(t = 0) = 110$. [External movie files: `movie_ENEave_PPF3D_Re500_still.avi`, `movie_OMEGAave_PPF3D_Re500_still.avi`]

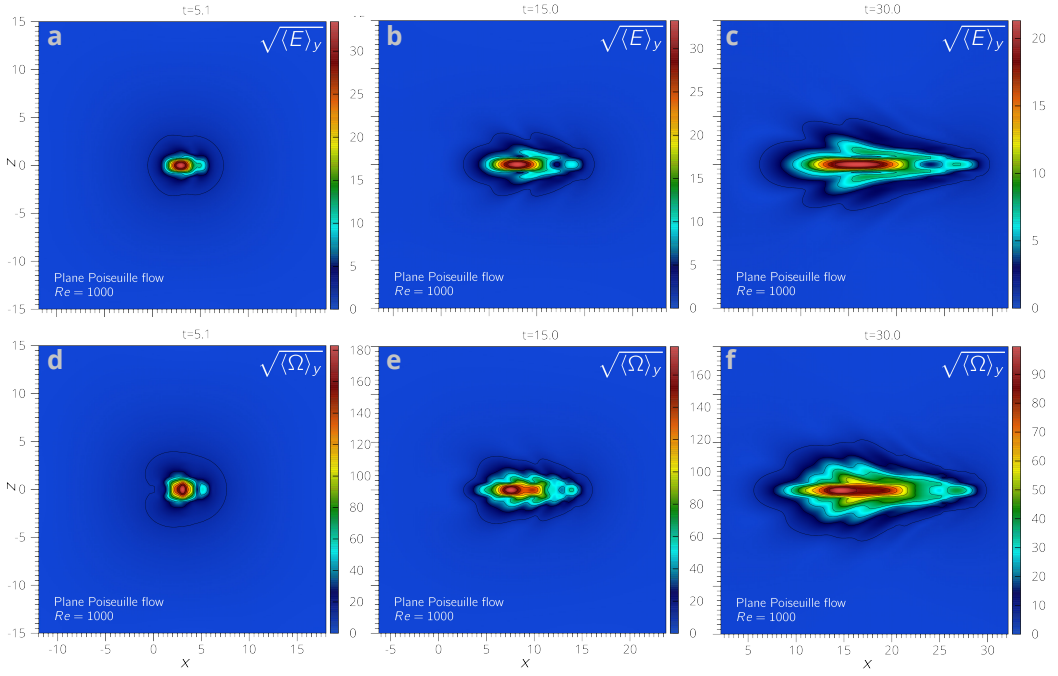

Figure 27: Linear 3D wave packet in plane Poiseuille flow at Re=1000, kinetic energy and enstrophy visualization. The square root of the disturbance y-averaged kinetic energy (top panels) and enstrophy (bottom) are shown at $T = 10, 20, 30$ (left to right). The initial peak values are $\sqrt{\langle E\rangle_y}_{\max}(t = 0) = 18$, $\sqrt{\langle \Omega\rangle_y}_{\max}(t = 0) = 110$. [External movie files: `movie_ENEave_PPF3D_Re1000_still.avi`, `movie_OMEGAave_PPF3D_Re1000_still.avi`]

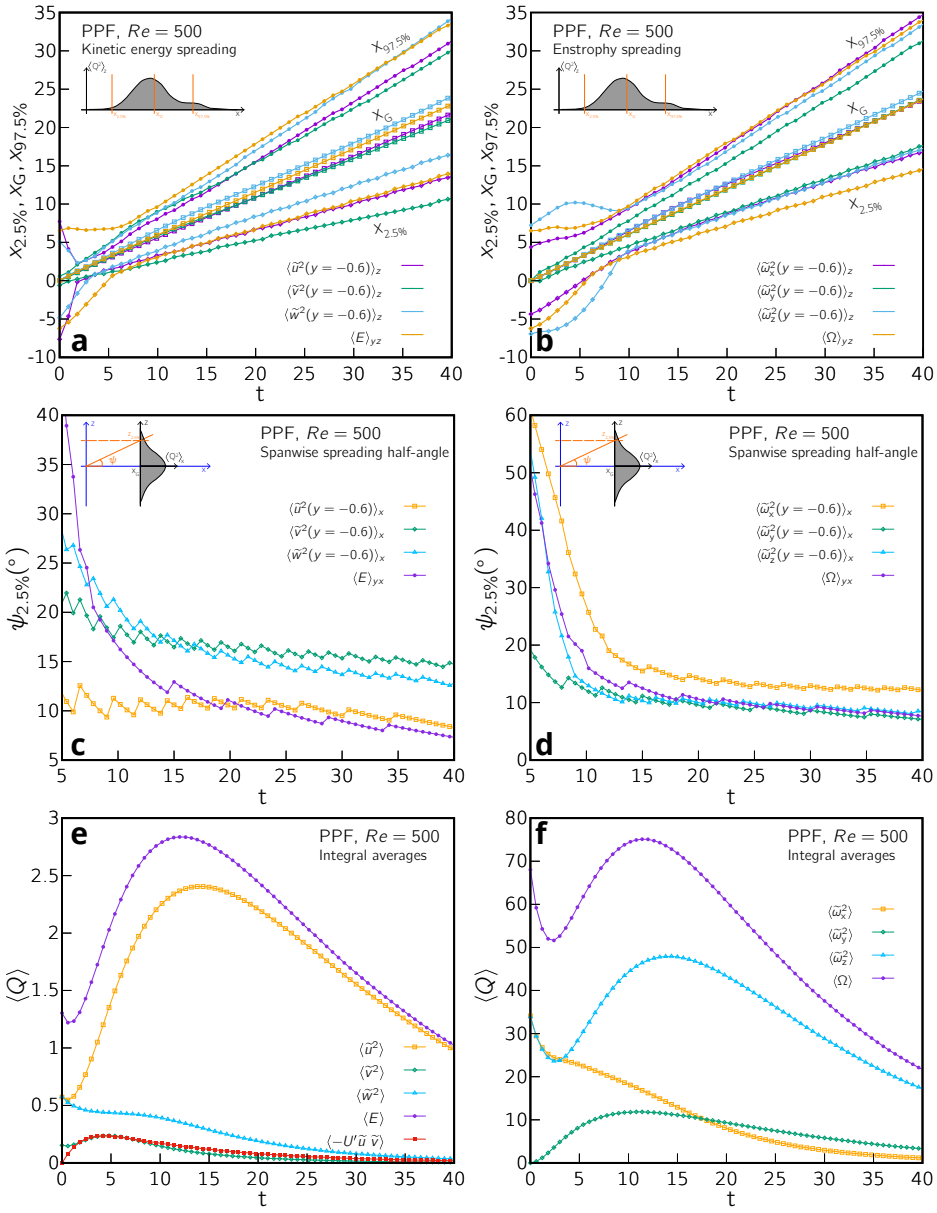

Figure 28: Spreading, spreading half-angle and volume-averaged quantities for a 3D wave packet at Re=500 in plane Poiseuille flow. Panels (**a**,**b**): time evolution of the wave packet center (x_G) and the streamwise spreading ($x_{2.5\%}, x_{97.5\%}$) for all the velocity and vorticity squared components at $y_0 = -0.6$, and the y-averaged kinetic energy and enstrophy. Panels (**c**,**d**): spreading half-angle. Panels (**e**,**f**): time evolution of volume-averaged quantities; velocity and vorticity squared components, kinetic energy, enstrophy and Reynolds stresses. Note that the oscillation of the spreading angle is due to the numerical domain discretization.

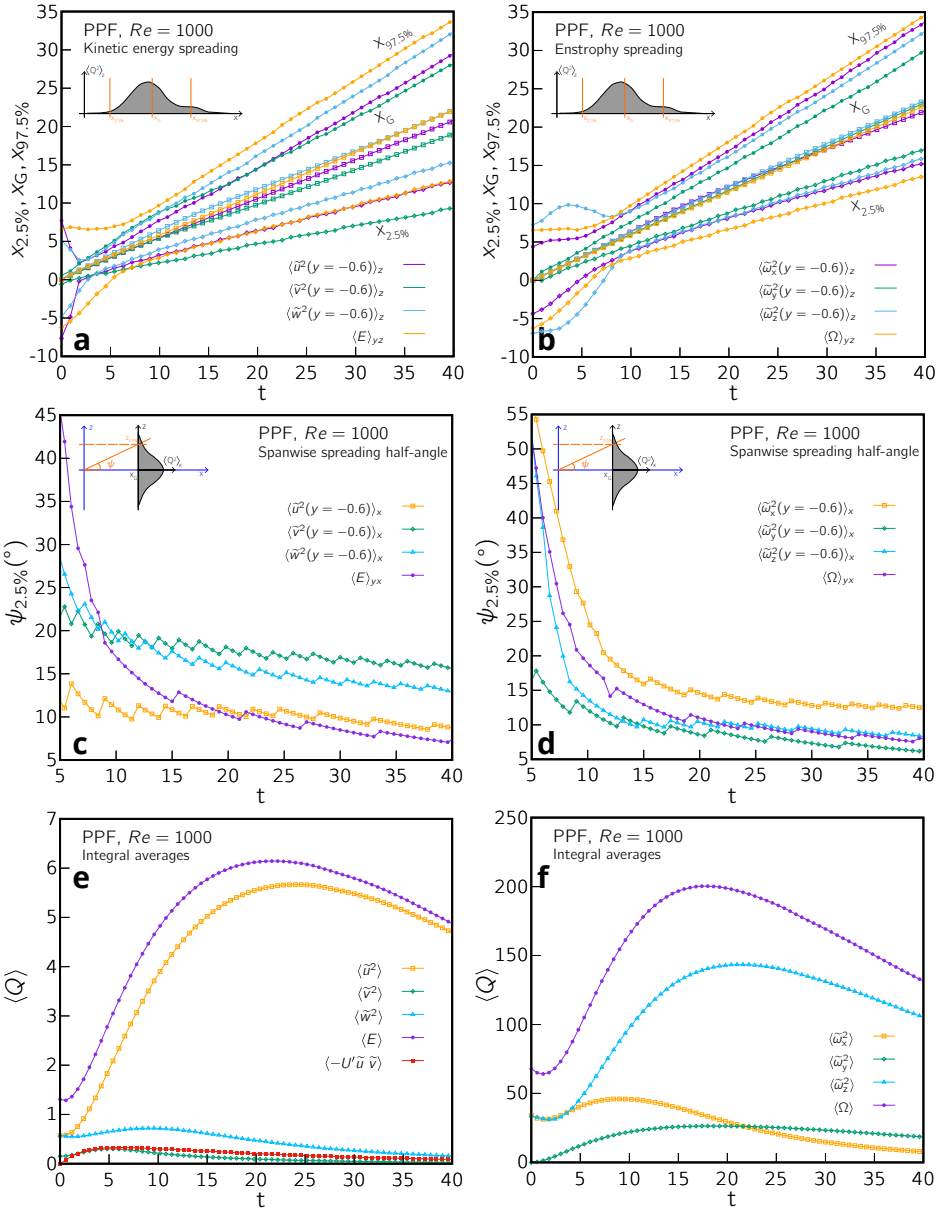

Figure 29: Spreading, spreading half-angle and volume-averaged quantities for a 3D wave packet at Re=1000 in plane Poiseuille flow. Panels (**a**,**b**): time evolution of the wave packet center (x_G) and the streamwise spreading ($x_{2.5\%}, x_{97.5\%}$) for all the velocity and vorticity squared components at $y_0 = -0.6$, and the y-averaged kinetic energy and enstrophy. Panels (**c**,**d**): spreading half-angle. Panels (**e**,**f**): time evolution of volume-averaged quantities; velocity and vorticity squared components, kinetic energy, enstrophy and Reynolds stresses. Note that the oscillation of the spreading angle is due to the numerical domain discretization.

2.5 **Wave packet asymptotic representation**

In this section, we apply concepts from the wave theory illustrated in §2.2 to get a temporal asymptotic representation of the three-dimensional wave packet in the plane Poiseuille flow.

Historically, the asymptotic behavior of wave packets developing from localized sources have been initially treated by Benjamin [1961, 17] and Criminale & Kovasznay [1962, 38]. The latter authors found an expanding ellipsoidal shape for the long-term perturbation in the boundary layer flow. Subsequently, a considerable body of work has been done, among others, by Gaster, Davey, Craik and Landahl. In particular, in 1965 and then in 1968 Gaster [52, 53] proposed to apply the saddle point method to evaluate the integral 29 (complex-valued dispersion relation was considered) using the Orr-Sommerfeld dispersion relation for the 2D boundary layer flow. They showed that this technique improved Criminale's elliptical shape. Three-dimensional wave packets in boundary layer and wake flows were then considered by Gaster [54] and Gaster & Davis [59], using the Squire's transformation, and these results were later improved in the 1980s [31, 56, 58, 57, 32, 89, 79]. In those days, the computational resources were not enough to get the exact form of the dispersion relation and its derivatives, in fact simplified model dispersion relations were used. Despite this, quite good agreement with experimental observations in boundary layers was achieved. Later on, the advent of DNSs overcame the studies based on analytical wave theory.

In the following, the dispersion relations for the least-stable mode in PPF shown in §2.3, together with the results 34 and 37, are used in combination to get an approximate representation of the asymptotic morphology of impulsive disturbances in the plane Poiseuille flow. At this early stage of the research, we have not computed the full approximate solution via Eq. 32. We computed the wave rays for each wavenumber and wave angle in the (discretized) domain for various values of Re. It should be reminded that for homogeneous media the stationary phase method leads to the conservation of the wavenumber and the frequency along straight trajectories $\mathbf{x}/t = \mathbf{v}_\mathrm{g}$. Since our problem is dissipative (real wavenumbers and complex eigenvalues), here we consider the real part of the dispersion relation to compute the group velocity and the wave rays. Our aim is to show that the nature of the shape that localized disturbances take during their temporal evolution is deeply inherent to the dispersion properties of the system. The aged but elegant wave theory coupled to the computational resources of these days allows one to easily investigate the physical mechanisms at the bases of the spot spreading.

We computed the dispersion relation of the least-stable wall-normal velocity mode for three-dimensional waves at $Re = [500, 1000, 2000, 4000]$. Uniform grids were set for both the streamwise and the spanwise wavenumber components, $\alpha \in [0.01, 10]$, $\beta \in$

$[-5, 5]$. The spacing was $\Delta\alpha = \Delta\beta = 0.0417$ so that the group velocity for 57600 vector wavenumbers was considered in total. Parallel computations have been performed on the computer cluster at the Department of Control and Computer Engineering of our institution. Results are shown in figures 31 and 32, showing for each wave the point defined by the group velocity components in the longitudinal and lateral directions, as defined by Eq. 34. The wavenumber is convected with the group velocity, according to the transport equation 37 (the right end side is zero for a homogeneous medium). Therefore, figure 31 shows in color the wavenumber modulus for each computed point, while figure 32 displays the wave angle.

The first observation is that the features of the 3D wave packets discussed in §2.4.2 are all present as regards the arrow pattern of the wave packet. This is made of a slower rear almond-shaped part, a fast front and a tongue which links the two. It is interesting to notice that what we called the "inner part", is can be clearly recognized from this analysis (see the red rhomboid which connects to the streaky tail).

In figure 31, the colorbar was set so that the non-dispersive components $k > k_{\mathrm{d}} \approx 2$ (orange/yellow) and the inner part (red) are highlighted. The values of the wavenumber in each part of the patch are comparable to those observed from the numerical simulations of the previous section. The front has a bulb shape, which is usually difficult to observe due to the highly damped nature of its wave components. Interestingly, high wave-focusing is observed at the wingtips of the inner region (note the high density of points). Moreover, here the wave components are quite oblique, as the wave angle is around 75° (see figure 32). These waves are the most algebraically unstable, that is they experience the largest kinetic energy growth in the intermediate term. The packet components at the leading edge are even more oblique, nearly orthogonal to the basic flow ($\phi \approx 85^\circ$).
The dominant large-scale non-dispersive modes of the subregion 1 discussed in §2.3 should appear in the cases of $Re > 546$, that is in all panels of figures 31,32 except the top one ($Re = 500$). However, we can see those waves only in the second panel ($Re = 1000$), where they appear as light-blue dots very focused at the centerline in correspondence to $x/t = 0.65$. There are only few points, which is due to the discretization. Reminding that the region shifts towards lower wavenumbers as Re increases, one can understand why these points are not visible in the other panels. In this regard, a computation has been performed using a uniform wavenumber distribution in the log-space, for the same range of values (results are shown in figure 30). In this way, we highlight the low-wavenumber range and in particular the wave components belonging to subregion 1 (light-blue dots in the top panel of figure 30, where $x/t \approx 0.65$).

The asymptotic spreading rates can be directly inferred from the figure axis. The lateral spreading rate $\dot{z}_{\mathrm{asy}}$ decreases as the Reynolds number increases. In the figures, two straight lines connect the origin with the points of maximum spreading for both

the global packet and for the inner rhomboidal region. These lines define the spreading angle, which is found to increase with Re. This fact is due to the concomitant decrease of dispersion and slowdown of the spot core as Re increases, which also results in an elongation of the arrowed shape, since the spot front is always convected with the flow speed. Such effect was also observed from our 2D and 3D linear simulations and discussed in the previous sections. The values of are shown in the figure panels and are in good agreement with the observations.

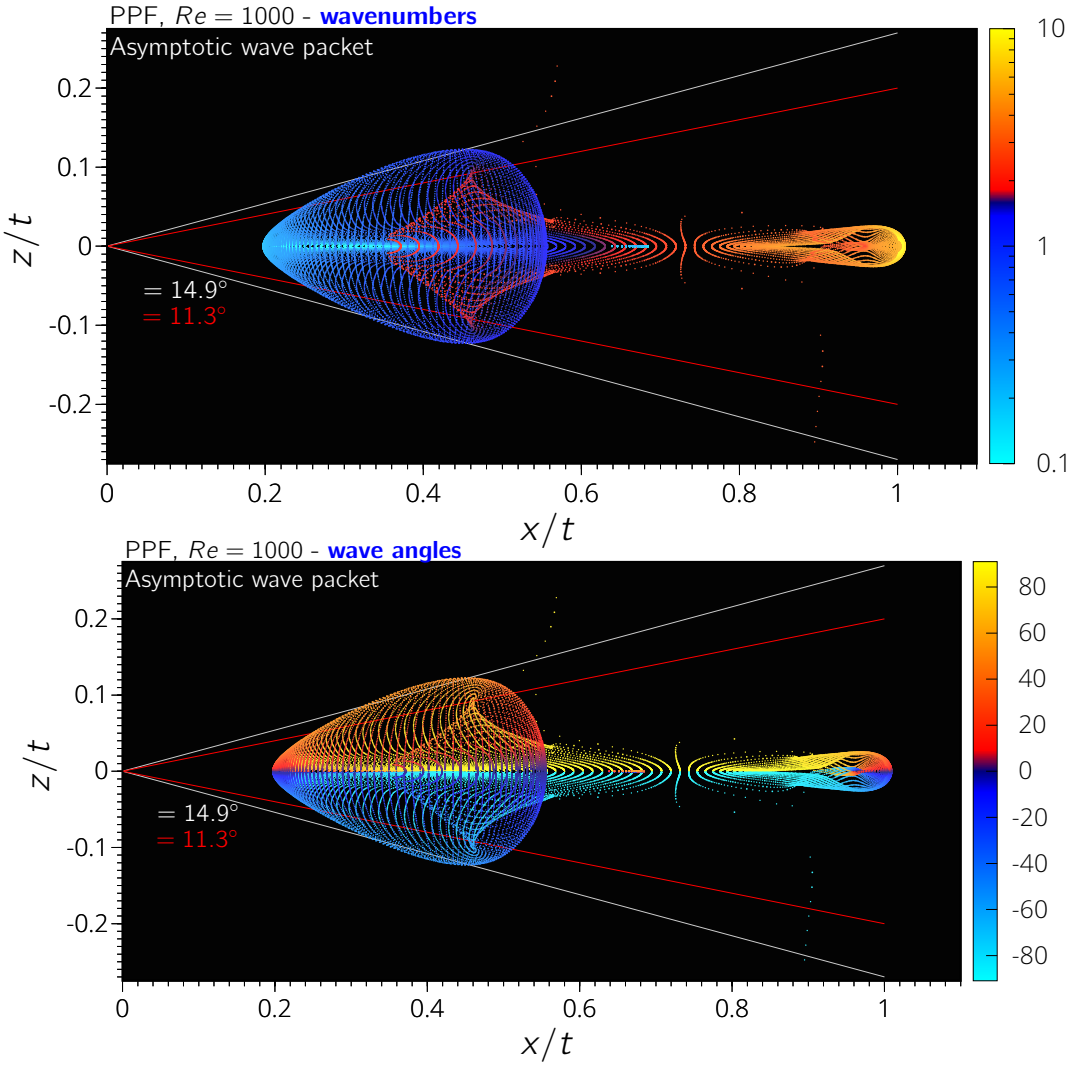

Figure 30: Asymptotic wave packet representation for PPF at $Re = 1000$ from uniform wavenumber distribution in log-space. Top: wavenumbers. Bottom: wave angles. Notice the presence of long wave components at $x/t \approx 0.65$ and $z/t \approx 0$, belonging to subregion 1 of figure 13.

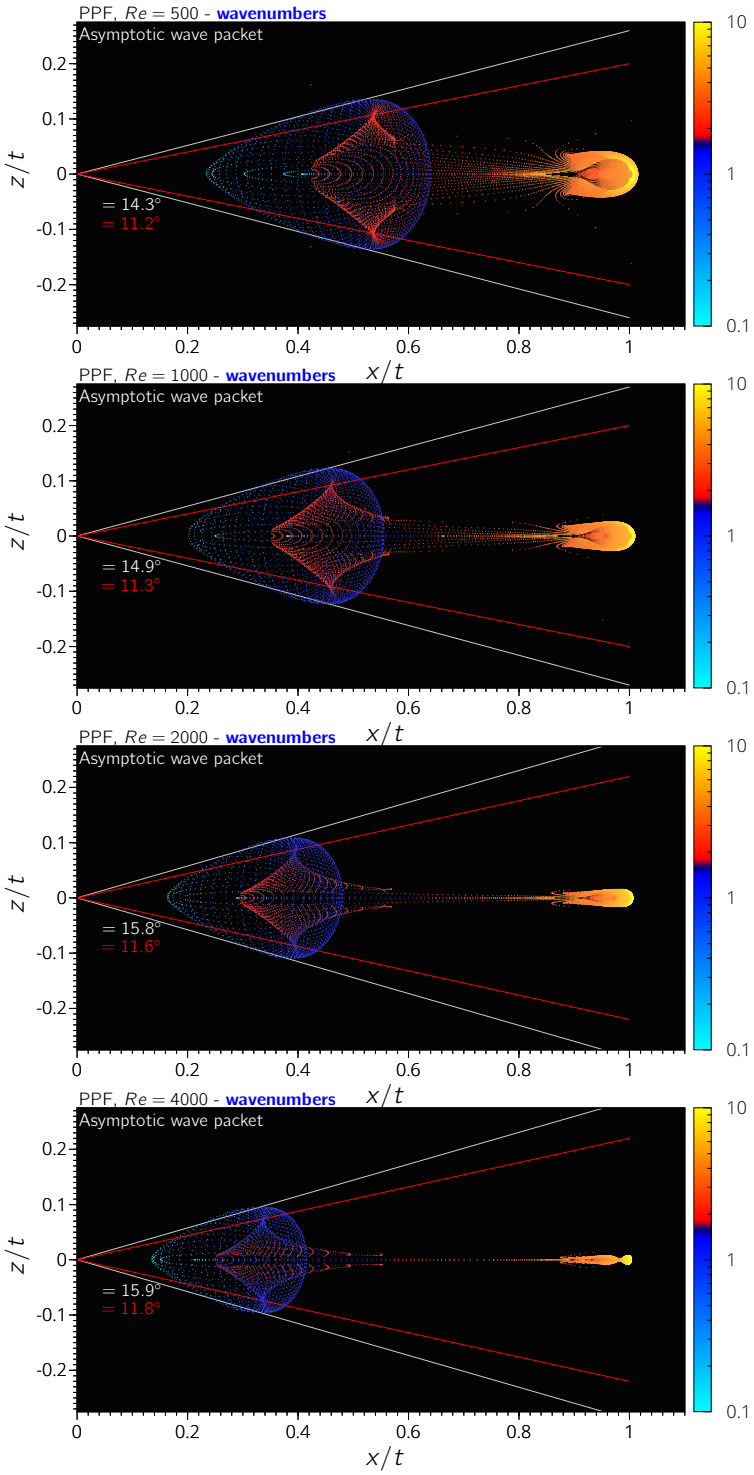

Figure 31: Asymptotic wave packet representation for the plane Poiseuille flow: wavenumbers visualization. The propagation of the wavenumber modulus given by the asymptotic group velocity is shown for $Re = [500, 1000, 2000, 4000]$. ψ is the spreading half-angle. Streamwise and spanwise wavenumbers are uniformly distributed, $\alpha \in [0.01, 10]$, $\beta \in [-5, 5]$, $\Delta\alpha = \Delta\beta = 0.0417$

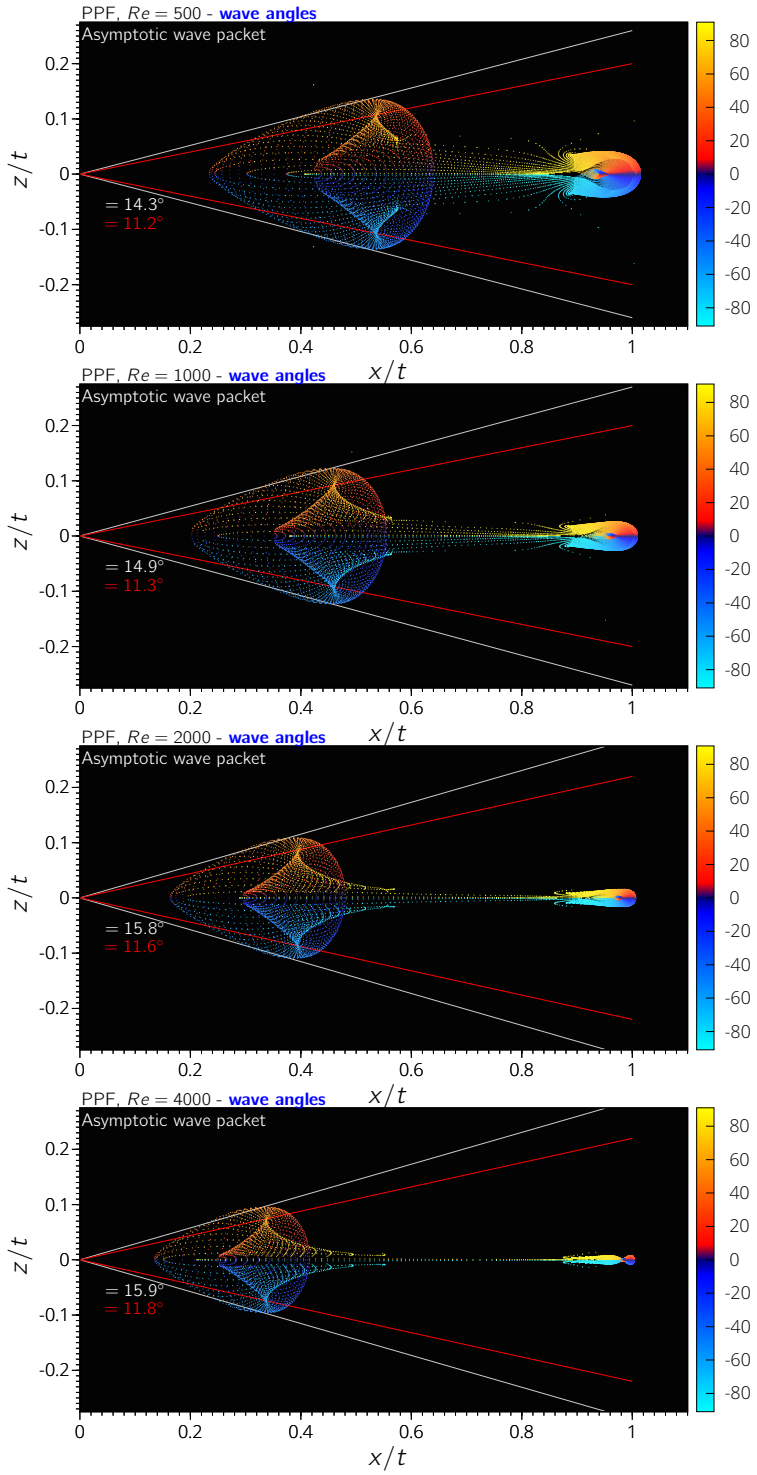

Figure 32: Asymptotic wave packet representation for the plane Poiseuille flow: wave angle visualization. The propagation of the wave angle given by the asymptotic group velocity is shown for $Re = [500, 1000, 2000, 4000]$. ψ is the spreading half-angle. Streamwise and spanvise wavenumbers are uniformly distributed, $\alpha \in [0.01, 10]$, $\beta \in [-5, 5]$, $\Delta\alpha = \Delta\beta = 0.0417$.

2.6 **Final remarks**

This ongoing study (a publication is currently in progress [4]), is the natural extension of the investigations on wave transient propagation properties, object of Chapter 1. The finding of a dispersive-to-nondispersive transition for the least-stable mode in the plane Poiseuille and wake flows motivated us to trace fine-resolved dispersion relation $Re - k$ maps over a range of Reynolds number of four decades, $Re \in [10, 10^5]$, which is of interest for a number of theoretical studies and applications, and was unavailable from the literature. The maps shown in this chapter, together with those which will be found in Chapter 3, are aimed at giving a scenario as complete as possible. Therefore, information was included on wave propagation and dispersion, kinetic energy and enstrophy growth, stability (instability) regions of the parameters space, and comparison with experimental threshold values. This was done for the plane Poiseuille and Couette flows. The wavenumber threshold - present in the plane Poiseuille flow and introduced in Chapter 1 - was found to be a decreasing function of Re, starting very close to the lower bound for kinetic energy transient growth. In addition, we found other subregions in the low-wavenumbers part of the stability map with propagation properties different than the surroundings, which have been traced back to the structure of the eigenvalues spectrum of the Orr-Sommerfeld equation.

The clean mathematical wave theory developed during the last century provides a simple and powerful tool to predict the evolution of dispersive wave packets, when coupled to the computation of the exact group velocity (no use of dispersion relation models) made possible by the computational resources available in these days. We exploited this theory to get the asymptotic shape of localized perturbations in the plane Poiseuille flow, known to be crucial in the subcritical process of transition to turbulence. In fact, the wave activity is strongly believed to act as a driver for the breakdown to turbulence and its self-sustainment.
We focused on open questions concerning the nature of the typical length scales developing from a small localized wave packet, the spreading rates and the effects of the Reynolds number. The comparison with numerical simulations of the initial-value problem and with experimental values from the literature proved that the dispersion relation contains precious information to understand several features of the disturbance evolution. Many of these persist when the spot becomes turbulent and coexists with the surrounding laminar flow.

Following this line of research, future investigations on non-dispersive wave components and analysis of wave-ray focusing could shed light on the onset of nonlinear interactions and instability. Future work directed towards unraveling the sufficient conditions for the departure to turbulence (and its self-sustainment) from the laminar state should, in our opinion, take into account for the propagation properties highlighted here

and in Chapter 1. In addition, the short-term algebraic growth of the wave amplitude in terms of both the kinetic energy and the enstrophy should be included in the analysis (this last point will be the object of the next chapter). To summarize, key ingredients to this aim are wave dispersion, wave-phase synchronization or focusing, transient growth in both kinetic energy and vorticity.

We believe that the approach followed here would be helpful to clarify the behavior of Alfvénic fluctuations in the magnetohydrodynamics context, where analysis on non-modal growth and wave dispersion at the fluid scales are still at an initial stage of research [2010 25], compared to the neutral-fluid hydrodynamics, and limited to the kinetic regime. In fact, as shown in §4.6, analogies are found between the waves treated here and the MHD shear Alfvén wave, which is typically considered nondispersive. In the case of a sheared background magnetic field, as it is typically the case of solar wind, dispersion could occur in a similar fashion to what shown in this chapter for neutral fluids.

3

LOWER BOUND OF THE ENSTROPHY TRANSIENT GROWTH FOR 2D LINEAR WAVES IN SHEARED FLOWS

The third chapter of this dissertation considers the transient growth of the wave amplitude, by looking at perturbation's vorticity. This piece of work is framed in the context of the MISTI-Seeds Italy MITOR project "Long-term interaction in fluid systems" (2012-2014), proposed by Prof. D. Tordella (PoliTo) and Prof. G. Staffilani[1] (MIT). This study is the subject of a publication which is currently under submission process. Loris Domenicale[2] contributed to the analytical calculations during his Master's thesis period carried out in our research group and is coauthor of this work. An ArXiv preprint is available online, see [49].

3.1 **Summary**

This study brings a new lower bound for the transient growth of the volume averaged perturbation's enstrophy (the squared vorticity size) for two-dimensional linear waves in the plane Couette and Poiseuille flows. This bound is less restrictive than the equivalent bound obtained in the past in terms of the wave kinetic energy (Orr 1907, Joseph 1976).

As a consequence, it is shown that the transient growth of kinetic energy of small-amplitude waves traveling inside incompressible, viscous, wall-bounded flows is not a sufficient condition for the enstrophy growth. Historically, the mathematical complexity connected to the unknown boundary values of the spanwise perturbation vorticity left the vorticity problem open. In fact, since the early studies by J. L. Synge in the 1930s [124, 125, 126] - overlooked, in the literature - analyses in terms of the enstrophy have not been carried out any longer. In the last decades of the 20th century, the discovery of the transient perturbation growth and its link to the subcritical transition to turbulence was still treated by means of energy-based analysis.

By using the non-modal approach we extend the work of J. L. Synge (1930s), which was an alternative way to attack the flow stability problem. Synge's study was based on the perturbation vorticity instead of the classical kinetic energy analysis, and it

1 Department of Mathematics, Massachusetts Institute of Technology, Cambridge, MA 02139-4307, USA

2 Department of Mathematical Sciences "G. L. Lagrange", Politecnico di Torino, Torino, Italy 10129

was conceived at a time when the transient growth mechanism was unknown. Our calculations lead to the smallest Reynolds number $Re_\Omega(\alpha)$ allowing algebraic enstrophy growth, as a function of the perturbation wavelength. This highlights that the enstrophy monotonic-decay region inside the wavenumber-Reynolds number parameters space is wider than that of the kinetic energy. In addition, we present the first maps of enstrophy maximal growth computed over broad ranges of Reynolds number and wavenumber ($Re \in [10, 10^5]$, $\alpha \in [10^{-2}, 10]$) which are of interest for most theoretical studies and applications. Beyond the determination of the above lower bound, this study opens up the possibility of deducing analytically the wall values of the vorticity, a priori not known. This can be of interest for several applications (for instance in the flow-control technology).

The dispersion variability inside the system stability map, already discussed in Chapter 2, is here recalled. In a context where wave packets undergo powerful and long-lasting transient growth of both kinetic energy and enstrophy, this information is key to the understanding of a potential process of nonlinear coupling onset.

3.2 **Introduction**

The dynamics of a fluid in motion is intrinsically linked to the evolution of the velocity gradient tensor. In recent decades, the local statistical and geometric structure of two and three-dimensional turbulent flows has been often described in terms of the properties of the velocity gradient tensor, in particular of the local strain rates and vorticity. The enstrophy (the vorticity squared) is an invariant of the velocity gradient tensor, widely considered statistically relevant in turbulence dynamics [50, 131, 2, 141, 122]. It has been indeed related to the evolution of the kinetic energy and to the dissipation of the velocity fluctuations (a nice discussion can be found in Tsinober's book [131]). Moreover, unlike the kinetic energy, the enstrophy is not a three-dimensional inviscid invariant. This is due to the vortex stretching terms, responsible for stretching and tilting of the vorticity. Actually, these terms appear as nonlinear terms in the enstrophy integral evolution equation, and they are responsible for self-amplification of vorticity. Hence, differently from the kinetic energy (see equation 215), the enstrophy growth rate depends on the amplitude of the initial perturbation. These reasons make considering the vorticity a useful tool to gain insight into the physics of fluid flows. In the context of hydrodynamic stability, however, the level of interest in the enstrophy has not been as high as that in kinetic energy.

One reason for the limited use of the enstrophy in the hydrodynamic theory is certainly due to the lack of knowledge of physical wall boundary conditions on the vorticity, see the discussion in [124]. Oppositely, the boundary conditions on the velocity field, for flows bounded by solid walls under the continuum hypothesis are well known (no-slip boundary

conditions). Nonetheless, this study is focused on the enstrophy of traveling perturbation waves in wall flows. We consider again the two-dimensional plane Poiseuille and Couette flows, which are iconic problems in hydrodynamics. One objective is to highlight the role of the enstrophy as well as its interrelationship with the more commonly considered kinetic energy.

Stability regions in the k-Re space

Departures from the basic laminar flow may occur in the subcritical range below Re_c, that is the threshold for *unconditional instability* (asymptotic exponential instability, for perturbations of any initial amplitude, even infinitesimal). The energy variational method [81] generates a lower bound to the *global stability* threshold, Re_g [95]. The global stability region is also referred to as *unconditional stability* region, since for $Re < Re_g, \forall \mathbf{k}, t \to \infty$, three-dimensional perturbations of any initial amplitude, shape, wavenumber content and transient growth experienced in the short term eventually decay over time. For $Re_g < Re < Re_c$ the stability of a generic perturbation is conditional, since it depends on the initial condition. Transition to turbulence can occur in this range, where typically turbulent spots grow and self-sustain; in this case the process is referred to as *subcritical* (or *bypass*) *transition*, and Re_g defines the smallest Reynolds number for which such transition has been observed from experiments or direct numerical simulations (the latest results are reported in table 8). The theoretical determination of Re_g is still missing and it is the object of most studies on transition. The lower bound for Re_g is named here Re^*_E, which defines the *monotonic stability* region, that is, it specifies the value below which the kinetic energy of small-amplitude perturbations of arbitrary initial shape can only decrease to zero monotonically, $\forall t$. See the schematic figure 33, and the discussion in §3.4. Further information can be found in Yaglom's book [§4, 140], or in the review paper by Manneville [95], whose terminology is adopted in this thesis.

In this study, for all possible initial conditions in 2D we obtain the limiting curve for the monotonic decay of the volume-averaged enstrophy in the α-Re space (α is the longitudinal wavenumber). This bound is shown to be less conservative than the limiting curve for the kinetic energy decay. This is achieved by extending to the non-modal approach a procedure proposed by J. L. Synge in a proceeding paper of the London Mathematical Society [1938 126] which has not been further exploited. The impact of this result is that the lower bound for the wave-amplitude transient growth is improved if the problem is formulated in terms of enstrophy instead of kinetic energy.

In synthesis, Synge's procedure was aimed to find analytical conditions satisfied by both the vorticity and the stream-function in a viscous fluid motion between fixed parallel planes. This procedure is based on the deduction of the cross-shear derivative of the flow vorticity by using the Orr-Sommerfeld equation, which is then coupled to an optimization

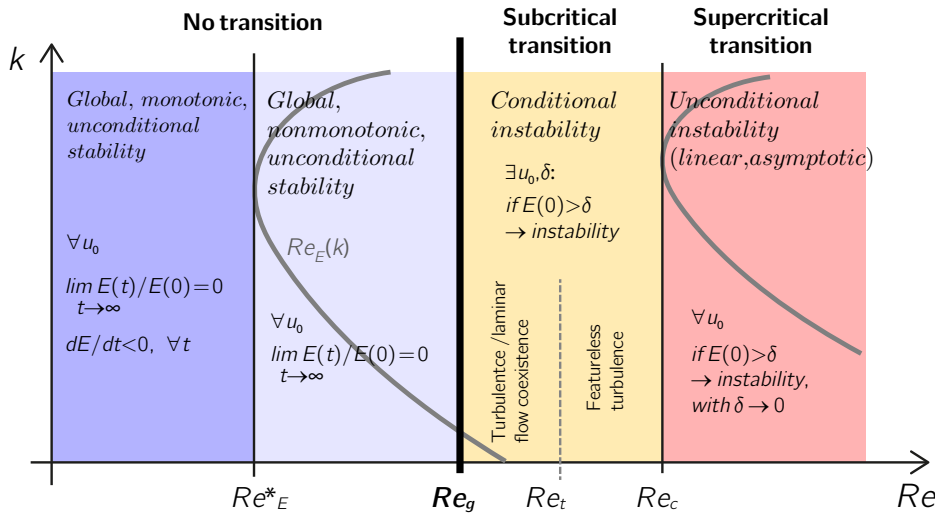

Figure 33: Stability regions in the k-Re space.

process acting directly on the vorticity integral. A noticeable observation is that the only terms able to produce a transient growth of volume-averaged enstrophy are the boundary terms which represent the vorticity and its y-variation at the walls.

3.3 Relationship between enstrophy and kinetic energy of small internal waves in parallel flows. The problem of enstrophy growth

The volume-averaged enstrophy for a traveling wave perturbation in two-dimensional parallel flow fields is introduced:

$$\Omega = \frac{1}{2|\mathcal{V}|}\int_{\mathcal{V}} \widetilde{\omega}^2 \, \mathrm{d}x \, \mathrm{d}y, \tag{52}$$

where $\mathcal{V}$ is an arbitrary two-dimensional domain and $|\mathcal{V}|$ its volume.

$$\widetilde{\omega} = \partial_x \widetilde{v} - \partial_y \widetilde{u} \tag{53}$$

is the vorticity of a perturbation velocity field of components $\widetilde{u}$ (streamwise) and $\widetilde{v}$ (wall-normal). In 2D, the spanwise vorticity $\widetilde{\omega}_z$ is the only non-zero component, therefore for simplicity the z-subscript is omitted.
We focus on the evolution equation of the volume-averaged enstrophy Ω, it is convenient to consider the viscous vorticity equation for small disturbances:

$$\partial_t \widetilde{\omega} - \widetilde{v} U'' + U \partial_x \widetilde{\omega} = \frac{1}{Re} \nabla^2 \widetilde{\omega}, \tag{54}$$

where the prime symbol stands for a total y-derivative, $U(y)$ is the basic state and Re is the Reynolds number based on the channel half-height and the reference velocity, the centerline speed for PPF and the wall speed for PCF (figure 34). The linearized enstrophy equation is then

$$\begin{aligned}\frac{\mathrm{d}}{\mathrm{d}t}\Omega &= \frac{1}{|\mathcal{V}|}\frac{\mathrm{d}}{\mathrm{d}t}\int_{\mathcal{V}}\left(\frac{\widetilde{\omega}^2}{2}\right)\mathrm{d}x\,\mathrm{d}y \\ &= \frac{1}{|\mathcal{V}|}\int_{\mathcal{V}}\left(\widetilde{v}U''\widetilde{\omega} - U\widetilde{\omega}\partial_x\widetilde{\omega} + \frac{1}{Re}\widetilde{\omega}\nabla^2\widetilde{\omega}\right)\mathrm{d}x\,\mathrm{d}y. \end{aligned} \tag{55}$$

In the following, we introduce the stream-function formulation $\widetilde{u} = \partial_y\,\widetilde{\ }$, $\widetilde{v} = -\partial_x\,\widetilde{\ }$ for the perturbation and adopt the usual Fourier representation

$$\widehat{q}(y,t;\alpha) = \int_{-\infty}^{+\infty}\widetilde{q}(x,y,t)e^{-i\alpha x}\,\mathrm{d}x, \tag{56}$$

where $\widetilde{q}$ is any generic perturbed quantity, i is the imaginary unit, α is the streamwise wavenumber. We will consider a single wave component at a time. The governing equation for 2D small-amplitude wave perturbations is the Orr-Sommerfeld initial-value problem introduced in Chapter 1 (Eqs. 11-15) that, in terms of the perturbation stream-function $\widehat{\ }(y,t)$, becomes:

$$\begin{aligned}&\partial_t(\partial_y^2\,\widehat{\ } - \alpha^2\,\widehat{\ }) \\ &= -i\alpha U(\partial_y^2\,\widehat{\ } - \alpha^2\,\widehat{\ }) + i\alpha U''\,\widehat{\ } \\ &\quad + \frac{1}{Re}(\partial_y^4\,\widehat{\ } - 2\alpha^2\partial_y^2\,\widehat{\ } + \alpha^4\,\widehat{\ }). \end{aligned} \tag{57}$$

Recall that the plane Poiseuille flow is

$$U(y) = 1 - y^2, \tag{58}$$

while the plane Couette flow is

$$U(y) = y. \tag{59}$$

The associated initial-value problem is then formulated by adding the initial condition

$$\widehat{\ }(y, t=0) = \widehat{\ }_0(y), \tag{60}$$

and the no-slip boundary conditions, which must be satisfied by the stream-function

$$\widehat{\ }(\pm 1, t) = \partial_y\,\widehat{\ }(\pm 1, t) = 0. \tag{61}$$

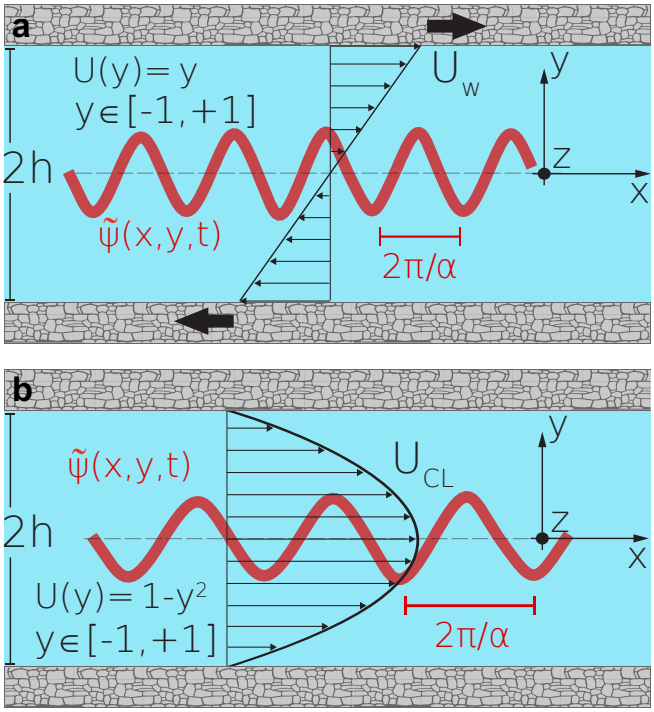

Figure 34: Sketch of basic flows, reference systems and reference quantities. Figure 1 is here reproduced for the reader's convenience **(a)** Plane Couette flow (PCF). The reference length is the channel half-heigth h, while the reference velocity is the wall speed U_w. The Reynolds number is $Re = U_w h/\nu$, where ν is the kinematic viscosity. **(b)** Plane Poiseuille flow (PPF). The reference length is again the channel half-height h, while the reference velocity is the centerline velocity U_{CL}. The Reynolds number is $Re = U_{CL} h/\nu$. The Cartesian reference system in both cases is located at the channel centerline; x is the longitudinal coordinate, y the normal and z the transversal one. The red oscillation represents a perturbation of wavenumber α.

By using Eqs. 53 and 56 we can write the local enstrophy as

$$\begin{aligned}\|\widehat{\omega}\|^2 &= \|i\alpha\widehat{v} - \partial_y\widehat{u}\|^2 = \|\alpha^2\,\widehat{\ } - \partial_y^2\,\widehat{\ }\|^2 \\ &= \alpha^4\|\,\widehat{\ }\,\|^2 + \|\partial_y^2\,\widehat{\ }\,\|^2 - 2\alpha^2\Re(\,\widehat{\ }\,)\Re(\partial_y^2\,\widehat{\ }\,) \\ &- 2\alpha^2\Im(\,\widehat{\ }\,)\Im(\partial_y^2\,\widehat{\ }\,),\end{aligned} \tag{62}$$

where $\Re$ and $\Im$ stand for real and imaginary part, respectively, and the volume-averaged enstrophy as

$$\begin{aligned}\Omega &= \frac{1}{4}\int_{-1}^{1} \|\widehat{\omega}\|^2 \,\mathrm{d}y \\ &= \frac{1}{4}\int_{-1}^{1} \left(\alpha^4 \|\widehat{\ }\|^2 + \|\partial_y^2 \widehat{\ }\|^2\right) \mathrm{d}y + \alpha^2 \int_{-1}^{1} \|\partial_y \widehat{\ }\|^2 \,\mathrm{d}y \\ &= \frac{1}{4}\int_{-1}^{1} \left(\|\partial_y^2 \widehat{\ }\|^2 + 2\alpha^2 \|\partial_y \widehat{\ }\|^2 + \alpha^4 \|\widehat{\ }\|^2\right) \mathrm{d}y. \end{aligned} \tag{63}$$

Note that the integral enstrophy can be split in two parts,

$$\Omega = \alpha^2 E + F, \tag{64}$$

where

$$E = \frac{1}{4}\int_{-1}^{1} (\|\partial_y \widehat{\ }\|^2 + \alpha^2 \|\widehat{\ }\|^2) \,\mathrm{d}y, \tag{65}$$

is the volume-averaged kinetic energy of the perturbation, and F is

$$F = \frac{1}{4}\int_{-1}^{1} (\|\partial_y^2 \widehat{\ }\|^2 + \alpha^2 \|\partial_y \widehat{\ }\|^2) \,\mathrm{d}y, \tag{66}$$

a positive quantity related to the streamwise component of the velocity disturbance and its cross-shear derivative. Note that for wavenumbers of order unity, the integral enstrophy is always greater than the integral kinetic energy. These wavenumbers are typically the most unstable, both asymptotically and in the transient [36, 121]. Note also that in the limit $\alpha \to 0$ the enstrophy is independent of the transversal perturbation velocity.

The temporal evolution equations for E and F are derived as follows:

$$\begin{aligned}\frac{\mathrm{d}E}{\mathrm{d}t} &= -\Re\Big\{\frac{1}{4}\int_{-1}^{1}\Big[\,\overline{\ }\;\partial_t(\partial_y^2 \widehat{\ } - \alpha^2 \widehat{\ })\Big]\,\mathrm{d}y\Big\} \\ &= -\Re\Big\{\frac{1}{4}\int_{-1}^{1}\Big[\,\overline{\ }\;\Big(-i\alpha U \partial_y^2 \widehat{\ } + i\alpha^3 U \widehat{\ } + i\alpha U'' \widehat{\ } \\ &\quad + Re^{-1}(\partial_y^4 \widehat{\ } - 2\alpha^2 \partial_y^2 \widehat{\ } + \alpha^4 \alpha^2 Re^{-1})\Big)\Big]\,\mathrm{d}y\Big\} \end{aligned} \tag{67}$$

$$\begin{aligned}\frac{\mathrm{d}F}{\mathrm{d}t} &= -\Re\Big\{\frac{1}{4}\int_{-1}^{1}\Big[\partial_y^2\,\overline{\ }\;\partial_t(\partial_y^2 \widehat{\ } - \alpha^2 \widehat{\ })\Big]\,\mathrm{d}y\Big\} \\ &= \Re\Big\{\frac{1}{4}\int_{-1}^{1}\Big[\partial_y^2\,\overline{\ }\;\Big(-i\alpha U \partial_y^2 \widehat{\ } + i\alpha^3 U \widehat{\ } + i\alpha U'' \widehat{\ } \\ &\quad + Re^{-1}(\partial_y^4 \widehat{\ } - 2\alpha^2 \partial_y^2 \widehat{\ } + \alpha^4 \alpha^2 Re^{-1})\Big)\Big]\,\mathrm{d}y\Big\}, \end{aligned} \tag{68}$$

where the bar symbol stands for the complex conjugate. The right-hand side of 67, 68 comes directly from 57. The enstrophy equation for small-amplitude waves is then obtained as $\mathrm{d}/\,\mathrm{d}t(\alpha^2 E + F)$ from the two equations above, by considering the expressions of the basic flows 58, 59 and the boundary conditions 61:

$$\begin{aligned}\frac{\mathrm{d}\Omega}{\mathrm{d}t} =& \frac{1}{Re}\Re\left[\partial_y^3\,\widehat{}\,\partial_y^2\,\bar{}\,\right]_{-1}^{1} \\ &- \frac{1}{Re}\int_{-1}^{1}\left(3\alpha^2\|\partial_y^2\,\widehat{}\,\|^2 + 3\alpha^4\|\partial_y\,\widehat{}\,\|^2\right. \\ &\left.+ \alpha^6\|\,\widehat{}\,\|^2 + \|\partial_y^3\,\widehat{}\,\|^2\right) = \frac{1}{Re}H. \end{aligned} \tag{69}$$

Note that all the convective terms which are those containing the basic flow U, coming from the term $(\mathbf{u}\cdot\nabla)\boldsymbol{\omega}$, do not appear in the above enstrophy equation. In fact, many of them drop out when the real part of Eq. 67 and 68 is taken. Other terms vanish because they are contained in both $\alpha^2 E$ and F with opposite sign. As a consequence, the temporal evolution of the enstrophy is physically determined by the diffusive terms of the motion equation and Re^{-1} can be factored out. On top of that, it is relevant and surprising that the only terms that can produce a temporal vorticity growth are boundary terms related to the cross-shear variation of the streamwise velocity disturbance.

The aim of this study is to find a lower bound Re_Ω for the enstrophy transient growth, *whatever the initial condition*. That is, we look for the monotonic stability region in the parameters space, for the volume-averaged enstrophy. The problem is formulated as follows:

$$Re_\Omega(\alpha; U(y)) = \sup_{\hat{\psi}(y,t=0)}\left\{Re \;:\; \frac{\mathrm{d}}{\mathrm{d}t}\Omega \le 0,\;\; \forall t\right\}, \tag{70}$$

meaning that for $Re > Re_\Omega$ there exists at least one initial condition leading to enstrophy temporal growth in the transient.

It is interesting to focus on the term $\Re[\partial_y^3\,\widehat{}\,\partial_y^2\,\bar{}\,]_{-1}^{1}$ in Eq. 69 since, as observed above, it is the only term that can be positive and thus inducing a possible growth. However, boundary conditions on the spanwise vorticity are notoriously unknown. As an example of discussion, the reader may see Synge 1936 [124]. This fact has represented the main obstacle to the solution of problem 70. The mathematical formulation developed by Synge in 1938 was a peculiar application of the modal temporal theory to the vorticity equation. In synthesis, the method is the following. By multiplying the OS equation by $e^{\epsilon\alpha y}$ (where $\epsilon = \pm 1$) and integrating, Synge obtained the two expressions 87 (which he called "the dynamical condition" in [124]) which link the wall values of the vorticity to its y-derivative (actually, the part of the vorticity associated with the cross-flow momentum variation). By using these relationships, he wrote a new integral enstrophy equation which was then optimized in order to maximize the enstrophy growth rate as a

function of the Reynolds number. At the time, the author aimed at finding a lower bound for linear asymptotic stability and, ultimately, conditions for linear instability. That is, the focus was on seeking the marginal stability curve and the *unconditional instability* threshold Re_c (showed in figure 35), which justifies the use of the exponential time factor in the perturbative hypothesis. Today we know that $Re_c = 5772$ [104] for PPF, while for PCF [113] $Re_c = \infty$. At the time, the phenomenon of non-modal transient growth was unknown - it was discovered in the late nineties [130]- therefore Synge could not be aware that his computations would lead instead to a much lower bound for the algebraic transient growth of the vorticity. His calculations worked out for the plane Poiseuille flow but not for the plane Couette flow. In our work, in the place of the exponential time dependence $= \widehat{\ }(y)e^{i\alpha x - \sigma t}$, we used the non-modal approach $= \widehat{\ }(y,t)e^{i\alpha x}$ and solved Eq. 70 for both the plane Couette and Poiseuille flows. Our calculations follow the formalism used by Synge and are shown in §3.5 at the end of this chapter.

3.4 Results and discussion: lower bound for the perturbation's enstrophy growth.

The mathematical formulation developed in order to solve Eq. 70 does not impose any temporal dependence. The route to the solution of the problem 70 consists of:
(i) Using the conditions (see also [124]):

$$\left[(\partial_y^3\widehat{\ } \pm \alpha\partial_y^2\widehat{\ })e^{\alpha y}\right]_{-1}^{1} = \mp 2i\alpha^2 Re\int_{-1}^{1} U'\,\widehat{\ }e^{\alpha y}\,\mathrm{d}y; \tag{71}$$

(ii) Use Eq. 71 in the enstrophy equation 69. Get the enstrophy growth rate, $\mathrm{d}\Omega/\,\mathrm{d}t$, parametrized with all the possible boundary terms $\partial_y^2\,\hat{\ }(\pm 1,t)$:

$$\begin{aligned}\frac{\mathrm{d}}{\mathrm{d}t}\Omega =& Re^{-1}H = Re^{-1}\Big[\alpha a b^{-1}\Theta - \alpha b^{-1}\Phi + i\alpha^2 Re\, b^{-1}B + \\ &- (I_3^2 + 3\alpha^2 I_2^2 + 3\alpha^4 I_1^2 + \alpha^6 I_0^2)\Big],\end{aligned} \tag{72}$$

where, using the bar symbol for the complex conjugate,

$$I_i^2 = \int_{-1}^{1} \partial_y^{(i)} \hat{} \partial_y^{(i)} \bar{} \, \mathrm{d}y, \tag{73}$$

$$\Theta = \partial_y^2 \hat{}(1,t)\partial_y^2 \bar{}(1,t) + \partial_y^2 \hat{}(-1,t)\partial_y^2 \bar{}(-1,t), \tag{74}$$

$$\Phi = \partial_y^2 \hat{}(1,t)\partial_y^2 \bar{}(-1,t) + \partial_y^2 \hat{}(-1,t)\partial_y^2 \bar{}(1,t), \tag{75}$$

$$\begin{aligned} B = \int_{-1}^{1} \Big[\hat{}(y,t)\partial_y^2 \bar{}(1,t) - \bar{}(y,t)\partial_y^2 \hat{}(1,t) \Big] U' \\ \times \cosh[\alpha(y+1)] \, \mathrm{d}y - \int_{-1}^{1} \Big[\hat{}(y,t)\partial_y^2 \bar{}(-1,t) \\ - \bar{}(y,t)\partial_y^2 \hat{}(-1,t) \Big] U' \cosh[\alpha(y-1)] \, \mathrm{d}y. \end{aligned} \tag{76}$$

(iii) By calculus of variations, get the following 6th-order PDE for the perturbation $\hat{}_m(y;t)$ which maximizes the enstrophy growth rate,

$$\begin{aligned} \partial_y^6 \hat{}_m(y,t) - 3\alpha^2 \partial_y^4 \hat{}_m(y,t) + 3\alpha^4 \partial_y^2 \hat{}_m(y,t) - \alpha^6 \hat{}_m(y,t) \\ = i\alpha^2 Re\, b^{-1} U'(y) \Big\{ \partial_y^2 \hat{}_m(1,t) \cosh[\alpha(1+y)] \\ - \partial_y^2 \hat{}_m(-1,t) \cosh[\alpha(1-y)] \Big\}, \end{aligned} \tag{77}$$

and eventually find the region of the $\alpha - Re$ space where transient enstrophy growth is not allowed, i.e. the curve $Re_\Omega(\alpha)$ (solved both analytically and via numerical optimization, see the details in §3.5). The expression for the plane Couette flow appears more complicated due to an additional term (the last term in 118).

The minimum value of Re_Ω for which 2D perturbations can experience transient enstrophy growth is named Re_Ω^*. In the case of plane Couette flow, the result is 56.5, and it occurs at a wavenumber $\alpha_\Omega^* = 1.42$. For the plane Poiseuille flow, $Re_\Omega^* \approx 155$, $\alpha_\Omega^* = 2.36$ (see figure 35 **a**,**b**).

Figure 35 compares the lower bound for the enstrophy transient growth with the bound for the kinetic energy, that is the curve $Re_\mathrm{E}(\alpha)$ (note that throughout this discussion we adopt the terminology used by Manneville [95]). The kinetic energy problem was first formulated by Orr [102], and subsequently by Synge [125] and Joseph [81], while numerical solutions for the three-dimensional case have been obtained many years later by Reddy & Henningson [109]. Recalling the definitions introduced in §3.2, the monotonic decay threshold for the kinetic energy $Re_\mathrm{E}(\alpha)$ is considered a lower bound for the *global stability* threshold Re_g. Thus, for Reynolds number values below Re_g the flow returns to the laminar state for initial disturbances of any amplitude and form. For $Re_\mathrm{g} < Re < Re_\mathrm{c}$, the stability is *conditional*, since it depends on the initial perturbation. In this range, finite-amplitude perturbations (which may also arise from transient growth and/or synchronization [34] of small-amplitude waves) can give birth to self-sustained

Table 8: Reynolds number typical thresholds, from table 1 in Ref. [97]. Here, we extend the picture by adding the 2D enstrophy bounds for PPF and PCF.

	Re	$Re_{\mathrm{E\ 2D}}$	$Re_{\mathrm{E\ 3D}}$	Re_{g}	Re_{c}	Re_{t}
HPF	? (3D)	-	81.5	$\sim$2040	∞	$\sim$ 2700
PCF	56.5 (2D)	44.3	20.7	$\sim$325	∞	$\lesssim$415
PPF	155 (2D)	87.6	49.6	$\sim$840	5772	$\gtrsim$1600

turbulent spots which coexist with the surrounding laminar flow. The theoretical determination of Re_{g} and the physical mechanisms at the heart of turbulence self-sustainment constitute fundamental, challenging and still open questions. We hope that our work could contribute at a better understanding in this direction. For completeness, we cite another threshold, Re_{t}, which delimits the so-called *transitional range*. For $Re > Re_{\mathrm{t}}$, uniform turbulence is observed, in place of coexistence of laminar flow and turbulent patches. The values of such characteristic Reynolds numbers are presented in table 8, for the pipe flow (Hagen-Poiseuille flow), PPF and PCF.

Even if our study is two-dimensional, a brief review of the experimental values of Re_{g} and the related literature, for the three-dimensional problem, is reported in figure 37.

We computed Re_{E} using the well known energy method, based on a variational formulation [103, 81, 109]. This is shown by the white curves in figure 35, and by the right boundary of the white regions in figure 37 and 38, top panels. A relevant outcome is that the threshold for enstrophy monotonic decay $Re_{\Omega}(\alpha)$ for longitudinal waves is greater than the threshold for the kinetic energy $Re_{\mathrm{E}}(\alpha)$, for any wavenumber. This is highlighted by the pink region of figure 35. This means that there exists a region in the α-Re space where transient kinetic energy growth can occur, while it is forbidden for the enstrophy, for any initial perturbation.

In support to the results given by the analytical procedure, we performed numerical simulations of the initial-value problem 57-61 by using the method described in Appendix A and published in [40]. Wavenumber-Reynolds number maps of the maximal kinetic energy and enstrophy normalized to the initial values, $E_{\max}/E_0$, $\Omega_{\max}/\Omega_0$, are shown in figure 37. Figure 38 presents the non-dimensional times corresponding to the maximal values. We considered the range $Re \in [10, 10^5]$ and $\alpha \in [10^{-2}, 10]$, a uniform discretization was set for both the Reynolds number and the wavenumber. Each map contains of 3600 simulations of the initial value problem.

To our knowledge, enstrophy maps have not yet been presented in the literature. A fortiori, neither have stability maps including both enstrophy and wave dispersion properties. Maps of kinetic energy have been previously shown [63, 110, 121], but they typically present the maximum amplification over all possible initial conditions. Here we

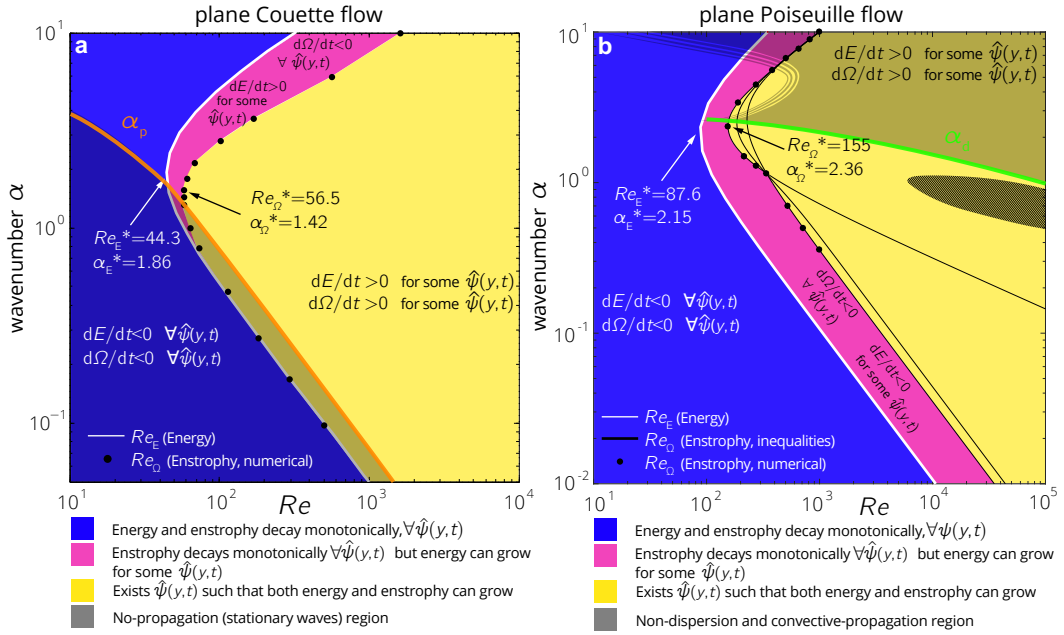

Figure 35: Lower bounds for the transient growth of the enstrophy and the kinetic energy of small 2D waves. *Blue region*: both the kinetic energy (E) and the enstrophy (Ω) of any initial perturbation $\hat{\psi}(y,0)$ decay monotonically with time. *Pink region*: in this portion of the map there exists at least one initial perturbation experiencing transient algebraic energy growth, but enstrophy growth is not possible. *Yellow region*: a growth of both kinetic energy and enstrophy is allowed. **(a)** Plane Couette flow. In this case, the threshold curve (black dotted) for the enstrophy was computed numerically through the optimization procedure described in §3.5. The smallest Reynolds number allowing enstrophy growth is $Re^*_\Omega = 56.5$, at $\alpha^*_\Omega = 1.42$. For PCF, the shaded area indicates a region where wave propagation is forbidden [51]. **(b)** Plane Poiseuille flow. In this case the bound for enstrophy growth was computed both analytically via 134 and 135 (black curves), and by the numerical optimization procedure (black dots). In the shaded region the waves are non-dispersive in the long temporal term, while dispersion is observed in the lower part of the map, see §2.3 (note both the sharp lower boundary and the smooth transition in the upper part). In black-dashed, the asymptotic instability region [104], not existing in the PCF case [113]. This picture will be published in ref. [49].

follow a different approach, by keeping fixed the initial condition. In this study, initial condition is smooth and excites both symmetric and antisymmetric Orr-Sommerfeld modes (figure 36). It was chosen in order to trigger a transient energy growth for almost any Re above the limit Re^*_E. By an optimization process, we get the perturbation giving the maximal kinetic energy growth rate $(E^{-1}\,\mathrm{d}E/\,\mathrm{d}t)_{t=0}$ in the surrounding of Re^*_E, α^*_E. For PCF, the optimized point is $Re = 50$,$\alpha = 2$. For PPF, the initial condition was optimized at $Re = 100$ and $\alpha = 2$. Note that for both flows, these values fall

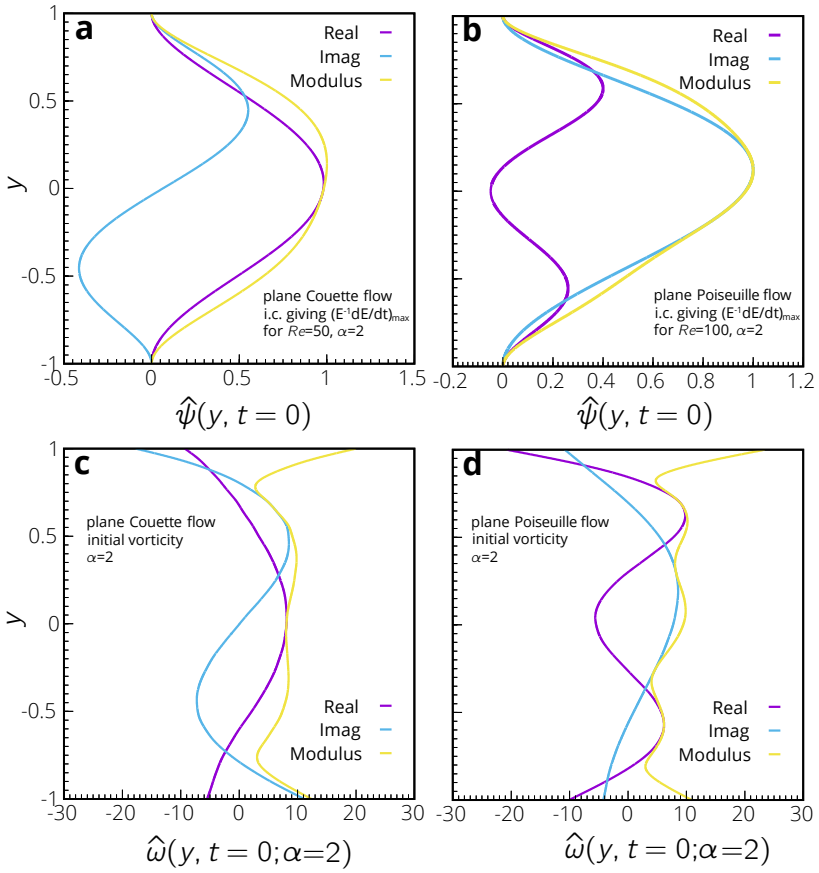

Figure 36: Initial conditions. Initial perturbations used for all the simulations in the present chapter and for the wave packets of Chapter 2 (see figure 37 and 38). **(a)** Plane Couette flow. This perturbation maximizes the initial kinetic energy growth rate at $Re = 50$ and $\alpha = 2$. **(b)** Plane Poiseuille flow. In this case the initial condition maximizes the energy growth rate at $Re = 100$ and $\alpha = 2$. These initial disturbances allow to show that a kinetic energy growth is not a sufficient condition for an enstrophy growth (see figures 37,38). Such perturbations, moreover, excite the least stable Orr-Sommerfeld eigenfunctions, are smooth and contain both symmetric and antisymmetric modes. Panels **(c)** and **(d)** show the shape of the corresponding initial vorticity for $\alpha = 2$ (recall that in the Fourier space $\widehat{\omega}_z = \alpha^2\widehat{\psi} - \partial_y^2\widehat{\psi}$) . This picture will be published in ref. [49].

inside the pink region of figure 35. In this way, it is possible to show that the kinetic energy growth is not a sufficient condition for enstrophy growth. Indeed, as expected, the vorticity starts to experience a transient growth only for $Re > Re_\Omega(\alpha)$, see figure 37 (**c**, **d**).

Comments are now proposed about the map structure. It is possible to observe that the internal structure of both kinetic energy and enstrophy maps reflects the trend of the lower bound for transient growth. This fact can be observed from the iso-lines of $G_{\max}$ and $\Omega_{\max}$ in the low-wavenumber region of figure 37. This translates into the scaling laws $G_{\max} \sim (\alpha Re)^{\delta_1}$, $\Omega_{\max} \sim (\alpha Re)^{\delta_2}$. The exponents δ_1,δ_2 depend on the initial condition, and for the cases span here $\delta_1 \approx 0.59$ for PCF, $\delta_1 \approx 0.33$ for PPF; $\delta_2 \approx 0.82$ for PCF, $\delta_2 \approx 0.21$ for PPF. Moreover, inside the region of the parameters space where both the wave kinetic energy and the enstrophy can grow, we observe that smooth vortical initial disturbances - optimized to maximize their initial kinetic energy rate - show a comparatively more intense amplification of their integral enstrophy. Further investigations are needed to understand if this fact is general, i.e. if it occurs for arbitrary initial disturbances.

Considering the non-dimensional time necessary to achieve the maximal growth, it appears to be only weakly dependent on the Reynolds number, in the limit of high Re and small wavenumber. A unique scaling is observed for both the perturbation enstrophy and kinetic energy, and for both PCF and PPF, as shown in figure 38: $T_{E_{\max}} \sim \alpha^{-1}$, $T_{\Omega_{\max}} \sim \alpha^{-1}$.

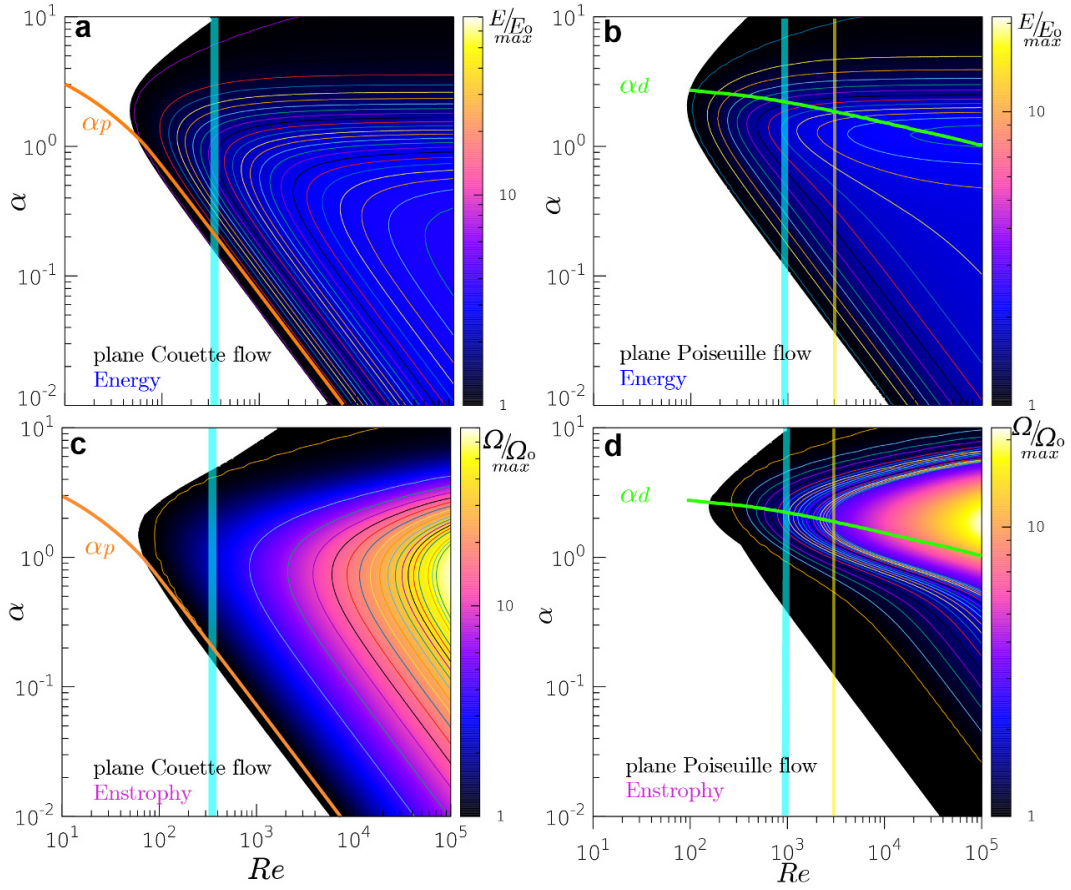

Figure 37: Maximal transient growth of perturbation enstrophy and kinetic energy. A case study. Wavenumber-Reynolds number maps of maximal transient growth of kinetic energy (E/E_0, top panels: **a**, **b**) and enstrophy (Ω/Ω_0 bottom panels: **c**, **d**), normalized to the initial value. Left panels regard the plane Couette flow (PCF), while right panels the plane Poiseuille flow (PPF). Each map is built from 3600 numerical simulations of the initial-value problem 57 (60 values of wavenumber α in the range $[10^{-2}, 10]$ and 60 values of Reynolds number in $[10, 10^5]$, uniformly distributed in the log space). The initial condition is shown in figure. 36(**a**) and 36(**b**) for PCF and PPF, respectively. Contours start from the value 1.01 and their spacing is set to 0.1 in panels (**a**, **b**, **d**), while it is set to 3 in panel **(c)**. The blue vertical bands represent the 3D experimental findings for the *global stability* threshold Re_g. Values are around 325 for PCF and 840 for PPF. In 2D, nonlinear analysis of PPF led to a transitional value of about 2900 [13] (vertical yellow line), while for PCF no results are yet available. The width of the bands stands for the range of values found in the extensive literature on the subcritical transition to turbulence [105, 26, 93, 39, 130, 134, 133, 20, 19, 43, 96, 132, 97]. The maps include information about the wave propagation and dispersion. In the PPF panels, the green curve represents the threshold $\alpha_d(Re)$, between dispersive and non-dispersive longterm behavior (below and above the curve, respectively). For the PCF case instead, in the region below the orange curve $\alpha_p(Re)$, waves cannot propagate [51]. This picture will be published in ref. [49].

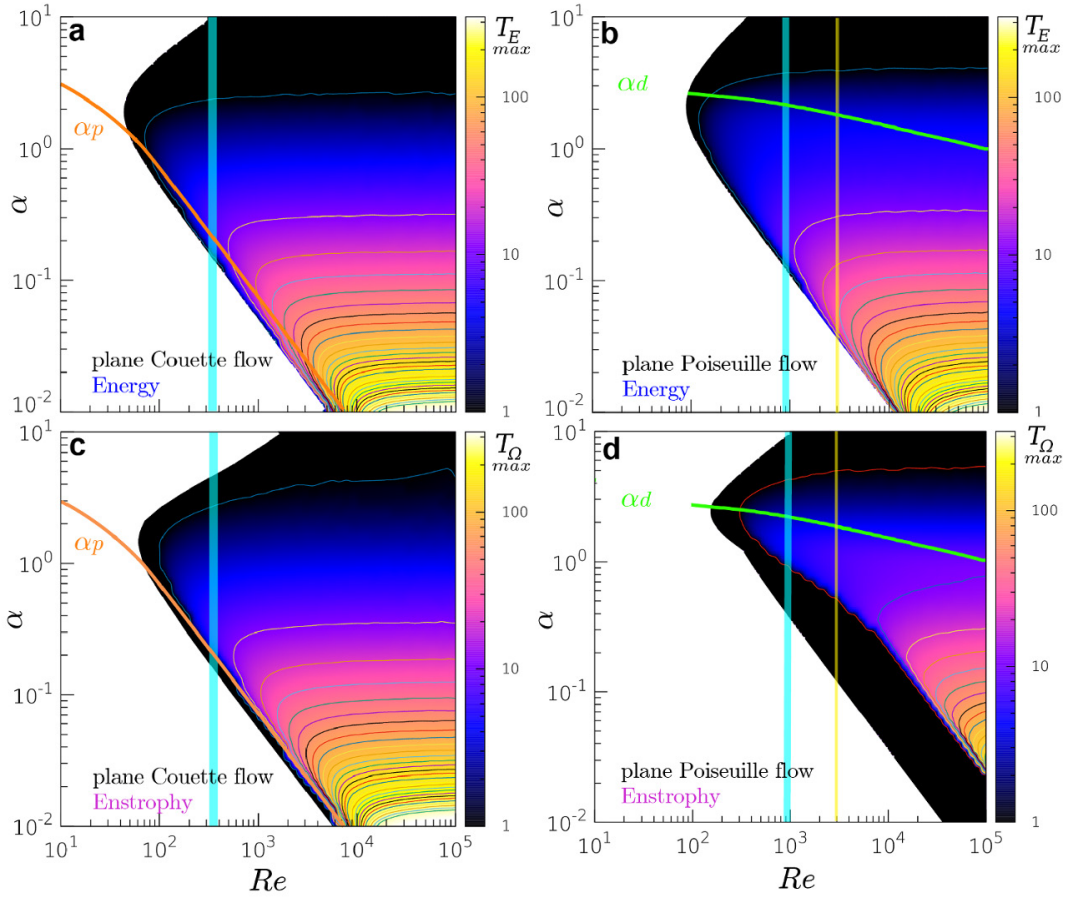

Figure 38: Time instant of maximal transient growth. A case study. Wavenumber-Reynolds number maps of the time instant of maximal transient growth of kinetic energy ($T_{\mathrm{E}_{\mathrm{max}}}$, top panels **a**, **b**) and enstrophy ($T_{\Omega_{\mathrm{max}}}$, bottom panels **c**, **d**), for the case study of the above figure 37. Scaling laws can be derived for the high-Reynolds and low-wavenumber limit: $T_{\mathrm{E}_{\mathrm{max}}} \sim \alpha^{\delta_3}$, $T_{\Omega_{\mathrm{max}}} \sim \alpha^{\delta_4}$. In fact, times iso-contours show a very weak dependence on the Reynolds number, in lower part of the maps. Moreover, a unique dependence on the wavenumber, as computed from these numerical simulations, is observed for both PCF and PPF, for the kinetic energy and the enstrophy. The exponent is $\delta_3 \approx \delta_4 \approx -1$ (linear fits on log scale at different values of $Re \in [10^4, 10^5]$ give $\delta_{3,4} = -0.97 \pm 0.02$ for PPF and -0.99 ± 0.01 for PCF). This picture will be published in ref. [49].

Figures 35, 37, 38 and 39 also include synthetic information on the wave propagation properties discussed in Chapter 1 and 2. As shown in §2.3, we measure the dispersion intensity in terms of the difference between group velocity and phase velocity. We underline that the parameters space $\alpha - Re$ is split in regions which have different dispersion characteristics. In particular, we observed the existence of a dispersive-to-nondispersive transition associated with a jump in the phase velocity of the least damped eigenmode. Below this boundary (reported in figures 37, 38 **b**, **d**), waves travel dispersively, see figure 13 (**e**). Above, the propagation becomes convective and the behavior is mostly non-dispersive for $Re > 1000$, see the shaded region in figure 35 (**b**). For PCF, such an abrupt transition between dispersive and non-dispersive behavior does not exist, since small traveling waves always disperse. In general the dispersion is mild, but becomes intense in the neighborhood of a boundary curve that we call $\alpha_{\mathrm{p}}(Re)$, below which waves become stationary (see the shaded part of figure 35 (**a**) and the orange curves in figures 37 and 38. This threshold was first found by Gallagher & Mercer in 1962 [51]). The dispersion intensity for PCF was shown in 13 (**f**). The phase and group velocity are also presented here in figure 39 for some values of Re and finer wavenumber discretization (1024 points).

As shown in Chapter 2, the significance of the above picture is that any spatially localized perturbation - which may contain a broad range of traveling wave components - presents both the dispersive and non-dispersive behavior at fixed flow conditions. Namely, there is a subset of dispersive waves that will spread information in the surrounding environment, enhancing the probability to catch other similar perturbations propagating in the neighborhood. In case the enstrophy is sufficiently high (see figure 37), this can trigger a nonlinear coupling between two close perturbations. Beside, there will be a non-dispersive subset of waves which propagates with the convective speed of the basic flow. Once again, if the enstrophy and kinetic energy content is sufficiently high, since this subset cannot unpack, the onset of a nonlinear coupling is expected. In our vision, wave propagation properties, in particular the dispersion or non-dispersion of adjacent wavenumber waves, play a key role in triggering the nonlinear cascade, and beside the kinetic energy growths, the enstrophy amplification should be considered.

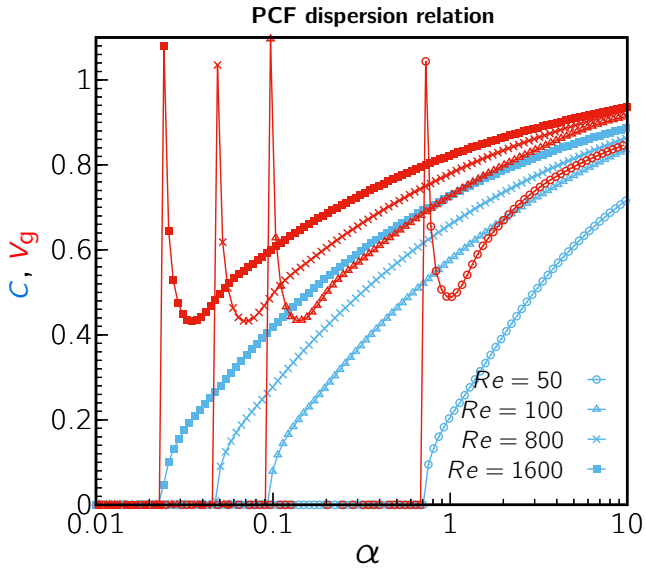

Figure 39: Dispersion relation of the least-damped mode for the plane Couette flow. The phase velocity c (light blue) and the group velocity $v_g = \mathrm{d}\omega/\,\mathrm{d}\alpha$ (red) are shown for the least-damped OS mode in the plane Couette flow for $Re = [50, 100, 800, 1600]$. Since the three-branched eigenvalues spectrum of PCF is symmetric about the frequency axis, there always are two modes equally damped, traveling in opposite directions. Note that below a certain threshold, $\alpha_p(Re)$, wave propagation is forbidden (mathematically, all eigenvalues become purely imaginary, as a consequence the phase speed is zero). For higher wavenumbers wave dispersion is always observed. Dispersion is high in the neighborhood of α_p and it decreases as $(\alpha Re \to \infty)$, as can be inferred from the discrepancy between the phase and the group velocity in the above diagram. The computation was performed by a 4th-order finite difference scheme [40], the wavenumber is uniformly discretized in the log-space (1024 points). For clarity, only one every ten points is shown in the figure, for each curve.

3.5 Mathematical procedure to get the lower bound for enstrophy transient growth

This section reports the complete mathematical formulation developed to find the enstrophy monotonic decay region in the system stability map. As a starting point, the enstrophy equation 69 is recalled below:

$$\begin{aligned}\frac{\mathrm{d}\Omega}{\mathrm{d}t} =& \frac{1}{Re}\Re\Big[\partial_y^3\,\widehat{}\,\partial_y^2\,\widehat{}^{\,*}\Big]_{-1}^{1} \\ &- \frac{1}{Re}\int_{-1}^{1}\left(3\alpha^2\|\partial_y^2\,\widehat{}\,\|^2 + 3\alpha^4\|\partial_y\,\widehat{}\,\|^2\right. \\ &\left.+ \alpha^6\|\,\widehat{}\,\|^2 + \|\partial_y^3\,\widehat{}\,\|^2\right)\mathrm{d}t = \frac{1}{Re}H. \end{aligned} \tag{78}$$

The procedure starts by eliminating $\partial_y^3\,\widehat{}\,(\pm 1, t)$; this is done by multiplying the Orr-Sommerfeld equation 57 (which is the governing equation for $\widehat{}$) by the factor $e^{\epsilon\alpha y}$ and integrating over $[-1, 1]$. By setting $\epsilon = 1$, and $\epsilon = -1$, two independent equations are obtained, which are then solved for $\partial_y^3\,\widehat{}\,(1, t)$ and $\partial_y^3\,\widehat{}\,(-1, t)$. Following Synge's notation, Eq. 57 is rewritten as follows:

$$LL\,\widehat{}\, = Re\,\widetilde{\sigma}L\,\widehat{}\, + i\alpha Re\,\widetilde{M}\,\widehat{}\,, \tag{79}$$

where

$$L = (\partial_y^2 - \alpha^2), \tag{80}$$

$$\widetilde{\sigma} = Re\Big(\partial_t + i\alpha U\Big), \tag{81}$$

$$\widetilde{M} = -U''. \tag{82}$$

The Orr-Sommerfeld equation is multiplied by $e^{\epsilon\alpha y}$ and integrated over $[-1, 1]$. The left-hand side of Eq. 79, after integration by parts and by considering the boundary conditions 61, reads:

$$\begin{aligned}&\int_{-1}^{1} LL\,\widehat{}\, e^{\epsilon\alpha y}\,\mathrm{d}y = \int_{-1}^{1}\partial_y^4\,\widehat{}\, e^{\epsilon\alpha y}\,\mathrm{d}y - 2\alpha^2\int_{-1}^{1}\partial_y^2\,\widehat{}\, e^{\epsilon\alpha y}\,\mathrm{d}y \\ &+ \alpha^4\int_{-1}^{1}\,\widehat{}\, e^{\epsilon\alpha y}\,\mathrm{d}y = \Big[(\partial_y^3\,\widehat{}\, - \epsilon\alpha\partial_y^2\,\widehat{}\,)e^{\epsilon\alpha y}\Big]_{-1}^{1}. \end{aligned} \tag{83}$$

The right-hand side of Eq. 79 requires some passages, since the operator $\widetilde{\sigma}$ contains both a time derivative and the function $U(y)$:

$$\begin{aligned}
&\int_{-1}^{1}\left(Re\,\widetilde{\sigma}L\,\widehat{\ }+i\alpha Re\,\widetilde{M}\,\widehat{\ }\right)e^{\epsilon\alpha y}\,\mathrm{d}y\\
&=Re\frac{\partial}{\partial t}\overbrace{\int_{-1}^{1}\partial_y^2\,\widehat{\ }e^{\epsilon\alpha y}\,\mathrm{d}y}^{A}-Re\frac{\partial}{\partial t}\alpha^2\int_{-1}^{1}\widehat{\ }e^{\epsilon\alpha y}\,\mathrm{d}y\\
&\quad+i\alpha Re\overbrace{\int_{-1}^{1}\partial_y^2\,\widehat{\ }Ue^{\epsilon\alpha y}\,\mathrm{d}y}^{B}-i\alpha^3 Re\int_{-1}^{1}\widehat{\ }Ue^{\epsilon\alpha y}\,\mathrm{d}y\\
&\quad-i\alpha Re\int_{-1}^{1}\widehat{\ }U''e^{\epsilon\alpha y}\,\mathrm{d}y\\
&=Re\frac{\partial}{\partial t}\alpha^2\int_{-1}^{1}\widehat{\ }e^{\epsilon\alpha y}\,\mathrm{d}y-Re\frac{\partial}{\partial t}\alpha^2\int_{-1}^{1}\widehat{\ }e^{\epsilon\alpha y}\,\mathrm{d}y\\
&\quad+i\alpha Re\int_{-1}^{1}\widehat{\ }(U''+2\epsilon\alpha U'+\alpha^2U)e^{\epsilon\alpha y}\,\mathrm{d}y\\
&\quad-i\alpha^3 Re\int_{-1}^{1}\widehat{\ }Ue^{\epsilon\alpha y}\,\mathrm{d}y-i\alpha Re\int_{-1}^{1}\widehat{\ }U''e^{\epsilon\alpha y}\,\mathrm{d}y\\
&=2i\alpha^2\epsilon Re\int_{-1}^{1}U'\,\widehat{\ }e^{\epsilon\alpha y}\,\mathrm{d}y. \qquad (84)
\end{aligned}$$

The terms **A** and **B** were evaluated separately by integrating by parts and using the boundary conditions 61:

$$\begin{aligned}
\mathbf{A}&=-\int_{-1}^{1}\partial_y\,\widehat{\ }\epsilon\alpha e^{\epsilon\alpha y}\,\mathrm{d}y=\epsilon^2\alpha^2\int_{-1}^{1}\widehat{\ }e^{\epsilon\alpha y}\,\mathrm{d}y\\
&=\alpha^2\int_{-1}^{1}\widehat{\ }e^{\epsilon\alpha y}\,\mathrm{d}y, \qquad (85)\\
\mathbf{B}&=-\int_{-1}^{1}\partial_y\,\widehat{\ }\partial_y(Ue^{\epsilon\alpha y})\,\mathrm{d}y=\int_{-1}^{1}\widehat{\ }\partial_y^2(Ue^{\epsilon\alpha y})\,\mathrm{d}y\\
&=\int_{-1}^{1}\widehat{\ }(U''+2\epsilon\alpha U'+\epsilon^2\alpha^2U)e^{\epsilon\alpha y}\,\mathrm{d}y. \qquad (86)
\end{aligned}$$

The system of equations to find $\partial_y^3\,\widehat{\ }(-1,t)$ and $\partial_y^3\,\widehat{\ }(1,t)$ is the following:

$$\begin{cases}\left[(\partial_y^3\,\widehat{\ }-\alpha\partial_y^2\,\widehat{\ })e^{\alpha y}\right]_{-1}^{1}=2i\alpha^2Re\int_{-1}^{1}U'\,\widehat{\ }e^{\alpha y}\,\mathrm{d}y\\ \left[(\partial_y^3\,\widehat{\ }+\alpha\partial_y^2\,\widehat{\ })e^{-\alpha y}\right]_{-1}^{1}=-2i\alpha^2Re\int_{-1}^{1}U'\,\widehat{\ }e^{-\alpha y}\,\mathrm{d}y.\end{cases} \qquad (87)$$

Substituting these expressions in 69 and naming

$$\begin{aligned}
a&=\cosh(2\alpha),\\
b&=\sinh(2\alpha),
\end{aligned}$$

a new form for H is obtained:

$$\frac{\mathrm{d}}{\mathrm{d}t}\Omega = \frac{1}{Re}H = \frac{1}{Re}\Big[\alpha a b^{-1}\Theta - \alpha b^{-1}\Phi + i\alpha^2 Re\, b^{-1}B + - (I_3^2 + 3\alpha^2 I_2^2 + 3\alpha^4 I_1^2 + \alpha^6 I_0^2)\Big], \tag{88}$$

where

$$I_i^2 = \int_{-1}^{1} \partial_y^{(i)}\,\widehat{}\,\partial_y^{(i)}\,\bar{}\,\,\mathrm{d}y, \tag{89}$$

$$\Theta = \partial_y^2\,\widehat{}\,(1,t)\partial_y^2\,\bar{}\,(1,t) + \partial_y^2\,\widehat{}\,(-1,t)\partial_y^2\,\bar{}\,(-1,t), \tag{90}$$

$$\Phi = \partial_y^2\,\widehat{}\,(1,t)\partial_y^2\,\bar{}\,(-1,t) + \partial_y^2\,\widehat{}\,(-1,t)\partial_y^2\,\bar{}\,(1,t), \tag{91}$$

$$\begin{aligned} B = \int_{-1}^{1}\Big[\,\widehat{}\,(y,t)\partial_y^2\,\bar{}\,(1,t) - \bar{}\,(y,t)\partial_y^2\,\widehat{}\,(1,t)\Big]U' \\ \times \cosh[\alpha(y+1)]\,\mathrm{d}y - \int_{-1}^{1}\Big[\,\widehat{}\,(y,t)\partial_y^2\,\bar{}\,(-1,t) \\ - \bar{}\,(y,t)\partial_y^2\,\widehat{}\,(-1,t)\Big]U'\cosh[\alpha(y-1)]\,\mathrm{d}y. \end{aligned} \tag{92}$$

Note that H depends on the parameters α and Re and the stream-function $\widehat{}$. In order to get to conditions on α and Re implying non-positivity of H, calculus of variations is used to maximize H with respect to the function $\widehat{}$, with $\partial_y^2\,\widehat{}\,(-1,t) = q(t)$ and $\partial_y^2\,\widehat{}\,(1,t) = p(t)$ being assigned.
Considering the part of H depending on $\widehat{}$:

$$H_{\widehat{\psi}} = i\alpha^2 Re\, b^{-1}B - (I_3^2 + 3\alpha^2 I_2^2 + 3\alpha^4 I_1^2 + \alpha^6 I_0^2), \tag{93}$$

introducing the variations on the perturbation, we evaluate

$$\underline{H}(\epsilon) = H_{\widehat{\psi}}(\,\widehat{}\,+\epsilon\varphi) \quad \rightarrow \quad \frac{\mathrm{d}\underline{H}}{\mathrm{d}\epsilon}|_{\epsilon=0} = 0.$$

Calculus of variations leads to a sixth-order differential equation for the disturbance $\widehat{}$ which maximizes the enstrophy rate. This particular function will be named $\widehat{}_m$ in the following:

$$\begin{aligned} \partial_y^6\,\widehat{}\,_m(y,t) - 3\alpha^2\partial_y^4\,\widehat{}\,_m(y,t) + 3\alpha^4\partial_y^2\,\widehat{}\,_m(y,t) - \alpha^6\,\widehat{}\,_m(y,t) \\ = i\alpha^2 Re\, b^{-1}U'(y)\Big\{\partial_y^2\,\widehat{}\,_m(1,t)\cosh[\alpha(1+y)] \\ - \partial_y^2\,\widehat{}\,_m(-1,t)\cosh[\alpha(1-y)]\Big\}. \end{aligned} \tag{94}$$

To express in convenient form the corresponding maximum value of H, named $H_{\max}$ in the following, 94 is multiplied by $\bar{\ }$, and integrated over the range $(-1,1)$. Then the complex conjugate is added. This gives:

$$\begin{aligned}&\left[\partial_y^2\,\hat{}_m\partial_y^3\,\bar{}_m+\partial_y^2\,\bar{}_m\partial_y^3\,\hat{}_m\right]_{-1}^{1}\\&-2(I_3^2+3\alpha^2I_2^2+3\alpha^4I_1^2+\alpha^6I_0^2)\\&=-i\alpha^2Re\,b^{-1}B,\end{aligned}\tag{95}$$

and so from the definition of H:

$$\begin{aligned}H_{\max}=&\,\alpha ab^{-1}\Theta-\alpha b^{-1}\Phi+\frac{1}{2}i\alpha^2Re\,b^{-1}B\\&-\frac{1}{2}\left[\partial_y^2\,\hat{}_m\partial_y^3\,\bar{}_m+\partial_y^2\,\bar{}_m\partial_y^3\,\hat{}_m\right]_{-1}^{1},\end{aligned}\tag{96}$$

where $\hat{}_m$ here is the maximizing function, solution of Eq. 94.
The procedure followed up to this point leads to an expression for $H_{\max}$ formally identical to that found by Synge (Eq. 2.12 in [126]). The difference is that here, having adopted the nonmodal approach, $\hat{}$ is time dependent. In the following, we solve the problem for the plane Couette flow and than for the plane Poiseuille flow.

3.5.1 *Plane Couette flow: sufficient conditions for no enstrophy growth. Analytical method and final numerical optimization.*

Conditions for no-growth of perturbation enstrophy are now derived for the plane Couette flow. In this case $U(y)=y$, so equation 94 together with the boundary conditions is as follows:

$$\begin{aligned}&\partial_y^6\,\hat{}_m(y,t)-3\alpha^2\partial_y^4\,\hat{}_m(y,t)+3\alpha^4\partial_y^2\,\hat{}_m(y,t)-\alpha^6\,\hat{}_m(y,t)\\&=96i\,k\,\alpha^4\left\{p(t)\,\cosh[\alpha(1+y)]-q(t)\cosh[\alpha(1-y)]\right\},\end{aligned}\tag{97}$$

$$\hat{}_m(\pm1,t)=0,\tag{98}$$

$$\partial_y\,\hat{}_m(\pm1,t)=0,\tag{99}$$

$$\partial_y^2\,\hat{}_m(+1,t)=p(t),\tag{100}$$

$$\partial_y^2\,\hat{}_m(-1,t)=q(t),\tag{101}$$

where $k=Re/96\alpha^2b$. The associated homogeneous equation is

$$\hat{}^{(6)}_{m_H}-3\alpha^2\,\hat{}^{(4)}_{m_H}+3\alpha^4\,\hat{}^{(2)}_{m_H}-\alpha^6\,\hat{}_{m_H}=0,\tag{102}$$

where the $\widehat{\ }_{m_H}$ stands for the homogeneous solution. Since the solutions of the characteristic equation are $+\alpha$ and $-\alpha$ both with multiplicity of 3, it is possible to write the solution as:

$$\widehat{\ }_{m_H} = (a_0 + a_1\, y + a_2\, y^2)e^{-\alpha y} + (b_0 + b_1\, y + b_2\, y^2)e^{\alpha y} \quad (\alpha \neq 0). \tag{103}$$

Based on the form of the forcing term and in order to get a simpler computation of the constants when the boundary conditions are applied, a different basis is chosen. In particular we wrote the solution as:

$$\begin{aligned}\widehat{\ }_{m_H} =&(a_0 + a_1(1-y) + a_2(1-y)^2)\sinh[\alpha(1+y)] \\ &+ (b_0 + b_1(1+y) + b_2(1+y)^2)\sinh[\alpha(1-y)].\end{aligned} \tag{104}$$

To show that this is indeed allowed, we prove that the two basis

$$\mathscr{B}_1 = (e^{-\alpha y}, e^{\alpha y}, ye^{-\alpha y}, ye^{\alpha y}, y^2e^{-\alpha y}, y^2e^{\alpha y}) \tag{105}$$

$$\begin{aligned}\mathscr{B}_2 = &(\sinh[\alpha(1+y)], \sinh[\alpha(1-y)], (1-y)\sinh[\alpha(1+y)], \\ &(1+y)\sinh[\alpha(1-y)], (1-y)^2\sinh[\alpha(1+y)], \\ &(1+y)^2\sinh[\alpha(1-y)])\end{aligned} \tag{106}$$

are linearly independent. We write $\mathscr{B}_2 = \mathscr{A}\mathscr{B}_1$, where

$$\mathscr{A} = \frac{1}{2}\begin{pmatrix} -e^{-\alpha} & e^{\alpha} & 0 & 0 & 0 & 0 \\ e^{\alpha} & -e^{-\alpha} & 0 & 0 & 0 & 0 \\ -e^{-\alpha} & e^{\alpha} & e^{-\alpha} & -e^{\alpha} & 0 & 0 \\ e^{\alpha} & -e^{-\alpha} & e^{\alpha} & -e^{-\alpha} & 0 & 0 \\ -e^{-\alpha} & e^{\alpha} & 2e^{-\alpha} & -2e^{\alpha} & -e^{-\alpha} & e^{\alpha} \\ e^{\alpha} & -e^{-\alpha} & 2e^{\alpha} & -2e^{-\alpha} & e^{\alpha} & -e^{-\alpha} \end{pmatrix}. \tag{107}$$

Since $\mathscr{A}$ is a triangular block matrix, the determinant is the product of the determinants of the three matrices on the diagonal. $Det(\mathscr{A}) = 4b^3 \neq 0$, which implies linear independence.

To solve Eq. 97, a particular solution was to be found. The forcing term was considered as a superposition of two terms, one containing $\cosh[\alpha(1+y)]$ and the other one with $\cosh[\alpha(1-y)]$. We first found a particular solution $\widehat{\ }_{m_{P1}}$ of the equation:

$$\begin{aligned}&\partial_y^6\,\widehat{\ }_{m_{P1}}(y,t) - 3\alpha^2\partial_y^4\,\widehat{\ }_{m_{P1}}(y,t) + 3\alpha^4\partial_y^2\,\widehat{\ }_{m_{P1}}(y,t) \\ &- \alpha^6\,\widehat{\ }_{m_{P1}}(y,t) = 96ik\alpha^4 p\cosh[\alpha(1+y)].\end{aligned} \tag{108}$$

We looked for a solution with the form

$$\widehat{\ }_{m_{P1}}(y,t) = -i\,k\,p\,\{A_1\sinh[\alpha(1+y)] + A_2\cosh[\alpha(1+y)]\}\,, \tag{109}$$

and obtained $A_2 = 0$ and $A_1 = -2\alpha$, so the solution for this equation is

$$\widehat{}_{m_{P1}}(y,t) = 2i\,k\,\alpha\,y^3 p\,\sinh[\alpha(1+y)]. \tag{110}$$

By proceeding in the same way, we found a second particular solution $\widehat{}_{m_{P2}}$ for

$$\begin{aligned}&\partial_y^6\,\widehat{}_{m_{P2}}(y,t) - 3\alpha^2\partial_y^4\,\widehat{}_{m_{P2}}(y,t) + 3\alpha^4\partial_y^2\,\widehat{}_{m_{P2}}(y,t)\\ &-\alpha^6\,\widehat{}_{m_{P2}}(y,t) = -96ik\alpha^4 m\,\cosh[\alpha(1-y)],\end{aligned} \tag{111}$$

leading to

$$\widehat{}_{m_{P2}}(y,t) = 2i\,k\,\alpha\,y^3 m\,\sinh[\alpha(1-y)]. \tag{112}$$

The complete solution can be written as follows:

$$\begin{aligned}&\widehat{}_m(y,t) = \widehat{}_{m_H}(y,t) + \widehat{}_{m_{P1}}(y,t) + \widehat{}_{m_{P2}}(y,t)\\ &= \left\{a_0 + a_1(1-y) + a_2(1-y)^2 + 2ik\alpha y^3 p\right\}\sinh[\alpha(1+y)]\\ &+ \left\{b_0 + b_1(1+y) + b_2(1+y)^2 + 2ik\alpha y^3 q\right\}\sinh[\alpha(1-y)].\end{aligned} \tag{113}$$

By applying the boundary conditions it is possible to find the six constants (this was done by means of symbolic calculus via the software Mathematica®):

$$
\begin{aligned}
a_0 =& -2i\alpha kp,\\
b_0 =& \ 2i\alpha kq,\\
a_1 =& -\{2i\alpha(-48\alpha^4 kp\cosh^2(2\alpha)+i\sinh^2(2\alpha)(q+4i\alpha^2 kp)\\
&-4\alpha^2(4\alpha^2 kp-2\alpha kp\sinh(4\alpha)+iq)+\cosh(2\alpha)(64\alpha^4 kq\\
&-4i\alpha^2 p)-8\alpha kq\sinh^3(2\alpha)+3kp\sinh^4(2\alpha)+2i\alpha p\\
&\times\sinh(2\alpha))\}/\{8\alpha^4\cosh(4\alpha)-8\alpha^3(\alpha+\sinh(4\alpha))\\
&+12\alpha^2\sinh^2(2\alpha)-\sinh^4(2\alpha)\},\\
a_2 =&\{-64i\alpha^5 kp\cosh^2(2\alpha)+2\alpha^2\sinh(4\alpha)(-16i\alpha^2 kp+8i\alpha\\
&\times kq\sinh(2\alpha)+q)+8\alpha^3(q-8i\alpha^2 kp)+8\alpha^3\cosh(2\alpha)\\
&\times(p+16i\alpha^2 kq)+i\sinh(2\alpha)(64\alpha^4 kq+\sinh(2\alpha)(16\alpha^3 kp\\
&+\sinh(2\alpha)(-48\alpha^2 kq+12\alpha kp\sinh(2\alpha)+ip)+4i\alpha q))\}\\
&/\{32\alpha^4\cosh^2(2\alpha)-2(8\alpha^3(2\alpha+\sinh(4\alpha))-12\alpha^2\sinh^2(2\alpha)\\
&+\sinh^4(2\alpha))\},\\
b_1 =& -\{2i\alpha(16\alpha^4 kq+48\alpha^4 kq\cosh^2(2\alpha)-8\alpha^3 kq\sinh(4\alpha)\\
&+\sinh(2\alpha)(\sinh(2\alpha)(4\alpha^2 kq+k\sinh(2\alpha)(8\alpha p-3q\\
&\times\sinh(2\alpha))+ip)+2i\alpha q)-4\alpha^2\cosh(2\alpha)(16\alpha^2 kp+iq)\\
&-4i\alpha^2 p)\}/\{8\alpha^4\cosh(4\alpha)-8\alpha^3(c+\sinh(4\alpha))+12\alpha^2\\
&\times\sinh^2(2\alpha)-\sinh^4(2\alpha)\},\\
b_2 =&\{64i\alpha^5 kq\cosh^2(2\alpha)+2\alpha^2\sinh(4\alpha)(16i\alpha^2 kq-8i\alpha kp\\
&\times\sinh(2\alpha)+p)+8\alpha^3(p+8i\alpha^2 kq)+8\alpha^3\cosh(2\alpha)(q-\\
&16i\alpha^2 kp)-i\sinh(2\alpha)(64\alpha^4 kp+\sinh(2\alpha)(16\alpha^3 kq\\
&+\sinh(2\alpha)(-48\alpha^2 kp+12\alpha kq\sinh(2\alpha)-iq)-4i\alpha p))\}\\
&/\{32\alpha^4\cosh^2(2\alpha)-2(8\alpha^3(2\alpha+\sinh(4\alpha))-12\alpha^2\sinh^2(2\alpha)\\
&+\sinh^4(2\alpha))\}.
\end{aligned}
\tag{114}
$$

Once the solution of equation 97 is available, it is possible to evaluate the maximal enstrophy growth 96. We first evaluated B in Eq. 92, and the boundary term $\left[\partial_y^2\,\widehat{}_m\partial_y^3\,\bar{}_m+\partial_y^2\,\bar{}_m\partial_y^3\,\widehat{}_m\right]_{-1}^{1}$:

$$B = -4\,i\,k\left(Q_1\Theta - Q_2\Phi - \frac{Q_3}{k}\Im[p\overline{q}]\right), \tag{115}$$

$$\left[\partial_y^2\,\widehat{}_m\partial_y^3\,\bar{}_m+\partial_y^2\,\bar{}_m\partial_y^3\,\widehat{}_m\right]_{-1}^{1}$$
$$= 2\left(F_1\Theta - F_2\Phi - kF_3\,\Im[p\overline{q}]\right), \tag{116}$$

where $\Im$ is the imaginary part and

$$
\begin{aligned}
\gamma_1 =& 384\alpha^3(8\alpha^4\cosh(4\alpha) + 12\alpha^2\sinh(2\alpha)^2 - \sinh(2\alpha)^4 \\
& - 8\alpha^3(\alpha + \sinh(4\alpha))), \\
2\gamma_1 Q_1 =& -(8\alpha(3+16\alpha^2)(-9+24\alpha^2+64\alpha^4) - 32\alpha(-9 \\
& + 36\alpha^2 + 240\alpha^4 + 256\alpha^6)\cosh(4\alpha) + 24\alpha(-3 \\
& + 72\alpha^2 + 128\alpha^4)\cosh(8\alpha) + (45 + 32\alpha^2(27 \\
& + 108\alpha^2 + 640\alpha^4 + 256\alpha^6))\sinh(4\alpha) - 4(9 \\
& + 4\alpha^2(27 + 252\alpha^2 + 64\alpha^4))\sinh(8\alpha) \\
& + 9\sinh(12\alpha)), \\
2\gamma_1 Q_2 =& -8\alpha(-9 - 432\alpha^2 - 288\alpha^4 + 512\alpha^6)\cosh(2\alpha) \\
& + 4\alpha(-27 - 936\alpha^2 - 576\alpha^4 + 1024\alpha^6)\cosh(6\alpha) + \\
& 36(\alpha + 8\alpha^3)\cosh(10\alpha) - 4(45 + 4\alpha^2(297 + 780\alpha^2 \\
& + 1536\alpha^4 + 640\alpha^6))\sinh(2\alpha) - 2(-45 + 4\alpha^2(-243 \\
& + 4\alpha^2(-231 + 64\alpha^2(2+\alpha^2))))\sinh(6\alpha) - 6(3 \\
& + 36\alpha^2 + 16\alpha^4)\sinh(10\alpha)), \\
\gamma_1 Q_3 =& -((-12\alpha(9 + 56\alpha^2 + 64\alpha^4) - 16\alpha(-9 - 44\alpha^2 \\
& - 48\alpha^4)\cosh(4\alpha) + 4\alpha(-9 - 8\alpha^2)\cosh(8\alpha) \\
& - 16\alpha^2(9 + 72\alpha^2 + 32\alpha^4)\sinh(4\alpha) \\
& + 72\alpha^2\sinh(8\alpha)), \\
\gamma_2 =& (-4\sinh(2\alpha)^3 + 16\alpha^2(-4\alpha\cosh(2\alpha) \\
& + (3 + 4\alpha^2)\sinh(2\alpha))), \\
\gamma_2 F_1 =& \alpha((3 - 48\alpha^2 + 64\alpha^4)\cosh(2\alpha) - 3\cosh(6\alpha) \\
& + 16\alpha(3 + 4\alpha^2)\sinh(2\alpha)), \\
\gamma_2 F_2 =& (2\alpha(-3 + 16\alpha^2 + 32\alpha^4 + (3 + 8\alpha^2)\cosh(4\alpha) \\
& - 12\alpha\sinh(4\alpha)), \\
\gamma_2 F_3 =& -((16\alpha^2(36\sinh(2\alpha)^3 + 2\alpha((9 + 144\alpha^2 + 64\alpha^4) \\
& \times \cosh(2\alpha) - 9\cosh(6\alpha) + 4\alpha(-3(7 \\
& + 8\alpha^2)\sinh(2\alpha) + \sinh(6\alpha))))).
\end{aligned}
\tag{117}
$$

This allowed to rewrite Eq. 96 as

$$\begin{aligned} H_{\max} =& \Phi \left\{ F_2 - \frac{\alpha}{b} - \frac{Re^2 Q_2}{48 b^2} \right\} - \Theta \left\{ F_1 - \frac{\alpha\, a}{b} - \frac{Re^2 Q_1}{48 b^2} \right\} \\ &+ \Im[p\overline{q}] \left\{ k\, F_3 - \frac{Re^2}{48 b^2} \frac{1}{k} Q_3 \right\} \\ =& \Phi \left\{ F_2 - \frac{\alpha}{b} - \frac{Re^2 Q_2}{48 b^2} \right\} - \Theta \left\{ F_1 - \frac{\alpha\, a}{b} - \frac{Re^2 Q_1}{48 b^2} \right\} \\ &+ \Im[p\overline{q}] \left\{ \frac{Re}{96 \alpha^2 b} F_3 - \frac{2\alpha^2 Re}{b} Q_3 \right\}. \end{aligned} \tag{118}$$

The conditions for no-growth were obtained by looking for the region in the wavenumber-Reynolds space were $H_{\max} \leq 0$. In the case of the plane Couette flow, this was done via a numerical optimization procedure on the right-hand side of Eq. 118 as described below. Results are shown in figures 35,37, and 38.

We proceeded as follows. Supposing the existence of a limit curve $Re_\Omega(\alpha)$, which separates the region where $H_{\max} > 0$ from the region where $H_{\max} < 0$, we fixed the wavenumber α and looked for the Reynolds number for which $H_{\max} = 0$ over all the possible boundary terms p and q. This was done through the genetic optimization Fortran 90 algorithm based on the open source software PIKAIA [27, 28] already introduced in §2.4. An appropriate range for the parameters p and q was set, so that increments of the numerical range for p and q had no influence on the result. The functional (fitness function) to be minimized was $|H_{\max}|$. We chose a set of wavenumbers and performed the computation by optimizing over p, q and Re . The Reynolds number associated with the minimum of $|H_{\max}|$ from this procedure is represented by black bullets in figure 35.

3.5.2 *Plane Poiseuille flow: sufficient conditions for no enstrophy growth. Analytical method and final numerical optimization.*

Here conditions for no enstrophy growth are found for the plane Poiseuille flow. We recall that the following analytic procedure for PPF was also present in Synge [126] and it was here adopted to the non-modal formulation. Let's consider Eq. 94 with $U' = -2y$. The solution to the homogeneous equation is the same as the Couette flow:

$$\begin{aligned} \widehat{\ }_{m_H} =& \left[a_0 + a_1(1-y) + a_2(1-y)^2 \right] \sinh[\alpha(1+y)] \\ &+ \left[b_0 + b_1(1+y) + b_2(1+y)^2 \right] \sinh[\alpha(1-y)]. \end{aligned}$$

The forcing term differs from the PCF case due to the presence of U' in the right-hand side. We sought for a particular solution in the following form:

$$\begin{aligned}\widehat{\ }_{m_P} = &- ik\left\{p\left[\alpha y^4\sinh[\alpha(1+y)] - 6y^3\cosh[\alpha(1+y)]\right]\right.\\ &\left.+q\left[\alpha y^4\sinh[\alpha(1-y)] + 6y^3\cosh[\alpha(1-y)]\right]\right\}.\end{aligned} \tag{119}$$

The complex constants a_i and b_i have been determined by imposing the boundary conditions: vanishing $\widehat{\ }$ and $\partial_y\widehat{\ }$, and assigned values of $\partial_y^2\widehat{\ }$. Direct calculation yields the following expressions:

$$\begin{aligned}a_0 =& ik\left(S_0p + T_0q\right),\\ b_0 =& ik\left(T_0p + S_0q\right),\\ a_1 =& \left(W_1 + ikS_1\right)p + \left(V_1 + ikT_1\right)q,\\ b_1 =& \left(V_1 + ikT_1\right)p + \left(W_1 + ikS_1\right)q,\\ a_2 =& \left(W_2 + ikS_2\right)p + \left(V_2 + ikT_2\right)q,\\ b_2 =& \left(V_2 + ikT_2\right)p + \left(W_2 + ikS_2\right)q,\end{aligned} \tag{120}$$

where real functions of α are involved:

$$\begin{aligned}&=\tfrac{1}{4}\alpha^{-2}b^4 - 3b^2 + 4\alpha ab - 4\alpha^2b^2,\\ W_1 =& \ {}^{-1}(-b + 2\alpha a), \quad V_1 = \ {}^{-1}(-\tfrac{1}{2}\alpha^{-1}b^2 + 2\alpha),\\ W_2 =& \ {}^{-1}(\tfrac{1}{8}\alpha^{-2}b^3 - \alpha a),\\ V_2 =& \ {}^{-1}(\tfrac{1}{2}\alpha^{-1}b^2 - \tfrac{1}{2}ab - \alpha),\\ S_0 =& -6ab^{-1} + \alpha, \quad T_0 = 6b^{-1},\\ S_1 =& \ {}^{-1}\left[\tfrac{9}{2}\alpha^{-2}ab^3 - \alpha^{-1}b^2(12 + b^2) - 6ab\right.\\ &\left.+ 4c(6 + 7b^2) - 72\alpha^2ab + 16\alpha^3b^2\right],\\ T_1 =& \ {}^{-1}\left[-\tfrac{9}{2}\alpha^{-2}b^3 + 12\alpha^{-1}ab^2 + 6b - 4b^3 - 24\alpha a - 8\alpha^2b\right],\\ S_2 =& -\tfrac{9}{2}\alpha^{-1} + 3ab^{-1} - \tfrac{1}{2}S_1 + \tfrac{1}{4}\alpha^{-1}bT_1,\\ T_2 =& \tfrac{9}{2}\alpha a - 3b^{-1} - b - \tfrac{1}{4}\alpha^{-1}bS_1 + \tfrac{1}{2}T_1,\end{aligned} \tag{121}$$

where $a = \cosh(2\alpha)$ and $b = \sinh(2\alpha)$.
Once the maximizing perturbation $\widehat{\ }_m$ is known, it is possible to evaluate the maximal enstrophy rate 96. As done for PCF, B and $\left[\partial_y^2\widehat{\ }_m\partial_y^3\bar{\ }_m + \partial_y^2\bar{\ }_m\partial_y^3\widehat{\ }_m\right]_{-1}^{1}$ have been evaluated. Given $\widehat{\ }_m$,

$$\begin{aligned}\int_{-1}^{1}\widehat{\ }_m y\cosh[\alpha(1+y)]\,\mathrm{d}y &= (P_1 + ikQ_1)p - (P_2 + ikQ_2)q,\\ \int_{-1}^{1}\widehat{\ }_m y\cosh[\alpha(1-y)]\,\mathrm{d}y &= (P_2 + ikQ_2)p - (P_1 + ikQ_1)q,\end{aligned} \tag{122}$$

where P_1, P_2 are real constants and Q_1, Q_2, are in terms of the constants just reported by:

$$\begin{aligned}
Q_1 =& \tfrac{1}{2}L_1\left\{a\left(S_0+S_1+S_2\right)-\left(T_0+T_1+T_2\right)\right\}\\
&-\tfrac{1}{2}bL_2\left(S_1+2S_2\right)+\tfrac{1}{2}L_3\left(aS_2-T_2\right)+3aL_4\\
&-\tfrac{1}{2}\alpha aL_5+\tfrac{6}{5}a+\tfrac{1}{3}b\left(T_1+2T_2\right),\\
Q_2 =& \tfrac{1}{2}L_1\left\{S_0+S_1+S_2-a\left(T_0+T_1+T_2\right)\right\}\\
&+\tfrac{1}{2}bL_2\left(T_1+2T_2\right)+\tfrac{1}{2}L_3\left(S_2-aT_2\right)+3L_4\\
&-\tfrac{1}{2}\alpha L_5+\tfrac{6}{5}a-\tfrac{1}{3}b\left(S_1+2S_2\right),
\end{aligned} \tag{123}$$

where

$$L_n=\int_{-1}^{1}y^n e^{2\alpha y}\,\mathrm{d}y,\quad n=1,2,\ldots.$$

Then, by direct calculation

$$B=-4ik\left(Q_1\Theta-Q_2\Phi\right), \tag{124}$$

$$\left[\partial_y^2\,\widehat{}_m\partial_y^3\,\bar{}_m+\partial_y^2\,\bar{}_m\partial_y^3\,\widehat{}_m\right]_{-1}^{1}=2\left(F_1\Theta-F_2\Phi\right), \tag{125}$$

where

$$F_1=\ {}^{-1}\Big(\frac{3}{4}ab^3\alpha^{-1}-3b^2+3\alpha ab-4\alpha^2b^2-4\alpha^3ab\Big), \tag{126}$$

$$F_2=\ {}^{-1}\Big(\frac{3}{4}b^3\alpha^{-1}-3ab^2+\alpha b(3+2b^2)+4\alpha^3b\Big). \tag{127}$$

Substituting Eqs. 124 and 125 in Eq. 96, we eventually obtained

$$H_{\max}=-\Theta(t)\Big\{F_1-\frac{\alpha a}{b}-\frac{Re^2Q_1}{48b^2}\Big\}+\Phi(t)\Big\{F_2-\frac{\alpha}{b}-\frac{Re^2Q_2}{48b^2}\Big\}, \tag{128}$$

which is an explicit function of Re, of the wavenumber α through a, b, F_1, F_2, Q_1, Q_2, and of the boundary terms $p=\partial_y^2\,\widehat{}_m(1,t), m=\partial_y^2\,\widehat{}_m(-1,t)$ through Θ and Φ. Note that the expression 128 for the Poiseuille flow appears less complicated than the analogous found for the Couette flow, 118. This simplification allows to solve the problem for PPF in an analytical way, as shown in the following subsection.

From the definitions 89 one can note that $\Theta\geq 0$, $\Phi^2\leq\Theta^2$ for all times t and for any complex value of p and q. We see from 128 that it is possible to have $H_{\max}\leq 0$ for disturbances of wavelength $\lambda=2\pi/\alpha$ if Re satisfies the two conditions:

$$\left.\begin{aligned}
&\frac{Re^2Q_1}{48b^2}\leq F_1-\frac{\alpha a}{b},\\
&\left[F_2-\frac{\alpha}{b}-\frac{Re^2Q_2}{48b^2}\right]^2\leq\left[F_1-\frac{\alpha a}{b}-\frac{Re^2Q_1}{48b^2}\right]^2
\end{aligned}\right\}, \tag{129}$$

where all the constants have already been defined.
To discuss these inequalities, we have to know the sign of , as defined in 121. By expanding in series, one note that all coefficients are positive and therefore is positive. Writing $\xi = 2\alpha$ so that $a = \cosh\xi$, $b = \sinh\xi$, and substituting 121 in 123:

$$\begin{aligned}
Q_1 =& \frac{1}{\xi^7} b\Big\{ a(A'_0 + A'_2 b^2 + A'_4 b^4) + \xi b(B'_0 + B'_2 b^2 + B'_4 b^4)\Big\},\\
A'_0 =& -624\xi^4 - 80\xi^6 - \tfrac{8}{5}\xi^8,\\
A'_2 =& -1260\xi^2 - 1296\xi^4 - 148\xi^6 - \tfrac{4}{3}\xi^8,\\
A'_4 =& 204 + 12\xi^2,\\
B'_0 =& 1668\xi^2 + 672\xi^4 + \tfrac{252}{5}\xi^6 + \tfrac{4}{5}\xi^8,\\
B'_2 =& 12 + 1628\xi^2 + \tfrac{2856}{5}\xi^4 + \tfrac{64}{3}\xi^6,\\
B'_4 =& -96,
\end{aligned} \tag{130}$$

and

$$\begin{aligned}
Q_2 =& \frac{1}{\xi^7} b\Big\{ A''_0 + A''_2 b^2 + A''_4 b^4 + \xi ab(B''_0 + B''_2 b^2)\Big\},\\
A''_0 =& -624\xi^4 - 80\xi^6 - \tfrac{8}{5}\xi^8,\\
A''_2 =& -1260\xi^2 - 1404\xi^4 - 228\xi^6 - \tfrac{124}{15}\xi^8,\\
A''_4 =& 204 - 312\xi^2 - 108\xi^4 - \tfrac{4}{3}\xi^8,\\
B''_0 =& 1668\xi^2 + 674\xi^4 + \tfrac{252}{5}\xi^6 + \tfrac{4}{5}\xi^8,\\
B''_2 =& 12 + 248\xi^2 + \tfrac{96}{5}\xi^4.
\end{aligned} \tag{131}$$

From Eq. 126:

$$\begin{aligned}
\left(F_1 - \frac{\alpha a}{b}\right) =& \xi^{-1} ab(3\xi^2 + b^2) - \xi^2 - b^2(3 + 2\xi^2),\\
\xi \quad \left(F_2 - \frac{\alpha}{b}\right) =& b(3\xi^2 + \xi^4) + b^3(1 + \xi^2) - a\xi(\xi^2 + 3b^2).
\end{aligned} \tag{132}$$

To solve the inequalities 129, it is convenient to define a function $\chi(\xi, \eta)$ with $\eta = 0, \pm 1$ by

$$\chi(\xi, \eta) = \frac{F_1 - \alpha a b^{-1} + \eta\left(F_2 - \alpha b^{-1}\right)}{Q_1 b^{-2} + \eta Q_2 b^{-2}}. \tag{133}$$

Then, considering that $Q_1 > 0$, $Q_1 + Q_2 > 0$, $Q_1 - Q_2 > 0$, the first of 129 can be written as:

$$\frac{Re^2}{48} \leq \chi(\xi, 0). \tag{134}$$

The second inequality of 129 becomes

$$\left\{\frac{Re^2}{48} - \chi(\eta, 1)\right\}\left\{\frac{Re^2}{48} - \chi(\eta, -1)\right\} \geq 0. \tag{135}$$

Hence we see that we have $\mathrm{d}\Omega/\,\mathrm{d}t \leq 0$ if:

- $\frac{Re^2}{48}$ does not exceed $\chi(\xi, 0)$;
- $\frac{Re^2}{48}$ is not between $\chi(\xi, -1)$ and $\chi(\xi, 1)$.

The three functions $Re = [48\chi(\xi, 0)]^{\frac{1}{2}}$; $[48\chi(\xi, +1)]^{\frac{1}{2}}$; $[48\chi(\xi, -1)]^{\frac{1}{2}}$ correspond to the black curves in figure 35 (**b**). The region where small perturbations can experience transient enstrophy growth is the yellow region in the same figure. Equation 128 was also solved numerically as described in the above section for the Couette case, see the dotted curve in figure 35 (**b**). The nice match with the results from the two analytical conditions above allowed us to validate the algorithm in order to solve the problem 118 for the plane Couette flow, where analytical inequalities were not available.

3.6 **Final remarks**

For linear, viscous, incompressible, 2D waves in the plane Couette and Poiseuille flows, the exact lower bound for enstrophy algebraic growth ($Re_\Omega(\alpha)$) was determined. In particular, we explored the wavenumber and Reynolds number parameters space in the region $\alpha \in [0.01, 10], Re \in [10, 10^5]$. This result was obtained by adapting the analytical modal procedure conceived by the mathematician J. L. Synge in late 1930s to the initial-value (non-modal) problem. It should be noted that after Synge's work, which was framed in the modal theory, no other analysis have been conducted on the integral enstrophy evolution. This happened because the vorticity boundary conditions on solid walls are not physically known. To overcome this difficulty, Synge proposed a procedure based on the concomitant parameterization of the unknown boundary terms and the optimization of the perturbation's vorticity rate. Unfortunately, the procedure has not been exploited in the following years because of its computationally difficult implementation.

We believe that this methodology could also be exploited for other physical/mathematical problems where the boundary conditions are unknown. It should be noted that together with the determination of the above mentioned lower bound, with this study it is also possible to deduce the wall values on the vorticity. A fact that can be of interest for applications (for instance in the flow-control technology).

The new Reynolds number threshold for the enstrophy transient growth is a function of the wavenumber, $Re_\Omega = Re_\Omega(\alpha)$. We found that this bound is closer - with respect to the kinetic energy one, Re_E, to the region of the map where nonlinear coupling can be expected, that is $Re_\Omega(\alpha) > Re_E(\alpha), \forall\alpha$. Moreover, this proves that the growth of kinetic energy is not a necessary condition for the vorticity growth. With this study we

also give information on the scaling laws for the maximal kinetic energy and enstrophy growth and the related time scales. We highlight that Poiseuille and Couette maps differ more in the enstrophy rather than in the kinetic energy. Inside the region of the map were both the wave kinetic energy and the enstrophy can grow, smooth initial conditions - optimized to maximize the initial kinetic energy rate - show a comparatively much more intense amplification of their integral enstrophy. We suggest therefore that the occurrence of the nonlinear coupling can be better looked at in terms of the enstrophy rather than in terms of the wave kinetic energy content. At the same time, we stress that the propagation properties of small internal waves (in particular the dispersion/non-dispersion dual nature) should be considered jointly with the wave-amplitude growth, in order to better understand the onset non-linear coupling.

Future analysis will focus first on deeper investigating the shape of the optimal stream-function $\widehat{\ }_m$ and on the values taken by the boundary terms $\left[\partial_y^2 \widehat{\ }_m \partial_y^3 \bar{\ }_m + \partial_y^2 \bar{\ }_m \partial_y^3 \widehat{\ }_m\right]_{-1}^{1}$, which can now be obtained from the optimal stream-function whose expression has been analytically computed. This will likely provide useful information to understand the conditions leading to the maximal enstrophy growth, for arbitrary values of the flow control parameter and the wavenumber. Secondly, the analysis will be extended to the three-dimensional case.

P.1 BIBLIOGRAPHY

[1] F. De Santi, F. Fraternale, and D. Tordella. "Dispersive-to-nondispersive transition and phase-velocity transient for linear waves in plane wake and channel flows." In: *Phys. Rev. E* 93.3 (2016). DOI: 10.1103/PhysRevE.93.033116 (cit. on p. 7).

[2] R. V. Abramov and A. J. Majda. "Statistically relevant conserved quantities for truncated quasigeostrophic flow." In: *PNAS* 100.7 (2003), pp. 3841–3846. DOI: 10.1073/pnas.023045110 (cit. on p. 86).

[3] F. Fraternale, L. Domenicale, G. Staffilani, and D. Tordella. "Linear waves in sheared flows. Lower bound of the vorticity growth and propagation discontinuities in the parameters space." In: *Submitted, preprint version on Arxiv* (2017). URL: https://arxiv.org/abs/1611.02964 (cit. on p. 8).

[4] F. Fraternale, G. Nastro, and D. Tordella. "Existence of niches of non-dispersion for long perturbation waves in the Poiseuille flow." In: *In preparation* () (cit. on pp. 8, 41, 83).

[5] F. Alavyoon, D. S. Henningson, and P. H. Alfredsson. "Turbulent spots in plane Poiseuille flow–flow visualization." In: *Phys. Fluids* 29.4 (1986), pp. 1328–1331. DOI: 10.1063/1.865884 (cit. on pp. 67, 68).

[6] L. Domenicale, F. Fraternale, G. Staffilani, and D. Tordella. "Perturbation enstrophy decay in Poiseuille and Couette flows according to synge's method." In: *Bulletin of the American Physical Society - 68th Annual Meeting of the APS Division of Fluid Dynamics*. Vol. 60. 21. Boston, MA, USA, Nov. 2015. URL: http://meetings.aps.org/link/BAPS.2015.DFD.G16.2 (cit. on p. 9).

[7] F. De Santi, F. Fraternale, and D. Tordella. "Dispersive to nondispersive transition in the plane wake and channel flows." In: *Proceedings of the 15th European Turbulence Conference*. Delft, Netherlands, Aug. 2015. URL: http://www.etc15.nl/proceedings/proceedings/documents/492.pdf (cit. on p. 9).

[8] M. Asai and J. M. Floryan. "Experiments on the linear instability of flow in a wavy channel." In: *Eur. J. Mech. B/Fluids* 25.6 (2006), pp. 971–986. DOI: 10.1016/j.euromechflu.2006.03.002 (cit. on pp. 20, 21).

[9] K. Avila, D. Moxey, A. De Lozar, M. Avila, D. Barkley, and B. Hof. "The onset of turbulence in pipe flow." In: *Science* 333.6039 (2011), pp. 192–196. DOI: 10.1126/science.1203223 (cit. on p. 55).

[10] D. Barkley. "Linear analysis of the cylinder wake mean flow." In: *Europhys. Lett.* 75.5 (2006), pp. 750–756. DOI: 10.1209/epl/i2006-10168-7 (cit. on pp. 21, 22).

[11] N. S. Barlow, B. T. Helenbrook, and S. P. Lin. "Transience to instability in a liquid sheet." In: *J. Fluid Mech.* 666 (11), pp. 358–390. DOI: 10.1017/S0022112010004416 (cit. on p. 66).

[12] N. S. Barlow, B. T. Helenbrook, S. P. Lin, and S. J. Weinstein. "An interpretation of absolutely and convectively unstable waves using series solutions." In: *Wave Motion* 47.8 (2010), pp. 564–582. DOI: 10.1016/j.wavemoti.2010.04.003 (cit. on p. 66).

[13] B. J. Bayly, S. A. Orszag, and T. Herbert. "Instability mechanisms in shear-flow transition." In: *Annual Rev. Fluid Mech.* 20 (1988), pp. 359–391. DOI: 10.1146/annurev.fl.20.010188.002043 (cit. on pp. 66, 99).

[14] M. Belan and D. Tordella. "Asymptotics expansions for two dimensional symmetrical laminar wakes." In: *Z. Angew. Math. Mech.* 82.219–234 (2002) (cit. on p. 13).

[15] M. Belan and D. Tordella. "Convective instability in wake intermediate asymptotics." In: *J. Fluid Mech.* 552 (2006), pp. 127–136. DOI: 10.1017/S0022112006008627 (cit. on pp. 13, 21, 22).

[16] C. M. Bender and S. A. Orszag. *Advanced mathematical methods for scientists and engineers I: asymptotic methods and perturbation theory*. Advanced Mathematical Methods for Scientists and Engineers. Springer, 1978. ISBN: 9780387989310 (cit. on p. 44).

[17] T. Brooke Benjamin. "The development of three-dimensional disturbances in an unstable film of liquid flowing down an inclined plane." In: *J. Fluid Mech.* 10.3 (1961), pp. 401–419. DOI: 10.1017/S0022112061001001 (cit. on p. 77).

[18] D. Biau and A. Bottaro. "An optimal path to transition in a duct." In: *Phil. Trans. R. Soc. A* 367.1888 (2009), pp. 529–544. DOI: 10.1098/rsta.2008.0191 (cit. on p. 25).

[19] S. Bottin and H. Chate. "Statistical analysis of the transition to turbulence in plane Couette flow." In: *Eur. Phys. J. B* 6.1 (1998), pp. 143–155. DOI: 10.1007/s100510050536 (cit. on p. 99).

[20] S. Bottin, F. Daviaud, P. Manneville, and O. Dauchot. "Discontinuous transition to spatiotemporal intermittency in plane Couette flow." In: *Europhys. Lett.* 43.2 (1998), pp. 171–176. DOI: 10.1209/epl/i1998-00336-3 (cit. on p. 99).

[21] Luca Brandt. "The lift-up effect: The linear mechanism behind transition and turbulence in shear flows." In: *Eur. J. Mech. B/Fluids* 47 (2014), pp. 80–96. DOI: 10.1016/j.euromechflu.2014.03.005 (cit. on pp. 26, 66).

[22] K. S. Breuer and J. H. Haritonidis. "The evolution of a localized disturbance in a laminar boundary layer. Part 1. Weak disturbances." In: *J. Fluid Mech.* 220 (1990), pp. 569–594. DOI: 10.1017/S002211209000338X (cit. on p. 55).

[23] K. S. Breuer and M. T. Landahl. "The evolution of a localized disturbance in a laminar boundary-layer.2. Strong disturbances." In: *J. Fluid Mech.* 220 (1990), pp. 595–621. DOI: 10.1017/S0022112090003391 (cit. on p. 55).

[24] K. M. Butler and B. F. Farrel. "3-dimensional optimal perturbations in viscous shear flow." In: *Phys. Fluids A* 4.8 (1992), pp. 1637–1650. DOI: 10.1063/1.858386 (cit. on p. 25).

[25] E. Camporeale, T. Passot, and D. Burgess. "Implications of a non-modal linear theory for the marginal stability state and the dissipation of fluctuations in the solar wind." In: *Astrophys. J.* 715.1 (2010), pp. 260–270. DOI: 10.1088/0004-637X/715/1/260 (cit. on pp. 11, 84).

[26] D. R. Carlson, S. E. Widnall, and M.F. Peeters. "A flow-visualization study of transition in plane Poiseuille flow." In: *J. Fluid Mech.* 121.AUG (1982), pp. 487–505. DOI: 10.1017/S0022112082002006 (cit. on pp. 52, 66–68, 99).

[27] P. Charbonneau. "Genetic algorithms in astronomy and astrophysics." In: *Astrophys. J. Suppl. S.* 101.2 (1995), pp. 309–334. DOI: 10.1086/192242 (cit. on pp. 52, 112).

[28] P. Charbonneau and B. Knapp. "A User s Guide to PIKAIA 1.0." In: (1995). URL: http://www.hao.ucar.edu/modeling/pikaia/pikaia.php#sec9 (cit. on pp. 52, 112).

[29] G. Chimonas. "Algebraic disturbamces in stratified shear flows." In: *J. Fluid Mech.* 90 (1979), pp. 1–19. DOI: 10.1017/S0022112079002056 (cit. on p. 66).

[30] J. Colliander, M. Keel, G. Staffilani, H. Takaoka, and T. Tao. *Local and global well-posedness for non-linear dispersive and wave equations*. http://www.math.ucla.edu/~tao/Dispersive/. 2016 (cit. on p. 42).

[31] A. D. D. Craik. "The development of wavepackets in unstable flows." In: *P. Roy. Soc. Lond. A Mat.* 373.1755 (1981), pp. 457–476. DOI: 10.1098/rspa.1981.0004 (cit. on pp. 46, 77).

[32] A. D. D. Craik. "The growth of localized disturbances in unstable flows." In: *J. Appl. Mech.- Trans. ASME* 49.2 (1982), pp. 284–290 (cit. on pp. 46, 77).

[33] A. D. D. Craik. *Wave interactions and fluid flows*. Cambridge University Press, 1985 (cit. on pp. 11, 25).

[34] A. D. D. Craik. "On the development of singularities in linear dispersive systems." In: *J. Fluid Mech.* 538 (2005), pp. 137–151. DOI: 10.1017/S0022112005005343 (cit. on p. 94).

[35] W. O. Criminale and P. G. Drazin. "The evolution of linearized perturbations of parallel shear flows." In: *Stud. Applied Math.* 83.2 (1990), pp. 123–157 (cit. on p. 25).

[36] W. O. Criminale, T. L. Jackson, and R. D. Joslin. *Theory and Computation in Hydrodynamic Stability*. Cambridge University Press, 2003 (cit. on pp. 11, 15, 18, 26, 91).

[37] W. O. Criminale, T. L. Jackson, D. G. Lassaigne, and R. D. Joslin. "Perturbation dynamics in viscous channel flows." In: *J. Fluid Mech.* 339 (1997), pp. 55–75. DOI: 10.1017/S0022112097005235 (cit. on p. 26).

[38] W. O. Criminale and L. S. G. Kovasznay. "The growth of localized disturbances in a laminar boundary layer." In: *J. Fluid Mech.* 14.1 (1962), pp. 59–80. DOI: 10.1017/S002211206200107X (cit. on pp. 41, 46, 77).

[39] F. Daviaud, J. Hegseth, and P. Berge. "Subcritical transition to turbulence in plane Couette flow." In: *Phys. Rev. Lett.* 69.17 (1992), pp. 2511–2514. DOI: 10.1103/PhysRevLett.69.2511 (cit. on p. 99).

[40] F. De Santi, F. Fraternale, and D. Tordella. "Dispersive-to-nondispersive transition and phase-velocity transient for linear waves in plane wake and channel flows." In: *Phys. Rev. E* 93.3 (2016). DOI: 10.1103/PhysRevE.93.033116 (cit. on pp. 9–11, 21, 27, 30, 31, 33, 35–37, 46, 51, 95, 102).

[41] R. C. DiPrima and G. J. Habetler. "A completeness theorem for non-selfadjoint eigenvalue problems in hydrodynamic stability." In: *Archive for Rational Mechanics and Analysis* 34.3 (1969), pp. 218–227 (cit. on p. 10).

[42] *Dispersive Wiki*. http://wiki.math.toronto.edu/DispersiveWiki/index.php/Main_Page. 2016 (cit. on p. 42).

[43] Y. Duguet, P. Schlatter, and D. S. Henningson. "Formation of turbulent patterns near the onset of transition in plane Couette flow." In: *J. Fluid Mech.* 650 (2010), pp. 119–129. DOI: 10.1017/S0022112010000297 (cit. on pp. 42, 99).

[44] Y. Duguet, A. P. Willis, and R. R. Kerswell. "Slug genesis in cylindrical pipe flow." In: *J. Fluid Mech.* 663 (2010), pp. 180–208. DOI: 10.1017/S0022112010003435 (cit. on p. 55).

[45] J. J. Duistermaat. "Oscillatory integrals, lagrange immersions and unfolding of singularities." In: *Communications on Pure and Applied Mathematics* 27.2 (1974), pp. 207–281. DOI: 10.1002/cpa.3160270205 (cit. on p. 44).

[46] Howard W. Emmons. "The laminar-lurbulent transition in a boundary layer-Part I." In: *J. Aeronaut. Sci.* 18.7 (1951), pp. 490–498. DOI: 10.2514/8.20106 (cit. on p. 66).

[47] J. M. Floryan. "Two-dimensional instability of flow in a rough channel." In: *Phys Fluids* 17.4 (2005). DOI: 10.1063/1.1865252 (cit. on p. 21).

[48] F. Fraternale. "Frequency transient of three-dimensional perturbations in shear flows. Similarity properties and wave packets linear formation." MA thesis. Politecnico di Torino, 2013 (cit. on pp. 14, 43, 48).

[49] F. Fraternale, L. Domenicale, G. Staffilani, and D. Tordella. "Linear waves in sheared flows. Lower bound of the vorticity growth and propagation discontinuities in the parameters space." In: *Submitted, preprint version on ArXiv* (2017). URL: https://arxiv.org/abs/1611.02964 (cit. on pp. 17, 85, 96, 97, 99, 100).

[50] Uriel Frisch. *Turbulence: the legacy of A.N. Kolmogorov*. Cambridge university press, 1995. ISBN: 0-521-45713-0 (cit. on p. 86).

[51] A. P. Gallagher and A. McD. Mercer. "On the behaviour of small disturbances in plane Couette flow." In: *J. Fluid Mech.* 13.1 (1962), pp. 91–100. DOI: 10.1017/S0022112062000531 (cit. on pp. 43, 46, 48, 96, 99, 101).

[52] M. Gaster. "On the generation of spatially growing waves in a boundary layer." In: *J. Fluid Mech.* 22.3 (1965), pp. 433–441. DOI: 10.101anics7/S0022112065000873 (cit. on p. 77).

[53] M. Gaster. "Growth of disturbances in both space and time." In: *Phys. Fluids* 11.4 (1968), pp. 723–727. DOI: 10.1063/1.1691990 (cit. on pp. 46, 77).

[54] M. Gaster. "The development of three-dimensional wave packets in a boundary layer." In: *J. Fluid Mech.* 32.1 (1968), pp. 173–184. DOI: 10.1017/S0022112068000649 (cit. on pp. 41, 44, 46, 77).

[55] M. Gaster. "Series representation of eigenvalues of Orr-Sommerfeld euqation." In: *J. Comp. Phys.* 29.2 (1978), pp. 147–162. DOI: 10.1016/0021-9991(78)90148-1 (cit. on p. 46).

[56] M. Gaster. "Propagation of linear wave packets in laminar boundary layers." In: *AIAA J.* 19.4 (1981), pp. 419–423. DOI: 10.2514/3.50964 (cit. on pp. 41, 46, 77).

[57] M. Gaster. "Estimates of the errors incurred in various asymptotic representations of wave packets." In: *J. Fluid Mech.* 121 (1982), pp. 365–377. DOI: 10.1017/S0022112082001943 (cit. on p. 77).

[58] M. Gaster. "The development of a two-dimensional wavepacket in a growing boundary layer." In: *P. Roy. Soc. Lond. A Mat.* 384.1787 (1982), pp. 317–332. DOI: 10.1098/rspa.1982.0161 (cit. on p. 77).

[59] M. Gaster and A. Davey. "The development of three-dimensional wave-packets in unbounded parallel flows." In: *J. Fluid Mech.* 32.4 (1968), pp. 801–808. DOI: 10.1017/S0022112068001047 (cit. on pp. 46, 77).

[60] F. Giannetti and P. Luchini. "Structural sensitivity of the first instability of the cylinder wake." In: *J. Fluid Mech.* 581 (2007), pp. 167–197 (cit. on pp. 21, 22).

[61] C. E. Grosch and H. Salwen. "The continuous spectrum of the Orr-Sommerfeld equation. Part 1. The spectrum and the eigenfunctions." In: *J. Fluid Mech.* 87.01 (1978), pp. 33–54 (cit. on pp. 10, 11, 14, 46).

[62] C. E. Grosh and H. Salwen. "The stability of steady and time-dependent plane Poiseuille flow." In: *J. Fluid Mech.* 34 (1968), pp. 33–54 (cit. on pp. 11, 20, 21, 46).

[63] L. H. Gustavsson. "Energy growth of three-dimensional disturbances in plane Poiseuille flow." In: *J. Fluid Mech.* 224 (1991), pp. 241–260. DOI: 10.1017/S002211209100174X (cit. on pp. 11, 95).

[64] L. H. Gustavsson and L. S. Hultgren. "A resonance mechanism in plane Couette flow." In: *J. Fluid Mech.* 98 (1980), pp. 149–159. DOI: 10.1017/S0022112080000079 (cit. on p. 25).

[65] G. Hagen. "Über die Bewegung des Wassers in engen cylindrischen Röhren." In: *Annalen der Physik* 122.3 (1839), pp. 423–442. DOI: 10.1002/andp.18391220304 (cit. on p. 51).

[66] W. D. Hayes. "Conservation of action and modal wave action." In: *P. Roy. Soc. Lond. A Mat.* 320.1541 (1970), pp. 187–208. DOI: 10.1098/rspa.1970.0205 (cit. on p. 45).

[67] D. S. Henningson. "The inviscid initial value problem for a piecewise linear mean flow." In: *Stud. Appl. Math.* 78.1 (1988), pp. 31–56. DOI: 10.1002/sapm198878131 (cit. on p. 66).

[68] D. S. Henningson and P. H. Alfredsson. "The wave structure of turbulent spots in plane Poiseuille flow." In: *J. Fluid Mech.* 178 (1987), pp. 405–421. DOI: 10.1017/S0022112087001289 (cit. on pp. 67, 68).

[69] D. S. Henningson and J. Kim. "Turbulence characteristics inside a turbulent spot in plane Poiseuille flow." In: *7th Symposium on Turbulent Shear Flows, Volume 1*. Vol. 1. 1989, pp. 2–3 (cit. on p. 67).

[70] D. S. Henningson and J. Kim. "On turbulent spots in plane Poiseuille flow." In: *J. Fluid Mech.* 228 (1991), pp. 183–205. DOI: 10.1017/S0022112091002677 (cit. on pp. 67, 68).

[71] D. S. Henningson, A. Lundbladh, and A. V. Johansson. "A mechanism for bypass transition from localized disturbances in wall-bounded shear flows." In: *J. Fluid Mech.* 250 (1993), pp. 169–207. DOI: 10.1017/S0022112093001429 (cit. on pp. 16, 26, 52, 55, 67).

[72] D. S. Henningson, A. Lundbladh, and A. V. Johansson. "A mechanism for bypass transition from localized disturbances in wall-bounded shear flows." In: *J. Fluid Mech.* 250 (1993), pp. 169–207. DOI: 10.1017/S0022112093001429 (cit. on p. 25).

[73] D. S. Henningson and S. C. Reddy. "On the role of linear mechanism in transition to turbulence." In: *Phys. Fluids* 6.3 (1994), pp. 1396–1398. DOI: 10.1063/1.868251 (cit. on pp. 11, 25).

[74] D. S. Henningson, P. Spalart, and J. Kim. "Numerical simulations of turbulent spots in plane Poiseuille and boundary-layer flow." In: *Phys. Fluids* 30.10 (1987), pp. 2914–2917. DOI: 10.1063/1.866067 (cit. on p. 67).

[75] D. S. Henningson, Johansson A. V., and P. H. Alfredsson. "Turbulent spots in channel flows." In: *J. Eng. Math.* 28.1 (1994), pp. 21–42. DOI: 10.1007/BF02383603 (cit. on pp. 42, 67).

[76] T. Herbert. "Secondary instability of boundary-layers." In: *Annu. Rev. Fluid mech.* 20 (1988), pp. 487–526. ISSN: 0066-4189 (cit. on p. 66).

[77] M. Iovieno, G. Passoni, and D. Tordella. "A new large-eddy simulation near-wall treatment." In: *Phys. Fluids* 16.11 (2004), pp. 3935–3944. DOI: 10.1063/1.1783371 (cit. on p. 53).

[78] N. Ito. In: *Trans. Japan Soc. Aero. Space Sci.* 17 (1974), p. 65 (cit. on pp. 20, 21).

[79] F. Jiang. "Asymptotic evaluation of three-dimensional wave packets in parallel flows." In: *J. Fluid Mech.* 226 (1991), pp. 573–590. DOI: 10.1017/S0022112091002525 (cit. on p. 77).

[80] Javier Jimenez. "How linear is wall-bounded turbulence?" In: *Phys. FLuids* 25.11 (2013). DOI: 10.1063/1.4819081 (cit. on p. 26).

[81] Daniel D Joseph. *Stability of fluid motions vols I and II*. Springer-Verlag, 1976 (cit. on pp. 87, 94, 95).

[82] K. R. King, S. J. Weinstein, P. M. Zaretzky, M. Cromer, and N. S. Barlow. "Stability of algebraically unstable dispersive flows." In: *Phys. Rev. Fluids* 1.7 (2016). DOI: 10.1103/PhysRevFluids.1.073604 (cit. on pp. 32, 66).

[83] P. S. Klebanoff, K. D. Tidstrom, and L. M. Sargent. "The three-dimensional nature of boundary-layer instability." In: *J. Fluid Mech.* 12.1 (1962), pp. 1–34. DOI: 10.1017/S0022112062000014 (cit. on p. 66).

[84] B. G. B. Klingmann. "On transition due to three-dimensional disturbances in plane Poiseuille flow." In: *J. Fluid Mech.* 240 (1992), pp. 167–195. DOI: 10.1017/S0022112092000065 (cit. on pp. 52, 55, 67, 68).

[85] B. G. B. Klingmann and P. H Alfredsson. "Turbulent spots in plane Poiseuille flow - measurement of the velocity-field." In: *Phys. Fluids A* 2.12 (1990), pp. 2183–2195. DOI: 10.1063/1.857805 (cit. on pp. 52, 67, 68).

[86] M. T. Landahl. "Wave mechanics of breakdown." In: *J. Fluid Mech.* 56.28 (1972), pp. 775–802. DOI: 10.1017/S0022112072002654 (cit. on p. 42).

[87] M. T. Landahl. "Wave breakdown and turbulence." In: *SIAM J. App. Math.* 28.4 (1975), pp. 735–756. DOI: 10.1137/0128061 (cit. on p. 55).

[88] M. T. Landahl. "A note on an algebraic instability of inviscid parallel shear flows." In: *J. Fluid Mech.* 98.2 (1980), pp. 243–251. DOI: 10.1017/S0022112080000122 (cit. on p. 66).

[89] M. T. Landahl. "The application of kinematic wave theory to wave-trains and packets with small dissipation." In: *Phys. Fluids* 25.9 (1982), pp. 1512–1516. DOI: 10.1063/1.863930 (cit. on p. 77).

[90] D. G. Lassaigne, R. D. Joslin, and W. O. Criminale. "The transient period for boundary layer disturbances." In: *J. Fluid Mech.* 381 (1999), pp. 89–119. DOI: 10.1017/S002211209800353X (cit. on pp. 25, 26).

[91] G. Lemoult, K. Gumowski, J-L. Aider, and J. E. Wesfreid. "Turbulent spots in channel flow: An experimental study." In: *Eur. Phys. J. E* 37.4 (2014), pp. 1–11. DOI: 10.1140/epje/i2014-14025-2 (cit. on p. 42).

[92] P. Luchini. "Reynolds-number-independent instability of the boundary layer over a flat surface." In: *J. Fluid Mech.* 404 (2000), pp. 289–309. DOI: 10.1017/S0022112099007259 (cit. on p. 25).

[93] A. Lundbladh and A. V. Johansson. "Direct simulation of turbulent spot in plane couette flow." In: *J. Fluid Mech* 229 (1991), pp. 499–516. DOI: 10.1017/S0022112091003130 (cit. on pp. 66, 99).

[94] Leslie M. Mack. "A numerical study of the temporal eigenvalue spectrum of the Blasius boundary layer." In: *J. Fluid Mech.* 73 (1976), pp. 497–520 (cit. on pp. 18, 19, 46, 47).

[95] P. Manneville. "Transition to turbulence in wall-bounded flows: where do we stand?" In: *Mech. Eng. Rev.* 3.2 (2016), pp. 1–23. DOI: 10.1299/mer.15-00684 (cit. on pp. 42, 87, 94).

[96] Paul Manneville. "On the growth of laminar-turbulent patterns in plane Couette flow." In: *Fluid Dyn. Res.* 44.3 (2012). DOI: 10.1088/0169-5983/44/3/031412 (cit. on p. 99).

[97] Paul Manneville. "On the transition to turbulence of wall-bounded flows in general, and plane Couette flow in particular." In: *Eur. J. Mech B-Fluid* 49.B, SI (2015), pp. 345–362. DOI: 10.1016/j.euromechflu.2014.03.017 (cit. on pp. 55, 95, 99).

[98] A. Meseguer and L. N. Trefethen. "Linearized pipe flow to Reynolds number 10^7." In: *J. Comp. Phys.* 186.1 (2003), pp. 178–197. DOI: 10.1016/S0021-9991(03)00029-9 (cit. on pp. 11, 26, 51).

[99] M. Nishioka, S. Iida, and Y. Ichikawa. "An experimental investigation of the stability of plane Poiseuille flow." In: *J. Fluid Mech.* 72 (1975), pp. 731–751 (cit. on pp. 20, 21).

[100] M. Nishioka and H. Sato. "Measurements of velocity distributions in the wake of a circular cylinder at low Reynolds numbers." In: *J. Fluid Mech.* 65.1 (1974), pp. 97–112 (cit. on pp. 21, 22).

[101] C. Norberg. "An experimental study of the flow around a circular cylinder: Influence of aspect ratio." In: *J. Fluid Mech.* 258 (1994), pp. 287–316 (cit. on pp. 21, 22).

[102] W. McF. Orr. "The stability or instability of the steady motions of a perfect liquid and a viscous liquid. Part I." In: *Proc. R. Irish. Acad.* 27 (1907), pp. 9–68 (cit. on p. 94).

[103] W. McF. Orr. "The stability or instability of the steady motions of a perfect liquid and a viscous liquid. Part II." In: *Proc. R. Irish. Acad.* 27 (1907), pp. 69–138 (cit. on p. 95).

[104] S. A. Orszag. "Accurate solution of the Orr-Sommerfeld stability equation." In: *J. Fluid Mech.* 50.4 (1971), pp. 689–703 (cit. on pp. 46, 93, 96).

[105] S. A. Orszag and L. C. Kells. "Transition to turbulence in plane Poiseuille and plane Couette flow." In: *J. Fluid Mech.* 96.JAN (1980), pp. 159–205. DOI: 10.1017/S0022112080002066 (cit. on pp. 46, 99).

[106] P. Paranthoën, L. W. B. Browne, S. LeMasson, F. LeMasson, and J. C. Lecordie. "Characteristics of the near wake of a cylinder at low Reynolds numbers." In: *Eur. J. Mech. B/Fluids* 18.4 (1999), pp. 659–674. DOI: 10.1016/S0997-7546(99)00105-3 (cit. on pp. 21, 22).

[107] B. Pier. "On the frequency selection of finite-amplitude vortex shedding in the cylinder wake." In: *J. Fluid Mech.* 458 (2002), pp. 407–417. DOI: 10.1017/S0022112002008054 (cit. on pp. 21, 22).

[108] J. L. M. Poiseuille. "Recherches expérimentales sur le mouvement des liquides dans le stubes de trés petits diamètres, Parts I-IV." In: *C. R. Academy of Sciences* 11,12 (1949-1941), pp. 11, 961–967, 12, 112–115 (cit. on p. 51).

[109] S. C. Reddy and D. S. Henningson. "Energy growth in viscous channel flows." In: *J. Fluid Mech.* 252 (1993), pp. 209–238. DOI: 10.1017/S0022112093003738 (cit. on pp. 10, 11, 94, 95).

[110] S. C. Reddy, P. J. Schmid, and D. S. Henningson. "Pseudospectra of the Orr-Sommerfeld operator." In: *Siam J. Appl. Math.* 53.1 (1993), pp. 15–47. DOI: 10.1137/0153002 (cit. on p. 95).

[111] O. Reynolds. "An experimental investigation of the circumstances which determine whether the motion of water shall be direct or sinuous, and of the law of resistance in parallel channels." In: *Phil. Trans. R. Soc.* 174 (1883), pp. 935–982 (cit. on p. 51).

[112] J. J. Riley and M. Gad-el-Hak. *The dynamics of turbulent spots*. 1985, pp. 123–155. ISBN: 978-3-642-46543-7. DOI: 10.1007/978-3-642-46543-7_7 (cit. on p. 66).

[113] V. A. Romanov. "Stability of plane-parallel Couette flow." In: *Doklady Akademi Nauk SSSR* 196.5 (1971), pp. 1049–& (cit. on pp. 93, 96).

[114] A. Roshko. "On the Development of Turbulent Wakes from Vortex Streets." In: *NACA* 1932 (1954) (cit. on pp. 21, 22).

[115] H. Salwen, F. W. Cotton, and C. E. Grosh. "Linear stability of Poiseuille flow in a circular pipe." In: *J. Fluid Mech.* 98 (1980), pp. 273–284. DOI: 10.1017/S0022112080000146 (cit. on p. 25).

[116] H. Salwen and C. E. Grosh. "The continuous spectrum of the Orr-Sommerfeld equation. Part 2. Eigenfunction expansions." In: *J. Fluid Mech.* 104 (1981), pp. 445–465. DOI: 10.1017/S0022112081002991 (cit. on pp. 10, 25, 46).

[117] F. De Santi, S. Scarsoglio, W. O. Criminale, and D. Tordella. "Parametric perturbative study of the supercritical cross-flow boundary layer." In: *International Journal of Heat and Fluid Flow* 52 (2015), pp. 64–71. DOI: 10.1016/j.ijheatfluidflow.2014.11.007 (cit. on p. 14).

[118] S. Scarsoglio, D. Tordella, and W. O. Criminale. "An exploratory analysis of the transient and long-term behavior of small three-dimensional perturbations in the circular cylinder wake." In: *Stud. Applied Math.* 123.2 (2009), pp. 153–173 (cit. on pp. 7, 9, 11, 14, 16, 26, 28).

[119] S. Scarsoglio, D. Tordella, and W. O. Criminale. "Role of long waves in the stability of the plane wake." In: *Phys. Rev. E* 81.3, 2 (2010). DOI: 10.1103/PhysRevE.81.036326 (cit. on pp. 11, 13).

[120] P. J. Schmid and D. S. Henningson. *Stability and Transition in Shear Flows*. Springer, 2001 (cit. on pp. 11, 15, 18, 20, 26).

[121] Peter J. Schmid. "Nonmodal stability theory." In: *Annual Rev. Fluid Mech.* 39 (2007), pp. 129–162. DOI: 10.1146/annurev.fluid.38.050304.092139 (cit. on pp. 66, 91, 95).

[122] Joerg Schumacher, Paul Goetzfried, and Janet D. Scheel. "Enhanced enstrophy generation for turbulent convection in low-Prandtl-number fluids." In: *PNAS* 112.31 (2015), pp. 9530–9535. DOI: 10.1073/pnas.1505111112 (cit. on p. 86).

[123] *Stationary phase, method of the. Encyclopedia of Mathematics*. http://www.encyclopediaofmath.org/index.php?title=Stationary_phase,_method_of_the&oldid=16013. 2016 (cit. on p. 44).

[124] J. L. Synge. "Conditions satisfied by the vorticity and the stream-function in a viscous liquid moving in two dimensions between fixed parallel planes." In: *P. Lond. Math. Soc.* 40.1 (1936), pp. 23–36. DOI: doi:10.1112/plms/s2-40.1.23 (cit. on pp. 85, 86, 92, 93).

[125] J. L. Synge. "Hydrodynamical stability." In: *Semicentenn. Publ. Amer. Math. Soc.* 2 (1938), pp. 227–269 (cit. on pp. 85, 94).

[126] J. L. Synge. "The stability of plane Poiseuille motion." In: *Proc. Fifth Intern. Congress of Appl. Mechanics* 2 (1938), pp. 326–332 (cit. on pp. 85, 87, 106, 112).

[127] D. Tordella and M. Belan. "A new matched asymptotic expansion for the intermediate and far flow behind a finite body." In: *Phys. Fluids* 15.7 (2003), pp. 1897–1906. DOI: 10.1063/1.1580482 (cit. on pp. 13, 33).

[128] D. Tordella, S. Scarsoglio, and M. Belan. "A synthetic perturbative hypothesis for multiscale analysis of convective wake instability." In: *Phys. Fluids* 18.5 (2006). DOI: 10.1063/1.2201114 (cit. on pp. 13, 21, 22).

[129] L. N. Trefethen. "Wave packet pseudomodes of variable coefficient differential operators." In: *Proc. Royal Soc. A* 461.2062 (2005), pp. 3099–3122. DOI: 10.1098/rspa.2005.1500 (cit. on p. 11).

[130] L. N. Trefethen, A. E. Trefethen, S. C. Reddy, and T. A. Driscoll. "Hydrodynamic stability without eigenvalues." In: *Science* 261.5121 (1993), pp. 578–584. DOI: 10.1126/science.261.5121.578 (cit. on pp. 10, 11, 46, 93, 99).

[131] Arkady Tsinober. *An informal introduction to turbulence*. Vol. 63. Kulver Academic Publishers, 2001. ISBN: 1-4020-0110-X (cit. on p. 86).

[132] T. Tsukahara and T. Ishida. "The lower bound of subcritical transition in plane Poiseuille flow." In: *EUROMECH Colloquium EC565, Subcritical Transition to Turbulence, May 6th-9th 2014, Corsica, France*. 2014 (cit. on p. 99).

[133] F. Waleffe. "Hydrodynamic stability and turbulence - beyond transients to a self-sustaining process." In: *Stud. Applied Math.* 95.3 (1995), pp. 319–343 (cit. on p. 99).

[134] F. Waleffe. "Transition in shear flows - nonlinear normality vresus nonnormal linearity." In: *Physics of Fluids* 7.12 (1995), pp. 3060–3066. DOI: 10.1063/1.868682 (cit. on p. 99).

[135] G. B. Whitham. "A general approach to linear and non-linear dispersive waves using a Lagrangian." In: *J. Fluid Mech.* 22.2 (1965), pp. 273–283. DOI: 10.1017/S0022112065000745 (cit. on pp. 43, 45).

[136] G. B. Whitham. "Non-linear dispersive waves." In: *P. Roy. Soc. Lond. A Mat.* 283.1393 (1965), pp. 238–261. DOI: 10.1098/rspa.1965.0019 (cit. on p. 45).

[137] G. B. Whitham. *Linear and nonlinear waves*. 1974 (cit. on p. 23).

[138] C. H. K. Williamson. "Oblique and parallel modes of vortex shedding in the wake of a circular cylinder at low Reynolds numbers." In: *J. Fluid Mech.* 206 (1989), pp. 579–627. DOI: 10.1017/S0022112089002429 (cit. on pp. 21, 22).

[139] I. J. Wygnanski and F. H. Champagne. "On transition in a pipe. Part 1. The origin of puffs and slugs and the flow in a turbulent slug." In: *J. Fluid Mech.* 59.2 (1973), pp. 281–335. DOI: 10.1017/S0022112073001576 (cit. on p. 55).

[140] Akiva M. Yaglom. *Hydrodynamic instability and transition to turbulence*. Springer, 2012 (cit. on pp. 51, 87).

[141] P. K. Yeung, X. M. Zhai, and Katepalli R. Sreenivasan. "Extreme events in computational turbulence." In: *PNAS* 112.41 (2015), pp. 12633–12638. DOI: 10.1073/pnas.1517368112 (cit. on p. 86).

Part II

Internal waves and fluctuations in the solar wind at the edge of the heliosphere

PART 2 SUMMARY

Beyond any expectation, the Voyager 1 and 2 (V1, V2) spacecrafts will send data until 2025. They are providing the first and unique *in situ* measurements at the edge of the heliosphere. Waves, weak and strong turbulence, shocks, coherent structures, etc. coexist in the solar wind, and discriminating the different phenomenologies is still a challenging target.

In order to characterize the multi-scale nature of solar-wind fluctuations and identify the scales for which a power law for the energy decay applies, a spectral analysis over a wide frequency range is desirable. It should be noted that to achieve this goal the uncertainty in the spectral slope has to keep below 10%. Moreover, analysis of the outer heliosphere are needed to understand the evolution of such fluctuations in space and time. Unfortunately, data gaps represent a severe limitation to spectral analysis of solar-wind data, especially at heliocentric distances larger that 1 Astronomical Unit (AU). In fact, data from the Voyagers suffer from increasing sparsity as the probes move outward in the solar system (30% of data are missing at 5 AU, 70-97% in the heliosheath).

Given the issues stated above, the first stage of our research was aimed at computing reliable power spectra on the widest range of frequencies considered at present ($6.5 \cdot 10^{-8} - 10^{-2}$ Hz) from Voyagers data, at 5 AU (pre-Jupiter). These broadband spectra comprise the large-scale energy-injection and the inertial regimes of turbulence, and allow one to highlight changes in the spectral index. Opportune signal filtering is needed to interpret the low-frequency part of the spectrum, in order to distinguish the contribution of shocks, local trends and large-scale convected structures from active fluctuations (Burlaga, Mish and Roberts, *J. Geophys. Res.*, 1989).

From the velocity and the magnetic field components, we identify a possible inertial range at about $f > 2 \cdot 10^{-5}$ Hz and $f > 5 \cdot 10^{-5}$ Hz respectively, where the contribution of shocks in terms of spectral energy is lower than 40%. The -1.67 slope in the kinetic energy is in line with predictions of an evolution towards an asymptotic state dominated, at these scales, by nonlinear interactions (Roberts *J. Geophys. Res.*, 2010). This was also confirmed by a dedicated study on magnetic helicity and cross-helicity at 5 and 29 AU, published in the *Eur. J. Mech. B-fluids*, 2016 [3], which highlighted a decrease of Alfvénic fluctuations with the heliocentric distance, together with a tendency toward energy equipartition, at least at the small scales. The magnetic energy shows slightly faster decay ($\alpha \sim -1.8$). A $1/f$ scaling law was observed before the spectral breaks. This is typical of Alfvénic, imbalanced wave fluctuations of wind streams originating from

the Sun and observed also at 1 AU (see Wicks et al, *Astrophys J.*, 2013). The spectral break should move to lower frequencies with increasing radial distance as the velocity and magnetic field correlation diminishes, which is showed by our results published in *Physica Scripta*, 2016 [1] and extended in *J. Geophys. Res. Space Physics*, 2016 [2], also highlighted by the ArXiver wordpress. This part of the research is reported in Chapter 4.

A second part of our solar-wind investigation, subject of Chapter 5, focuses on magnetic field fluctuations in the heliosheath. Many observations in the heliosheath are not completely understood, as outlined by Richardson & Decker, *Astrophys. J.*, 2014, and Opher, *Space Sci. Rev.*, 2015. One of these is the discrepancy in the fluxes of energetic ions and electrons observed at V1 and V2. Particles transport and acceleration properties could be highly dependent on the region of space. In fact, researchers hypothesized the existence of a low-latitudes, turbulent, magnetically sectored heliosheath region (SHS), and a high-latitudes, laminar, unipolar region (UHS) (Opher *et al.*, *Astrophys. J.*, 2011 and Hill *et al.*, *Astrophys. J.*, 2014).

We put special focus on spectral analysis of different periods of several months for V2 (during 2007-2014) and V1 (2005-2012), based on SHS and UHS regions. To our knowledge, magnetic power spectra in the heliosheath from high-resolution (up to 48 s) data have not yet been reported in the literature. Such spectra show a flatter low-frequency range ($f < 10^{-5}$ Hz), a steeper intermediate range (about $10^{-5} < f < 3 \cdot 10^{-4}$ Hz) and a flatter hi-frequency range ($3 \cdot 10^{-4} < f < 10^{-2}$ Hz). Given the distance, greater than 100 AU, surprisingly a f^{-1} range manifest up to $f = 10^{-5}$ Hz, similarly to what observed in the solar wind upstream of the termination shock. This may suggest, in terms of deduction and not as a direct inference, the presence of large-scale Alfvén waves in the heliosheath, which are difficult to detect due to the lack of accurate velocity data. Even here, the spectral break indicates the beginning of an inertial range with a slope about -1.75. Differences between V1 and V2 increase considerably after 2009; for V1, fluctuations of the magnetic field orientation are much lower than for V2. Such differences are reflected in a different structure of the spectra: for V1 the slope is around -2 while V2 keeps a slower decay rate, about -1.7. The field at V1 also shows higher anisotropy, due to the higher energy of magnetic field fluctuations along the tangential component with respect to V2. Unfortunately, at the current stage of research the difference cannot be only addressed to the different physics presumably present in the SHS and UHS. These results were shown at the international conferences [5, 8, 10, 11], and a journal paper is in preparation [4].

As regards the methodology, the *Blackman-Tukey* method has been widely used in the literature. However, for large amounts of missing data, this computation suffers from poor convergence to the true correlation function, leading to incorrect spectral slopes and unphysical peaks in the power spectrum. Instead, we tested other techniques

and proposed in particular the following two: (i) *Compressed sensing* spectral estimation - adopted from the telecommunication area. (ii) Model-spectra from genetic optimization procedure. For the details, we remind at two papers published by our group [1, 2]. The first technique is innovative in terms of application (to our knowledge is was the first time the compressed sensing was applied to solar-wind data); the second, in terms formulation of an iterative/optimization procedure aimed at minimizing the uncertainty of the correlation method coupled to linear interpolation (results were shown at the conferences [5, 8, 10, 11]). The quality of each technique was verified on reference synthetic data sets prepared by us, with known spectral properties. Solar-wind contiguous data (Ulysses measurements in 1990-1991) were also considered as an alternative test base. In order to estimate the spectral error for each methodology, the same distribution of gaps as in Voyager data was projected on the reference signal. Exploiting the strengths of each technique, we managed to limit the uncertainty of the spectral slope below 10% in any frequency range, for the details see §4.5 and §5.2 and also section 3 in ref. [2].

Even though the spectral analysis provides precious information on the multi-scale structure of the field, further investigations are needed to draw conclusions on the nature of heliosheath fluctuations at the various scales. A multifractal analysis of the dissipation rate of magnetic field from high-resolution data was set up and preliminary results have been shown at the EPFDC conference [8] (see §5.5). This allows a comparison with the scaling properties of neutral fluid turbulence (see Meneveau & Sreenivasan, *Nuc. Phys. B*, 1987). Moreover, in the future, numerical simulations should be performed in order to understand the three-dimensional morphology of the fluctuation field. We believe that the present analysis will constitute a useful support for the numerical simulations. Our hope is that they will turn out to be important for modeling and understanding the heliopause, and we are happy that interest in this direction has already been shown (N. Pogorelov and T. Kim, private communication).

This part of my doctoral study was framed in the context of a Progetto MITOR[1,2] (MISTI-Seeds funds, supported by the Compagnia di San Paolo), which relied on the partnership started in 2013 between J. D. Richardson, J. W. Belcher (MIT Kavli Institute for Astrophysics and Space Research), D. Tordella, M. Iovieno (Politecnico di Torino) and M. Opher (Boston University).

1 MISTI-Seeds MITOR project “Laboratory simulation of planet-solar wind and interstellar medium/heliosphere interactions" 2012-2015

2 MISTI-Seeds MITOR project “Spectral analysis of the solar wind beyond the termination shock - interstellar medium/heliosphere interactions" 2015-2016.

4

SOLAR WIND FLUCTUATIONS UPSTREAM OF THE TERMINATION SHOCK. SPECTRAL ANALYSIS OF VOYAGER 2 DATA

This chapter reports the analysis of solar wind (SW) plasma and magnetic field fluctuations measured by the Voyager 2 spacecraft near 5 astronomical units (AU) from the Sun, just before the encounter with the Jupiter magnetosphere, and near 29 AU before the encounter with Neptune. Part of this study is dedicated to the spectral recovery methods that have been developed or adapted to this context, with the aim of obtaining the required accuracy for spectral analysis.

The material in this chapter is based on three publications from our group: Fraternale *et al.*, Phys. Scripta (2016) [53]; Gallana *et al.*, J. Geophys. Res. Space Physics (2016) [57]; Iovieno *et al.* (2016) [67], in full compliance with the journal policy.

4.1 **Summary**

The Voyagers spacecrafts (V1, V2) are the farthest man-made objects ever launched from Earth. Launched in 1977 (V2 on August 20, V1 on September 5) within the NASA program "Voyager Interstellar Mission"[1], they have been surfing the heliosphere and collecting solar wind data for 40 years now and, beyond any expectation, they will likely be operative until 2025. Since the crossing of the termination shock at 94 AU from the Sun (December 2004), V1 traveled inside the heliosheath and ultimately crossed the heliopause on August 2012, at about 120 AU. It is now flying as far as 139 AU, 35° North above the ecliptic, at 17 km/s speed. V2 instead crossed the termination shock at 84 AU (August 2007) and it is still inside the heliosheath, at 115 AU.
Solar wind fluctuations are disordered and involve a huge range scales and a number of different physical phenomena. Moreover, the turbulent wind evolves with the heliocentric distance, in a way which is not fully understood. Spectral analysis from data recorded *in loco* at larger distances than 1 astronomical unit are desirable but few, due to the increasing loss of data points in the signals with the distance.

This fact represents the major challenge to spectral analysis. We show indeed that the computed spectra typically inherit the frequency-domain characteristics of the sequence

1 Details on the Voyager Interstellar Mission can be found here: `https://voyager.jpl.nasa.gov/mission/interstellar.html`

of data gaps. In particular, for turbulence data sets with intermediate sparsity, the spectral index (the exponent of the power-law) is underestimated and discrete unphysical peaks are visible.

We have analyzed the solar wind velocity, density, and magnetic field fluctuations by means of six techniques for spectral analysis of nonuniform data: (i) averaged Fast Fourier Transform of linearly interpolated small subsets; (ii) correlation method without data interpolation (Blackman-Tukey); (iii) correlation of linearly interpolated data; (iv) maximum likelihood data recovery; (v) the novel compressed sensing spectral estimation; (vi) iterative optimization procedure based on (iii), mainly used for heliosheath analysis, see Chapter 5. We show that it is possible, even for the Voyager gapped measurements, to get an error on the spectral index smaller than 5%. This is necessary to distinguish the different multi-scale phenomena inside the wind. Tests have been performed on both synthetic turbulence data and on contiguous data from *Ulysses* measurements.

This study shows that it is feasible to obtain accurate power spectra at 5 AU form V2 gapped solar wind data, on a wide frequency range (more than five decades). We investigated the spectral decay exponents and their variations with the frequency, and other spectral properties such as micro and integral scales. Moreover, by considering data at 5 AU and 29 AU, a study was dedicated to the evolution of magnetic helicity and cross helicity.

4.2 Introduction

The solar wind is a flow of supersonic, collisionless, magnetized plasma which fills the heliosphere from the Solar corona to the termination shock (TS) at about 100 AU. Beyond this shock, the flow enters the heliosheath (HS), a subsonic region where the flows heats up and interacts with the gas of the local interstellar medium (LISM). The heliopause is the boundary between the solar wind plasma and the LISM plasma (these outer regions will be the subject of the next chapter). The very first indications of the existence of the solar wind go back to the observations of comets dust tail by Kepler in 1600s (now we know the existence of both a dust tail and a ion one). The development of the supersonic SW theory is due to Parker, which in 1958 found the equilibrium conditions for the corona, which require the presence of an outflow of plasma. Moreover, he found the structure of the heliospheric background magnetic field, which is actually referred to as the *Parker spiral* [108, 109]. This magnetic field topology is due to the fact that in the corona the magnetic energy is lower than the thermal energy ($\beta < 1$). This binds the magnetic fields lines to a surface at about 1 R_{sun} from the photosphere. Conversely, above this surface the thermal pressure is dominant ($\beta > 1$) and the magnetic field lines are dragged radially outward by the wind throughout the heliosphere. This determines the shape of the interplanetary magnetic field (IMF),

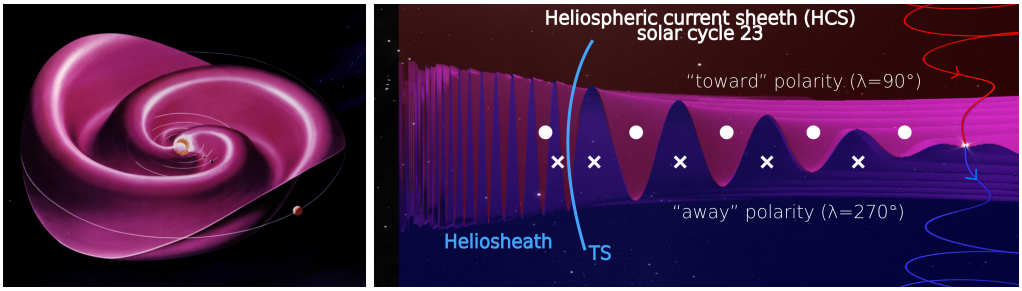

Figure 40: Representation of the heliospheric current sheet. The right panel shows the folded structure of the heliospheric current sheet, together with the magnetic field polarity during the solar cycle 23 (ending in 2008). This was the polarity measured by the Voyagers in the heliosheath region, in the period 2005-2012, due to the delay until 2013 of the solar polar magnetic field reversal for cycle 24, which is the current one. At the termination shock (TS) the plasma slows down to a subsonic regime and it is compressed, so the density, temperature, and magnetic field magnitude all increase. The sector spacing decreases after TS to about 2 AU. Credits: NASA `http://www.swpc.noaa.gov/phenomena/solar-wind`.

whose polarity switches across the heliospheric current sheet (HCS). In fact, above the HCS the solar wind typically has a dominant magnetic polarity, while below the polarity is opposite, see figure 40. A spacecraft located close to the ecliptic plane necessarily experiences several crossings of the sector boundary (SB), the speed of the wind (300-900 km/s) being usually much higher than the spacecraft speed (about 15 km/s). The above scenario, however, is continuously modified and distorted by the evolving coronal holes, ejecta and other non-stationary phenomena form our star.

This chapter is focused on the solar wind fluctuations inside the bubble delimited by the termination shock. It should be noted that the solar wind is turbulent, in the sense that disordered fluctuations are ubiquitous in the system. The flow is nonstationary at all scales and statistically non-homogeneous in that it expands with the distance from the Sun. The solar wind plasma and magnetic field fluctuate on a huge range of scales and frequencies. Think for instance of the system external scale ($\sim$ 100 AU $= 1.5 \cdot 10^{10}$ km), the spacing of magnetic sectors determined by the sun rotation ($\sim$ 7 AU $= 1.05 \cdot 10^{9}$ km for a wind speed of 500 km/s), the ion gyromotion scale ($\sim 10^{5}$ m) and the electron gyromotion ($\sim 10^{3}$ m). Typical spatial scales of the heliosphere and solar wind fluctuations are summarized in table 9, while possible regimes of turbulent fluctuations are discussed in §4.6. The solar wind is featured by a wide range of physical phenomena. Limiting the list to the hydrodynamic range (that is, to scales larger than the Larmor radius), we find magnetohydrodynamic waves (both Alfvénic and compressive fast/slow), shocks due to the interaction between streams of slow and fast wind in the ecliptic (CIRs), active turbulence, remnants of coronal turbulence frozen in the wind, coherent structures as interplanetary coronal mass ejections (ICMEs), sector boundary crossings,

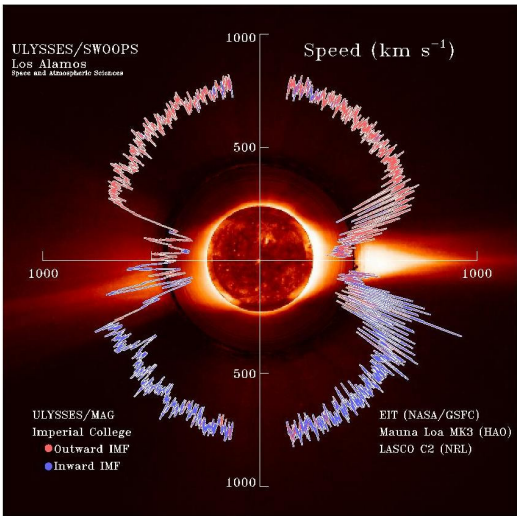

Figure 41: Solar wind speed from Ulysses observations during solar minimum. The slow wind ($\sim$ 400 km/s) originates at low latitude streamers, and the fast wind ($\sim$ 800 km/s) is accelerated in correspondence to coronal holes, associated with open magnetic field lines. Credits: NASA – Marshall Space Flight Center `https://solarscience.msfc.nasa.gov/SolarWind.shtml`.

etc.(see the brief review reported below about the role of waves and wave packets in astrophysical plasmas).

Solar wind fluctuations are not just convected outward, in fact they experience energy cascades between the various scales. A nice review paper on the possible spectral power decay laws has been written by Zhou, Matthaeus, and Dmitruk [2004, 151]. Solar wind turbulence observations have been comprehensively reviewed by Tu & Marsch [1995, 142] and by Bruno & Carbone [2013, 27], see also the book by Biskamp [2003, 20] on the general MHD turbulence theory, and the recent book by Belmont [2013, 17] on collisionless plasmas.

Table 9: Typical macro- and micro-scales of the solar wind system are reported. It should be recalled, however, that such scales evolve with the heliocentric distance. Here, values are reported for the wind at 5 AU (upstream TS) and for the early heliosheath, downstream TS. In regard to the plasma and magnetic field fluctuations, the ion Larmor scale (r_{ci}) discriminates the large-scale *magnetohydrodynamic regime* ($d > r_{ci}$) from the small-scale dissipative *kinetic regime* ($d < r_{ci}$), which extends down to the electron gyroradius [131].

Solar cycle	11 years
Solar sideral (Carrington) rotation	25.38 days
Solar radius	$6.96 \cdot 10^8$ m
Solar wind upstream the termination shock	
Sun-TS distance	$\sim 1.3 \cdot 10^{13}$ m (90 AU)
Magnetic sectors spacing	$\sim 9 \cdot 10^{11}$ m (6.5 AU)
Heliospheric Current Sheet thickness	$\sim 10^7$ m ($6 \cdot 10^{-5}$ AU)
Larmor radius (1eV thermal ions)	$\sim 1.5 \cdot 10^5$ m (10^{-6} AU)
Larmor radius (1eV thermal electrons)	$\sim 5 \cdot 10^3$ m ($5 \cdot 10^{-8}$ AU)
Debye length	~ 10 m ($7 \cdot 10^{-11}$ AU)
Average distance between two ions	$\sim 10^{-2}$ m ($7 \cdot 10^{-14}$ AU)
Solar wind in the inner heliosheath	
Heliosheath thickness	$\sim 4.5 \cdot 10^{12}$ m (30 AU)
Magnetic sectors spacing downstream TS	$\sim 3 \cdot 10^{11}$ m (2 AU)
Larmor radius (1keV pickup ions in HS)	$\sim 5 \cdot 10^7$ m ($3 \cdot 10^{-4}$ AU)
Heliospheric Current Sheet thickness	$\sim 10^7$ m ($6 \cdot 10^{-5}$ AU)
Larmor radius (12 eV thermal ions)	$\sim 5 \cdot 10^6$ m ($3 \cdot 10^{-5}$ AU)
Larmor radius (12 eV thermal electrons)	$\sim 8 \cdot 10^4$ m ($5 \cdot 10^{-7}$ AU)
Debye length	~ 1 m ($7 \cdot 10^{-12}$ AU)
Average distance between two ions	$\sim 10^{-1}$ m ($7 \cdot 10^{-13}$ AU)

The importance of hydromagnetic waves in the solar wind and astrophysical plasmas

The role of magnetohydrodynamic (MHD) waves, which permeate astrophysical flows at all the spatial and temporal scales, became increasingly important since their discovery in 1942 by Hannes Alfvén [9]. Small-scale Alfvén waves were first detected in solar wind by Belcher and Solodyna [15] in 1975. Alfvén waves have a central part in the dynamics of the solar corona, the interplanetary solar-wind, planetary magnetospheres and ionospheres, auroral dynamics, and MHD turbulence. Beside the transport of high fluxes of energy along the magnetic field lines, these fluctuations were found to be able, in inhomogeneous plasmas, to accelerate the wind through the wave pressure gradient, even at large distances from the Sun [17]. At the Large Plasma Device (LAPD) at UCLA it was shown experimentally that such waves convey information about currents and magnetic field topology [59, 60]. MHD turbulence, ubiquitous in a number of astrophysical systems, is currently depicted as Alfvénic. That is, the governing physical mechanism is the interaction among shear Alfvén wave packets moving in opposite directions [20]. The extent of inward-propagating and outward-propagating waves, whose measure is the normalized cross-helicity, determines the nonlinearity strength of such interactions. Moreover, only recently [43] it has been shown that both a continuous of scales, typical of strong turbulence, and discrete wave modes can coexist. Wave dynamics has a crucial role in the generation and heating of the solar wind; in this regard, future missions as Solar Probe Plus will provide in situ measurements at the solar corona, precious to unravel the mechanisms of solar wind acceleration. A big challenge towards the understanding the evolution of Alfvénic fluctuations and turbulence with the heliocentric distance have been represented by the contradiction between the observed reduction of cross helicity (see also our work [67]) and the theoretical prediction of "dynamic alignment", see [26]. Moreover, Alfvénic fluctuations recorded in the solar wind are mainly outward-directed and located at fast-wind streams, while inward modes are needed to drive nonlinear interactions responsible for cross helicity reduction. Mechanisms to explain such observations were proposed, based on local production of inward-propagating waves by wind velocity shear, which is seen as a driver for nonlinear interactions and instabilities [124, 90, 23].
Discriminating waves form turbulent fluctuations is a challenging task, we hope that this analysis will provide useful means of investigations in this direction.

Most studies of solar wind turbulence upstream TS use near-Earth, <1 AU data from spacecrafts in the ecliptic, see [142]. An exception is represented by *Ulysses* which provided the first observations at high latitudes, close the solar polar regions [65] up to 4.8 AU. These data showed that the plasma fluctuations kinetic energy in the inertial range of turbulence decay spectrally as a power law, with exponent evolving towards

-5/3 with the heliocentric distance for both the slow and the fast wind. Spectra at 1 AU have been shown to be far from the asymptotic state [121]. Recent investigations on spectral decay show that the kinetic energy power law is fit by exponents of -5/3, while the magnetic energy often decay with exponents closer to -3/2 [112].

A low-frequency non-turbulent f^{-1} range have been found below a certain break frequency, which decreases as the distance from the Sun. This range has been related to the Alfvénic wave character of large-scale imbalanced fluctuations (magnetically dominated waves mainly outward-propagating), originating from the solar corona and carrying out energy which act as a reservoir for the turbulent cascade developing during the wind evolution, see the works by Roberts [121] and Wicks *et al.* [144].

The aim of our work is to perform reliable spectral analysis of SW data recorded by the Voyagers in the outer heliosphere, on a broad range of scales so as to characterize the nature the wind fluctuations. In section §4.3 and §4.4 below, the Voyager data and some statistics are presented. The methods for spectral reconstruction we selected and adapted to the solar wind data to face the missing data problem are introduced in section §4.5. Solar wind power spectra at 5 AU from V2 data are then shown in section §4.7. The last section is dedicated to analysis of the helicity §4.8.

4.3 **Voyagers instrumentation and data sets**

The Voyager spacecrafts[2] are powered by three RTGs (Radioisotope Thermoelectric Generators), which currently provide about 315 W of electrical power per spacecraft. They are equipped with 10 instruments and currently five investigation teams are supported (PLS, MAG, LECP, CRS, PWS). Data transmission (downlink telemetry) is provided typically at 160 bits/s, and at 1.4 kbps for high-rate plasma wave data, via a 3.7 meter high-gain antenna, kept pointed towards Earth. The ground tracking station for V2 is the Canberra Deep Space Communication Complex (CDSCC, Australia) of the NASA Deep Space Network.

After elaboration, data are published and available to the public. Repositories we used include the NASA Space Physics Data Facility (COHOWeb) [40], the Voyager Magnetometer Experiment Data repository [100], the MIT Space Plasma Group repository [63].

Coordinate system. Solar wind plasma and magnetic field data are given in the Heliographic RTN coordinate system (HG), which has origin centred at the spacecraft. The radial (R) direction is defined as the line from the Sun's centre to the spacecraft. The tangential (T) axis is parallel to the solar equatorial plane. The normal (N) axis is such to make the triad orthonormal (South-North directed).

2 `https://voyager.jpl.nasa.gov/spacecraft/index.html`

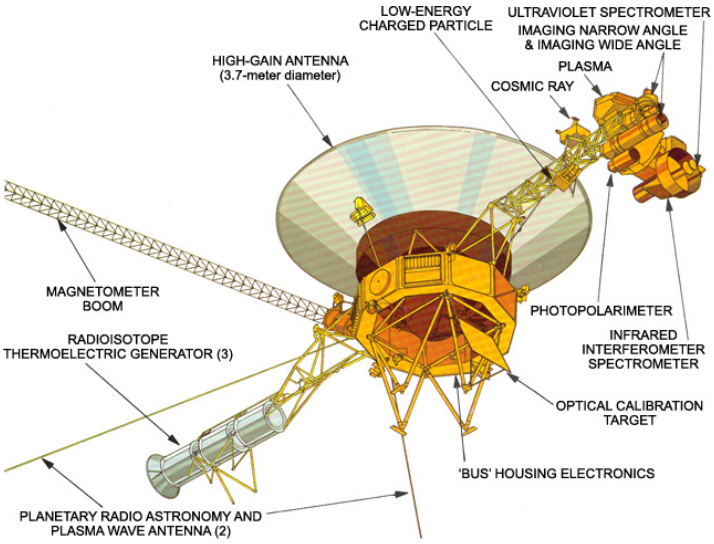

Figure 42: The Voyagers instrumentation. Credits: NASA – Marshall Space Flight Center (`https://solarscience.msfc.nasa.gov/SolarWind.shtml`).

PLS plasma data. The Voyager plasma (PLS) experiment measures the SW properties for particles with energy in the range [10 eV-6 keV] (ions) and [4 eV-6 keV] (electrons). The onboard payload consists of four grid-modulated Faraday cups detectors (for a complete description of the PLS[3] instrumentation see the review by Bridge [1977, 25]). Plasma currents are detected in the [10 - 5950 eV/q] energy/charge range. Then, a set of current vs energy spectra from the PLS cups are obtained at a certain sampling rate. These spectra are fit with convected isotropic Maxwellian proton distributions to obtain the plasma velocity, temperature and density. A single measurement comes form an integration time, for each cup, which can be set between 0.03 s and 0.93 s. The time between measurements varies between 12 s and 192 s. In 1979 it was 96 s. These fits require good data in at least three of the Faraday cups. Noise, low-densities, and high flow angles limit the number of acceptable output data and are therefore sources of data gaps. Plasma measurements can therefore be considered snapshots with a 96-s cadence, in that period (this fact has to be taken into account, since aliasing issues could in principle arise from spectral analysis as the Nyquist frequency is approached, see the discussion in §4.7).

About uncertainty in data, headers of published data report that for hi-resolution data (12 s, 96 s, 192 s) inside the termination shock, *"one sigma errors are typically less than 0.5% in the speed modulus and v_R, less than 5% for the density and thermal speed, and*

3 See also: `https://pds.nasa.gov/ds-view/pds/viewInstrumentProfile.jsp?INSTRUMENT_ID=PLS&INSTRUMENT_HOST_ID=VG1`

vary greatly for v_T and v_N". This practically means that for velocity data the uncertainty is about ± 2 km/s. Our analysis takes this into account and the instrumental accuracy is indicated in the power spectrum diagram (we assumed a white-noise distribution). For heliosheath data (V2, from 2007), the uncertainty can be much higher, as high as 10% for v_R, as shown by Richardson & Decker [2014, 119]. Such poor accuracy represents a very serious limitation to spectral analysis of plasma in the HS.

MAG - magnetic field data. The MAG experiment consists of a dual low-field and high-field magnetometer system (LFM, HFM), a configuration which ensures great reliability and a wide operational range. The system was indeed designed for dynamic ranges of $\pm$ 0.5 G ($\pm\ 5 \cdot 10^{-5}$ T) for the LFMs and $=\pm$ 20 G (2 mT) for the HFMs, a low quantization uncertainty of $\pm$ 0.002 nT in the most sensitive $\pm$ 8 nT LFM range, low sensor RMS noise level of 0.006 nT, in order to allow the study of a broad spectrum of phenomena during the mission. For a review on the MAG experiment, see Behannon [1977, 13], and Ness [1971, 102].

The sampling period for LMFs is 0.06 s in the first years of the mission. From this, 1.92 s, 9.6 s and 48 s averages have been computed and published by NASA. In the heliosheath, the sampling rate is smaller (2.08 samples/s), and the standard telemetry output are dataset of 48 s averages.

The 1-sigma uncertainty for the magnetic field components is typically in the interval $\pm(0.02 - 0.05)$ nT depending on the period. Estimates for V2 in 2005-2011 say ± 0.03, and a little smaller for V1. In fact, noise at V2 magnetometers is somewhat higher than at V1: an unintended manoeuvre led to an overheating of the V2 sensors which damaged the magnetometers. This generates an additional important noise signal, which cannot be separated from the other sources of noise and make the calibration through rolls difficult. The reader can find a discussion in ref. [28, 35].

Data gaps. In addition to noise, the data sets from V1 and V2 are incomplete time series. Data gaps are largely due to tracking issues related to limited telemetry coverage. For instance, data gaps of about 12 hours are typical of magnetic field data in the outer heliosphere. Smaller gaps are associated with removal of bad data coming from instrumental interferences, noise, command sequences, spacecraft malfunction (as in the period 2010, day-of-year 112-142, when V1 was crossing the termination shock), etc. See figure 44, left panels, and figure 43 below.

Data sets. The data set considered in this chapter consists of V2 plasma data (ion vector velocity, ion density, ion temperature) sampled every 96 s and magnetic field 48-s data in the 180-day period from January 1, 1979 00:00 GMT to June 29, 1979 19:00 GMT (1979 DOY 1-180), which is shown in figure 44, left panel. In addition, the period at 29 AU form January 5, 1989 GMT to April 4, 1989 GMT (1989 DOY 5-101) was considered to study the radial evolution of the magnetic and cross helicity. Such periods show a good degree of homogeneity. The six months of 1979 preceded

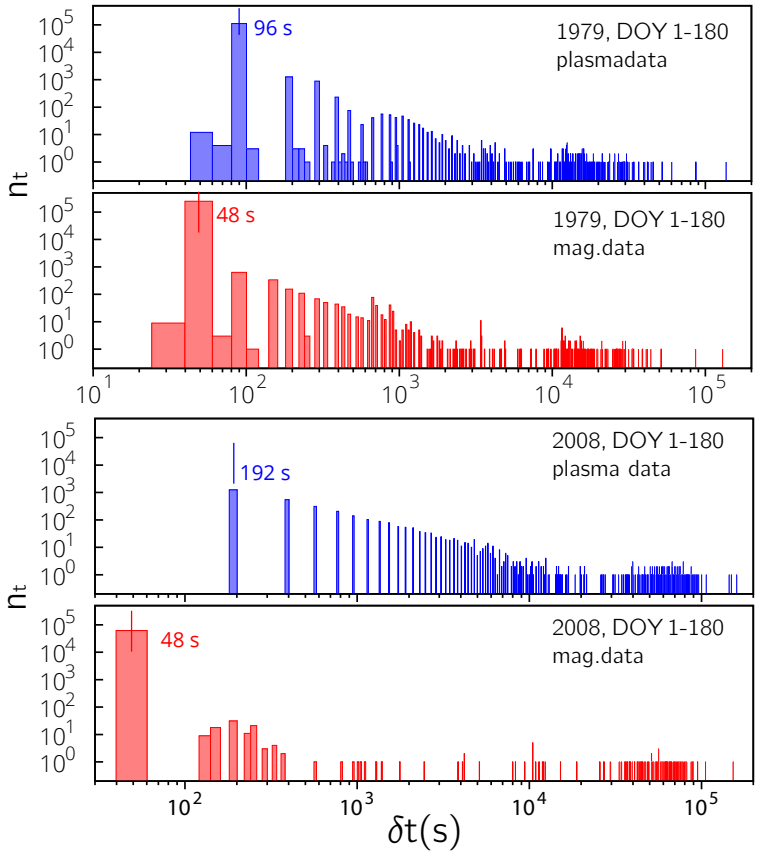

Figure 43: Data time-spacing distribution. Histograms of the number of data points with time spacing of δt. *Top panels*: V2 data at 5 AU (period 1979, DOY 1-180). *Blue:* plasma data, here the nominal resolution is 96 s, which is indeed the value which occurs most frequently. *Red*: magnetic field 48-s data. *Bottom panels*: heliosheath V2 data in 2008, DOY 1-180. Here the velocity resolution is 192 s. Note, in 1979 plasma and magnetic field datasets and in 2008 plasma dataset, the presence of intervals $\delta t = \delta t_s + j\delta t_s$, $j = 1, 2, \ldots$, where δt_s is the sampling time. Such intervals represent data gaps with $j - 1$ missing points.

the encounter of V2 with Jupiter's magnetosphere, which occurred on July 9, 1979. In this period, the total missing data were 28% for plasma data and 24% for magnetic field. In 1989, such amount rises up to about 60%.

4.4 **Statistical properties of the solar wind at 5 AU**

Considering the 1979 period, average quantities are shown in table 10, while statistics of the velocity and magnetic field components are presented in table 11. In this period, the mean wind speed V_{SW} is 454 km/s. Since the spacecraft was measuring plasma in the ecliptic, the wind had already been subject to shocks coming from the interaction between fast and slow streams at a smaller radial distance beyond 1 AU. As a consequence, there were lots of phenomena during these six months, including shocks (evident from the v_R signal), compression and rarefaction regions , SB crossings (associated with B_T). For this reason, special care has to be taken when solar-wind Fourier spectra are interpreted (results are discussed in §4.7). In table 10, average plasma quantities are shown.

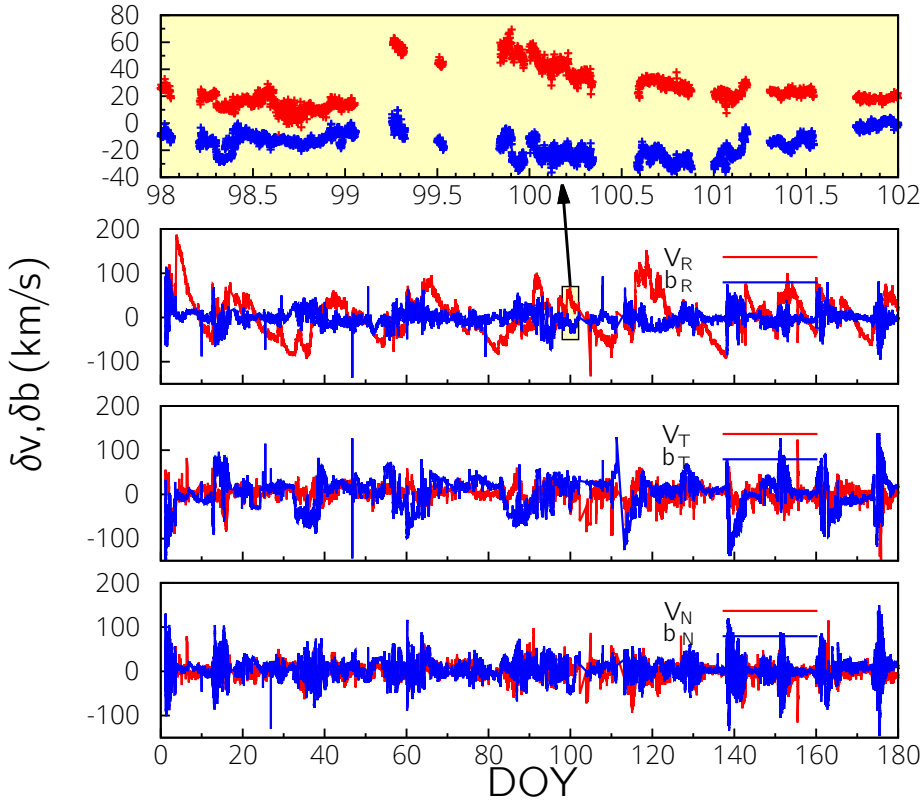

Figure 44: Voyager 2 data in 1979, DOY 1-180. Fluctuations of plasma velocity (red lines) and magnetic field (blue lines) recorded by Voyager 2 at 5 AU, in the first semester of 1979. The magnetic field is represented using Alfvén units, $\mathbf{b} = \mathbf{B}/\sqrt{4\pi\rho}$ where ρ is the ion mass density (quantities in cgs units). In right panels, a 4-day period is magnified to show details of data gaps. From Gallana *et al.* (2016) [57].

The wind is featured by magnetic fluctuations generally comparable to the mean field, with values of the magnetic energy ($E_\mathrm{m} = 2.84 \cdot 10^3$ km^{2}s^{-2}) greater than the kinetic energy ($E_\mathrm{k} = 2.45 \cdot 10^3$ km^{2}s^{-2}). This is most typical of slow streams, see e. g. Marsch and Tu [85] and McComas et al. [92]. Other typical plasma scales and frequencies have been computed. Among these, we included the ion "convective" Larmor frequency, defined as $f^* = V_\mathrm{SW}/(2\pi r_\mathrm{ci})$, where r_ci is the gyroradius. This formula comes from the general expression for the frequency Doppler shift from the plasma (PL) frame to the spacecraft (SC) frame

$$f_\mathrm{SC} = f_\mathrm{PL} + \frac{1}{2\pi}(\mathbf{k} \cdot \mathbf{V}), \tag{136}$$

where $\mathbf{k}$ is the vector wavenumber and $\mathbf{V}$ the relative velocity between the wind and the spacecraft (a spacecraft moving with the wind would always see the same plasma). The second term is due to the convection of fluctuations across the probe. If the Taylor hypothesis is verified (see the detailed study [66] on such hypothesis - it holds

Table 10: Voyager 2 average quantities and plasma parameters for the period 1979, day-of-year [1-180], 5 AU. $V_\mathrm{A} = \langle B/\sqrt{4\pi m_i n_i}\rangle$ (m_i proton mass); $E = E_\mathrm{k} + E_\mathrm{m} = \langle \mathbf{v}^2 + \mathbf{b}^2\rangle/2$; $H_c = \langle \boldsymbol{\delta b} \cdot \boldsymbol{\delta V}\rangle/2$; the plasma beta is defined as the ration between thermal and magnetic energy, that is $\beta = \langle 8\pi p/B^2\rangle$ where $p = n_i k_\mathrm{B} T$ is the ion thermal pressure. From Fraternale *et al.* (2016) [53].

V_{SW}	Mean velocity	$4.54 \cdot 10^2$	km/s
V_A	Alfvén speed	$4.94 \cdot 10^1$	km/s
E_v	Kinetic energy	$1.20 \cdot 10^3$	km^2/s^2
E_m	Magnetic energy	$1.37 \cdot 10^3$	km^2/s^2
E	Total energy	$2.57 \cdot 10^3$	km^2/s^2
H_c	Cross helicity	15.8	km^2/s^2
L_{E_v}	Kinetic correlation length	$3.68 \cdot 10^7$	km
L_{E_m}	Magnetic correlation length	$3.75 \cdot 10^7$	km
λ_v	Kinetic Taylor scale	$2.93 \cdot 10^7$	km
λ_m	Magnetic Taylor scale	$2.11 \cdot 10^7$	km
n_i	Ion numerical density	0.23	cm^{-3}
E_T	Ions thermal energy	2.29	eV
T	Ions temperature	$2.70 \cdot 10^4$	K
β_p	Ions plasma beta	0.22	
c_s	Ions sound speed	$1.93 \cdot 10^1$	km/s
f_{ci}	Ions Larmor frequency	0.02	Hz
f_{pi}	Ions plasma frequency	0.10	kHz
$f*$	Convective Larmor frequency	0.44	Hz
r_{ci}	Ions Larmor radius	150	km
r_i	Ion inertial radius	158	km

here since $V_{SC} \approx 15$ km/s), then $\mathbf{V} = \mathbf{V}_{SW} - \mathbf{V}_{SC} \approx \mathbf{V}_{SW}$. Gyromotion structures convected across the spacecraft could in principle be visible in power spectra at the frequency f^* [103, 130].
The field anisotropy can be quantified from the probability density functions (PDFs) of the field components, see figure 45. The radial component of plasma velocity is characterized by shocks due to the interaction of fast and slow wind streams, while the tangential component of the magnetic field is dominated by the effects of plasma compressions and rarefactions. The fluctuations of the other magnetic field components are more likely "true" turbulent fluctuations. Both the magnetic and velocity fields are anisotropic and intermittent, as shown in table 11 The presence of intermittency in the velocity and magnetic fields can also be observed by looking at the PDFs of the modules of the normalized vector fields, shown in figure 45 (**c**). The normalized vector fields are given by

$$|\boldsymbol{\delta}\mathbf{q}|^2 = \sum_i^3 \frac{(q_i - \mu_i)^2}{\sigma_i^2}, \tag{137}$$

where μ_i is the mean value and σ_i^2 the variance of the i-th component of the vector field $\mathbf{q}$. The same plot shows a three-component chi-square distribution as a reference. Intermittency is observed for a wide range of scales (see values of skewness and kurtosis in table 11).

In order to investigate anisotropic spectral energy cascades, is important know the direction of the vector wavenumber with respect to the background magnetic field. In particular the wavenumber parallel to the average magnetic field, $k_{\parallel}$, and normal to it, $k_{\perp}$, should be identified, as first suggested by Montgomery, Brown, and Matthaeus [99]. The angle between the local vector field and the radial direction is defined as

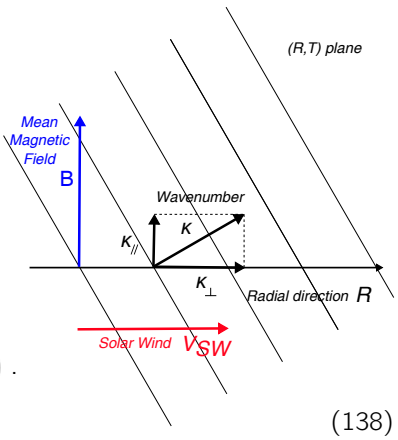

$$_v = \cos^{-1}\left(\frac{|v_r|}{|\mathbf{V}|}\right) \qquad _m = \cos^{-1}\left(\frac{|B_r|}{|\mathbf{B}|}\right). \tag{138}$$

PDFs of these angles are represented in panel (**a**)
of figure 45: the magnetic field vector is almost tangential-directed, the angle with respect to the radial direction being almost equal to $\pi/2$, as expected for a Parker spiral. Since the wind travels much faster than the spacecraft, the data collected in time can be interpreted as if they were measured along the radial direction. Therefore,

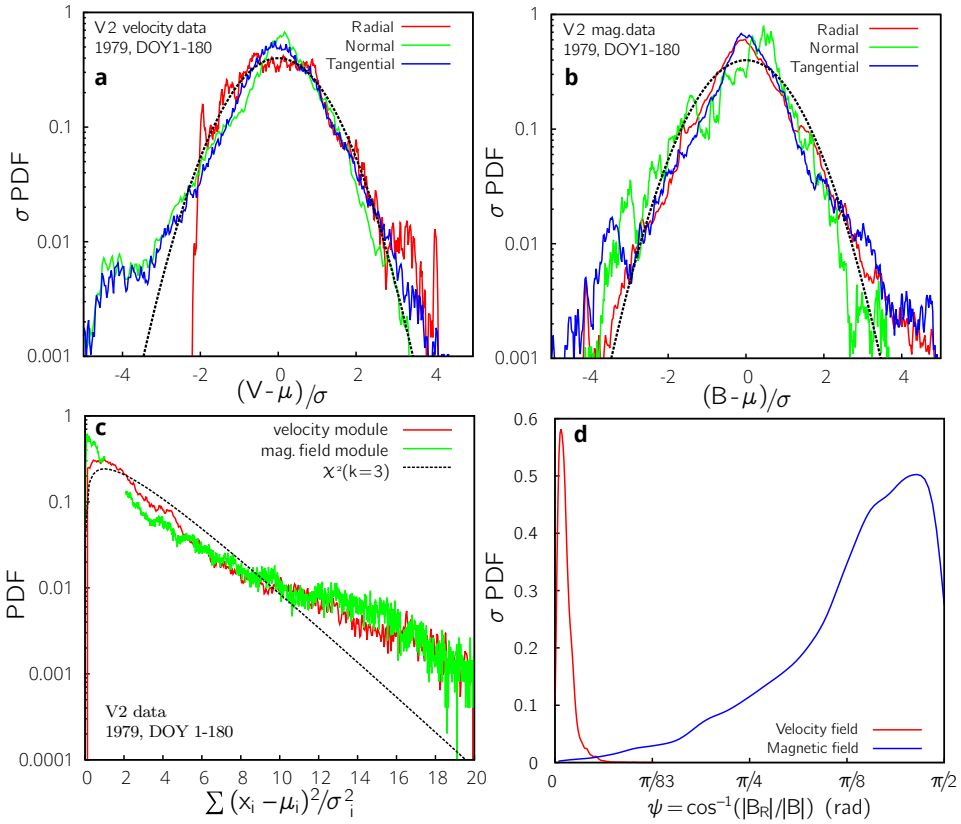

Figure 45: Normalized probability density functions of the velocity and magnetic field RTN components. **(a)** Velocity; **(b)** magnetic field. A comparison is shown with the Gaussian distribution (black line). **(c)** Normalized PDFs of fluctuation field strength, and comparison with a three-component (k = 3) chi-square distribution (black line). **(d)** Normalized PDF of the vector fields inclination angle with respect to the radial direction. From Fraternale *et al.* (2016) [53].

solar wind frequency spectra may be converted to wavenumber spectra by means of the approximation

$$f \approx V_{SW} k_R \approx V_{SW} k_\perp, \tag{139}$$

where V_{SW} is the mean plasma velocity and $k\perp$ are the wave-numbers normal to the mean magnetic field. This approximation can be considered valid since the radial direction is normal to the mean magnetic field, as shown in figure 45**d**. When power spectra are computed along one direction (1D spectra, also named *reduced spectra* [88]), all

Table 11: Mean values and first three statistical moments are shown for the velocity (v) and magnetic field (B) components and their strength; μ is the mean value, σ^2 the variance, Sk the skewness and Ku the kurtosis. The velocity is measured in km/s and the magnetic field in nT. The modules of the fluctuations are normalized on the standard deviation, see Eq. 137, such as to compare them with the chi-square distribution (standard 3-component chi-square distribution has mean 3, variance 6, skewness 1.63 and kurtosis 7) [57].

	μ	σ^2	Sk	Ku
v_R	454	1893	0.43	3.41
v_T	3.21	252.9	-0.99	7.35
v_N	0.51	250.3	-0.36	5.80
B_R	-0.04	0.173	0.53	6.71
B_T	0.06	0.85	-0.72	10.2
B_N	0.10	0.34	-0.24	7.65
$\|\boldsymbol{\delta V}\|^2$	3.00	10.47	2.40	10.27
$\|\boldsymbol{\delta B}\|^2$	2.48	17.41	3.17	14.90

the k-vector fluctuations are involved, leading to a *down-shift* effect on the wavenumber (typically small if multi-decade spectra are computed).

4.5 Spectral estimation methods for gapped solar wind data sets (30%-70% missing data)

Spectral analysis has long been a useful tool to investigate the multi-scale nature of fluctuating fields. Unfortunately, in the astronomical and astrophysical context complete data sets are often unavailable, due to several limitations as those discussed in §4.3. The problem of computing power spectra from nonuniformly sampled signals have been long standing (see the early works by Lomb [80] and Scargle [132]) and still open. A good overview of this topic can be found in a recent dissertation [12].
Here we show the limitations related to the specific case of solar wind turbulent data, and present the methodologies we used/developed to get reliable power spectra. This is a challenging target, since the field is multi-scale, with a continuum of frequencies spanning several decades, therefore not only specific frequencies need to be identified.

Spectral structure of the gap distribution. Before going into the details of the specific techniques, let me introduce a discrete characteristic signal which will be also referred to as the *gap signal*, in the following

$$\chi(t_i) = \begin{cases} 0 & \text{data at } \mathrm{t_i} \text{ is present,} \\ 1 & \text{data at } \mathrm{t_i} \text{ is missing.} \end{cases} \tag{140}$$

This binary function in the case of Voyagers data is a combination of unpredictable random components a component of periodic or near-periodic events related to tracking and/or acquisition and/or calibration issues.

Figure 46 (**b**) shows in red the power spectrum of the characteristic function for the gap distribution of V2 data in 1979. Note the f^{-1} slope and a number of discrete peaks. This slope is intermediate between the one resulting from a white noise component f^0 and the one given by a square-wave periodic component f^{-2} as shown the figure.

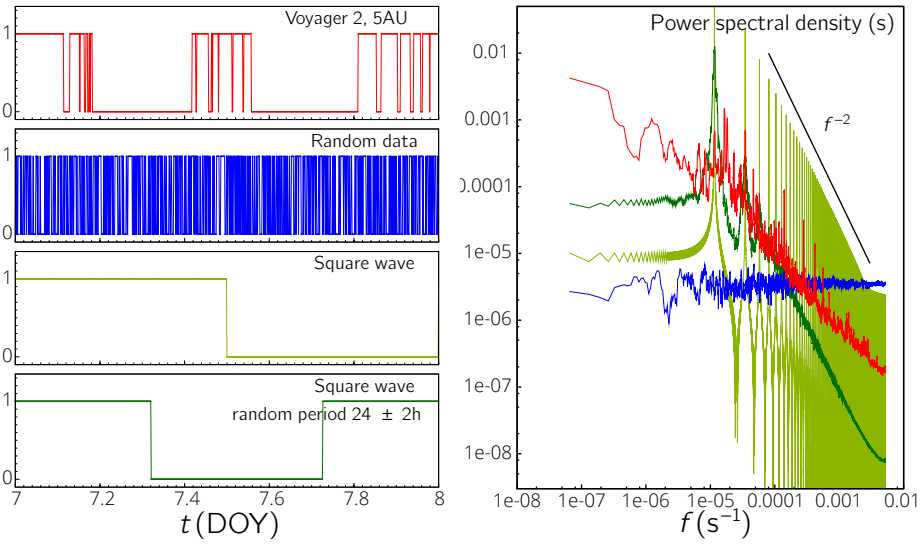

Figure 46: Spectrum of the gap signal for V2 data in 1979, DOY 1-180, and comparison with some gap distribution models: random gaps (blue), square wave (dark green), and square wave with random periodicity (light-green), each half-period has been randomly generated from a Gaussian distribution with an average of 12 hours and a standard deviation of 1 h). The left panel shows a sample of the four signals over one day. Related spectra are shown in the right panel. From Gallana et al. [57].

The above structure is inevitably inherited by the spectrum (power spectral density, PSD) of the actual signal one considers, when the PSD is computed by means of standard techniques as the Discrete Fourier Transform (DFT). Actually, most of the known classical methods developed for non-evenly distributed data based either on the computation of the correlation function (Blackman-Tukey [21]) or on direct estimation in the frequency space (Lomb periodogram [80], nonuniform-FFT algorithms) suffer form this issue. What is observed is indeed that non-physical peaks show up and wrong slopes are observed in the spectrum of the signal (see the figures below and the detail of figure 47).

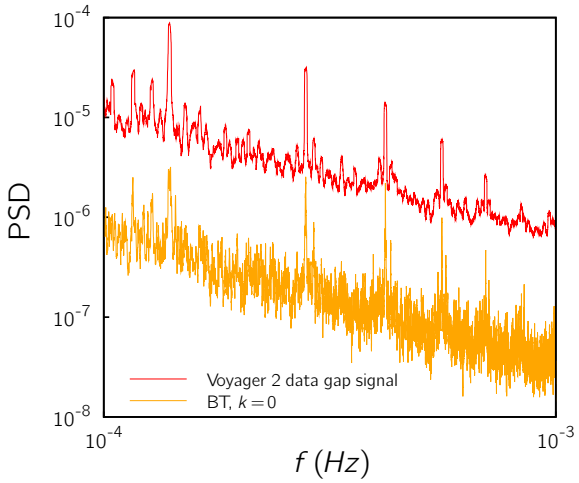

Figure 47: Inheritance of non-physical spectral peaks from the gap signal when the correlation method without any interpolation or re-sampling is used to compute spectra. Comparison between the PSD of synthetic gapped data (*Synt1*) with the gap distribution of V2 1979 data and the spectrum of the characteristic function. Taken from [57].

Therefore, as a starting point it is quite useful to know the shape of the spectrum of the gap signal χ, in order to be able to discriminate physical peaks (which may be present in SW analysis) from non-physical and, generally speaking, recognize the critical ranges of frequencies: for instance, beside peaks, problems will arise when the spectrum of χ decays slower than the true spectrum of the physical quantity. Such problems arise in solar wind analysis when missing data exceed 10%, which is typically the case for data sets beyond 1 AU. It will be shown that the missing data problem ends up to be destructive for the spectral estimation when the gap density gap goes beyond 70%, which is typical in the heliosheath region.

The result of this study is a simple method of investigation - which includes the concomitant use of a few different, uncorrelated, techniques - to estimate the spectrum of turbulent-like long (up to $\sim 5 \cdot 10^5$ points) signals with error in the spectral slopes below 10%. This permits analysis, in different plasma regimes, of the precious Voyagers data at the edge of our helioshpere (note that *in loco* measurements from the heliosheath will probably not be available for at least 20 years). To the best of our knowledge, this is the first work that shows spectra of the heliosheath magnetic field from hi-resolution data, see Chapter 5.

Six methods of spectral estimation were considered. They come from multi-disciplinary areas, spanning classical numerical analysis, astrophysics applications, telecommunication engineering and image processing (compressed sensing). The methods are listed below:

1. **BT**. Fourier transform of the correlation function computed from available points, the Blackman-Tukey method with prewhitening filter [21];

2. **SUB**. Windowed averaged Fourier transforms of arbitrary (typically short) data subsets, linearly interpolated on uniform grids, over gaps;
3. **CI**. FFT the autocorrelation function computed after linear data interpolation;
4. **RP**. Maximum likelihood stochastic data recovery by Rybicki and Press [129];
5. **CS**. *Compressed sensing* spectral estimation (see e.g. [44, 36]);
6. **OP**. Optimization procedure based on the minimization of the error of method 3, which leads to approximating model spectra [49, 51].

Test cases. Tests have been performed on synthetic turbulence data sets which mimic the Voyager data, in terms of integral scale, sampling period, number of samples and, of course, missing data distribution. The synthetic data set is generated by inverse Fourier transform from an imposed spectrum $E_{1D}(f)$ and phases of the harmonic components uniformly randomized.

The first tests have been conducted for 1979-gaps. Two 180-d reference synthetic dataset were generated by analogy to a scalar field which has a PSD similar to the typical one-dimensional spectrum of an hydrodynamical homogeneous and isotropic turbulent field. In this case, the 1D spectra $E_{1D}(f)$ were obtained by integration of the formula $E_{3D}(f) = -f\,\mathrm{d}E_{1D}(f)/\,\mathrm{d}f$ (see Monin and Yaglom [98]).

- *Synt 1*: has an energy-injection range and an inertial range
  $\rightarrow E_{3D}(n/n_0) = \frac{(n/n_0)^{\beta}}{(n/n_0)^{\alpha+\beta}}$
- *Synt 2*: has an energy-injection range, an inertial range and a dissipative range:
  $\rightarrow E_{3D}(n/n_0) = \frac{(n/n_0)^{\beta}}{(n/n_0)^{\alpha+\beta}}\left[1 - exp(\frac{n-N}{\gamma} + \epsilon)\right]$

where $\beta = 2, \alpha = 5/3, n_0 = 11, \quad = 10^4, \epsilon = 10^{-1}, N = 162000$ and $n = 1, 2, ...N/2$.

The analysis were then carried out after eliminating data from the synthetic sequences, according to the exact gap distribution of V2 data. It is true that these sets show three major differences with respect to SW data: (i) inherent periodicities are be present in SW data but not here. This will be discussed in the methods description; (ii) phases in SW are not random. Random phases have already been used, for instance, in Refs. [71, 136, 19]. However, to improve the validation process, we tested the techniques on a contiguous SW dataset. We found a 4-month magnetic field sequence from the Ulysses mission at 1 AU (1990, DOY 298 - 1991, DOY 45) and put on this the V2 gap distribution. Results from synthetic datasets are confirmed by this test, shown in figure 51 (**e**, **f**). (iii) SW spectra are often featured by the presence of spectral breakpoints, and different spectral indexes. In fact, in addition to Synt 1 and 2, a number of other data sets have been tested, with spectral slope in the reasonable range [-1,-3] and different values of the integral scale. This has been done with the aim of analyzing heliosheath datasets ($>$ 100 AU) where about 70% of data are missing.

Most spectra presented here have been smoothed by averaging neighboring frequencies in a bin of constant width (9 points), or varying width (linearly increasing). The smoothing is applied for visualization purpose, it always preserves the spectrum energy and spectral slopes. Spectral slopes are obtained from liner fits of the spectra in the log-log space. Unsmoothed and smoothed spectra typically give the same fit with discrepancy is below 0.5%.

All spectra reported in this work are traced so that the integral of the PSD is equal to the variance of the signal considered.
($\sum_i^{N/2} |\hat{q}_i|^2 \Delta f = \frac{1}{N-1} \sum_i^N (q - \langle q \rangle)^2$).

A number of FORTRAN90 numerical codes have been built and are available to the public (see the supplementary material in [57]). CS was instead implemented in MATLAB®. Beside the main software, routines have been written for: reading/merging/cleaning/rewriting data sets; computing FFTs (via Lapack libraries); filtering/smoothing; investigating aliasing effects; resampling/grid aligning; computing correlation functions/cross-helicity/magnetic helicity. Due to the size of datasets analyzed, where possible, codes have been developed to exploit multi-core machines via Message Passing Interface (MPI) protocol and multi-threaded computations via Open MP. This allowed, for instance, a fast computation of correlation functions and interpolations.

4.5.1 *Correlation spectra, the Blackman-Tukey method (BT).*

This overview starts from a description of the Blackman and Tukey [21] method (BT, in the following), since it has been used in solar wind analysis for long time, see e.g. the works in [88, 78, 135, 137, 70, 23, 69]. This section somehow contains the motivation of our work. The method is based on the computation of the covariance function, $C_{ij}^X(\tau) = \langle X_i(t) X_j(t+\tau) \rangle$, where X is the fluctuation of a generic quantity about its mean value. In the following we will call it the *two-point correlation function*. In fact, the two-point correlation function and the power spectrum are Fourier transform pairs, $P(f) = \int_{-\infty}^{\infty} C(\tau) e^{-i2\pi f \tau} \, \mathrm{d}f$. The strength of this method is that it provides a way to evaluate the power spectrum without the need to interpolate the data, overcoming in principle the problem of non-evenly distributed data. $C_{ij}^X(\tau)$ can be obtained, indeed, by direct application of its definition:

$$C_{ij}^X(\tau) = \langle X_i(t) X_j(t+\tau) \rangle \rightarrow C_{ij}^X(r) = \frac{1}{N-r} \sum_{n=1}^{N-r} X_i(n) X_j(n+r), \tag{141}$$

where indexes i and j represents the components of a vector field $\mathbf{X}$ (of size N) and $\tau = r\Delta t$ is the time lag, in the discrete case.

Operatively, we verified that much better spectra can be obtained if the correlations are computed as

$$C_{ij}^{X}(r) = \frac{1}{N}\sum_{n=1}^{N} Y_i(n)Y_j(n+r), \quad r = 1, 2, \ldots, N \tag{142}$$

where $Y = [X, X]$ is a doubled data set. In this case, an even function is obtained and its Fourier transform corresponds exactly to the modulus of the Fourier transform of X. An alternative is to compute C from 141 for r up to N/2 and then compute the FFT of the symmetrically doubled correlation, but this approach leads to errors in the spectrum close to the Nyquist frequency.

In the case of missing data, the unavailable products in 141 can just be ignored, so they do not contribute to the sum (141). The BT method evaluates the two-point correlation as

$$C_{ij}^{X}(r) = \frac{1}{N(r)}\sum_{n=1}^{N(r)} X_i(n)X_j(n+r)p(n,r) \quad \text{with} \quad r = 1, \ldots N/2, \tag{143}$$

$$N(r) = \sum_{n=1}^{N} p(n,r) \tag{144}$$

$$p(n,r) = \begin{cases} 1 & \text{if } (n) \text{ and } (n+r) \text{ exist} \\ 0 & \text{if } (n) \text{ or } (n+r) \text{ does not exist.} \end{cases} \tag{145}$$

Afterwards, the PSD is computed by means of a FFT after an (optional) tapered cosine window. Spectra computed in this way are shown in figure 49 and 51(**c**,**f**), see orange curves.

Of course, the BT method has been successfully used in many SW studies, mostly using datasets where missing data were the 10%, see e.g. Matthaeus and Goldstein [88] (gaps: 6%-11%); Bellamy, Cairns, and Smith [16] (gaps: 10%). Sometimes BT was performed on linearly interpolated data as in Leamon et al. [78] (gaps: 1%), Smith et al. [135], Smith, Vasquez, and Hamilton [137]. Also in the works by Joyce et al. [70] and Joyce et al. [69] missing data issues were not present. In this situation, the effects on the correlation function induced by data gaps is mild and does not significantly influence the result.

However, for SW data beyond 1 AU ($\gtrsim$ 30% missings), BT does not lead to an accurate spectral estimation. The reason of this resides in the slow convergence of the two-point correlation function when computed using (143), as shown in figure 48. The correlations result oscillating, with the same periodicity as the counter $N(r)$. As a result, the related PSD show non-physical peaks and biased values of the spectral decay slope, see the orange curves in figure 49 and 51. The issues related to the BT method in the presence of data gaps was also pointed out by Bieber et al. [19]; in appendix of that

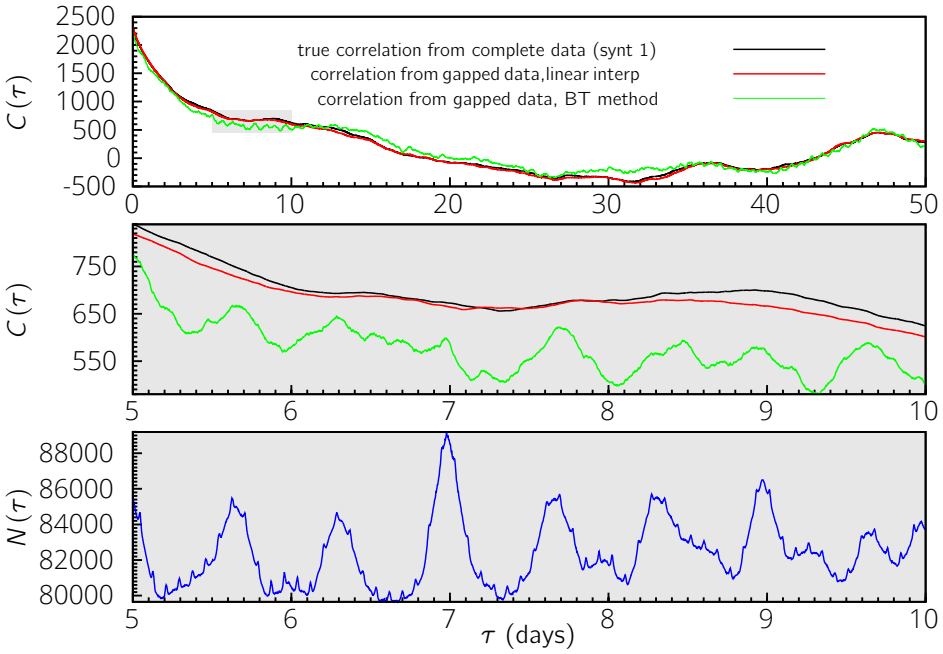

Figure 48: Two-point correlation function computed from *synt1* data (30% missing data). *Black*: true correlations, computed from the contiguous data-set (no gaps). *Red*: correlations computed from the gapped dataset after linear interpolation (the gap distribution is the same as V2 data). *Green*: correlations computed with the BT method via Eq. 143. In the central panel, a 5-day period is shown to highlight differences of the two approaches compared to the correct result. In the bottom panel, the number $N(\tau)$ of available pairs $X(t)$, $X(t+\tau)$ is shown as a function of the time lag τ. Note that $N(\tau)$ greatly influences the convergence of the correlation function (green lines).

work, the authors showed benefits given by a prewhitening filter. To provide a complete comparison for our data, we implemented the modern BT methodology, by including the prewhitening filter.

Prewhitening consists of a preprocessing filtering technique for reducing the spectral leakage typically occurring from frequency bands with high power to bands with low power (Blackman and Tukey [21],see also [126, 71]). In turbulence studies, this reduces the spectral distortion in the high-frequency range.
In practice, the simplest filter consists of computing the first-differences $Y_{\mathbf{n}} = X_{\mathbf{n}} - kX_{\mathbf{n-1}}$, where k is a constant factor (commonly set to 0.6). *In the case of contiguous,*

Table 12: Spectral slopes from tests performed on *synt1* for the Blackman-Tukey method with different values of prewhitening parameter k. Comparison with the linear interpolation method (CI).

	f (Hz)	original	corr+lin. interp	BT, k = 0.00	BT, k = 0.60	BT, k = 0.80	BT, k = 0.99
Synt	$10^{-5} \div 5 \cdot 10^{-4}$	-1.66±0.004	-1.70±0.005	-1.41±0.005	-1.48±0.005	-1.66±0.005	-1.77±0.003
	$5 \cdot 10^{-4} \div 5 \cdot 10^{-3}$	-1.67±0.003	-1.70±0.003	-1.03±0.001	-2.01±0.001	-1.98±0.001	-1.77±0.002

Table 13: Spectral slopes from tests performed on *synt2* for the Blackman-Tukey method with different values of prewhitening parameter k. Comparison with linear interpolation method (CI).

f (Hz)	original	corr+lin. interp	BT, k = 0.00	BT, k = 0.60	BT, k = 0.80	BT, k = 0.99
$10^{-5} \div 5 \cdot 10^{-4}$	-1.70±0.005	-1.75±0.003	-1.44±0.005	-1.51±0.005	-1.66±0.005	-1.80±0.003
$5 \cdot 10^{-4} \div 5 \cdot 10^{-3}$	-3.15±0.002	-3.05±0.004	-0.88±0.002	-2.11±0.003	-2.39±0.003	-2.49±0.001

uniformly sampled data, the power spectrum of Y, $P_{\mathbf{Y}}(f)$, is related to the spectrum of X ($P_{\mathbf{X}}(f)$), by a transfer function $H(f) = 1 + k^2 - 2k\cos(2\pi f \Delta t)$:

$$P_{\mathbf{X}}(f) = P_{\mathbf{Y}}(f)\frac{1}{|H(f)|^2} \tag{146}$$

The steps followed to compute the spectrum are

- Compute the first differences Y;
- Compute the autocorrelation function $\langle Y(t)Y(t+\tau)\rangle$;
- Compute the power spectrum $P_{\mathbf{Y}}$ (possibly windowing before computing the FFT. Hann window: $w(n) = 0.5[1 - \cos(\frac{2\pi n}{N-1})]$);
- Post-darken by using eq. 146, to get the spectrum $P_{\mathbf{X}}$.

The same procedure is applied when data points are missing in the sequence. However, prewhitening is not able to solve the problem (in fact, it was not designed to this purpose), especially when the missing data are considerable, as in our case.

By looking at figure 49 and tables 12 and 13, it is clear that in the case of no-prewhitening ($k = 0$) spectra computed with BT show biased values of the spectral index, energy density, and contain spurious peaks. About *synt1*, the error in the slope is 15.4% for $f = [10^{-5}, 5 \cdot 10^{-4}]$ Hz, and 38% for $f = [5 \cdot 10^{-4}, 5 \cdot 10^{-3}]$ Hz. For *synt2*, which has a steeper spectrum in such frequency range, the error goes up to 72%. The peaks correspond to the "resonant frequencies" of the gap distribution.

The use of a prewhitening filter with $k \in [0.6, 0.9]$ slightly improves the results of the BT method, especially in the hi-frequency range, but the spectra are still affected by spurious peaks and biased values spectral index (see tables 12 and 13). $k = 0.99$ provides good results at high frequencies. In this case the error in the slope is 6.2% for

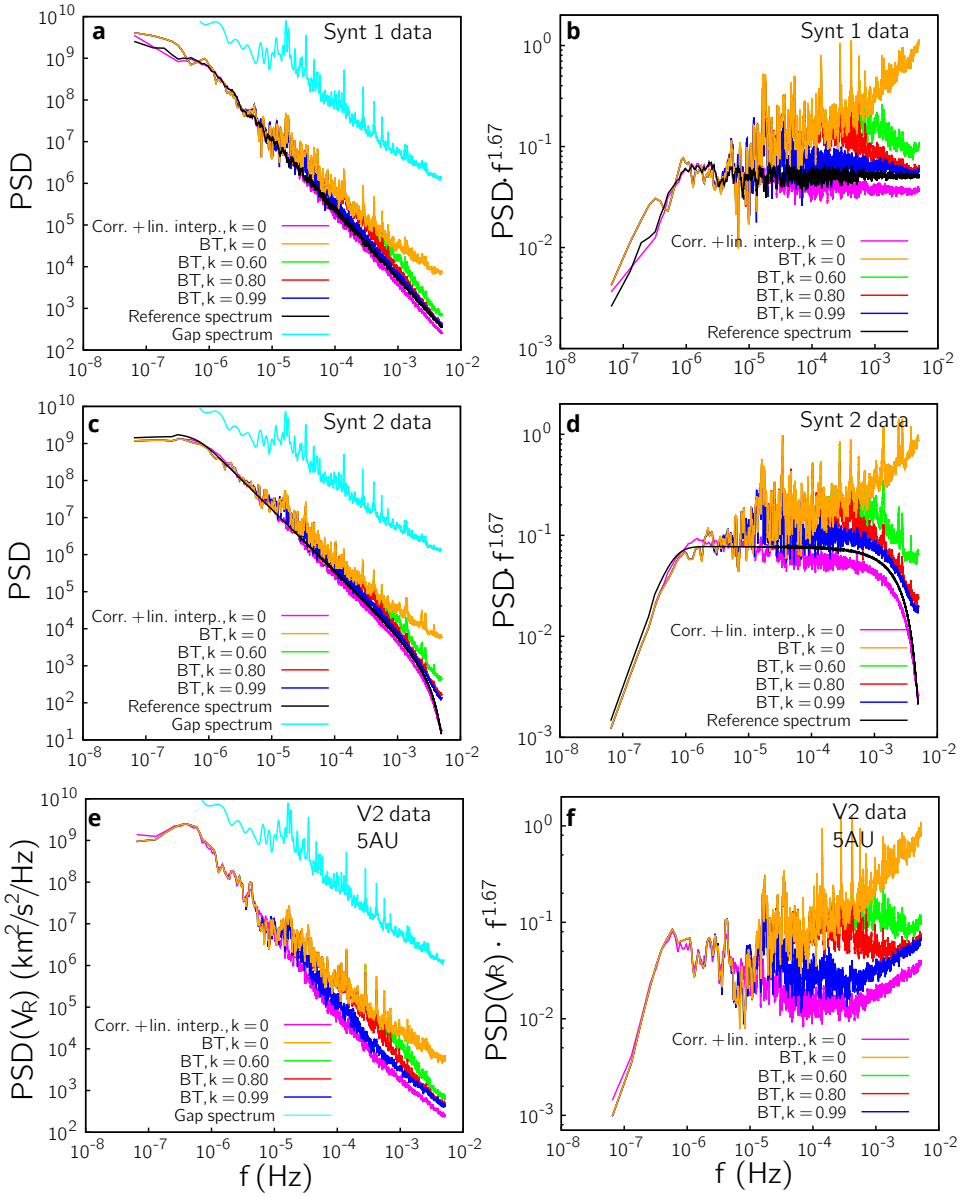

Figure 49: Spectral estimation (30% gaps), comparison of correlation methods (BT, CI). **(a-d)** tests on gapped (30% missing data) synthetic data sets and **(e,f)** solar wind V2 data at 5 AU. The gap spectrum is shown for comparison in left panes (it has been shifted for clarity). *Right panels*: compensated spectra.

$f > 10^{-5}$ Hz for *synt1*, while for *synt2* it is 5.8% for $f = [10^{-5}, 5 \cdot 10^{-4}]$ Hz, and 21% for $f = [5 \cdot 10^{-4}, 5 \cdot 10^{-3}]$ Hz. The spurious peak at $f \approx 1.5 \cdot 10^{-5}$ Hz is still present.

However, we would like to highlight that such improvement can not be considered a general fact, as it is not observed from the analysis of heliosheath data sets where 70% of data are missing.

We conclude therefore that the basic BT method is not suitable for solar-wind Voyager data beyond 1 AU.

4.5.2 *Correlation spectra, the method of linear interpolation (CI).*

Maybe the simplest technique is to interpolate missing data. We investigated the effect of a linear interpolation of the whole period, prior to the computation of the autocorrelation function. For data sets with 30% of missing data and a sufficiently high number of samples (about 10^5) the results are very good: in the specific case of *synt1* and *synt2*, the error is below 3% in the whole frequency range, as shown in tables 12 13, and in figure 49, see the pink curves. This method allowed to confidently compute SW power spectra for a frequency range over five decades, from V2 data at 5 AU. In fact the effect of the linear interpolation is, on the one hand, a better convergence of the correlation function to the correct values (compare the red and the black curves in figure 48). This completely prevents the non-physical peaks related to the gap distribution, while leaving physical peaks detectable. The spectra computation is fast, since it is done via FFT.

On the other hand, it is well known that the linear interpolator has a low-pass effect, yielding energy leakage from the higher to the lower frequency range of the spectrum. This effect makes the interpolation method unsuitable to heliosheath data, since where the it can overestimate the slope by more than 30% and underestimate the power in the higher frequency range. However, as shown in the next chapter, this method is useful to understand the spectral trend in the lower frequency range ($f < 10^{-5}$ Hz), where the other methods are less accurate. This is shown in figures 62, 63, 64. Moreover, the quite predictable behavior of this method allowed us to build a simple optimization procedure which aims at minimizing its error (see the method OP described below) .

Here it is worth mentioning a practical issue: before applying interpolation we set a uniformly-spaced grid ($t_I(n)$) which matches as much as possible the available points of the original grid. In fact, data-gaps which are not multiple of the nominal resolution make the interpolating grid not coincide with the original one, at least at some points. The resulting spectrum suffer form additional leakage in the higher frequency range leading to a considerable steepening of the spectrum. To prevent such leakage, we find the interpolating grid such that the $\sum_n |t_{\text{orig}}(n) - t_I(n)|$ is minimized. Another way consists of adjusting a little the original data by making all gaps multiple of the resolution δt_s.

4.5.3 *Windowed averaged spectra from arbitrary data subsets (SUB).*

A software was built to compute averaged spectra from selected data subsets. In this case the first parameter to be set is maximum size of gaps to be recovered by linear interpolation (L_g). This uniquely determines a number of subsets of the global dataset considered. These segments have variable length, depending on the gap distribution. Direct FFT after interpolation is then computed for those longer than a threshold, L_s, and the spectra are then averaged (ensembles of 80 to 400 subsets were considered). The codes use the dffti, dfftf, dfftb routines from FFTPack (Open source) libraries.

The low-pass feature of the linear interpolation results in an overestimation of the slope, increasing with L_g. For *Synt1*, the relative error on the spectral slope α lies between 1.9% ($T_g = 0.5$ h) and 5.4% ($T_g = 4$ h) in the range $f \in [10^{-5}, 10^{-3}]$ Hz, while in the last frequency decade it increases up to 8% for $T_g = 0.5$ h. For *Synt2*, the discrepancy lies between 0.4% ($T_g = 0.5$ h) and 2.4% ($T_g = 4$ h) in the range $f \in [10^{-5}, 10^{-3}]$ Hz. The Hann windowing was applied to reduce the leakage effect (spectral flattening) due to the segmentation. Indeed, the purpose is to reduce defects in the FFT output that are introduced by differences in the data at the start and end of the sequence. By comparing the pink and red curves in panel (**b**) of figure 51, one can perceive the windowing effect, that is a reduction of the $\approx 1/f$ noise. To preserve the total energy when the Hann window is applied, a factor of 2.66 to the PDS is needed.

This method works well also for magnetic field data in the heliosheath, where contiguous subsets of 12 h are available (this allows recovery of the range $f \in [2 \cdot 10^{-5}, 0.01]$ Hz, for 48-s data), see figures 62.

4.5.4 *Maximum likelihood stochastic data recovery (RP).*

The fourth procedure is a maximum likelihood data recovery method. This reconstruction is stochastic, but it is constrained by the true data where these are available. The complete description of the technique is given by Rybicki and Press [129] and an application in astrophysical context can be found in [115]. To our knowledge this is the first time such method is applied to recover spectra of solar wind turbulence. The recovery is reached in two steps: (i) a minimum variance recovery (equivalent to a Wiener filtering); (ii) an additional stochastic fluctuation about the former, based on a correlation function. In synthesis, following Rybicki's notations, the available, irregularly spaced data are the sequence $\mathbf{y} = \mathbf{s} + \mathbf{n}$, where $\mathbf{n}$ is the error array.

Minimum variance prediction (interpolation): the true value at a particular time, s_*, is expressed as a linear combination of the measured data:

$$s_* = \sum_{i=1}^{N} d_{*i} y_i + x_* = \mathbf{d}_* \mathbf{y} + \mathbf{x}_* \tag{147}$$

where $\mathbf{d}_*$ is a matrix of coefficients and $\mathbf{x}_*$ is the array of discrepancy of the estimate. When trying to understand the physical process which underlies the measurements, one can compute ensemble averages $\langle \cdot \rangle$. The minimum variance estimate at any specific point, $\widehat{s}_*$, is obtained by minimizing $\langle x_* \rangle$:

$$\widehat{s}_* = \mathbf{S}_*{}^{\mathsf{T}} [\mathbf{S} + \mathbf{N}]^{-1} \mathbf{y} \tag{148}$$

where $S_{ij} = \langle s(t_i) s(t_j) \rangle$ is the correlation matrix, $S_{*ij} = \langle s_* \mathbf{s} \rangle$ is a correlation vector, $N_{ij} = \langle n(t_i) n(t_j) \rangle$ is the error matrix. These should only depend on the time lags $t_i - t_j$, if the signal is *statistically stationary*. If *noise values are uncorrelated*, $\mathbf{N}$ is diagonal. Moreover we suppose that *signal and noise are uncorrelated*, $\langle \mathbf{s}\mathbf{n}^{\mathsf{T}} \rangle = 0$. The missing data points are treated by this procedure as available data with $n \to \infty$. Since the correlation matrix is unknown, one can use a correlation model or an estimate. We estimated the correlation matrix from the available data, as described below. The minimum variance reconstruction appears very smooth (see the green curve in figure 50), and "unlikely".

Stochastic process: a stochastic process is added to the minimum variance reconstruction, in a way to get possible realizations, constrained by the available data (see the red curve in figure 50). The procedure makes the Gaussian assumption for the random fluctuations, but the process still retain the correlation estimate used before (since solar-wind fluctuations are not Gaussian, this procedure cannot be used to study intermittency, though, it works well for power spectra). The final formula for the recovered data is (see the derivation in §4 of [129])

$$\mathbf{s} = \widehat{\mathbf{s}} + \mathbf{u}, \tag{149}$$

$$\mathbf{u} = \mathbf{s} - \mathbf{S}[\mathbf{S} + \mathbf{N}]^{-1} \mathbf{y}, \tag{150}$$

where $\mathbf{u}$ is a stochastic Gaussian process with correlation matrix $\mathbf{Q} = [\mathbf{S}^{-1} + \mathbf{N}^{-1}]^{-1}$. Operatively, the solution requires matrix inversion and eigenvalues computation (N^2 operations). It is therefore hard to recover the whole period of 180 days at once. Moreover, as discussed before, the estimate of the correlation function is not easy. However, since the biggest data gap is about 45 h at 5 AU (and 24 h in the heliosheath periods considered), it is not necessary to have the full correlation function. The correlation computation is quite good up to $\tau \sim 10$ days, as shown in figure 48. Therefore, it is possible to recover the complete sequence, provided it is split in several subsets. This is performed by our FORTRAN code, derived from routines published on the web page `http://www.lanl.gov/DLDSTP/fast/` which we have modified for the Voyagers solar

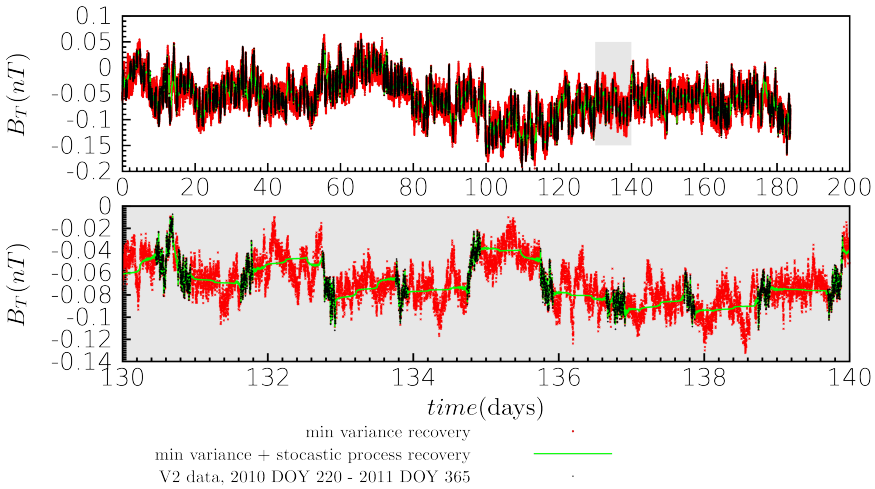

Figure 50: Maximum likelihood data recovery by RP. The figure shows an example of data reconstruction obtained from the RP method for magnetic field data in the heliosheath (V2, period form 2010 DOY 220 to 2011 DOY 365). *Black*: available data. *Green*: minimum variance estimation. *Red*: maximum likelihood recovery (minimum variance estimation with additional stochastic process). In the bottom panel a magnigication is shown.

wind data sets. Our code uses the DSYSV, DGEMV, DSYTRF, DSYTRI routines from the LAPACK libraries (open source). The code parameters include the length of the largest gaps to be interpolated, T_g, and the maximum subset length L_s.

Results are shown in figure 51 (**c**,**d**), green curves. This procedure is computationally more expensive than the others, but it improves the spectral estimation in the high frequency range by reducing the low-pass effect of the linear interpolator used in CI. Also in this case the discrepancy from the correct spectral slope is below 3%.

4.5.5 *Compressed sensing spectral estimation (CS)*

The methods presented above are considered classical methods. We investigated the possibility to exploit more recently developed techniques, coming from other scientific areas (as the telecommunication/image processing).

A first set of methods is based on adaptive FIR (Finite Impulse Response) filtering, introduced in 1996. These include Amplitude and Phase estimation techniques (APES,[79]), and their extension to gapped data (GAPES [138] and MAPES [143]).

The main issue related to APES-based algorithms is their computational complexity since they require inversion of a $N \times N$ matrix for each frequency, which is not viable for large datasets. For this reason, we did not consider these algorithms. Another set of techniques is based on an iterative adaptive approach [147], which have been proposed to improve APES. The IAA algorithm (and its missing-data versions MIAA[139] and SIAA [127]) allows to cope with spectral analysis of non-uniformly sampled data. However, it requires the inversion of a $N \times N$ covariance matrix at each iteration step, which make it unsuitable for our problem.

We opted for *Compressed Sensing* (CS), a new technique based on a recent theory which provides guarantees of exact or approximate recovery of sparse signals (that is, signals with few non-zero frequency components), see the works by Donoho [44], Candes, Romberg, and Tao [36, 37], and Candes and Wakin [38]). CS is a novel paradigm stating that certain signals can be recovered exactly even from fewer samples than those usually required by the Shannon theorem. These signals can be reconstructed in an exact way even if acquired in a "compressed" way (by storing only $m \ll n$ points), according to a sensing matrix $\mathbf{A}$ of size $m \times n$. In mathematical terms, CS studies the conditions to find the sparsest solution $\mathbf{x}$ of the undetermined linear system $\mathbf{y} = \mathbf{A}\mathbf{x}$. In particular, much effort has been devoted to study which families of sensing matrices A guarantee well-posedness of the problem and uniqueness of solution. In this regard, the need for *incoherence* between the sensing basis and the signal basis is an important concept of the theory. Partial Fourier matrices (say, discrete Fourier matrices with missing rows) are good matrices for CS (theoretical details on the number of rows etc can be found in [128, 46, 146]), motivated in particular by the applications in medical imaging problems such as MRI [81].

In the present study, CS is applied to solar wind data for the first time. [49, 57]. In this case:

- $\mathbf{y}$ consists of V2 available measurements (gapped=compressed), and $\mathbf{x}$ the complete data (actually, it is directly the spectrum).
- We can totally rely on CS is the signal is sparse. However, turbulent data usually are not, since all frequencies matter. However, we consider CS as a tool which returns an approximately good PSD for at least *some* frequencies. This should be enough to catch the power decay in the whole range of frequencies (see the discussion on HS data in the next chapter).
- Computational complexity is not a problem. Many algorithms which do not require matrix inversion are available. Moreover Fourier matrices do not need to be stored as they can be defined as functions. We formulated the problem as a Basis Pursuit DeNoising (BPDN)

$$\min_{\mathbf{x}} ||\mathbf{x}||_1 \quad \text{such that} \quad ||\mathbf{y} - \mathbf{A}\mathbf{x}||_2^2 < \sigma$$

and obtained the numerical solution through the SPGL1 Matlab® solver for sparse problems (suitable for the Fourier framework, see [18] for theoretical and practical details). Our script is published in the supporting information of [57] and reported below.

- Summary of results: very good spectral recovery in the intermediate/hi frequency range, some deficiency in the lower frequency range, especially for $f < 10^{-5}$ Hz for HS magnetic field data. The spectra require heavy smoothing, and cleaning of near-zero values.

```
clear all
close all
clc

%addpath spgl1-1.8/
dd=load('dati_U_hires_2008.0_2008.2.txt');% file format: [time(s), U1, U2, U2]
tot_run=1; % =n splits the data in n segments and computes averaged output
sigma=0.01;% noise parameter for bpdn compress sensing
step=192;  % data sampling time (sec)

nn=size(dd,1); % change nn if you want to read only the first nn point of file

d(:,1)=dd(1:nn,1)- dd(1,1);
d(:,2)=dd(1:nn,2)-mean( dd(1:nn,2) );
d(:,3)=dd(1:nn,3)-mean( dd(1:nn,3) );
d(:,4)=dd(1:nn,4)-mean( dd(1:nn,4) );

time=zeros(1,size(d,1));
time(1)=1;
for h=2:nn
gap(h-1)=round((d(h,1)-d(h-1,1))/step);
time(h)=time(h-1)+gap(h-1);
end

L=floor((floor(max(time)/tot_run))/2)*2% must be even
Vr=zeros(L/2, tot_run);
Vt=zeros(L/2, tot_run);
Vn=zeros(L/2, tot_run);

Vr_recovered=zeros(L, tot_run);

K=zeros(tot_run,1);
for run=1:tot_run
disp(run);
```

```
[~,ei]=min(abs(time-(L*(run-1)+1)));
[~,es]=min(abs(time-run*L));
window=[ei:es];
r=time(window)-time(window(1))+1;
K(run)=length(window);

% BASIS PURSUIT DENOISE

opA = @(x,mode) partialFourier(r,L,x,mode);
% This is now "A"
opts = spgSetParms('verbosity',0);
z = spg_bpdn(opA,d(window,2),sigma, opts);
% if one want to use bp instead of bpdn
%z = spg_bp(opA,d(window,2), opts);
% power spectrum
Vr(:,run)=K(run)*step*(abs(z(1:L/2))).^2;
z =  spg_bpdn(opA,d(window,3),sigma, opts);
%to check the correct recovery of input points
inverset2=ifft(z)*sqrt(L);
inverset1=partialFourier(r,L,z,1);
Vt(:,run)=K(run)*step*(abs(z(1:L/2))).^2;
z =  spg_bpdn(opA,d(window,4),sigma, opts);
Vn(:,run)=K(run)*step*(abs(z(1:L/2))).^2;
clear r

end

figure(1),hold on
plot(time(1:end),inverset1,'ob')
plot(time(1:end),d(:,3),'+r')
plot(time(end):-1:1,inverset2,'+c')

f=[1:L/2]'/(step*L)        %frequencies
Vr_mean=sum(Vr,2)/sum(K);
Vt_mean=sum(Vt,2)/sum(K);
Vn_mean=sum(Vn,2)/sum(K);
BP=[f, 2*Vr_mean, 2*Vt_mean, 2*Vn_mean, ...
2*(Vr_mean+Vt_mean+Vn_mean)];

%save('OUTPUT_CS.txt','BP', '-ascii');
figure(2)
loglog(BP(:,1), BP(:,5),'*r')
xlabel('f (Hz)');
ylabel('PSD |U|');
```

Results for synthetic datasets with 30% of missing points are shown in figure 51 (**c**,**d**), blue curves. The relative error in the spectral index, with respect to the true value (black curves) is below 2.5%, in the range $f \in [10^{-6}, 5 \cdot 10^{-3}]$ Hz of *Synt1*, and $f \in [10^{-6}, 10^{-3}]$ Hz of *Synt2*. Similar accuracy is obtained from tests conducted on Ulysses data with the same gap distribution as *synt1* and 2 (Panels **e**, **f** of figure 51).

Results for 70% of missing data are shown in the next chapter (§5.2), where the heliosheath region is considered.

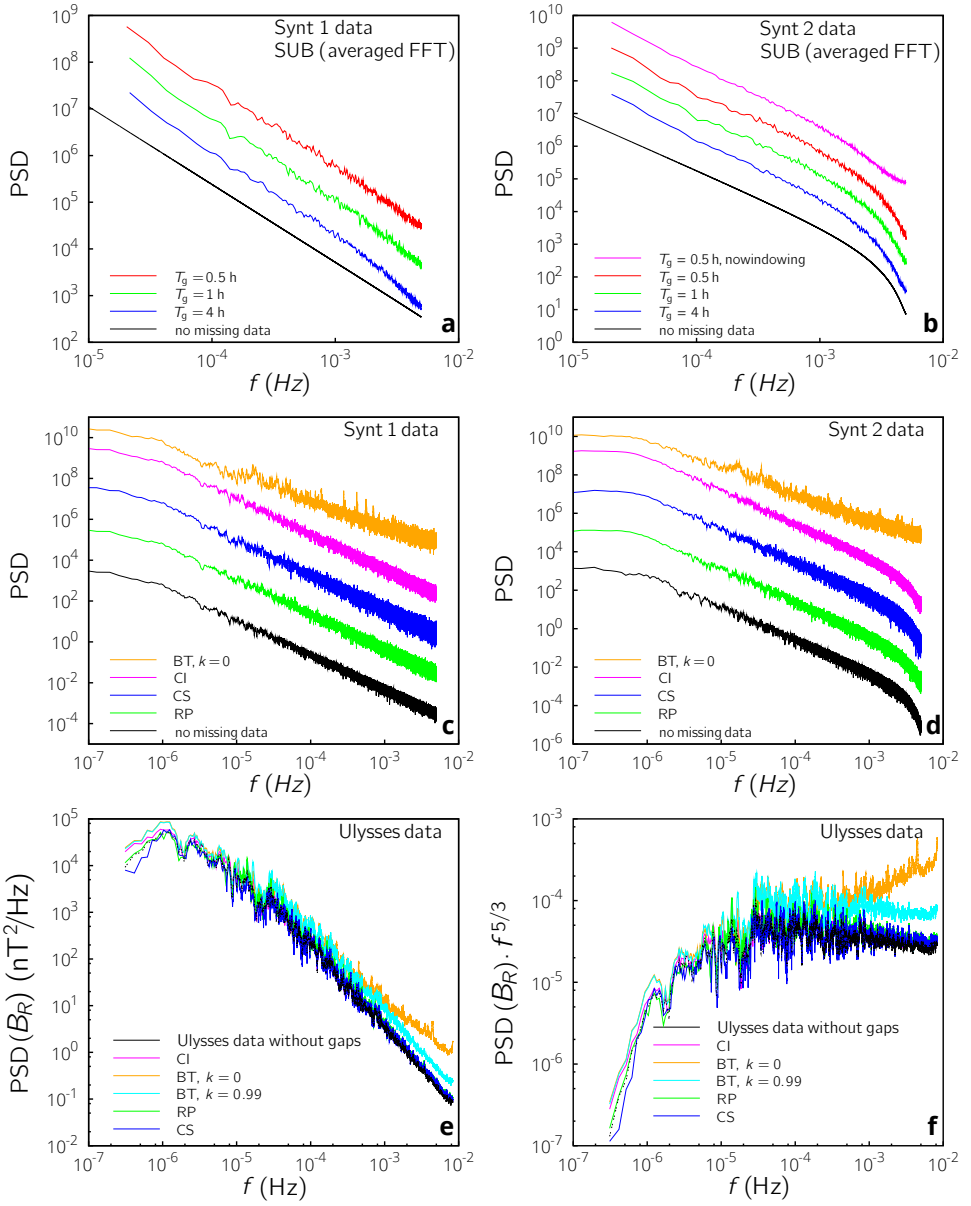

Figure 51: Spectral recovery validation on synthetic data sets and on Ulysses measurements. **(a,b)** Spectra by direct FFT on linearly interpolated subsets (SUB). Segments are selected so that the maximum gap length filled by the interpolation is T_g. Gap length is at least 12 h. The low-pass effect becomes evident as T_g increases, see (**a**), in the higher frequency range. The relative error on the spectral index in the range $f \in [10^{-5}, 10^{-3}]$ is between 1.9% ($T_g = 0.5$ h) and 5.4% ($T_g = 4$ h). For *Synt2* data, windowing helps to recover the correct spectral slopes (panel **b**). In this case, the error lies between 0.4% ($T_g = 0.5$ h) and 2.4% ($T_g = 4$ h) in the range $f \in [10^{-5}, 10^{-3}]$. **(c,d)** Spectral computation in the entire period. The discrepancy of the exponent is below 2.5% for the methods CI, RP, CS. A uniform smoothing is applied by averaging neighboring frequencies. The energy is preserved for all spectra, which have been shifted for clarity. **(e,f)** Spectrum of B_R as recorded by Ulysses in the period 1990, DOY 298 - 1991, DOY 45. Black line: spectrum from the complete dataset. The methods have been tested on Ulysses data after eliminating 30% of the points, obtaining the same gap distribution of V2 data. **(f)** compensated spectrum. From Gallana *et al.* [57].

4.5.6 *Optimization procedure leading to piecewise model spectra (OP)*

This procedure was set up by me in the hope of quantifying and fixing the error given by the linear interpolation method (CI). Despite the method is not supported by a sufficient theoretical background (at the current stage it is an heuristic technique), it leads to surprisingly good results which helped us to understand the shape of the spectrum, especially for heliosheath data.

We saw that the linear interpolation method (CI) returns a spectrum (labeled **AA** in the following, with reference to figure 52) having some discrepancy from the true spectrum (**A** in the following, unknown in principle), typically a lack of energy is observed after a certain frequency. This technique tries to answer to the following question. Would it be possible to do the inverse passage, that is recovering **A** from the knowledge of **AA**?

In principle this is not possible, since of course such problem does not have a unique solution. However, if some assumptions are made, our iterative optimization procedure in most cases converges to the correct spectrum. The assumption are similar to those made for RP:

- The signal is statistically homogeneous and uncorrelated to the gap distribution (roughly speaking, the behavior at unavailable times should not be much different than the one observed at measured points);
- The signal is multi-scale: with a continuum of frequencies, quasi-random phases, and a "simple" power spectrum which can be well described by power-laws.

The technique is explained with the help of figure 52, which shows a test made on synthetic data with 70% of missing points. In this case we know the true spectrum **A**. A movie showing the convergence is also available. The algorithm ultimately finds a model spectrum described by power laws (the red-dotted piecewise linear spectrum in the log-log space shown in the right panel). This is an approximation of the true spectrum. The model spectrum is determined by few control points (the red dots, in the figure), which can move in restricted frequency bands of arbitrary extension and boundaries. The procedure is made of the following steps:

1. From an initial model spectrum with random phases (**B** in figure 52, left panel), a dataset is obtained from inverse transform, analogously to what is usually done to generate synthetic datasets. The dataset has the same resolution and variance than the original.
2. Then, the sequence of missing points of the original dataset considered for the analysis (the only program input), is introduced in the synthetic data set.

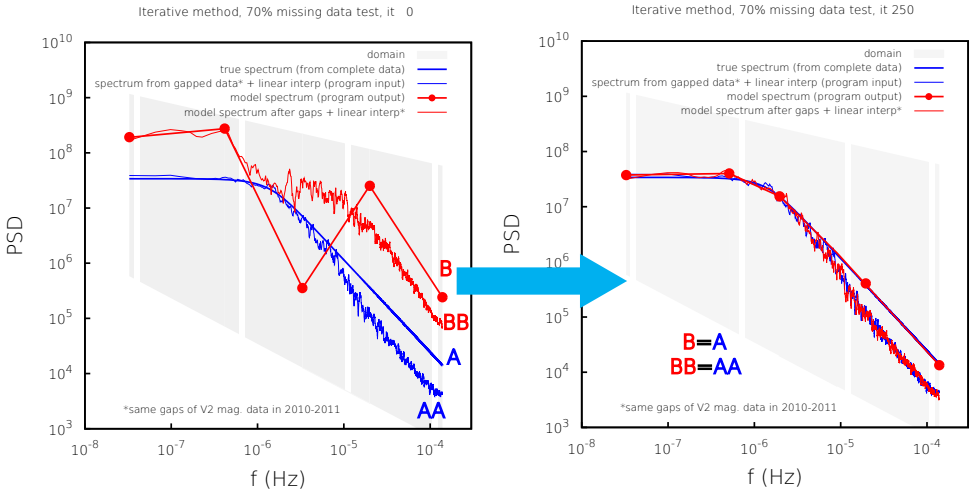

Figure 52: Optimization procedure, test on synthetic data with 70% gaps. *Left*: in red, the initial model spectrum (**B**) is shown for $M = 5$ control points. **BB** is the corresponding spectrum obtained after inverse transform $\rightarrow$ interpolation+correlation $\rightarrow$ FFT is applied (the method CI). The spectrum **AA** is the result of the correlation method CI on the Voyager gaped dataset (the only program input), while **A** is the true spectrum. *Right*: results after convergence by genetic optimization. Note that the model spectrum describes well the true spectrum. [External movie file: `movie_iterative_spectral_recovery.avi`]

3. The linear interpolation method CI is applied to the gapped dataset to get the power spectrum **BB**;

4. An average discrepancy functional at each k-iteration is defined as

$$\epsilon_k = \sum_{i=1}^{N/2} w_i |\log(BB_i) - \log(AA_i)|$$

   where the logarithm is used to ensure uniform convergence at all frequencies and a weights array (w_i) make all frequency ranges count equally (consider that in the discrete spectrum the number of points per decade increase linearly with the frequency)

5. An optimization process aims at minimizing ϵ, until **BB**=**AA**. This is done by modifying the parameters, namely the power level of the M control points and the frequency of the central ones, the first and the last being determined by the total signal duration and resolution. The total number of degrees of freedom is therefore $2M - 2$. After modification, a new model spectrum **B** is obtained and steps 2-4 are repeated. When **BB**=**AA**, then the model spectrum **B** should be a good approximation of the unknown true spectrum **A** (see the right panel of figure 52). This was indeed observed in all the tests carried out.

We observed that the convergence depends on M. $M \in [3,5]$ is a good option for our analysis (a number of points greater than ten often does not lead to convergence). Since the functional may not be convex, a genetic optimization algorithm was used, based of the software PIKAIA [41] already introduced in Part 1 of this dissertation. A faster version of our software have also been build, based on a gradient-descent algorithm. In this case, it is sometimes necessary to re-initialize the solution with a new random initial condition to get to convergence.

In addition to figure 52, results are shown in the next chapter, see §5.2.

4.6 The energy cascade in the inertial range of magnetohydrodynamic turbulence: a brief review

As for neutral fluid turbulence, even in magnetohydrodynamic (MHD) turbulence an inertial range ($k_{\mathrm{inj}} \ll k \ll k_{\mathrm{diss}}$) can be identified. This is typically characterized by an energy (kinetic and magnetic) power law cascade $E(k) \propto k^{\alpha}$ which describes the energy transfer among different scales, where many values for the spectral index α are possible, depending on the physical process which underlies the fluctuations behavior. In the collisionless plasma context, as the solar wind, the beginning of a dissipative range is not determined by particle collisions (the mean free path can be as long as few AUs), but on the electromagnetic interactions. In fact, a steeper ($\alpha \in [-4,-2]$) "dissipative" cascade is usually observed for scales smaller than the Larmor radius, see for instance Sahraoui et al. [131] and Alexandrova et al. [7] (this justifies the tests carried out on the *synt2* dataset).

Below a few inertial-range phenomenologies are described, without the claim to be exhaustive, since the topic is vast. For further details the reader may refer to the book by Biskamp [20] and the review by Zhou, Matthaeus, and Dmitruk [151]. Here the last authors' terminology is followed. The fluctuation spectral energy transfer rate is defined as

$$\varepsilon \sim \frac{u_k^2}{\tau_{sp}} \sim \tau_{\mathrm{t}} \frac{kE(k)}{\tau_{\mathrm{nl}}}, \tag{151}$$

where $u_{\mathrm{k}} = \sqrt{kE(k)}$ is the fluctuation velocity at the scale k^{-1}, $\tau_{sp}(k) = \tau_{\mathrm{nl}}^2(k)/\tau_{\mathrm{t}}(k)$ is the time scale of spectral transfer, $\tau_{\mathrm{nl}}(k) = (ku_k)^{-1}$ is the typical time scale of an eddy turnover, and τ_{t} the time scale of the third-order correlations. This last depends on the physical phenomenology and on the wavenumber range.

The classical Kolmogorov theory [75, 74] applied to MHD pictures a cascade scenario where local interaction occurs among similar scales. Such scenario is featured by the distortion of eddies due to *local straining*. About structures with large scale-separations,

a large-scale vortex can just advect the small eddies without exchanging energy. In this case, $\tau_t \approx \tau_{nl}$ and the well-known Kolmogorov spectrum is obtained:

$$E(k) = C_K \varepsilon^{2/3} k^{-5/3}, \tag{152}$$

where $C_K \approx 1.6 - 1.7$ is the Kolmogorov constant.

This model cannot satisfactorily and comprehensively describe MHD turbulence, which is highly anisotropic. Moreover, more than in neutral fluids, here *nonlocal interactions* of largely-separated scales may be marked. This intrinsically linked to the propagation of Alfvén wave packets, as can be seen from the incompressible equations of motion written in terms of the Eslässer variables $\mathbf{z}^{\pm} = \mathbf{v} \pm \mathbf{B}/\sqrt{4\pi\rho}$, representing the amplitude of Alfvén wave packets moving inward and outward, respectively:

$$\partial_t \mathbf{z}^{\pm} + \mathbf{z}^{\mp} \cdot \nabla \mathbf{z}^{\pm} = -\frac{1}{\rho_0}\nabla P + \frac{1}{2}(\nu + \eta)\nabla^2 \mathbf{z}^{\pm} + \frac{1}{2}(\nu - \eta)\nabla^2 \mathbf{z}^{\mp}, \nabla \cdot \mathbf{z}^{\pm} = 0, \tag{153}$$

where $P = p + \frac{1}{8\pi}B^2$ is the pressure, ν and η the kinematic viscosity and magnetic diffusivity, respectively. The first equation in terms of fluctuations about a background magnetic field $B = B_0$ result:

$$\partial_t \mathbf{z}^{\pm} \mp \mathbf{V}_A \cdot \nabla \mathbf{z}^{\pm} = -\mathbf{z}^{\mp} \cdot \nabla \mathbf{z}^{\pm} - \frac{1}{\rho_0}\nabla P + \frac{1}{2}(\nu + \eta)\nabla^2 \mathbf{z}^{\pm} + \frac{1}{2}(\nu - \eta)\nabla^2 \mathbf{z}^{\mp}, \tag{154}$$

where $\mathbf{V}_A = \mathbf{B_0}/\sqrt{4\pi\rho_0}$ is the average Alfvén velocity. From equations 154 it is possible to observe interesting physical aspects. First of all, note that while adding a uniform velocity does not change the dynamics of $\mathbf{z}^{\pm}$, a background magnetic field does. In this case, indeed, the two fields $\mathbf{z}^{+}$ and $\mathbf{z}^{-}$ are swept with the Alfvén speed in opposite directions (see the left hand side). Second, both $\mathbf{z}^{+}$ and $\mathbf{z}^{-}$ are needed for the occurrence of nonlinear coupling. Therefore, the effect of an average magnetic field is to separate the two components so as to inhibit the energetic cascade. On the basis of these arguments, in the case of dominant sweeping effect, Iroshnikov [68] and Kraichnan [77] proposed to assume the time scale of the triple correlations equal to the Alfvén time $\tau_A(k) = (V_A k)^{-1}$, obtaining the -3/2 IK spectrum (for isotropic turbulence)

$$E(k) = (V_A \varepsilon)^{1/2} k^{-3/2}, \tag{155}$$

The prediction of equipartition between kinetic and magnetic energy at high wavenumbers is known as the *Alfvén effect* and it was derived independently by Iroshnikov [68] and Kraichnan [77]. In this regard, the Alfvén ratio is defined as $r(k) = E_v(k)/E_m(k)$. Actually, even the last scaling law 155 is not always verified by observations. In fact, as pointed out by Matthaeus and Zhou [91], the two phenomenologies can coexist.

One step further was made in more recent theories which take into account for field anisotropy. This is the field of *weak turbulence* [58, 133], for which the sweeping is

dominant in the direction parallel to the mean magnetic field (the preferential direction of propagation of Alfvén waves, represented by wavenumbers $k_{\parallel}$), while the straining is dominant along the normal direction (wavenumbers $k_{\perp}$, the direction of no-propagation for Alfvén waves). In this condition, the scaling law of the energy along the normal direction is $E(k_{\perp}) \propto k_{\perp}^{-2}$ when $k_{\parallel} \neq 0$, and $E(k_{\perp}) \propto k_{\perp}^{-1}$ when $k_{\parallel} = 0$.

As regards strong anisotropic turbulence, investigations have been carried out on the so called *critical balance* conjecture [61], supposing the equivalence of the linear and the nonlinear time scales $k_{\parallel} V_{\mathrm{A}} \sim k_{\perp} u_{\perp}$ where $u_{\perp} = \delta B_{\perp} / \sqrt{4\pi\rho_0}$. In this case, the turbulence is considered strong and a relationship between parallel and perpendicular scales is found, $k_{\parallel} \sim k_{\perp}^{2/3}$, leading to different possible spectral decays in terms of $k_{\perp}^{-5/3 \text{ or } -2/3}$ and $k_{\parallel}^{-2}$ (find theoretical details in the work by Nazarenko and Schekochihin [101], and a partial evidence in [110, 111]).

Note, eventually, that the smallest relative discrepancy between the possible spectral power law exponents is about 10%. This justifies the need for highly accurate spectral recovery methods.

Dispersion of large-scale Alfvén waves, hydrodynamic analogy

In Part 1 of this dissertation, some specific issues related to the dispersion properties of hydrodynamic waves in neutral fluid have been highlighted. We plan as a future work to extend those concept to the field of magnetohydrodynamics, as they could give new perspectives about solar wind fluctuations and energy transport properties. In fact, from the classical MHD description based on the linearizion around a uniform mean magnetic field $\mathbf{B}_0 = B_0\hat{\mathbf{x}}$, dispersive effects do not arise. In this case, in fact, the dispersion relation for the MHD Shear Alfvén wave is $\omega^2 = (\mathbf{k}\cdot\hat{\mathbf{x}})^2 V_A^2$. Note that such dispersion relation is almost identical to the one observed in neutral hydrodynamics for small waves in uniform flow, $\omega = Uk\cos\phi$ (here, the direction of propagation is unique). Waves orthogonal to the mean flow are stationary; analogously, Alfvén waves do not propagate across magnetic field lines.

In hydrodynamics, we observed that a shear in the basic flow induces wave dispersion. We highlighted [42] that both nondispersive and dispersive components can coexist in the system for a fixed value of the control parameter (see 1.4).

For magnetized plasmas, two main classes of Alfvén waves can be identified based on their frequency scale: MHD waves (low-frequency compared to the Larmor frequency) and high-frequency waves (kinetic scales). Dispersion is usually studied for the second type of Alfvén waves. From a kinetic description, in fact, analytical dispersion relations can be derived. In this high-frequency regime, two sets can be distinguished: the kinetic Alfvén waves (KAW, $m_e/m_i << \beta < 1$) and the inertial Alfvén waves (IAW, $\beta << m_e/m_i$), depending on the electron plasma beta parameter [134]. Recent studies ([125, 73, 82, 116, 134, 56]) show that the kinetic description allows to take into account for dispersion effects due to finite gyroradius, electron thermal pressure and electron finite mass. Propagation and spreading of Alfvén waves across the magnetic field lines have also been detected at the Large Plasma Device in 1997 [59].

But what about the large-scale MHD shear Alfvén wave? In contrast to the kinetic case, dispersive effects do not arise from the classical MHD description.

However, only very recently wave dispersion was observed to show up from a multifluid analysis (see the recent work by Zank, ApJ 2014 [150]) from dissipative effects (ν,η), and from finite gyroradius effects. We suggest as another source of dispersion the presence of nonuniform background velocity and magnetic fields. The last point in particular is not investigated much in the literature.

We hypothesize that the presence of velocity and magnetic field gradients could change considerably the dispersion properties of the shear Alfvén wave, in analogy to what we observed in internal waves in sheared neutral fluid flows shown in Chapter 1. Analysis of dispersion for large-scale Alfvén waves due to magnetic shear may clarify the mechanisms underlying the transport properties in the heliosheath, as will be discussed in Chapter 5.

4.7 **Plasma and magnetic field power spectra at 5 AU**

Power spectra over 5 frequency decades ($6.4 \cdot 10^{-8} < f < 5 \cdot 10^{-3}$ Hz) from V2 data near 5 AU are shown in figure 54, for each component of velocity and magnetic field. A comparison between the methods CI, CS, RP is also given in figure 55, where the kinetic and magnetic energy spectra are shown. All of them provide a very good level of accuracy. Thermal speed and density spectra are reported in figure 56, together with the Alfvén ratio. A summary of the spectral power law exponents can be found in table 14, while the characteristic temporal scales of the fluctuations are presented in table 15.

Table 14: Spectral index near 5 AU from Voyager 2 data. The spectral power law exponents are computed via linear regression in the log-log space from both the smoothed and unsmoothed spectrum. The maximum error on spectral indexes is about 0.07. It includes the differences among different spectral recovery methods, and also the uncertainty on the linear fit.; $\mathbf{b} = \mathbf{B}/\sqrt{4\pi\rho}$ is the magnetic field in Alfvén units.

Spectral index, V2 1979 DOY 1-180				
f range	v_R	v_T	v_N	E_k
$10^{-6} \div 4 \cdot 10^{-4}$	-2.00	-1.49	-1.48	-1.67
$4 \cdot 10^{-4} \div 5 \cdot 10^{-3}$	-1.18	-1.26	-1.48	-1.33
f range	B_R	B_T	B_N	E_{mB}
$10^{-6} \div 3 \cdot 10^{-5}$	-1.21	-1.52	-0.88	-1.26
$3 \cdot 10^{-5} \div 5 \cdot 10^{-3}$	-1.62	-1.73	-1.82	-1.76
f range	b_R	b_T	b_N	E_{mb}
$10^{-6} \div 3 \cdot 10^{-5}$	-1.24	-1.49	-1.11	-1.34
$3 \cdot 10^{-5} \div 5 \cdot 10^{-3}$	-1.48	-1.67	-1.70	-1.65

4.7.1 *Plasma velocity fluctuations*

The plasma kinetic energy spectrum shows a power law decay with index $\alpha_{Ek} \approx -1.67$ in the frequency range $f \in [10^{-6}, 4 \cdot 10^{-4}]$ Hz. The energy cascade seem therefore consistent with the Kolmogorov prediction of -5/3 in the inertial range. However, as will be shown in the following paragraph, special attention should be paid to correctly interpret the spectral slopes. The system presents anisotropy which can be here observed from the different decay rate of the velocity components. It can be noted that the components orthogonal to the radial direction experience a spectral cascade closer to the Iroshnikov-Kraichnan value ($\alpha_{v_T} \approx \alpha_{v_N} \approx -1.5$). The radial component, on the

other hand, show a much steeper decay, $\alpha_{v_R} \approx -2$. In this regard, few considerations

Table 15: Integral scale and Taylor micro-scale near 5 AU. from Voyager 2 data. The integral scale (T) and the Taylor micro-scale (τ), are deduced from the one-dimensional spectra by using the classical formulas of homogeneous and isotropic turbulence [98] $T = \int_0^{+\infty} E(f) f^{-1} \mathrm{d}f / \int_0^{+\infty} E(f) \mathrm{d}f$ and $\tau^2 = \int_0^{+\infty} E(f) \mathrm{d}f / \int_0^{+\infty} f^2 E(f) \mathrm{d}f$, where $E(f)$ is the spectrum of the relevant quantity.

T_{E_v}	Kinetic macro-scale	26.8	days
T_{E_m}	Magnetic macro-scale	25.9	days
T_N	Density macro-scale	13.1	days
T_{vth}	Thermal speed macro-scale	11.0	days
T_{Hc}	Cross-helicity macro-scale *	25.1	days
τ_v	Kinetic Taylor micro-scale	1.54	h
τ_m	Magnetic Taylor micro-scale	0.85	h
τ_N	Ion density Taylor micro-scale	1.04	h
τ_{vth}	Ion thermal speed Taylor micro-scale	0.85	h
τ_{Hc}	Cross-helicity Taylor micro-scale *	5.17	h

* [67]

have to be made on the fluctuation time scales. If one thinks that the plasma traveling at the average speed of $V_{\mathrm{SW}} = 450$ km/s takes $t_{\mathrm{SW}} = 3.3 \cdot 10^5$ s (3.8 days) to reach 5 AU, and that the velocity fluctuations can be as high as $\delta V \leq V_{\mathrm{A}} \approx 50$ km/s, we can estimate the time necessary for one eddy turnover at a certain frequency as

$$\tau_{\mathrm{e}} \sim \frac{\lambda}{\delta V} \sim \frac{V_{\mathrm{SW}} f^{-1}}{\delta V} > \frac{V_{\mathrm{SW}} f^{-1}}{V_{\mathrm{A}}} \tag{156}$$

Where λ if the typical size and f is the frequency measured at the spacecraft, represented in our spectra (the validity of the Taylor hypothesis is implied in Eq. 156). The number of turnovers of such plasma fluctuation from the Sun to the spacecraft is then $n_e \sim t_{\mathrm{SW}}/\tau_{\mathrm{e}}$. Consequently, one can see that the condition for a fluctuation to experience at least one typical eddy turnover is

$$f > f_e = \frac{V_{\mathrm{SW}}}{t_{\mathrm{SW}} V_{\mathrm{A}}} \quad \text{at 5 AU} \quad f_{\mathrm{e}} \approx 2.7 \cdot 10^{-5} \text{ Hz}, \tag{157}$$

Fluctuations measured at lower frequencies lead to eddy turnover times greater than the age of the plasma, and therefore they cannot be considered "true" turbulent fluctuations. Indeed, a mild spectral flattening can be perceived for $f < f_{\mathrm{e}}$, for the T and N velocity components (top panel of figure 54 and left panel of figure 55). Such flattening is more visible in the magnetic field spectra (figure 54, bottom panel).

How is the steep f^{-2} spectrum explained? The 180-day period considered includes jumps in the plasma velocity and magnetic fields, mainly related to shocks delimiting interaction regions of slow and fast wind streams, crossings of the sector boundary, or indicating the presence of coherent structures ejected from the Sun. In order to discriminate the fluctuations due to turbulence from other phenomena, we followed the approach developed by Roberts and Goldstein [122], and Burlaga, Mish, and Roberts [29] for removing jump points from the time series. A jump point j is considered such if

$$|\langle x\rangle_j^{4h+} - \langle x\rangle_j^{4h-}| > M \cdot \min(\sigma_j^{4h+}, \sigma_j^{4h-}), \tag{158}$$

where $\langle x\rangle_j^{4h-}$ and σ_j^{4h-} represent the local average and standard deviation of a field component x in a 4-hour period, taken 1-h before the time instant t_j, while $\langle x\rangle_j^{4h+}$ and σ_j^{4h+} indicate the same statistics for a 4-hour period taken 1-h after t_j. Roberts and Goldstein [122] used $M = 20$, so that for their dataset the percentage of jump points was 8% of the total data. We tested $M = 20$ and $M = 10$. In these cases, the amount of jump points is 6.4% and 12.5%, respectively. Once the points have been detected, a piecewise linear trend signal is obtained by interpolating the jump points and it is then subtracted from the original signal, see figure 53, panels (**a**,**b**).

We applied this procedure to the radial component of plasma velocity and to the tangential component of the magnetic field, since such components feature the greatest large-scale variations. A cutoff frequency is found, which separates the frequency range where the jump series is dominant from the range where the fluctuations prevail. This cutoff frequency f_j falls inside the range $2 \cdot 10^{-6} < f_j < 6 \cdot 10^{-6}$ Hz.

As regards both v_R and b_T, the contribution to the spectrum is mainly due to:

- Field fluctuations $\rightarrow f > 2 \cdot 10^{-5}$ Hz (0.6 days, $\lambda \approx 0.15$ AU)
- Jumps $\rightarrow f < 10^{-6}$ (11.6 days, $\lambda \approx 3$ AU)

In the intermediate range $10^{-6} < f < 2 \cdot 10^{-5}$, both jumps and fluctuations contribute to the spectrum, see panels (**e**, **f**). Different choices of the multiplier H only produce a mild difference on the results. The fluctuation spectra flatten for frequencies below the cutoff, this effect is particularly evident for v_R (figure 53 **c**, **d**). However, the spectral decay after the break keeps fast, with a slope equal to -2.

In the higher frequency range $4 \cdot 10^{-4} < f < 5 \cdot 10^{-3}$, a flattening is observed in the velocity spectra ($\alpha_{E_k} \approx -1.33$). This fact has been observed, for instance, also by [89] and [121]. Similar spectral trends have been found for the proton density, thermal speed fluctuations, and Eslässer variables spectra [85, 86], especially in high-speed streams close to the Sun. The hypothesis of aliasing from higher-frequency phenomena could be excluded by some tests performed on synthetic data sets. It is possible, instead, that such flattening is due to the PLS instrument uncertainty, which is about $\pm$ 2 km/s (see

§4.3). If modeled as a white noise, it translates in the gray uncertainty band shown in figure 54. By means of tests on synthetic data (with the same noise/signal ratio as V2 radial velocity data) we showed that flattening in the last decade may actually occur (the reader may see figure 3 of Ref. [57]). Eventually, in this regard, the hypothesis of spectral leakage from low to high frequencies have been excluded by coupling the method CI to a prewhitening filter, which leads to same results without PW (the relative difference on the spectral index was below 1%).

A peak can be observed in the spectra of v_T and v_N at $f = 2.6 \cdot 10^{-3}$ Hz. While it is certainly not due to the data gap distribution (also the method SUB, FFTs of contiguous subsets, is able to see it), it may be due to instrumental interferences. In fact, it is sharp and far from the ion Larmor frequency and the other typical frequencies of the plasma (table 10).

4.7.2 *Magnetic field fluctuations*

Power spectra of the magnetic field components are presented in the bottom panel of figure 54, while the magnetic energy spectrum is shown in figure 54. Also in this case, power laws are found. The magnetic energy exponent measured in the inertial range at $f > 3 \cdot 10^{-5}$ Hz is typically higher than the velocity one, if the magnetic field B (nT) is considered ($\alpha_{mB} \approx -1.75$), while the locally normalized field $b = B/\sqrt{4\pi\rho}$ (km/s) shows an energy cascade similar to the kinetic energy one ($\alpha_{mb} \approx -1.65$, see table 14). The steeper magnetic energy cascade with exponents as high as -1.8 still lack an explanation. Anyways, it has been observed by a number of authors [89, 72, 121, 130], in contrast to other observations closer to the Kolmogorov slope [112].

The magnetic spectrum flattens in the range $f < 3 \cdot 10^{-5}$ Hz, where the slope approaches -1. The frequency range of this flatter part, in the magnetic field case, seems more extended in comparison to the velocity case. A discussion on such slow decay was made by Roberts [121], where the -1 slope have been associated with the degree of Alfvénicity of the wind, that is the presence of large-scale Alfvénic wave fluctuations taking origin at the Solar corona and carrying energy out in the system, and acting as a reservoir for the turbulent cascade. This range was found to reduce as the distance from the Sun. However, our analysis in the heliosheath region show the presence of such spectral decay even at distances as high as 100 AU (see §5.3 and §5.4).

Anisotropy characterizes the fluctuation dynamics at all scales, as can be inferred from the different spectral decays of the field components. In particular, in the low-frequency range the dominant T component is associated with large-scale magnetic field amplification or reduction due to compression and rarefaction regions resulting from the

interaction of fast and slow wind streams. Note also that the radial component decays slower ($\alpha_{b_R} \approx -1.6$) than the other two, in the inertial range.

Figure 56 (**a**) shows the Alfvén ratio, defined as

$$r_A(f) = \frac{E_k(f)}{E_m(f)} \tag{159}$$

where E_m is the magnetic energy spectrum in Alfvén units. The Alfvén ratio is usually less than one in the inertial range, where the magnetic energy exceeds the kinetic energy [142] [88]. Moreover, the minimum value is lower than 0.5, as observed in slow-wind streams at 1 AU [106, 85]. For completeness, the spectra of ion density and thermal speed are shown in figure 56 (**b**,**c**).

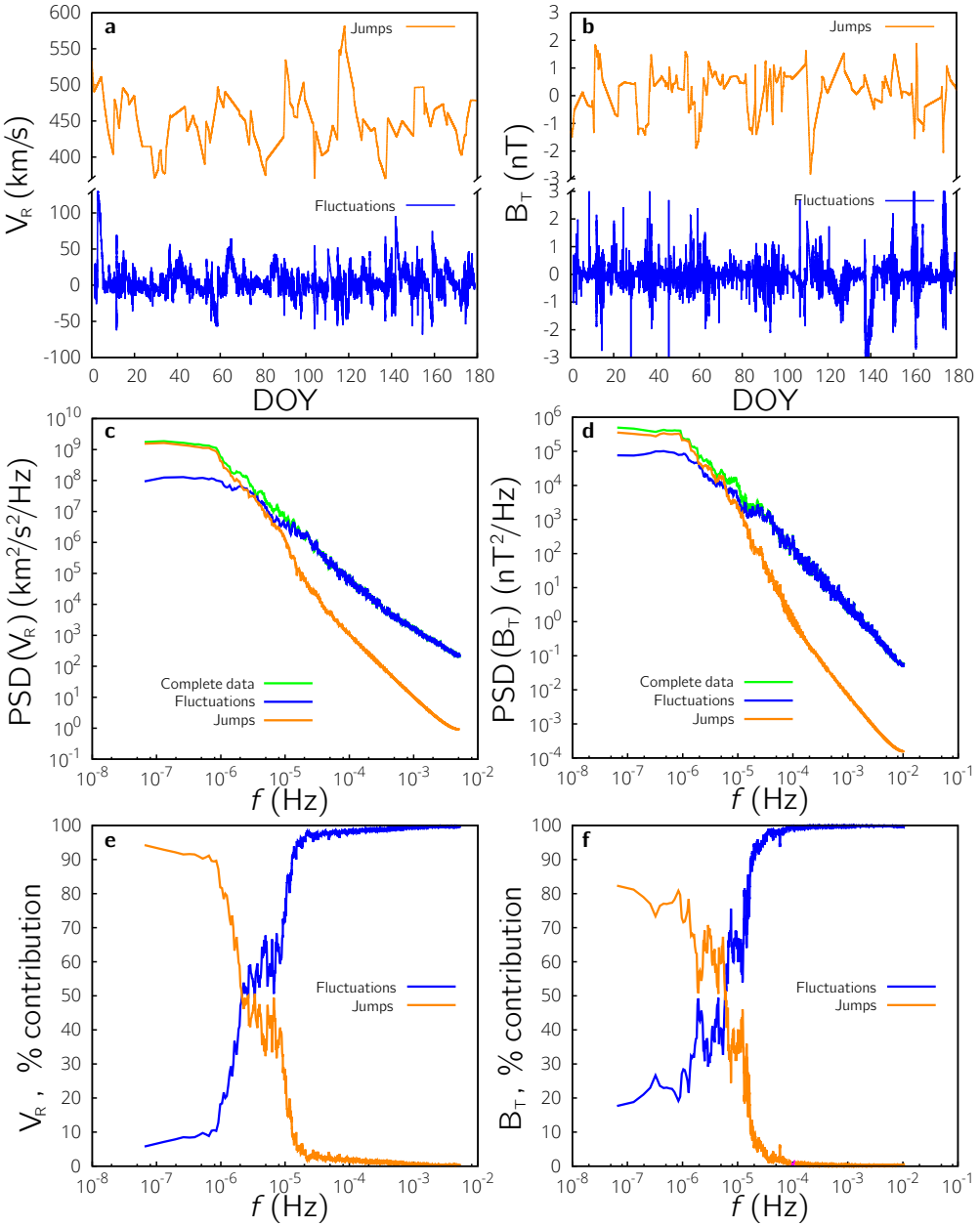

Figure 53: Effect of jumps in the V2 time series near 5 AU. Orange curves are used for the "jump series" obtained by linear interpolation of jump points, while blue curves are for the Voyager "fluctuation series", obtained by subtracting the jump series from the original dataset. In left panels, the radial velocity component v_R is considered, while the right panels show the tangential component of magnetic field, B_T. **(a, b)** Time series. **(c, d)** Power spectra. **(e, f)** Percentage contribution of the jump and fluctuation series to the spectrum of the original signal. Note that for $f \gtrsim 2 \cdot 10^{-5}$ Hz discontinuities in the data have a negligible effect on the power spectrum.

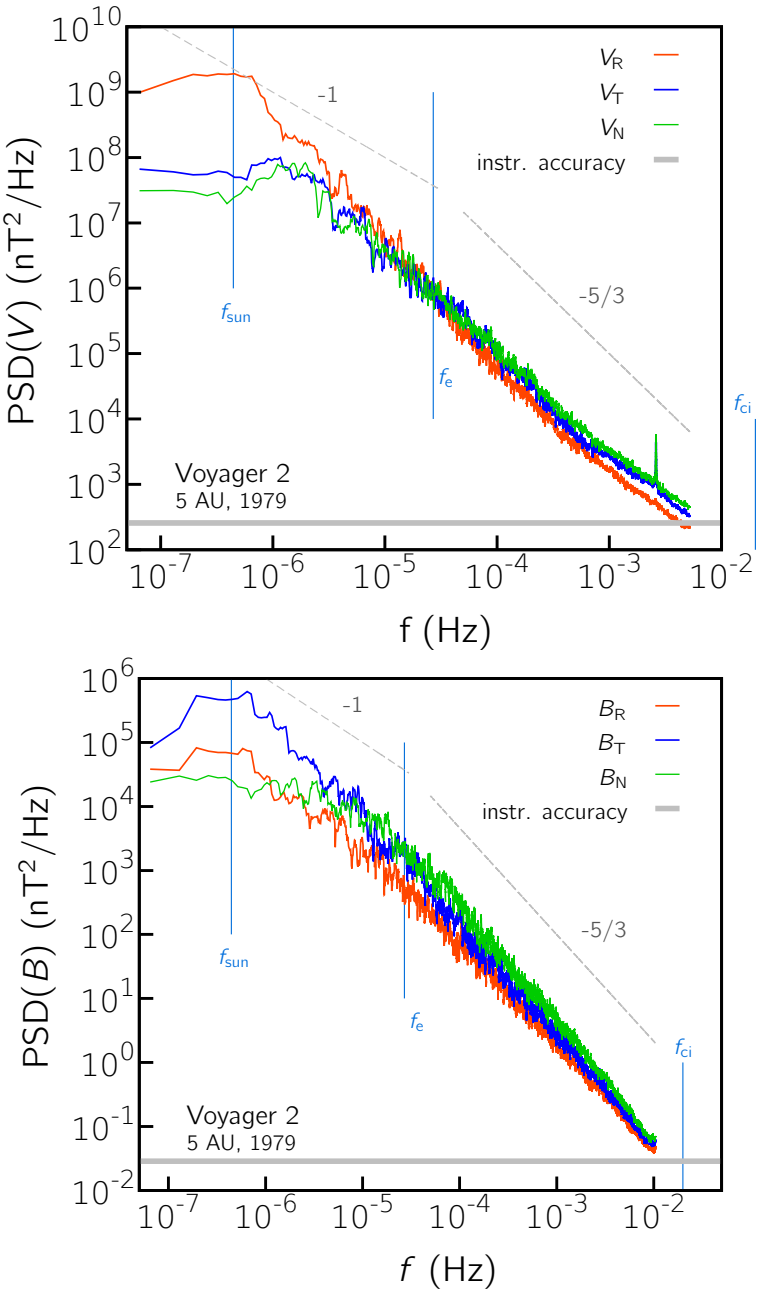

Figure 54: Solar wind velocity and magnetic field spectra from V2 data near 5 AU *Top:* Spectra of plasma velocity components computed via the correlation method CI. The solar rotation frequency, the cut-off frequency for active fluctuations f_e and the ion Larmor frequency f_{ci} are indicated. *Bottom*: spectra of magnetic field components. The grey bands in both panels indicate the instrumental uncertainty (modeled as a white noise). The computed spectral exponents are presented in table 14, here the -1 and -5/3 slopes are reported for a visual comparison only.

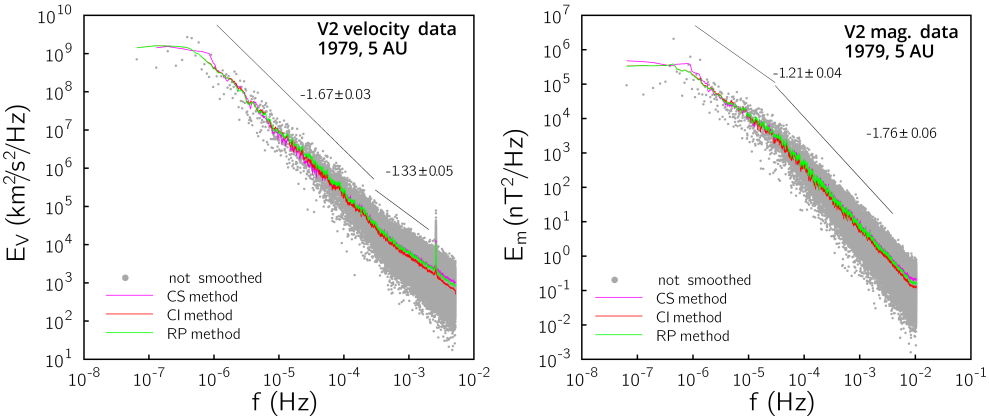

Figure 55: Solar wind kinetic and magnetic energy spectra from V2 data near 5 AU. *Left*: kinetic energy spectra, comparison of three methods of analysis (compressed sensing CS, correlation method after linear interpolation CI and maximum likelihood recovery RP). In gray, the unsmoothed CI spectrum is shown. **(c,d)** Magnetic field spectra. The computed spectral exponents are presented in table 14. Figure from [57].

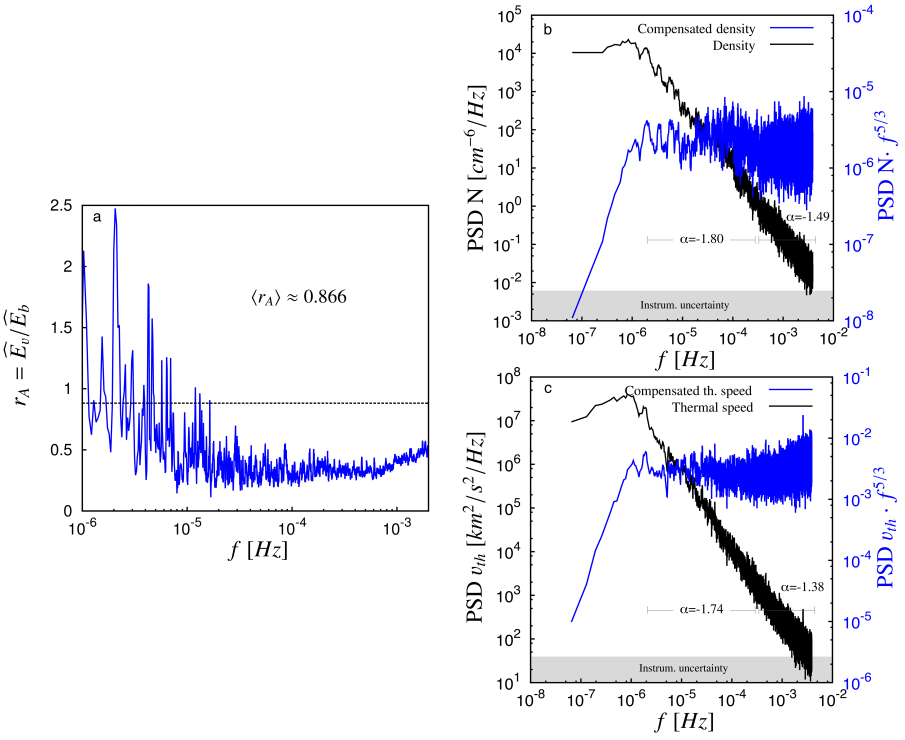

Figure 56: Alfvén ratio and spectra of ion density and thermal speed near 5 AU. **(a)** Alfvén ratio, r_A. **(b, c)** Ion density and thermal speed spectra. Figure published in Ref. [57].

4.8 **Cross and magnetic helicity at 5 and 29 AU**

Beside the total energy $E = \frac{1}{2}\int \mathbf{v}^2 + \mathbf{b}^2 \, \mathrm{d}\mathcal{V}$, other two integral quantities are known to be invariant in the ideal ($\nu, \eta = 0$), single-fluid magnetohydrodynamic regime, as first discussed by Woltjer [145]: the *cross-helicity* H_c and the *magnetic helicity* H_m. They play a fundamental role in the dynamics of plasmas, being related to field topology, wave propagation, dynamo processes, generation of large-scale structures and self-organization of turbulent motion Yokoi and Balarac [149] and Yokoi [148]. In the case of turbulent plasmas, a statistical description is usually adopted to describe the field. The study of these quantities, although they are not invariant in the dissipative case, provides significant insights into the flow dynamics as recognized by Moffatt [95]. The integral cross helicity and magnetic helicity are defined as

$$H_\mathrm{c} = \frac{1}{2}\int \mathbf{v}\cdot\mathbf{b} \, \mathrm{d}\mathcal{V}, \tag{160}$$

$$H_\mathbf{m} = \int \mathbf{A}\cdot\mathbf{B} \, \mathrm{d}\mathcal{V}, \tag{161}$$

where A is the magnetic vector potential so that $\mathbf{B} = \nabla \times \mathbf{A}$. Note that the definition of H_m is analogue to that of the kinetic helicity, material invariant for inviscid neutral fluid flows, $H_\mathrm{k} = \int \mathbf{v}\cdot\boldsymbol{\omega} \, \mathrm{d}\mathcal{V}$, where $\boldsymbol{\omega} = \nabla \times \mathbf{v}$ is the vorticity field (Thomson (Lord Kelvin) [141] was the very first who introduced concept of helicity, in 1869). The integrands $h_\mathrm{c} = \mathbf{v}\cdot\mathbf{b}$ and $h_\mathrm{m} = \mathbf{v}\cdot\mathbf{b}$ represent the helicity density. Typically, in solar wind analysis the fluctuating helicities are considered

$$H'_\mathrm{c} = \frac{1}{2}\int \delta\mathbf{v}\cdot\delta\mathbf{b} \, \mathrm{d}\mathcal{V}, \tag{162}$$

$$H'_\mathbf{m} = \int \delta\mathbf{A}\cdot\delta\mathbf{B} \, \mathrm{d}\mathcal{V}, \tag{163}$$

In practice, for fluctuating statistically homogeneous fields, volume averages are considered so that the fluctuating helicity densities are $h'_\mathrm{c} = \langle\delta\mathbf{v}\cdot\delta\mathbf{b}\rangle$ and $h'_\mathrm{m} = \langle\delta\mathbf{A}\cdot\delta\mathbf{B}\rangle$. Both the helicities are pseudoscalars (since the magnetic field is a pseudovector), this means that they change sign under coordinate inversion. In a statistically mirror-symmetric system therefore, these quantities vanish. When mirror symmetry is broken, non-vanishing helicity is observed.

Moreover, a topological interpretation can be given (1969, Moffatt [95]). In fact, the helicity can be considered as a measure of linkage between field lines. This can be easily shown with reference to the simple configurations of figure 57, representing a vortex tube linked to a magnetic flux tube. Here, the cross helicity here is $H_\mathrm{c} = 2n\Phi_\omega\Phi_b$, where

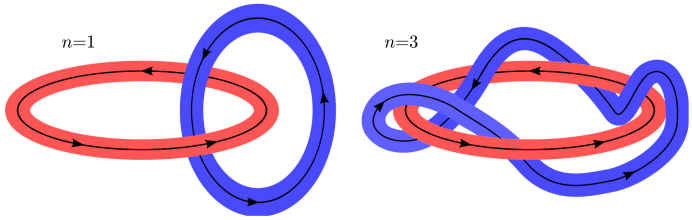

Figure 57: Topological interpretation of helicity. Sketch of linked vortex/magnetic-flux tubes with different number of windings n, generating non-vanishing helicity. In the case of cross helicity H_c, a vortex tube is linked to a magnetic flux tube. In the case of magnetic helicity H_m, two magnetic flux tubes are linked. If instead the kinetic helicity H_k is considered, both tubes are vortex tubes. From [67].

Φ_ω is the flux of vorticity, Φ_b the magnetic field flux, and n the number of windings between the two tubes. The same reasoning can be applied to the magnetic helicity. In this case, the linkage is between two magnetic field flux tubes, $H_m = 2n\Phi_B\Phi_B$. In other words, the helicity is an index of the knottedness of the magnetic field lines (or the knottedness of the vortex tube with the magnetic field flux tube). It is and therefore a measure of the topological complexity of the field.

From a more physical point of view, the turbulent cross helicity is related to the presence of Alfvén waves, being an index of the correlation (alignment) between the velocity and magnetic field. A non-zero H_c' indicates indeed a predominant direction of propagation of Alfvén waves (inward or toward the Sun, along the Parker's spiral large-scale magnetic field). This is also related to the presence of nonlinear mixing. In fact, from the relation

$$\frac{(\mathbf{v}\cdot\mathbf{b})^2}{|\mathbf{v}|^2|\mathbf{b}|^2} + \frac{(\mathbf{v}\times\mathbf{b})^2}{|\mathbf{v}|^2|\mathbf{b}|^2} = 1, \tag{164}$$

one can observe that when H_c is high, the nonlinear mixing contained in $\mathbf{v}\times\mathbf{b}$ (in the induction equation) is reduced.

The magnetic helicity is known to play a key role in the α-dynamo effect, that is the generation of turbulent electromotive force $\langle\delta\mathbf{v}\times\delta\mathbf{b}\rangle$ proportional to the magnetic field [96, 148, 97]. Moreover, unlike the total energy and the cross helicity, H_m experiences an inverse cascade. Consequently, a tendency to generate large-scale helical structures can be expected [6]. It should be mentioned that also the cross helicity contributes to the turbulent electromotive force (cross-helicity dynamo).

The following nondimensional parameters are key to understand solar wind fluctuations

$$\sigma_c = \frac{2h'_c}{E} = \frac{2\langle \delta\mathbf{v}\cdot\delta\mathbf{b}\rangle}{\langle \delta\mathbf{v}^2\rangle + \langle \delta\mathbf{b}^2\rangle} \qquad \text{Normalized cross helicity} \tag{165}$$

$$\sigma_r = \frac{\langle \delta\mathbf{v}^2\rangle - \langle \delta\mathbf{b}^2\rangle}{\langle \delta\mathbf{v}^2\rangle + \langle \delta\mathbf{b}^2\rangle} \qquad \text{Normalized residual energy} \tag{166}$$

$$r_A = \frac{\langle \delta\mathbf{v}^2\rangle}{\langle \delta\mathbf{b}^2} \qquad \text{Alfven ratio} \tag{167}$$

The condition $\sigma_c = \pm 1$ indicates fields alignment and presence of Alfvén waves. The sign of cross helicity is the sign of $-\mathbf{k}\cdot\mathbf{B}_0$, where $\mathbf{k}$ is the wavenumber and $\mathbf{B}_0$ the mean magnetic field. The first detection of Alfvénic small-scales fluctuations in the interplanetary medium is due to Belcher and Davis [14].
The normalized residual energy and the Alfvén ratio are indexes of imbalance between kinetic energy and magnetic energy.

We analyzed the evolution of cross and magnetic helicity by using Voyager 2 data at 5 AU (1979, DOY 1-180) and at 29 AU (1989, DOY 5-100). The computation of magnetic helicity is delicate and requires some assumptions, since in principle it is not possible to compute it from a one-dimensional time series. An expression for the 1D spectrum $H_m(k)$ has been derived by Matthaeus, Goldstein, and Smith [89] and used in [88] under the only hypothesis of statistical homogeneity of fluctuations, field solenoidality, and the Taylor hypothesis. Note that no isotropy assumption is made, and that the helicity spectrum measured along one direction (R, in our case) depends on the antisymmetric part of one component of the magnetic-energy spectrum tensor, namely $S_{TN}(k)$. From integration then, the total averaged magnetic helicity can be computed.

$$H_m(k_R) = \frac{2}{k_R}\Im[S_{TN}(k_R)], \tag{168}$$

$$S_{ij}(k_R) = \frac{1}{2\pi}\int \langle B_i(x)B_j(x+r)\rangle e^{-ik_R r}\,dr \tag{169}$$

The cross-helicity spectrum can be computed, similarly, from

$$H_c(k_R) = \frac{1}{2\pi}\int \frac{1}{2}\langle v_i(x)b_i(x+r) + b_i(x)v_i(x+r)\rangle e^{-ik_R r}\,dr \tag{170}$$

Results from our publication [67] are reported in tables 16 and 17 and figures 60, 59. Probability density functions of σ_c and σ_r have been computed from different temporal averages (1 h, 3 h, 12 h, 24 h). Generally, results show low values of the total cross helicity, and a sensible reduction with the distance, indicating a decrease of the Aflvénic character of the solar wind fluctuations. Moreover, we observed a reduction of imbalance between the magnetic and the kinetic energy at the small scales. This can be observed

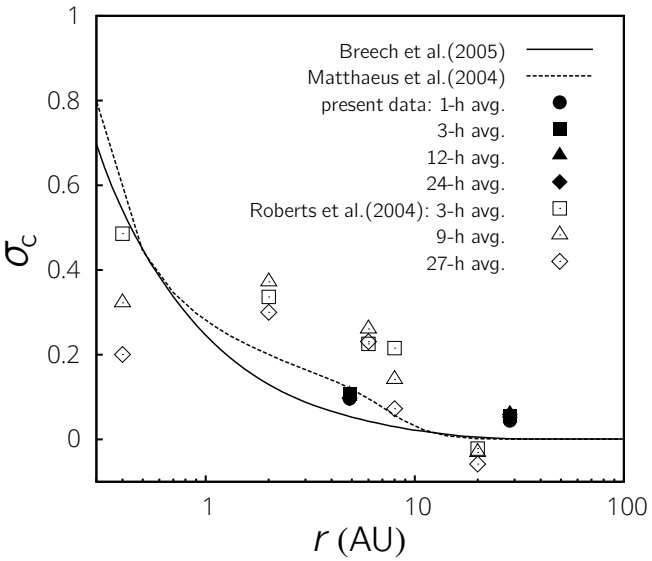

Figure 58: Evolution of the normalized cross helicity with the heliocentric distance. *FIlled bullets*: present analysis, V2 data. *Empty bullets*: literature observations by Roberts et al. [123]. *Continuous line*: MHD RANS-based model by Breech et al. [24]. *Dashed line*: model by [90]. Image published in ref. [67].

by the average values of σ_r reported in table 17 (all averages give $\sigma_r \approx -0.4$ at 5 AU, while at 29 AU 1-h averages give -0.1).

Probability density functions of cross helicity show a higher variance in 1979, especially at small scales, while the distribution functions become narrower, more symmetric and centered at zero at 29 AU. PDFs of the residual energy are instead rather focused on negative values for 1979 data, and become broader and almost double-peaked in 1989, where positive values of σ_r are found, in particular at small scales for 1-h averages. Such trend are highlighted from the joint PDFs shown in figure 59. The evolution of σ_c with the heliocentric distance observed from our analysis has been compared to literature observations by Roberts et al. [123] (Helios 1 and Voyager 2 data from 0.3 AU to 20 AU), and to models obtained from MHD RANS simulations by Matthaeus et al. [90] and Breech et al. [24]. Such comparison is shown in figure 58. These observations, as introduced in §4.2, contradict the hypothesis of a *dynamic alignment* found in MHD numerical simulations ([87, 22]). This is a debated open point and the presence of shear layers, effects of compressibility and turbulent diffusion may explain the observations in the solar wind system.

Equipartition of positive and negative values of spectral cross helicity and magnetic helicity were found in the whole frequency range (see figures 4 and 5 in [67]). Analyzing the normalized magnetic helicity $k\widehat{h}_m(k)/E_m(k)$, we see the absence of a strong polarization at all scales. In particular, at the small scales no polarization is found at 5 AU; on the other hand, the polarization is small and positive at 29 AU in the last two decades ($f > 10^{-4}$ Hz, $k > 10^{-6}$ km^{-1}). At the large scales instead, polarization

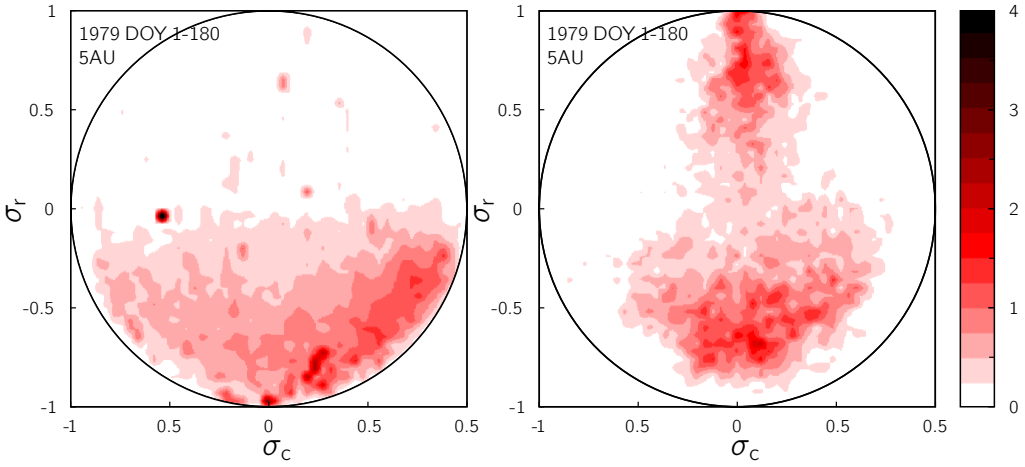

Figure 59: Joint probability density functions of normalized cross helicity and residual energy. Data presented in [67].

is weak in both cases, positive at 5 AU and negative at 29 AU. The change of sign is made possible by the inverse cascade mechanism, which also determines high spectral slopes ($\alpha \approx -2.66$ in 1979, $\alpha \approx -2.92$ in 1989) for the magnetic helicity.

Table 16: Average cross-helicity and magnetic helicity at 5 and 29 AU. Statistics are obtained by averaging the datasets over the total period. The magnetic helicity instead which is computed by integrating its spectrum [67].

		1979 DOY 1-180	1989 DOY 5-100
r	(AU)	$4.48 \div 5.28$	$28.03 \div 28.94$
$\langle v \rangle$	(km/s)	454 ± 43	464 ± 39
$\langle B \rangle$	(nT)	0.981	0.207
E_k	(km^2/s^2)	$1.224 \cdot 10^3$	$1.005 \cdot 10^3$
E_m	(km^2/s^2)	$1.376 \cdot 10^3$	$2.341 \cdot 10^3$
H'_c	(km^2/s^2)	$1.58 \cdot 10^1$	$-3.04 \cdot 10^2$
H'_m	(km^3/s^2)	$4.16 \cdot 10^{10}$	$-9.79 \cdot 10^{10}$

Table 17: Average values of the normalized cross-helicity σ_c and of the normalized residual energy σ_R of the fluctuations, as a function of the averaging time [67].

	σ_c		σ_R	
	1979	1989	1979	1989
1 hour	$9.63 \cdot 10^{-2}$	$4.43 \cdot 10^{-2}$	-0.408	-0.133
3 hours	$1.07 \cdot 10^{-1}$	$5.59 \cdot 10^{-2}$	-0.459	-0.194
12 hours	$1.06 \cdot 10^{-1}$	$6.09 \cdot 10^{-2}$	-0.460	-0.322
24 hours	$9.67 \cdot 10^{-2}$	$5.88 \cdot 10^{-2}$	-0.405	-0.404

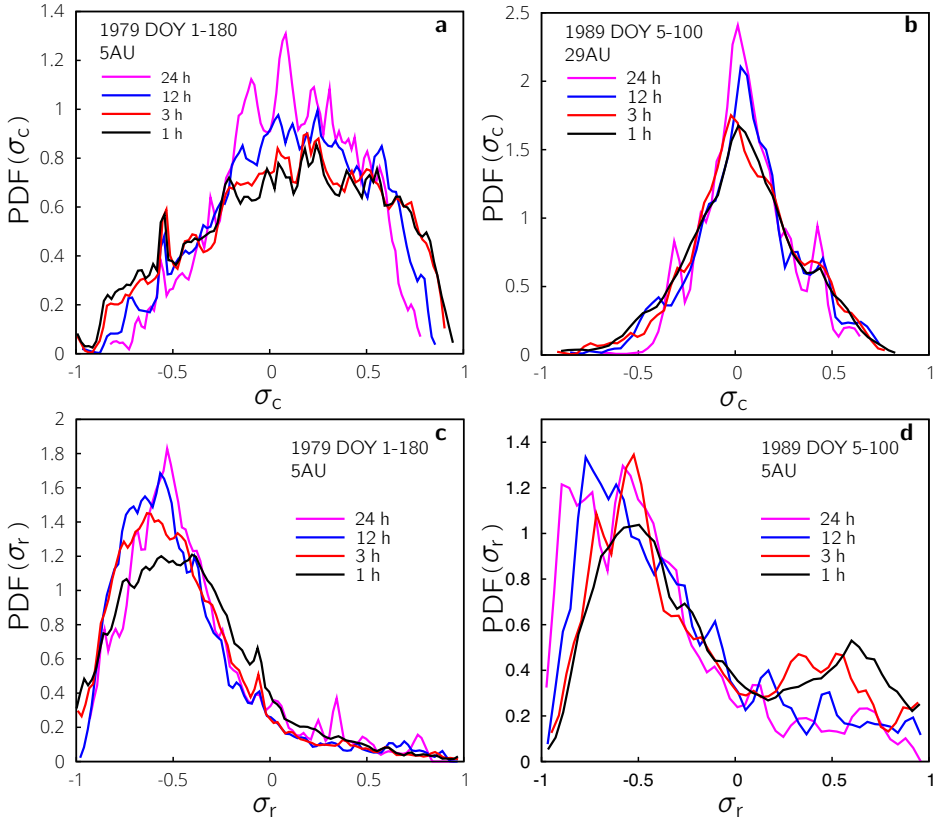

Figure 60: Probability density functions of the normalized cross helicity and the normalized residual energy. Left panels regard the period when V2 was near 5 AU, right panels regard the 29-AU period. PDFs of the normalized cross helicity are shown in panels **(a)** and **(b)**, while PDFs of the normalized residual energy are shown in panels **(c)** and (**d**). Different time averages are considered. This data have been presented in ref. [67].

4.9 **Final remarks**

This first part of the present solar-wind analysis was focused on the external heliosphere at 5 AU and 29 AU. The lack of *in loco* measurements at large heliocentric distances represents a limitation towards the understanding of the nature and evolution of "turbulent" fluctuations of the solar wind plasma. This issue motivates the efforts done to test and validate some simple and effective procedures for spectral analysis of the Voyager's large gapped data sets. We are now able to estimate power spectra of solar wind data sets where the missing data are as many as 70% of the nominal total, with an error estimate on the spectral index lower than 10% in the worst case (at 5 AU the uncertainty was 3%). This permits to investigate the energy spectral cascades of the multiscale plasma and magnetic fields, by eliminating the spurious peaks and noise arising from the distribution of missing points. In particular, we suggest the concomitant use of such independent techniques to reduce the uncertainty on the spectral estimation at all frequencies in the range, and to look at the "gap spectrum" to identify the critical frequencies which would most affect the power spectrum.

We managed to compute the 1D spectra for a frequency range extending over five decades ($10^{-7} - 10^{-2}$ Hz), which is wider than in most other previous studies at this distance. A broad frequency range allows catch breaks in the spectral slope and to investigate both the energy-injection and inertial regimes of the fluctuation dynamics.

At 5 AU, a possible inertial range dominated by nonlinear interaction was identified for $f \gtrsim 2.7 \cdot 10^{-5}$ Hz, which corresponds to spatial scales of 0.11 AU. In this range, the plasma velocity experiences kinetic energy cascade with exponent close to -1.67. However, high anisotropy in the speed components is observed. The magnetic energy cascade is faster, with a spectral index about -1.76 in the inertial range. In the lower frequency range, spectra of all quantities flatten and the power law exponent assumes values close to -1.2. This may be indicative of a (non-turbulent or weakly-turbulent) regime, dominated by large-scale Alfvén waves, which take origin at the Solar corona and provide the energy to the cascade of turbulent fluctuations. The Alfvén ratio in this region shows equipartition of kinetic and magnetic energy.

5

SOLAR WIND FLUCTUATIONS IN THE HELIOSHEATH. SPECTRAL ANALYSIS OF VOYAGER 1 AND 2 DATA

.

The last chapter of this dissertation is dedicated to the analysis of magnetic field fluctuations in the heliosheath, from Voyager 1 and Voyager 2 data. These results have been shown at the international conferences [48, 49, 117, 50, 52, 51] and a journal paper is in preparation [54].

5.1 **Summary**

At present, the Voyagers are the only spacecrafts providing *in loco* measurements of the wind in the outermost region of the heliosphere, beyond the termination shock (TS). V2 is traveling inside the *Heliosheath* (HS) since August 2007, while V1 has entered the *Local Interstellar Medium* (LISM) in August 2012. Characterization of the wind turbulent fluctuations in this regions is fundamental to understand a number of processes, as dissipation mechanisms, plasma heating, energetic particles transport, and several still unexplained observations. By tuning some of the spectral estimation methods presented in Chapter 4, we first show that it is possible to compute accurate power spectra of the wind fluctuations in the HS (where $> 70\%$ of data are missing). Despite the analysis of plasma velocity is highly affected by the noise in data rather than by data gaps, magnetic field signals allow to obtain good spectral estimates.

Periods have been chosen on the basis of the intensity of energetic particles fluxes (from 40 keV suprathermal ions to $>$ 1 GeV Cosmic Rays). In fact, high variation of such fluxes with the heliocentric distance has been recorded by V2, while almost constant trends were observed by V1. This fact was supposed to be indicative of different transport properties between the *sectored HS* and the *unipolar HS*, leading to the turbulence hypothesis for the first region.

We then provide a collection of broadband (over 5 decades) spectra of the heliosheath plasma from both 1-h and 48-s resolution data sets recorded by the Voyagers from 84 AU to 120 AU. Moreover, a comparison between the field fluctuations at V1 and at V2 is made. To our knowledge, this is the first time such a spectral analysis was attempted.

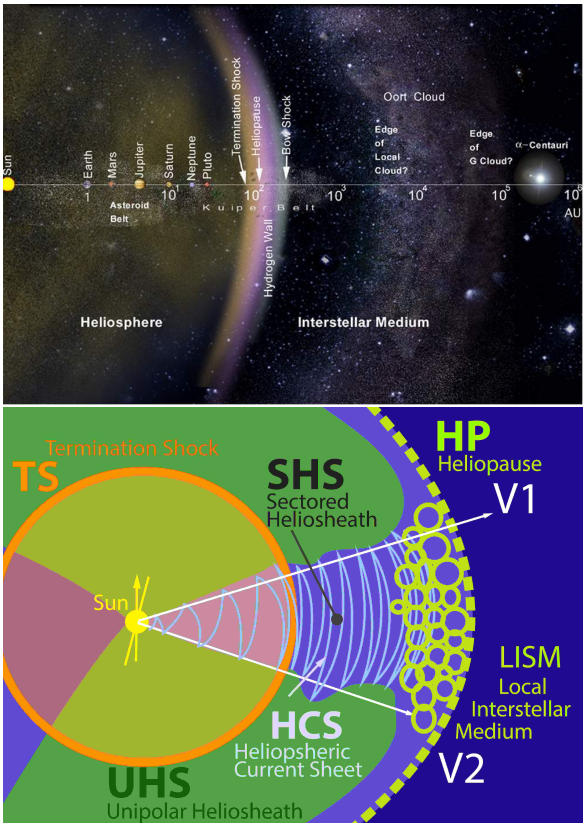

Figure 61: *Top*: a representation of the heliosphere and its spatial extension. Credits: NASA `http://voyager.jpl.nasa.gov`. *Bottom*: nomenclature and schematic structure of the heliosphere nose. The yellow circles represent the possible presence of turbulent fluctuations and reconnection of magnetic field.

Spectral estimation tests on highly-gapped synthetic data sets are reported in Section 5.2. Section 5.3 shows results in terms of magnetic field spectra from hourly data in different periods between 2005 and 2012. In section 5.4, broadband spectra from high-resolution data are shown for six periods between 2009 and 2014. Eventually, preliminary multifractal analysis of the dissipation rate of magnetic energy from high-resolution data are presented in Section 5.5.

5.2 **Spectral estimation tests for 70% to 90% of missing data**

The methods of spectral estimation described in the previous chapter (see §4.5) are now tested on synthetic data sets with gap distributions as Voyagers data in the heliosheath.

In figures 62, 63, 64, results from eight test cases are presented. The characteristics of these sets are given in table 18. The spectral estimation accuracy certainly depends on the parameters reported in the table (sampling resolution, signal duration, percentage of missing data, gap distribution and type of signal). Varying these parameters provided comprehensive tests of the gap-filling techniques, performed in order to determine how well such techniques are able to recover different spectra. All these synthetic sets are turbulent-like, as described in §4.5. The case studies shown here well represent the various situations for Voyagers HS data. The first two cases (*synt3*, *synt4*) give the best results. These sets simulate Voyagers magnetic field high-resolution (48 s) data. The gap distribution is quite regular, with 12 hours of missing data per day and some minor gaps. As can be observed from figures 62 and form the analysis in the following sections, this gap distribution is such as to generate a spectral irregularity at $f^* \approx 10^{-5}$ Hz and a lack of energy at lower frequencies in the CS estimates (see the green curves in the figures). On the other hand, the CS spectral recovery in the higher frequency range is very good, in that the method predicts the correct spectral index (with error below 10%) and correct levels of spectral energy density. The linear interpolation used by the correlation technique (CI, red curves in 62, blue curves in 63, 64) is evident as it leads to a pronounced steepening of the spectrum for $f > f^*$ and to highly underestimated values of the PSD. Notice though, that the spectrum is quite acceptable at lower frequencies (at $f < f^*$, a small boosting effect has to be taken into account). The optimization method (OP, see the dotted curves in the figures) seems to be the most effective method for all spectra. It is able to quickly converge to the correct solution in all cases. However, convergence is not always easy as it may require several tests and careful interpretation,

Table 18: Synthetic datasets properties.

Label	Δt_s	Signal length	Missings	Gap distribution	slope
Synt 3	48 s	178 d (320000 pt)	70%	B-data, 2010.7-2011.7 (B2)	-1.67
Synt 4	48 s	178 d (320000 pt)	70%	B-data, 2010.7-2011.7 (B2)	-1
Synt 5	1 h	213 d (5120 pt)	75%	U-data, 2008.4-2009.15	-3
Synt 6	1 h	213 d (5120 pt)	75%	U-data, 2008.4-2009.15	-1.67
Synt 7	1 h	213 d (5120 pt)	75%	U-data, 2008.4-2009.15	-1
Synt 8	192 s	178 d (80000 pt)	95%	U-data, 2007.7- 2008.5	-3
Synt 9	192 s	178 d (80000 pt)	95%	U-data, 2007.7- 2008.5	-1.67
Synt 10	192 s	178 d (80000 pt)	95%	U-data, 2007.7- 2008.5	-1

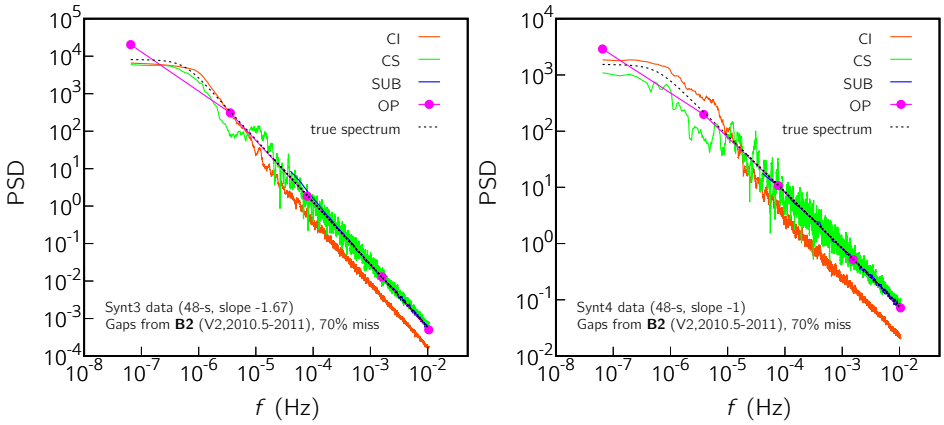

Figure 62: Spectral recovery with 70% of missing data: gaps of magnetic-field data. Here we show analysis of the gapped synthetic turbulent datasets *synt3* and *synt4*. These sequences are representative of magnetic field 48-s data in 2010.7-2011.7, but such gap distribution is actually typical of the whole heliosheath.

especially in the lower frequency range where the method lacks accuracy. Notice that figure 62 also shows the averaged spectra from contiguous subsets (blue curves), which can effectively describe the last two decades. The Blackman-Tukey method totally fails these tests, even when a prewhitening filter is used. This is not shown here but it can be found in the poster presentation at ICTAM 2016 Fraternale et al. [51].

The gap distribution of plasma velocity data from V2 has instead more drastic effects on the spectral estimates. In this case, hourly averages have about 70% of missing points, similarly to magnetic field data. Instead, the amount of missing data for high resolution measurements (192 s) is as high as 95%. The *synt5-synt10* test cases represent therefore the most serious conditions. We report the results in figures 63 and 64. CS is very noisy, since it does not recover many frequencies. However, the recovered PSD values are aligned with the true spectrum. The steepest test ($\alpha = -3$) led to machine-accuracy issues due to the 12 orders of magnitude difference between the biggest and the smallest PSD values. Surprisingly, OP converged to the true spectrum in all cases.

In order to accurately estimate power spectra of the heliosheath wind, all these techniques will be used in the following analysis.

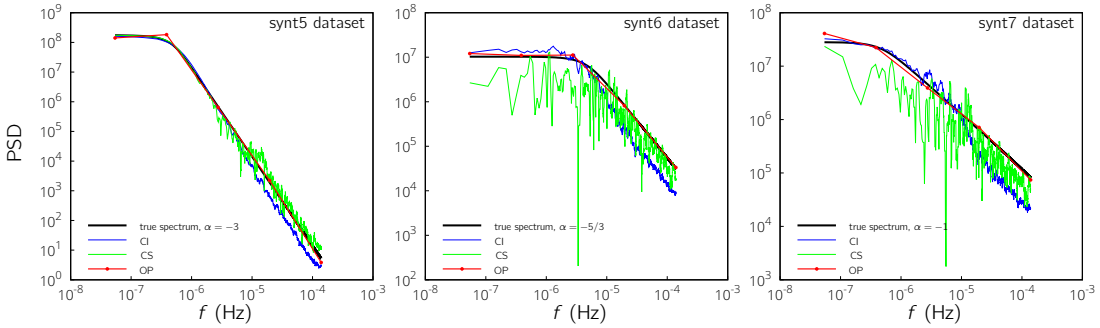

Figure 63: Spectral recovery with 70% of missing data: synthetic sequences with gaps as velocity field 1-h data recorded at Voyager 2 in 2008-2009 [48, 49].

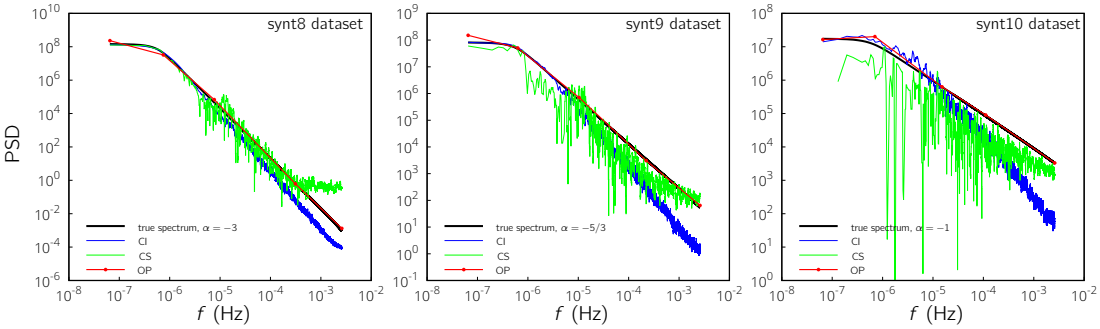

Figure 64: Spectral recovery with 95% of missing data: synthetic sequences with gaps as in the velocity field 192-s data recorded at Voyager 2 in 2007-2008 [48, 49].

5.3 Spectral analysis of the early Heliosheath before 2011 from 1-h data

Both the Voyager 1 and 2 have crossed the termination shock and entered the heliosheath (V1 in December 2004 [140], V2 in August 2007 [120]). In this region, many observations, comprehensively reviewed by Richardson and Decker [2008, 119] and Opher et al. [2015 105], are not yet completely understood. One of these is the difference between the flux of energetic ions (from about 40 keV suprathermal ions to Galactic Cosmic Rays, >1 GeV) and electrons (from about 50 keV to >100 MeV) observed by V1 and V2 [64]. In particular, while the particle profiles at V1 were almost constant in the period 2007-2012, at V2 large variations up to a factor of 100 have been recorded. According to Hill *et al.* [2014, 64], possible physical interpretations to explain the enhancement or depression of energetic particle intensity are related to the Helioshperic Current Sheet (HCS) maximum latitudinal extensions.

These northern and southern boundaries enclose the so called *sectored* heliosheath region (SHS), where the magnetic field changes polarity as the helioshperic current sheet (HCS) is crossed, according to the Parker spiral structure. At higher North and South latitudes, outside the sectored region, the heliosheath is *unipolar* (UHS). Traveling at a latitude of about 30° S, V2 is thought to have crossed different times the boundary of the SHS, and a correlation was found between the energetic particles flux at V2 and the alternating of unipolar, high-latitude, and sectored, low-latitude, heliosheath regions. Different particle transport properties are expected in these regions. Opher et al. [2011, 104] suggested that in the sectored region the magnetic field was not laminar but disordered and turbulent, with the sector structure being replaced by a sea of nested magnetic islands. These "bubbles" would take origin from magnetic reconnection processes occurring near the Heliopause (HP), triggered by the compression of sectors and by the narrowing of the HCS (see Drake et al. [2010, 45]). These structures, of dimension similar to the original distance between the HCS folds, would then develop upstream the HP and act as traps for energetic ions and electrons by slowing their travel. This interpretation is not the only one, and different scenarios and physical processes may coexist. For instance, the particle transport across sectors is enhanced when the Larmor radius becomes equivalent to the sector spacing, as shown by Florinski [2011, 47]. Eventually, the presence of magnetic reconnection or turbulence in the SHS may as well increase the ions and electrons transport.

The scope here is to characterize the spectrum of magnetic field fluctuations in different regions within the HS. The first part of our study considers the four V2 periods identified by Hill et al. [2014, 64] on the basis of the intensity of energetic particles flux. The periods labeled EP1, EP2 showed enhanced intensity of energetic particles, while in DP1, DP2 particles intensity was low (depressed periods), see figure 69. In the authors view, EP periods might correspond to sectored regions of the HS, while DPs to unipolar ones (see figures 1 and 2 in their paper). It must be stressed, however, that the tracking of the HCS location, and its crossing by the spacecraft is not easy, see the discussion in §5.4.

- **EP1** 2007.7 - 2008.0, Sectored Heliosheath (SHS)
- **DP1** 2008.0 - 2008.2, Unipolar Heliosheath (UHS)
- **EP2** 2008.2 - 2009.15, Sectored Heliosheath (SHS)
- **DP2** 2009.15 - 2010.5, Unipolar Heliosheath (UHS)

Figure 66 shows the probability density functions of the azimuthal component of the orientation angle of the magnetic field, defined as $\lambda = \tan^{-1}(B_T/B_R)$. The elevation angle (shown in figure 65) is instead $\theta = \sin^{-1}(B_N/|\mathbf{B}|)$. The ion average quantities for each period are shown in table 19.

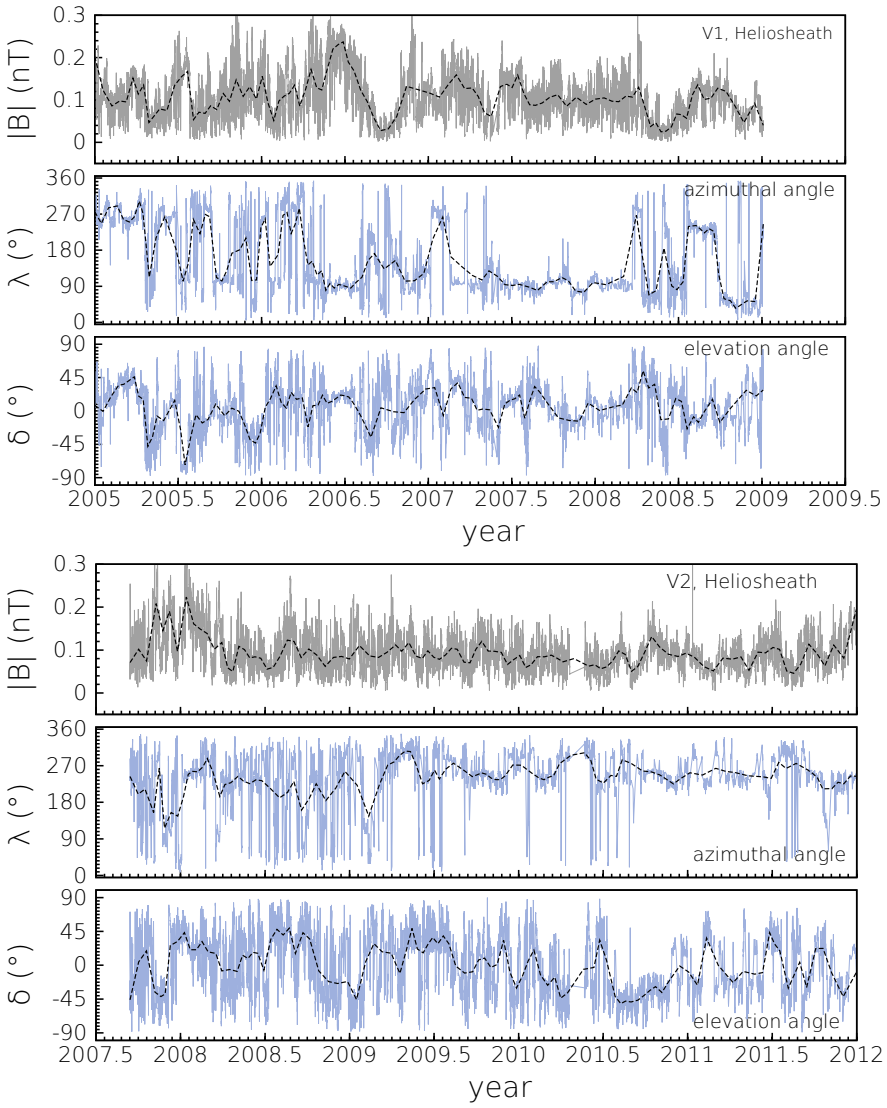

Figure 65: Magnetic field measurements at V1 and V2 in the heliosheath in the four-year period following the termination shock crossing. The top figure shows Voyager 1 observations, while the bottom one regards Voyager 2. The data are presented in terms of magnetic field strength, azimuthal and elevation angles. Further information about the plasma flow observed by V2 until 2014 (104 AU) can be found in the publication by Richardson and Decker [119].

The power spectra of magnetic field from 1-h resolution data (hourly averaged data) are presented in figure 67. The spectral power law exponents are shown in table 20, while integral scales and Taylor micro-scales can be found in table 21 and 22, respectively.

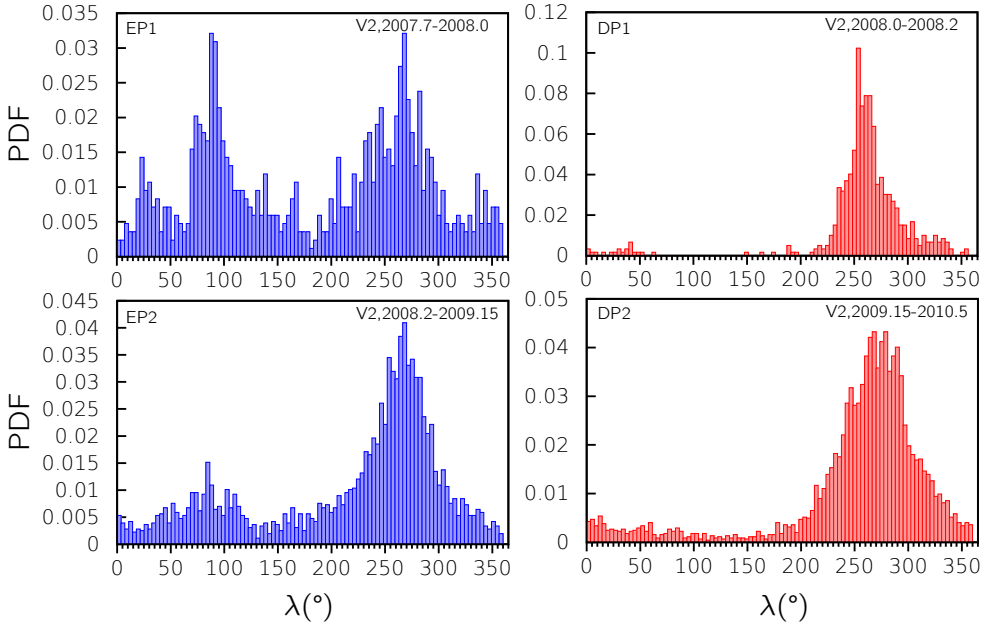

Figure 66: Probability density functions of the azimuthal angle of the magnetic field in the periods EP1, EP2 (left panels) and DP1, DP2 (right panels). The double-peaked distribution in EP regions indicates the presence of both "away" and "toward" magnetic field polarity in the signal ($\lambda \approx 270^\circ$ and $\lambda \approx 90^\circ$, respectively). A dominant polarity is instead observed in DP periods. Only data points with B-components greater than 0.03 nT are used for the PDFs computation.

The spectra are fit to a power law $E(f) \approx f^{\alpha}$ in two frequency ranges. In fact, a spectral break is observed at a frequency close to 10^{-5} Hz, similarly to observations upstream the termination shock at 5 AU. However, here such spectral trend was not observed before, and still lacks an explanation. A first comment should be made about the data-gap distribution which, unfortunately, as shown in the section above, affects the spectral estimates exactly in the neighborhood of 10^{-5} Hz. However, the combined use of three techniques allows to discriminate physical spectral trends from spurious effects.

The spectral index in the lower frequency range assumes values between -1.1 and -1.3, while values around -1.75 are seen for $f > 10^{-5}$ Hz, when a "turbulent" cascade seem to start (see the next section). The $1/f$ spectral trend was also inferred by Burlaga and Ness [31] from multifractal analysis on daily averages of unipolar data at 91 AU. The highest anisotropy occurs in this regime, as can be noted from the spectra of magnetic-field components. This description applies to all four periods with

Table 19: Ion average quantities from V2 measurements in the four periods considered between 2007.7 and 2010.5.

	EP1 (SHS)	DP1 (UHS)	EP2 (SHS)	DP2 (UHS)	**Global**
$\langle \mathbf{n_i} \rangle$ (dm^{-3})	2.16	1.71	1.17	1.14	**1.38**
$\mathbf{E}_k$ (km^2/s^2)	1511.8	1365.4	2210.1	1626.0	**1943.8**
$\mathbf{E}_m$ (km^2/s^2)	2498.7	1527.4	2226.0	1376.4	**1894.7**
$\langle \mathbf{V} \rangle$ (km/s)	153.2	159.2	164.0	143.7	**152.3**
$\langle \mathbf{V}_A \rangle$ (km/s)	65.7	52.3	60.25	58.9	**60.2**
$\langle \mathbf{B} \rangle$ (nT)	0.123	0.154	0.088	0.086	**0.095**
$\langle \mathbf{T}_i \rangle$ (10^5K)	1.54	1.67	0.96	0.55	**0.98**
$\mathbf{c}_{si}$ (km/s)	1021.4	1119.2	997.7	803.6	**928.5**
$\boldsymbol{\beta}_i$	2.43	3.59	1.36	0.69	**1.48**
$\mathbf{f}_{pi}$ (Hz)	9.05	8.53	7.08	6.98	**7.62**
$\mathbf{f}_{ci}$ (Hz)	0.0018	0.0014	0.0013	0.0013	**0.0014**
$\mathbf{f}_*$ (Hz)	0.037	0.029	0.041	0.046	**0.040**
$\mathbf{r}_i$ (km)	5542	5812	6975	7043	**6576**
$\mathbf{r}_{ci}$ (km)	4142	5517	4037	3138	**3778**

no perceivable discrepancies between EPs and DPs, at least at the current state of our research.

The flat region is typical of the solar wind upstream TS, where it may be indicative of large-scale MHD waves with origin at the Solar corona. Moreover, such range almost extinguishes in the outer heliosphere (at 29 AU we did not observe any flattening in the lower frequency range).

But what happens here, in the inner heliosheath?

The lack of accurate velocity data makes is hard to compute the velocity/magnetic field correlations and the cross-helicity spectrum. On the basis of considerations on temporal scales as those leading to the expression 157, one might look for the time necessary to an eddy generated at the TS (~ 84 AU for V2) to complete one turnover: $f_e = V_{wind}/(t_{TS} V_A)$, where $V_{wind} \approx 150$ km/s is the wind average speed, and $t_{TS} \approx (r_{SC} - r_{TS})/V_{wind}$ is the time taken to the plasma to travel from the termination shock to the spacecraft. For instance, in mid 2009 $r_{SC} \approx 89.5$ AU, leading to $f_{\mathbf{e}} \approx 5 \cdot 10^{-7}$ Hz. This frequency is of course too small to explain the spectral break. Another scale present in the system is the sector spacing. Simulations showed that in the early HS, soon after the TS, the distance between sectors of opposite magnetic field polarity is about 2 AU [104]. Converted in frequency, considering the sectors convected with the wind, this scale leads to $f_{sect} \approx 5 \cdot 10^{-7}$ Hz. Also this frequency is rather small. Regardless, it may be possible that it be representative of the energy-injection range in

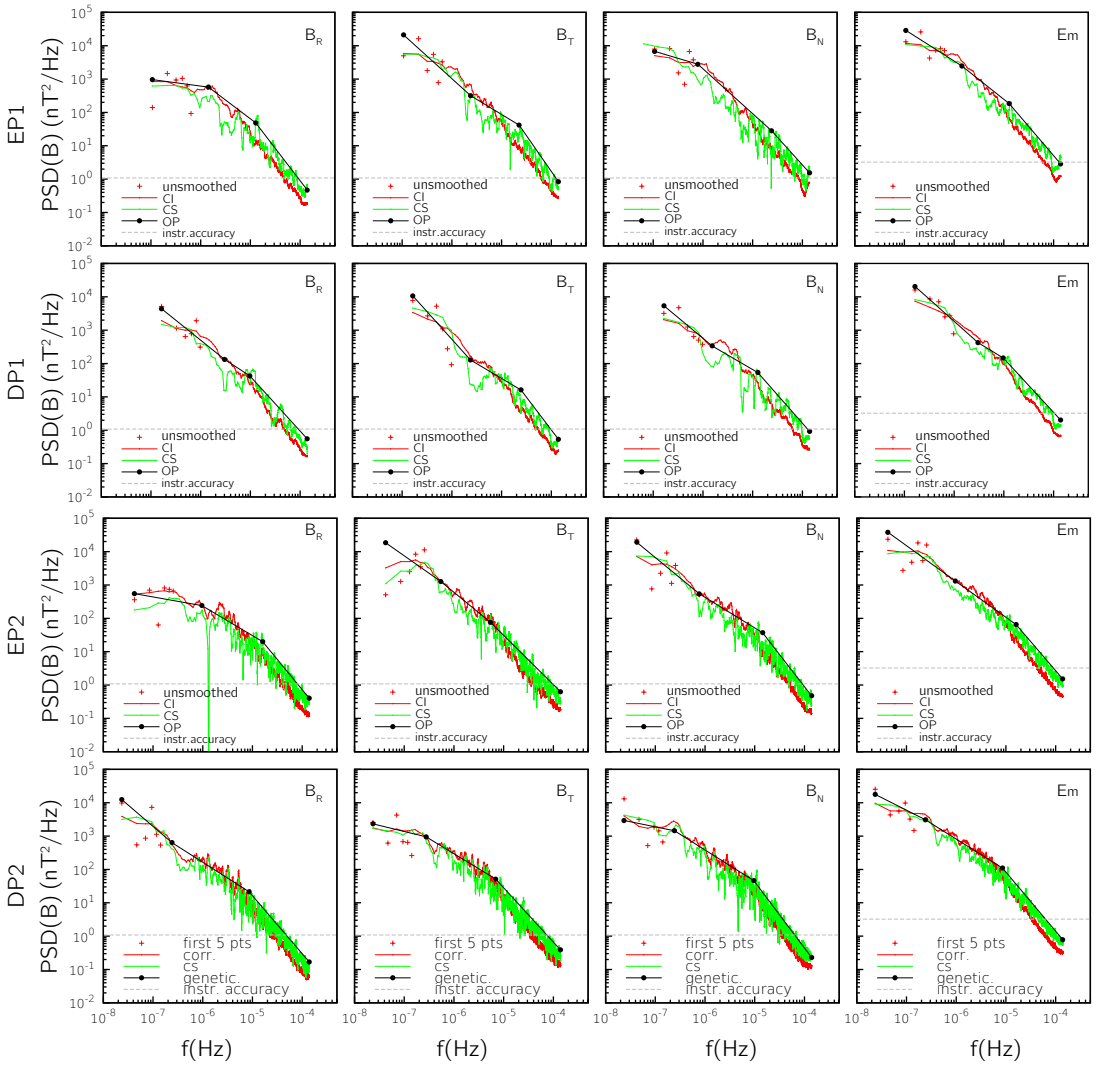

Figure 67: Magnetic field spectra from V2 observations i the periods EP1, DP1, EP2, DP2. Each row of the multi-panel figure corresponds to a period, while the columns are for the magnetic field components. The right column reports the magnetic energy spectra. Three different techniques are used to estimate the power spectra: CI (red), CS (green), OP(black). A uniform smoothing is applied to reduce the spectral variance, however the first five unsmoothed are also shown (red points). A good convergence of the all the methods is achieved. In the higher frequency range ($f \gtrsim 10^{-5}$ Hz), the most accurate results come from CS and OP. It is interesting to note that a spectral break (physical, not due to gaps) seem to occur in most cases, at about $f \sim 10^{-5}$ Hz. This is particularly evident in DP2 (bottom panels). Spectral indexes are shown in table 20.

Table 20: Spectral slopes in the lower ($f < 10^{-5}$ Hz) and in the higher ($f > 10^{-5}$ Hz) frequency range. In the first case, power law fits were computed from the correlation spectra (CI), while in the second case from the compressed sensing (CS) and from the linear model given by the iterative procedure (OP).

	$f < 10^{-5}$ Hz				$f > 10^{-5}$ Hz			
period	B_R	B_T	B_N	$\|B\|$	B_R	B_T	B_N	$\|B\|$
EP1	-0.91	-1.40	-1.36	-1.30	-1.83	-1.91	-1.66	-1.74
DP1	-1.38	-1.33	-1.30	-1.33	-1.63	-1.92	-1.69	-1.70
EP2	-1.00	-1.19	-1.11	-1.13	-1.62	-1.60	-1.83	-1.74
DP2	-1.20	-1.16	-1.09	-1.13	-1.73	-1.63	-1.85	-1.77

place of the HS width, which is about 27 AU as measured by Voyager 1. Note, however, that the sector boundaries are not regular (soon after 10 AU a periodic structure is no more discernible) nor easily detectable, due to the nonstationarity of the latitudinal extension of the HCS owed to variations of solar activity. The integral scale (T) and the Taylor micro-scale (τ) shown in tables 21 and 22 are purely indicatory, as they have been obtained via formulas for isotropic and homogeneous turbulence [98], applied to the i-th field component:

$$T_i = \frac{1}{\sigma^2_{B_i}} \sum_f \frac{\hat{B}^2_i}{f} \qquad \tau_i = \frac{1}{\sqrt{\sum_f f^2 \hat{B}^2_i / \sigma^2_{B_i}}}$$

The integral scale increases as distance from the sun, the early periods EP1 and DP1 seem influenced by the solar rotation (it is reminded that TS is not stationary), while later periods show larger time scales as big as 100 days. An oscillation with periodicity of about 85 days was found in 2011 by Burlaga, Ness, and Richardson [34], but the source of such oscillations is not known.

It must be underlined that the fluctuations in the HS show very complex and inhomogeneous profiles which comprise a number of phenomena, not fully understood [118]. Burlaga and Ness [30] showed that in the unipolar region of 2008 (corresponding to our DP1) fluctuations are nearly compressive (azimuthal and elevation angles were indeed constant) and Gaussian-distributed at the large scales (daily data). The same trend was observed in the unipolar period of 2011 ([34]). Different statistics were observed in sectored regions as in the post-TS period EP1, showing a log-normal distribution of the magnetic field fluctuations.

Fluctuations in the HS include also ordered events as magnetic holes, sheets related to reconnection [32], and gyromotion effects on scales up to $\sim 100\ r_{ci}$ are important. The term "turbulence" must be therefore used with caution and not in the classical Kolmogorov's view.

Table 21: Integral scale (days / AU).

period	B_R	B_T	B_N	$\|B\|$
EP1	12.6 / 1.11	28.9 / 2.55	27.6 / 2.43	25.8 / 2.27
DP1	29.5 / 2.60	34.4 / 3.03	37.5 / 3.31	28.8 / 2.54
EP2	23.5 / 2.22	43.1 / 4.07	50.7 / 4.79	55.3 / 6.74
DP2	130 / 10.8	47.2 / 3.91	32.2 / 2.67	86.9 / 7.21
2007.7-2012.0	142 / 12.3	106 / 9.21	113 / 9.81	137 / 11.9

Table 22: Taylor micro-scale (hr/ AU).

period	B_R	B_T	B_N	$\|B\|$
EP1	$8 / 2.94{\cdot}10^{-2}$	$10 / 3.67{\cdot}10^{-2}$	$16 / 5.87{\cdot}10^{-2}$	$11 / 4.04{\cdot}10^{-2}$
DP1	$10 / 3.69{\cdot}10^{-2}$	$11 / 4.16{\cdot}10^{-2}$	$8 / 2.98{\cdot}10^{-2}$	$9 / 3.30{\cdot}10^{-2}$
EP2	$8 / 3.14{\cdot}10^{-2}$	$16 / 6.30{\cdot}10^{-2}$	$10 / 3.93{\cdot}10^{-2}$	$11 / 4.33{\cdot}10^{-2}$
DP2	$11 / 3.80{\cdot}10^{-2}$	$12 / 4.14{\cdot}10^{-2}$	$13 / 4.49{\cdot}10^{-2}$	$12 / 4.14{\cdot}10^{-2}$
2007.7-2012.0	$10 / 3.60{\cdot}10^{-2}$	$13 / 4.68{\cdot}10^{-2}$	$13 / 4.68{\cdot}10^{-2}$	$12 / 4.32{\cdot}10^{-2}$

We believe that the presence of waves within sectors, with propagation properties affected by the presence of magnetic and velocity shear should be further investigated. Power spectra similar to those shown here are indeed compatible with a scenario of weakly interacting Alfvénic waves, at least at the large scales. The origin of such fluctuations could be related to instabilities at the heliopause, documented by recent numerical simulations as shown bt Pogorelov et al. [114]. By hydrodynamic analogy with the dispersion phenomena highlighted in parallel neutral flows in Part 1 of this dissertation, threshold wavelengths might be expected to exist in a system where the folded-structure of the HCS determines magnetic sectors. These might determine the extension of the energy-injection range of chaotic fluctuations.

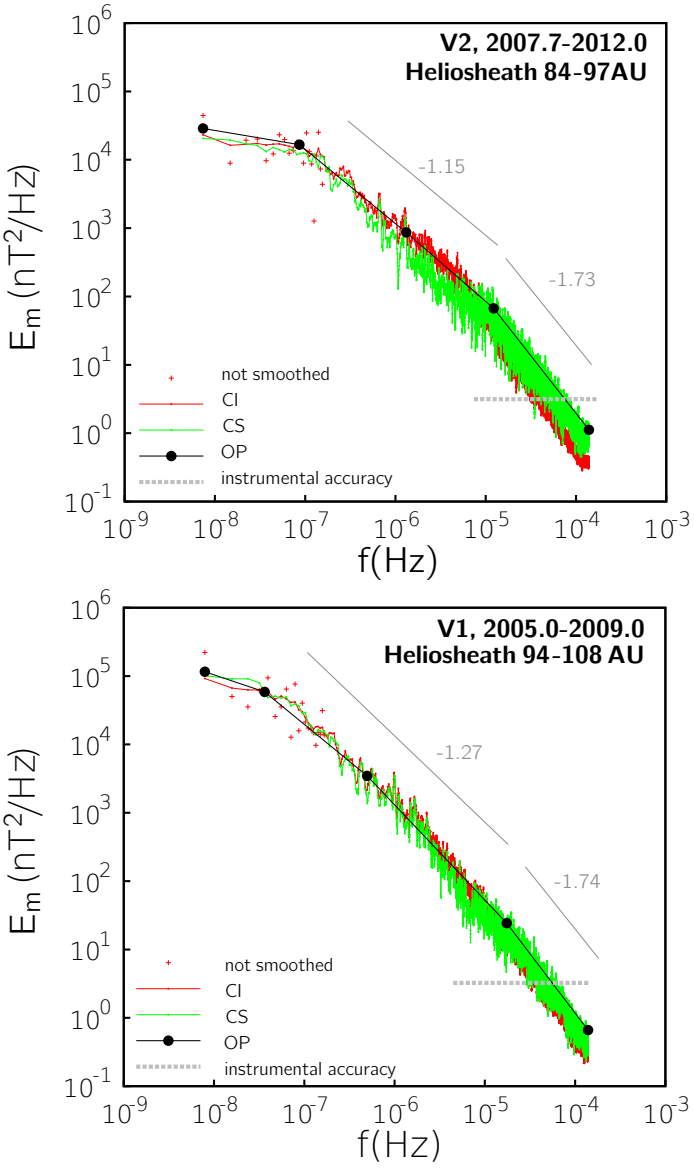

Figure 68: Magnetic field 4-year spectra form V1 and V2 data. The magnetic energy spectra are computed here form both V2 (left panel) and V1 (right) 1-h data, over a frequency range exceeding four decades. This range corresponds to the four-year period which follows the TS crossing by the Voyagers. For V2, the period 2007.7-2012.0 is considered, while for V1 the period is 2005.0-2009.0. This wide range includes various physical sources of fluctuations. Note also the presence of discrete peaks at $f = 6.7 \cdot 10^{-7}$ Hz ($\sim$ 1.5 AU) and its harmonic $f = 1.3 \cdot 10^{-6}$ Hz ($\sim$ 0.75 AU) in the V2 spectrum. An inertial regime seem to begin in the vicinity of $f = 10^{-5}$ Hz, above which a slope $\alpha \approx 1.75$ can be observed. The lower frequency range show a flatter spectrum ($\alpha \approx -1.2$), with slower energy decay at V2 than at V1. The instrumental accuracy level here is largely overestimated, it corresponds to ± 0.03 nT but hourly averaged data reduce this variance. The spectrum is indeed confirmed by analysis on 48-s data, see §5.4.

5.4 Magnetic field spectral analysis in the HS from 48-s data after 2009 (89-117 AU). V1-V2 comparison.

In the following, a spectral analysis is performed from high-resolution magnetic field data, in order to investigate the possible inertial range introduced in the previous section. Data with 48-s resolution (the highest provided now) were available after 2009. These analyses are still in progress, but at present we looked at six periods of several months from both V1 and V2 measurements, in the range 89-117 AU. Again, periods were chosen according to the energetic particle intensity (for V2), and the magnetic field polarity (for V1), see figure 69.

We first considered four magnetic field datasets collected by the Voyagers during the period 2009-2012. The time history of the magnetic field strength, the azimuthal and elevation angles are shown in figure 70. In particular, for V1 we analyzed the sequences 2009 DOY 1-180 (**A1**, 108.5 AU-110.2 AU) and 2010 DOY 180 - 2011 DOY 180 (**B1**, 113.8 AU-117.4 AU). According to computations of the latitude of the sectored-HS boundary (BSHS), V1 was supposed to be in the sector region during both periods (see figure 1 in Hill et al. [64]), even if the magnetic field polarity suggests that V1 remained within just one sector all the time. In average, in fact, the B vector points in the toward-Sun direction along the Parker spiral, as can be seen from the angle reported in the top panels of figure 70.

For V2, we choose again the interval 2009 DOY 219 - 2010 DOY 180 (here labeled **A2**, corresponding to the period DP2 of §5.3), when V2 was supposed to fly between 89.7 AU and 92 AU inside the southern unipolar region, recording a low flux of energetic particles. A second period was also considered, 2010 DOY 255 - 2011 DOY 256 (named **B2**, 93.2 AU-96.4 AU). Here, V2 was measuring an enhanced flux of energetic particles, and the magnetic field was mainly directed in the T direction pointing away from the Sun, due to the minimum low-latitude extension of the HCS during 2011 (see figure 70, top panels). This was probably related to the long-lasting solar minimum of 2009, whose effects arrived at V2 one year later (differing opinions are found in the literature about if V2 was or not inside the sectored zone, see [64, 34]). Eventually, we show the power spectra for two additional periods of V2 data, the whole years 2012 (**C2**, 97 AU-100 AU) and 2013 (**D2**, 100 AU- 104 AU). The study of these and other successive periods is, however, still in progress.

Note that applying propagation techniques to estimate the position of the HCS at positive (northward) latitudes is more difficult than at southern latitudes, since the wind velocity is not directly measured by V1. In the HS, Voyager 1 often observed single-polarity periods; however, this does not necessarily mean that V1 was in the unipolar heliosheath. For instance, it is possible that V1 was in one sector of the SHS, and traveling with the sector due to a low-wind speed. It should be recalled that the definition of

SHS and UHS may not actually represent a separation between two unconnected regions of different topology. The question is complicated and highly debated: for instance, simulations by Pogorelov et al. [114] via the multiscale fluid-kinetic model (MS-FLUKSS, see [113]) did not reproduce the results of Opher et al. [104]. Pogorelov's simulations suggested that a tangential discontinuity defining the region covered by the wavy HCS may not exist. Moreover the low latitude portion of the inner heliosheath could undergo transition to chaos as the heliopause is approached.

- **Period A1** → V1, 2009 DOY 1-180 (SHS, but unipolar mag. field)
- **Period B1** → V1, 2010 DOY 180 - 2010 DOY 180 (SHS, but unipolar mag. field)
- **Period A2** → V2, 2009 DOY 219 -2010 DOY 111 (UHS)
- **Period B2** → V2, 2010 DOY 255 -2011 DOY 256 (UHS or SHS, but unipolar mag. field)
- **Period C2** → V2, 2012 DOY 1 -2012 DOY 365 (SHS)
- **Period D2** → V2, 2013 DOY 1 -2014 DOY 365 (SHS)

Power spectra of the magnetic field components in the usual RTN reference system are shown for the four periods (A1, B1, A2, B2) in panels of figures 72 and 73. For C2 and D2, refer to figure 74. The magnetic energy spectra of all periods are presented in figure 75. Tables 23 and 24 show the results in terms of spectral slopes, temporal scales, and anisotropy. The anisotropy for each component is here defined as $A_i = \sum_k \widehat{B}_i^2(k) / \widehat{E}_m(k)$, which indicates the overall deviation from the energy spectrum ($A = 0.33$ for all the components in the isotropic case) .

Table 23: Spectral index, temporal scales and anisotropy for the periods A1 and B1.

Period A1	α_1	α_2	T (days)	τ (hr)	A
radial	-1.27	-1.47	30.1	0.26	0.25
tangential	-1.24	-2.21	29.5	0.77	0.5
normal	-1.28	-1.47	14.3	0.23	0.25
mag. energy	-1.27	-1.9	28.6	0.5	
Period B1	α_1	α_2	T (days)	τ (hr)	A
radial	-1.5	-1.63	142	0.55	0.27
tangential	-1.33	-2.31	98	1.32	0.52
normal	-1.44	-1.86	127	0.90	0.21
mag. energy	-1.44	-1.86	113	0.90	

As we have already noted form analyses of hourly data in §5.3, a few aspects are typical of all spectra. A spectral break occurs at $f^* \approx 10^{-5}$ Hz. For $f < f^*$, the

Table 24: Spectral index, temporal scales and anisotropy for the periods A2 and B2.

Period A2	α_1	α_2	T (days)	τ (hr)	A
radial	-1.10	-1.56	48.8	0.57	0.39
tangential	-0.95	-1.73	37.5	0.68	0.30
normal	-1.12	-1.72	30	0.80	0.3
mag. energy	-1.03	-1.70	37.2	0.69	
Period B2	α_1	α_2	T (days)	τ (hr)	A
radial	-1.32	-1.55	54.6	0.59	0.37
tangential	-1.20	-1.68	76.4	0.72	0.39
normal	-1.28	-1.65	107	1.03	0.24
mag. energy	-1.27	-1.65	85	0.76	

energy decay rate is mild, $\alpha \approx [-1.5, -0.95]$. This will be referred to as the low-frequency range. At $f > f^*$ the spectral decay is faster, the slope is in the interval $\alpha \in [-2.2, -1.47]$. Generally, a subsequent flattening occurs at $f > 3 \cdot 10^{-4}$ Hz: here the magnetometers accuracy probably affects the observed decay, however, the influence of kinetic phenomena is also possible. This will be the object of future investigations. The frequency f^* may be interpreted as the starting point for a possible turbulent cascade where nonlinear coupling is dominant, but this is not the only phenomenology determining the fluctuations behavior.

By looking at the spectra in figures 72 and 73, it can be noted that the spectral break strength depends on the magnetic field component. Some uncertainty on its location is also present, due to its closeness with the gap frequency. These gap distributions typically lead to a lack of energy between 10^{-6} and 10^{-5} Hz in the compressed sensing spectra (purple, in figures). This is more evident in the periods B2 and C2. In all figures the results are shown from three methods of analysis, in order to prevent misinterpretations (see figure 62). As a general strategy, as suggested in §5.2, we consider the correlation spectrum CI in the low-frequency range, and CS elsewhere.

For instance, the break is clearly visible for the tangential spectra from V1 data (A1, A2). In these cases indeed, B_T contains nearly half of the magnetic energy ($A = 0.5$) and presents a f^{-1} low-frequency range. Than it experiences the fastest decay ($\alpha \approx -2.2$) for $f > f^*$. The other components instead present slow energy cascades in the whole range of frequencies. On the other hand, the transition between the two regimes is smoother for V2 periods, where the break frequency is not always easily detectable (see in particular A2 and D2). In all cases the change of slope is less evident in the radial component than in the other two. The anisotropy level is much lower at V2 than at V1, in the whole spectral range. The energy decay laws obtained for V2 in the inertial regime

are comparable to the Kolmogorov's, with exponent about -5/3, while the cascade is faster for V1 (see figure 75 and table 23, 24).

All the spectra show sharp peaks - harmonics of $3.26 \cdot 10^{-3}$ Hz (64 times the 48-s sampling) - which might therefore be related to instrumental interference. Beside these, however, we observed a broader bump at $f_b = 5 \cdot 10^{-4}$ Hz (5.55 hours), showing up only in 2009 in both V1 and V2 periods (A1, A2). This peak is distributed on $\Delta f = 8 \cdot 10^{-5}$ Hz, and its energy density is above the instrumental accuracy threshold. The range of frequency, the bump shape, and the fact that it does not show up in 2011, suggest that it could be physical, due for instance to the gyromotion of some species of energetic particles. For example, in 2005, fluctuations of B over time scales of 10-20 min were related to 1-4 keV protons [118]. Magnetic helicity spectra, see Fraternale et al. [51], show that the peak in our spectra is negative-polarized. This is in agreement with the findings of Cannon et al. [39], who showed spectral bumps in power spectra of the parallel component of magnetic field, due to pickup ion/wave interaction. Despite this, the instrumental bias hypothesis cannot be excluded since the peak at f_b is not evident in the radial component. Furthermore, note that f_b is the same for V1 and V2 but the plasma speed measured at the two spacecraft is different (about 150 km/s for V2, and 20 km/s for V1). The coexistence of discrete modes and turbulence have been investigated in recent studies [62, 43], underlining the importance of the large-scale wavy range, which typically acts as a reservoir of energy for the turbulent cascade. To our knowledge, the origin and extension of such range in the heliosheath has not been deeply investigated yet. We hope that spectra provided by the present study would help to clarify the physical processes at the basis of the magnetic field fluctuations in the inner heliosheath.

Eventually, figure 76 shows the spectral magnetic energy transfer per unit volume, in the cgs system of units. This may be of help to set initial conditions for large-scale numerical simulations.

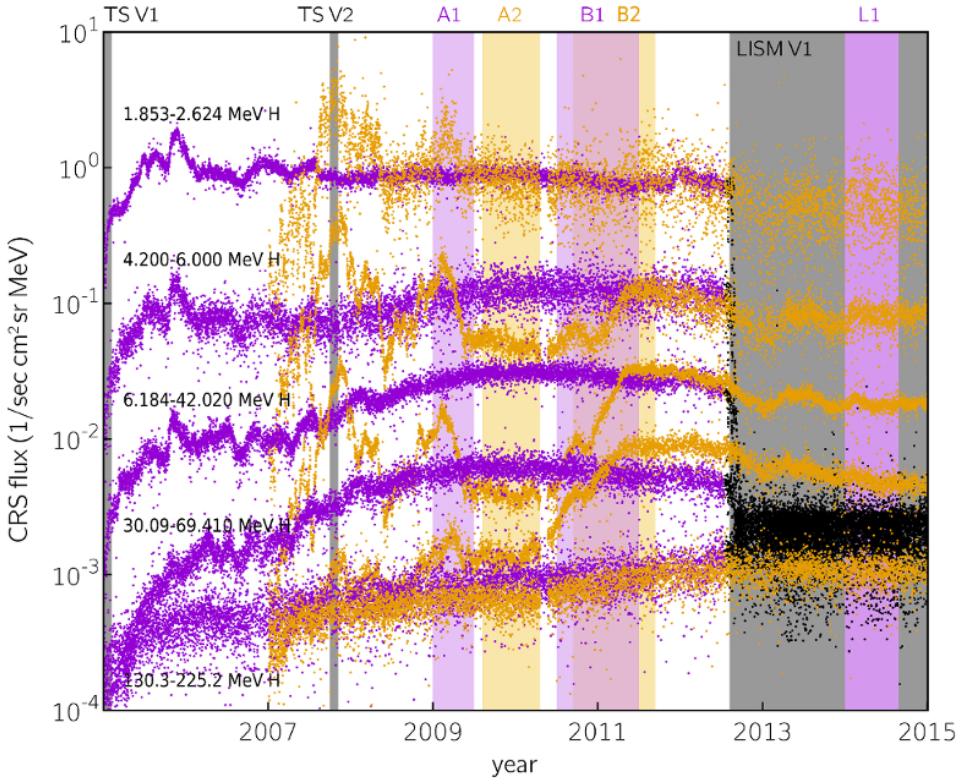

Figure 69: Cosmic Rays intensity. Energetic particles (protons) fluxes for different energy levels (ions from 1.8 MeV to 225 MeV) measured at both V1 (purple) and V2 (orange). The black bands represent (left to right) the termination shock crossing by V1, by V2, and the LISM region reached only by V1. One puzzle is the difference between particles intensity at V2 and V1. In fact, V1 shows quite smoother trends while large temporal variations have been recorded by V2. The colored bands show the periods A1, A2, B1, B2 considered for spectral analysis. L1 is a sequence of data in the LISM, not presented in this work.

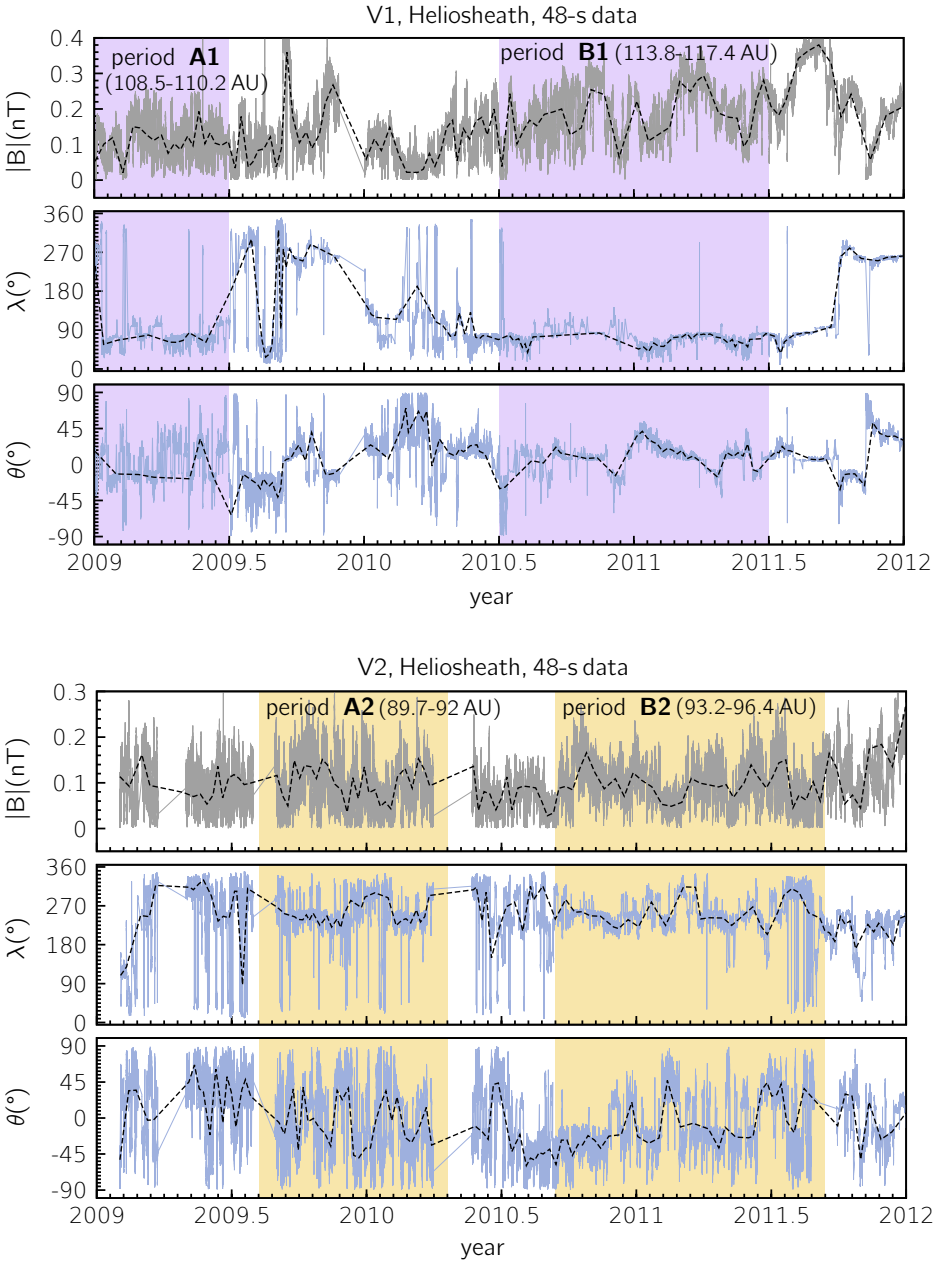

Figure 70: Magnetic field time history for periods A1, B1, A2, B2. Magnetic field strength, azimuthal and elevation angles from 2009 to 2012 as measured by Voyager 1 (top) and 2 (bottom).

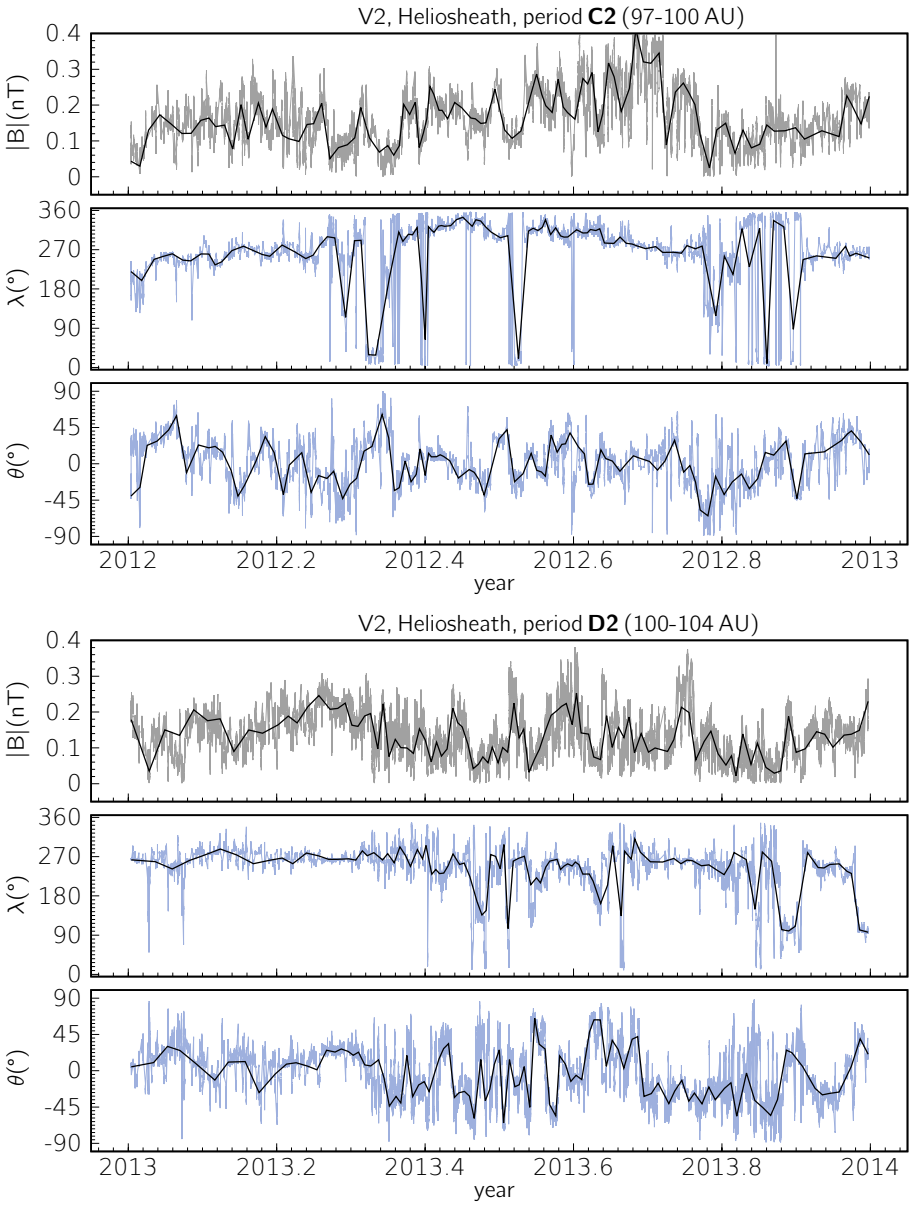

Figure 71: Magnetic field time history for periods C2, D2. Magnetic field strength, azimuthal and elevation angles from 2012 to 2014 as measured by Voyager 2.

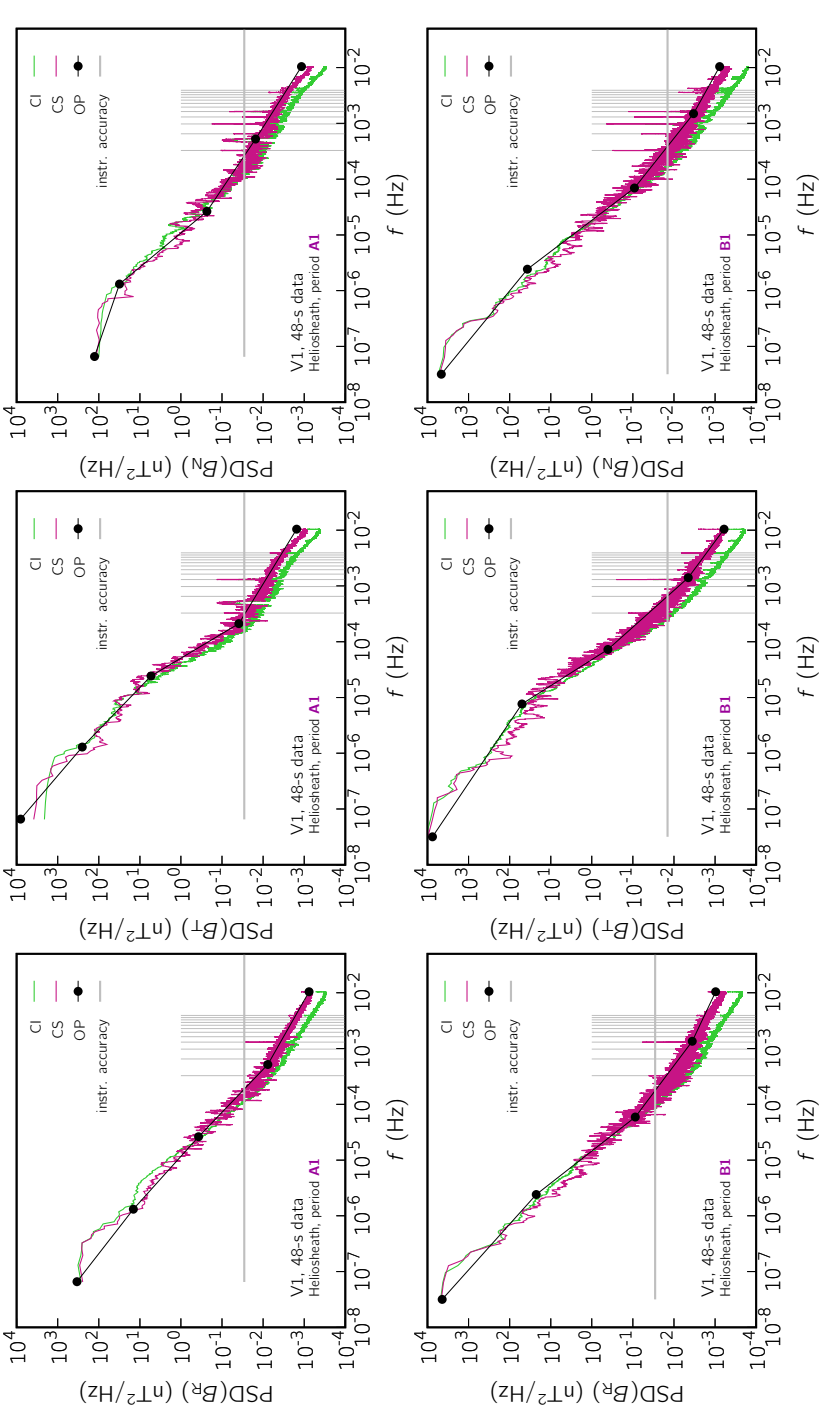

Figure 72: Magnetic field spectra at 108-117 AU from 48-s V1 (periods A1, B1). *Left column*: radial component; *central column*: tangential component; *right column*: normal component. From top to bottom, magnetic field fluctuation spectra are presented for the periods **A1** (Voyager 1, 2009.0-2009.5) and **B1** (Voyager 1, 2010.5-2011.5). Three methods of spectral estimation (CI,CS,OP) are compared. CS (purple spectra) leads to better estimates in the higher frequency range at about $f > 10^{-5}$ Hz, while below this threshold it lacks accuracy. In contrast, in the lower frequency range CI (green spectra) seems more reliable. OP gives directions in this sense. Vertical gray lines are drawn in correspondence to probably instrumental-related peaks.

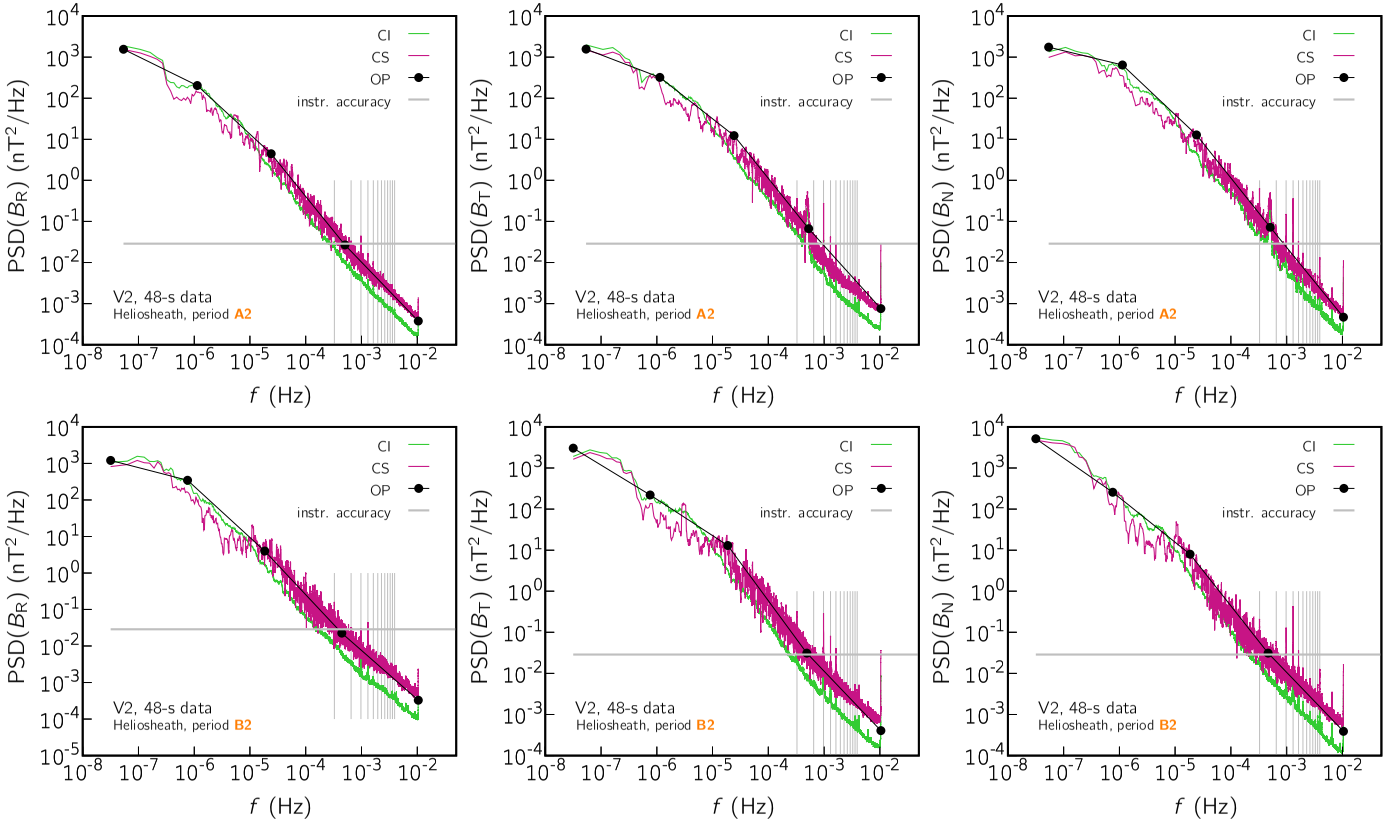

Figure 73: Magnetic field spectra at 89 -96 AU from 48-s V2 data (periods A2, B2). *Left column*: radial component; *central column*: tangential component; *right column*: normal component. From top to bottom, magnetic field fluctuation spectra are presented for the periods **A2** (Voyager 2, 2009.6-2010.3) and **B2** (Voyager 2, 2010.7-2011.7). Three methods of spectral estimation (CI, CS, OP) are compared.

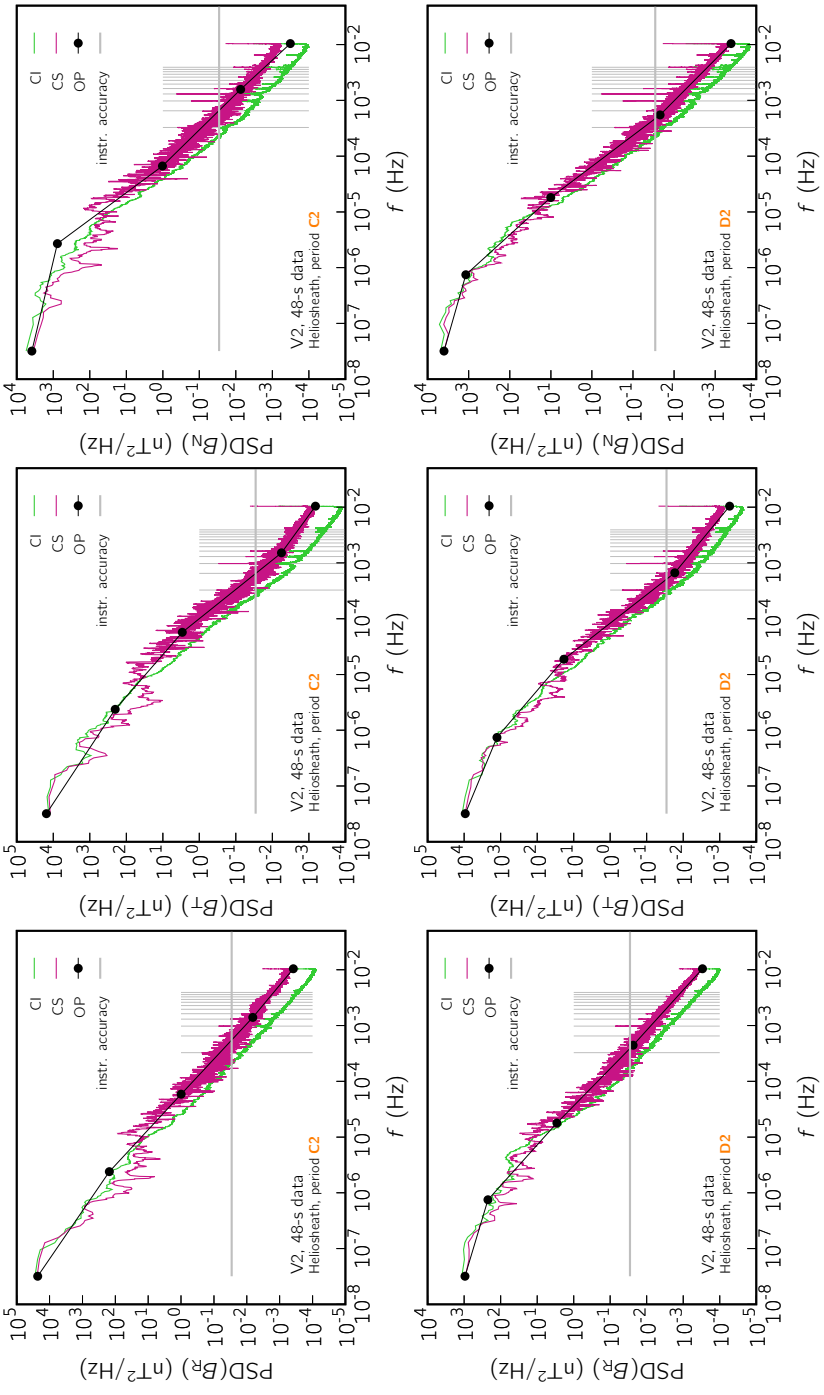

Figure 74: Magnetic field spectra at 97-104 AU for 48-s V2 data (periods C2, D2). *Left column*: radial component; *central column*: tangential component; *right column*: normal component. Spectra for the periods **C2** (Voyager 2, 2012.0-2013.0) and **D2** (Voyager 2, 2013.0-2014.0) are presented (top to bottom).

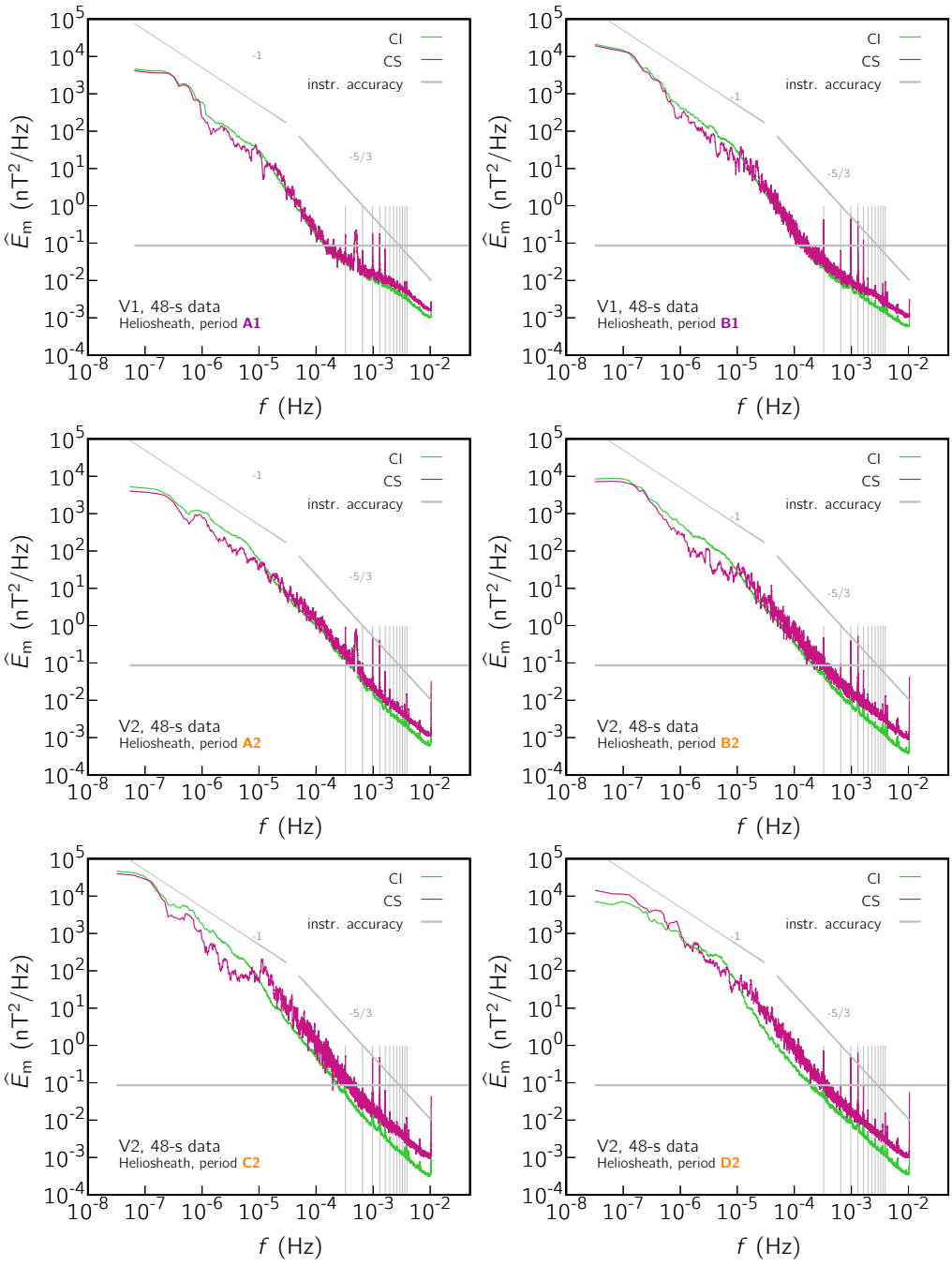

Figure 75: Magnetic energy spectra at 97-104 AU for 48-s V2 data.

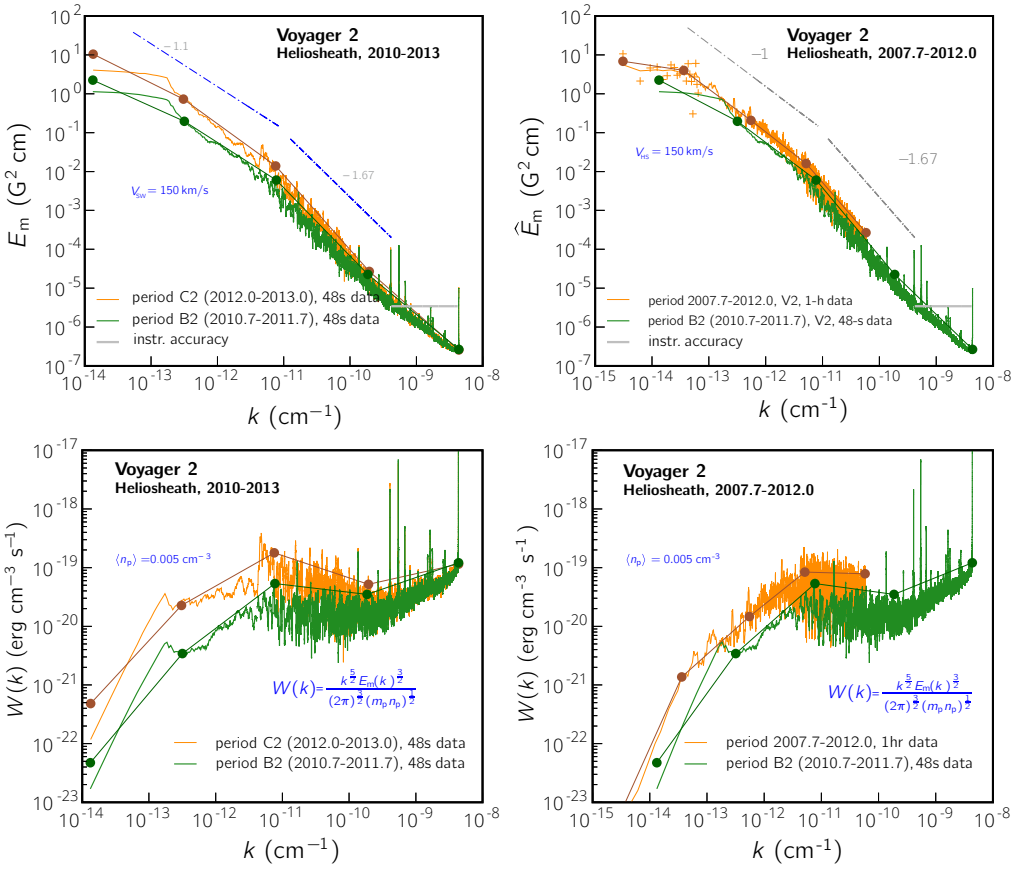

Figure 76: Spectral magnetic energy transfer at V2. Left panels show the power spectra (top) and the spectral energy transfer per unit volume, W (bottom) for the periods B2 and C2. Right panels show a comparison for the 4-year period after the TS crossing (2007.7-2012) and, again, the period C2. Frequency spectra have been converted to spatial spectra by using $V = 150$ km/s. The formula used to compute spectral transfer was first obtained from dimensional analysis by Kovasznay in 1948 [76].

5.5 Fractal analysis of the dissipation rate of magnetic energy in the Heliosheath

Figures 77 and 78 show preliminary results of multifractal analysis of the magnetic-field components derivative in the heliosheath (in the periods A1, B1, A2, B2). In fact, the squared spatial derivatives are representative of the dissipation field of magnetic energy. Of course, from the Voyagers one-point temporal measurements one can just compute time derivatives, which correspond to the spatial derivative in the wind direction if the Taylor hypothesis is valid. This analysis was attempted in order to investigate the intermittent character of the rate of dissipation ϵ_B of the turbulent magnetic energy. Based on the classical turbulence theory [94, 55], such analysis is performed in the inertial range of turbulence. From spectra computed in the previous section, it seems that in order to catch the inertial range, at least 1-h data are needed. However, all multifractal analysis of solar wind (at least in the literature explored so far) are performed on scales grater than 1 day, see for instance [33, 84, 83]. This choice is certainly justified by the difficulty in the computation arising from the missing data problem, when higher-resolution data are used. Moreover, most studies are in terms of the strength of B, in place of the approximate dissipation field. We put big efforts to obtain good fits using 48-s data, and even if this investigation is at an early stage, results are encouraging. The qth-order fractal dimensions are defined as follows [107]

$$D_{\mathrm{q}} = \frac{1}{1-q} \lim_{\epsilon \to 0} \frac{\ln\ I(q,\epsilon)}{\ln(1/\epsilon)} \qquad I(q,r) = \sum_{i=1}^{N(\epsilon)} \mu_i^q. \tag{171}$$

where μ_i is the measure (a probability density) for the i-th box of size ϵ and $N(\epsilon)$ is the total number of boxes. As a measure, we chose the squared derivatives of the magnetic field components

$$\mu_i = \left\langle \frac{\partial B_j}{\partial r}^2 \right\rangle, \quad i = 1, \ldots, N(\epsilon) \tag{172}$$

normalized so that $\sum_i \mu_i = 1$. This measure is taken as an approximation of the dissipation rate ϵ_B. Rescaling of the induction MHD equation ($x_i' = \lambda x_i$, $B_i' = \lambda^{\alpha/3} B_i$) leads to $\langle \epsilon_B \rangle_\epsilon \sim \epsilon^{\alpha-1}$ where α arbitrary. Multifractality means that each moment of order q has a different *fractal dimension* D_{q} An iso-α set has dimension $f(\alpha)$, so that a *singularity spectrum* is obtained

$$\alpha = \frac{\mathrm{d}}{\mathrm{d}q} \left[(q-1) D_{\mathrm{q}} \right], \tag{173}$$

$$f(\alpha) = \alpha q - (q-1) D_{\mathrm{q}}. \tag{174}$$

We observed that fairly good fractal dimensions and singularity spectra are obtained if in only the cubes of size ϵ containing a sufficiently high number data points are

retained in the sum (we do not interpolate data, just clean outliers which can affect the derivatives). The computation is then performed as described in detail by Meneveau and Sreenivasan [93], by calculating the limit 171 as the slope of the curve ln $I(q,\epsilon)$ vs $\ln(1/\epsilon)$, computed where good linear trends are observed.

Fractal dimensions are related to other quantities as the power spectrum slope and the structure function exponents, see below:

- $\alpha_0 = \alpha(q=0)$ physically meaningful if > 1.
- $\xi_p = (p/3-1)D_{p/3}+1$ structure functions scaling exponent.
- $= -5/3 - 1/3(1-D_{2/3})$ energy spectrum slope.
- $\langle \epsilon^2 \rangle_r \sim r^m \quad m = 1 - D_2$ intermittency exponent.
- $\Delta = \alpha_{max} - \alpha_{min}$ multifractality degree.
- $S = (\alpha_0 - \alpha_{min})/(\alpha_{max} - \alpha_0)$ asymmetry degree.

These quantities have been computed for the four periods considered and are reported in tables 25. Good values are found for the power spectral slope, which is around -1.7. The intermittency index is analogous to what found in the literature for dissipation rate of turbulent neutral fluid flows [93].

Table 25: Characteristic quantities obtained from multifractal analysis: information dimension D_1, correlation dimension D_2, multifractality degree Δ,, asymmetry degree S, intermittency exponent m, slope of the power spectrum γ.

$\left(\frac{\partial B_{\mathbf{R}}}{\partial r}\right)^2$	α_0	D_1	D_2	$D_{2/3}$	Δ	S	m	γ
period A2	1.08	0.82	0.69	0.86	1.13	1.40	0.31	-1.71
period B2	1.04	0.83	0.74	0.86	1.03	1.05	0.26	-1.71
period A1	1.008	0.831	0.73	0.87	0.91	1.16	0.27	-1.71
period B1	1.01	0.81	0.71	0.84	0.93	1.13	0.29	-1.72
$\left(\frac{\partial B_{\mathbf{T}}}{\partial r}\right)^2$	α_0	D_1	D_2	$D_{2/3}$	Δ	S	m	γ
period A2	1.088	0.830	0.76	0.865	1.09	0.98	0.24	-1.71
period B2	1.08	0.80	0.69	0.83	1.11	1.21	0.31	-1.72
period A1	1.040	0.803	0.69	0.84	1.01	1.24	0.31	-1.72
period B1	1.07	0.78	0.68	0.83	1.07	1.15	0.32	-1.73
$\left(\frac{\partial B_{\mathbf{N}}}{\partial r}\right)^2$	α_0	D_1	D_2	$D_{2/3}$	Δ	S	m	γ
period A2	1.085	0.820	0.70	0.86	1.11	1.21	0.30	-1.71
period B2	1.06	0.81	0.74	0.85	1.03	0.95	0.26	-1.72
period A1	1.001	0.861	0.77	0.88	0.86	1.52	0.24	-1.71
period B1	1.01	0.80	0.69	0.484	1.01	1.15	0.31	-1.72

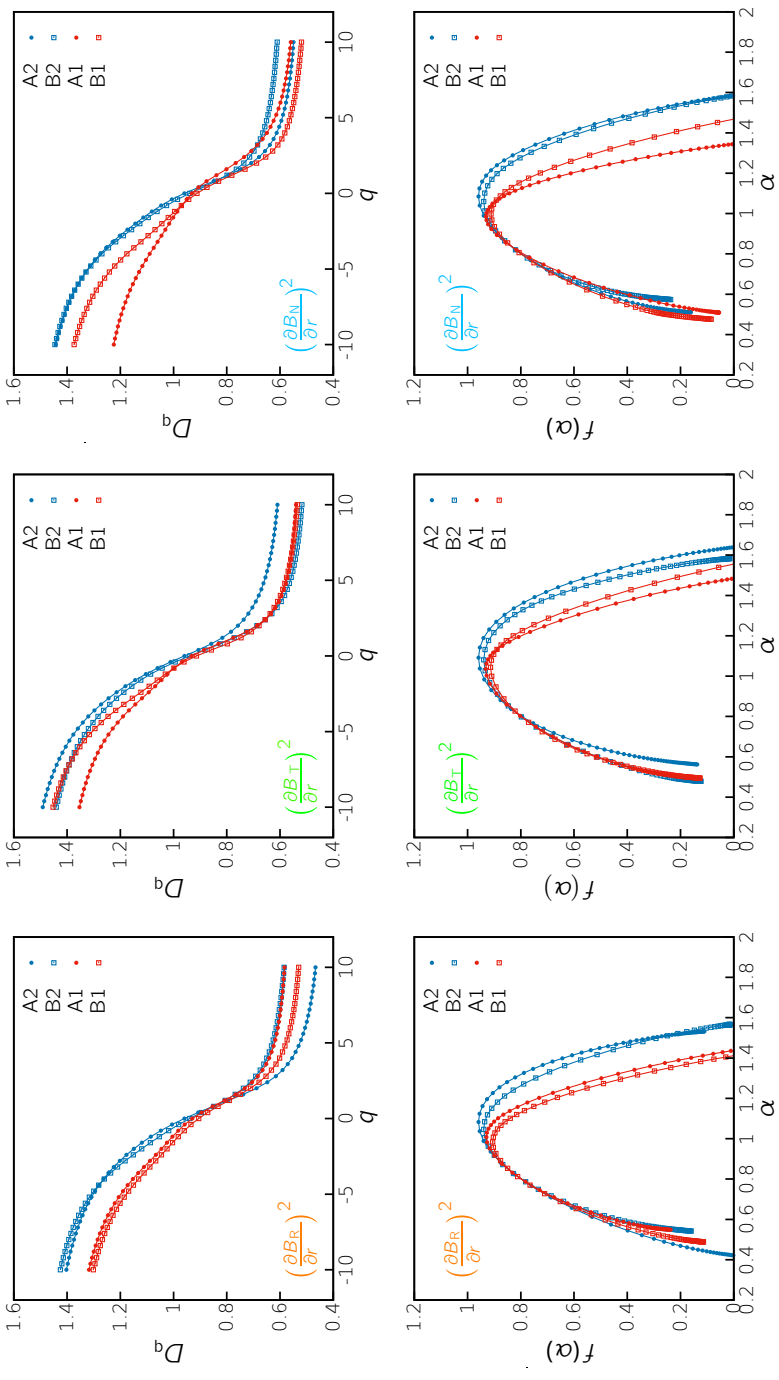

Figure 77: Multifractal dimensions and singularity spectra of the magnetic energy dissipation rate. Analysis of periods A1, B1, A2, B2. The computation is performed in the range of (temporal) scales $\epsilon \in [9h - 0.5h]$, corresponding to the frequency range $f \in [3 \cdot 10^{-5}, 5.5 \cdot 10^{-4}]$ Hz in the power spectra. Each period (A1-B2) was split in 6 to 10 sub-periods so that averaged fractal dimensions and singularity spectra are shown.

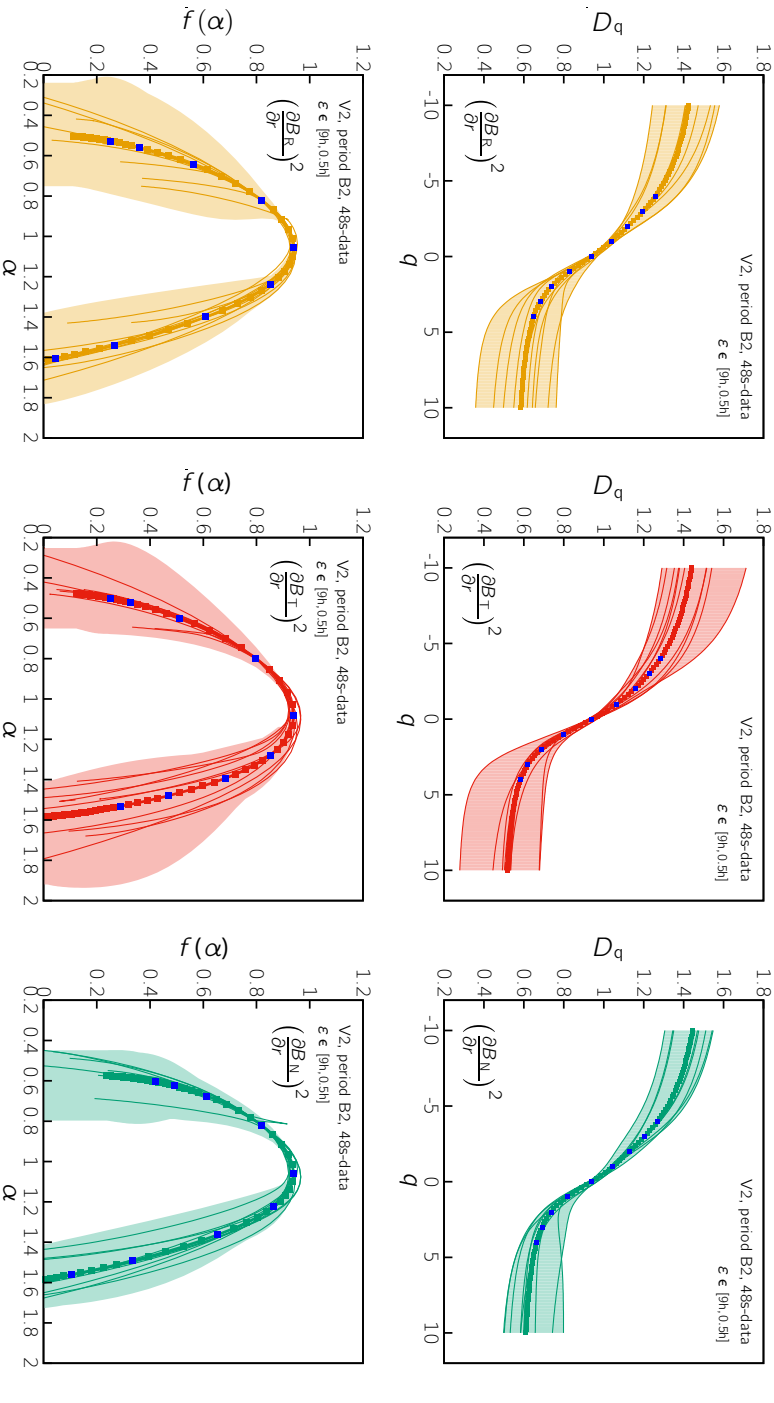

Figure 78: Multifractal analysis of the magnetic energy dissipation rate, period B2. Here detailed results on the computation of fractal dimensions (top) and singularity spectra (bottom) are shown for the period B2. The computation is performed in the range of temporal scales $\epsilon \in [9h - 0.5h]$. Each period (A1, A2, B1, B2) was split in 10 sub-periods.

5.6 **Final remarks**

This study provides magnetic field power spectra from Voyager 1 and 2 high-resolution measurements in the inner heliosheath. This is the outermost region of the heliosphere, located downstream of the termination shock and upstream of the heliopause, which is the separation surface between the solar wind plasma and the interstellar gas. To our knowledge, this was the first attempt to compute power spectra in this portion of the heliosphere, especially for a frequency range over five decades up to 0.02 Hz. A collection of several periods has been considered, according to the temporal distribution of the energetic particles and the polarity of the magnetic field. Power spectra of magnetic energy show a break frequency nearly equal to $f = 10^{-5}$ Hz (with some variations, depending on the component of the magnetic field under consideration), separating a low-frequency $1/f$ range similar to what is observed in the solar wind at a much smaller heliocentric distance.

This range is consistent to the presence of large-scale Alfvén waves, but no proof could be provided since plasma velocity data miss nearly 97% points and the uncertainty due to noise does not permit a reliable computation of the cross helicity. The extent of such energy-containing range still misses an explanation, but we suggest it may be related to the spacing of the folds of the heliospheric current sheet. We believe that wave analysis similar to those done in hydrodynamics in Part 1 of this thesis could shed light on this point.

Unfortunately, no relevant differences on the structure of the fluctuation field could be highlighted between sectored and unipolar regions whose existence is actually under scientific debate. For this reason, further investigations are planned in this direction. Differences are observed instead between the magnetic field fluctuations measured at Voyager 1 and at Voyager 2. Beyond the break frequency, all spectra show a power-law steeper decay with spectral index nearly between -2 and -1.68. Typically, the fastest decay occurs at V1, as well as the highest anisotropy. The frequency range above 10^{-3} Hz may be affected by instrumental accuracy effects, but it is characterized by spectral trends typical of kinetic regimes, which is consistent with the computed gyromotion frequency.

Eventually, we focused on higher order statistics, in order to get insights into the dissipation rate of magnetic field and intermittency. Unlike other studies, we considered 48-s data in order to perform the analysis on the inertial range of the turbulent fluctuations. Evidence of intermittency is provided, comparable to what is observed in developed turbulent fields. This study is still in progress, and we hope that it will also be of support for future numerical large-scale simulations, and serve as reference for theoretical and other data analysis works.

P.2 BIBLIOGRAPHY

[1] F. Fraternale, L. Gallana, M. Iovieno, M. Opher, J. D. Richardson, and D. Tordella. "Turbulence in the solar wind: spectra from Voyager 2 data at 5 AU." In: *Phys. Scripta (Invited Comment)* 91.2 (2016), pp. 394–401. DOI: 10.1088/0031-8949/91/2/023011. URL: http://iopscience.iop.org/article/10.1088/0031-8949/91/2/023011/meta (cit. on pp. 134, 135).

[2] L. Gallana, F. Fraternale, M. Iovieno, S. M. Fosson, E. Magli, M. Opher, J. D. Richardson, and D. Tordella. "Voyager 2 solar plasma and magnetic field spectral analysis for intermediate data sparsity." In: *J. Geophys. Res.: Space Physics* 121.5 (2016), pp. 3905–3919. DOI: 10.1002/2015JA021830. URL: http://dx.doi.org/10.1002/2015JA021830 (cit. on pp. 134, 135).

[3] M. Iovieno, L. Gallana, J. D. Fraternale F. and Richardson, M. Opher, and D. Tordella. "Cross and magnetic helicity in the outer heliosphere from Voyager 2 observations." In: *Eur. J. Mech. B/Fluids* 55.2 (2016), pp. 394–401. DOI: 10.1016/j.euromechflu.2015.08.009 (cit. on p. 133).

[4] F. Fraternale, M. Iovieno, M. Opher, J. D. Richardson, and D. Tordella. "Magnetic fluctuation spectra comparison inside and outside sectored heliosheath regions." In: *In preparation* () (cit. on p. 134).

[5] F. Fraternale, L. Gallana, M. Iovieno, M. Opher, J. D. Richardson, and D. Tordella. "Magnetic field spectral analysis in the Heliosheath from Voyagers data." In: *Proceedings of the 24th International Congress of Theoretical and Applied Mechanics*. Montrèal, Canada, Aug. 2016. URL: http://areeweb.polito.it/ricerca/philofluid/includes/proceedings/ICTAM2016_Fraternale_131134.pdf (cit. on pp. 134, 135).

[6] A. Alexakis, P. D. Mininni, and A. Pouquet. "Turbulent cascades, transfer, and scale interactions in magnetohydrodynamics." In: *New J. Physics* 9.8 (2007), p. 298 (cit. on p. 184).

[7] O. Alexandrova, C. Lacombe, A. Mangeney, R. Grappin, and M. Maksimovic. "Solar wind turbulent spectrum at plasma kinetic scales." In: *Astroph. J.* 760.2 (2012). DOI: 10.1088/0004-637X/760/2/121 (cit. on p. 171).

[8] F. Fraternale, L. Gallana, M. Iovieno, M. Opher, J. D. Richardson, and D. Tordella. "Magnetic field spectral analysis in the Heliosheath from Voyagers data." In: *Proceedings of the European Postgraduate Fluid Dynamics Conference*. Warszawa, Poland, July 2016 (cit. on pp. 134, 135).

[9] Hannes Alfvén. "Existence of electromagnetic-hydrodynamic waves." In: *Nature* 150 (1942), pp. 405–406 (cit. on p. 142).

[10] F. Fraternale, L. Gallana, M. Iovieno, S. M. Fosson, E. Magli, M. Opher, J. D. Richardson, R. Morgan, and D. Tordella. "Turbulence in the heliosheath: spectral analysis from Voyager 1 and 2 data." In: *Bulletin of the American Physical Society - 68th Annual Meeting of the APS Division of Fluid Dynamics*. Vol. 60. 21. Boston, MA, USA, Nov. 2015. URL: `http://meetings.aps.org/link/BAPS.2015.DFD.A8.9` (cit. on pp. 134, 135).

[11] F. Fraternale, L. Gallana, S. M. Fosson, E. Magli, M. Opher, J. D. Richardson, M. Iovieno, and D. Tordella. "Solar wind spectral analysis in heliosheath from Voyager data." In: *Proceedings of the 15th European Turbulence Conference*. Delft, Netherlands, Aug. 2015. URL: `http://www.etc15.nl/proceedings/proceedings/documents/489.pdf` (cit. on pp. 134, 135).

[12] P. Babu. "Spectral analysis of nonuniformly sampled data and applications." PhD thesis. Uppsala Universitet, 2012 (cit. on p. 151).

[13] K. W. Behannon, M. H. Acuna, L. F. Burlaga, R. P. Lepping, N. F. Ness, and F. M. Neubauer. "Magnetic field experiment for Voyagers 1 and 2." In: *Space Sci. Rev.* 21.3 (1977), pp. 235–257 (cit. on p. 145).

[14] J. W. Belcher and L. Davis. "Large-amplitude Alfvén waves in the interplanetary medium, 2." In: *J. Geophy. Res.* 76.16 (1971), pp. 3534–3563. DOI: `10.1029/JA076i016p03534` (cit. on p. 185).

[15] John W. Belcher and Craig V. Solodyna. "Alfvén waves and directional discontinuities in the interplanetary medium." In: *J. Geophys. Res.* 80.1 (1975), pp. 181–186. DOI: `10.1029/JA080i001p00181` (cit. on p. 142).

[16] B. R. Bellamy, I. H. Cairns, and C. W. Smith. "Voyager spectra of density turbulence from 1 AU to the outer heliosphere." In: *J. Geophys. Res.* 110.A10 (2005) (cit. on p. 156).

[17] G. Belmont, R. Grappin, F. Mottez, F. Pantellini, and G. Pelletier. *Collisionless plasmas in astrophysics*. John Wiley & Sons, 2013. ISBN: 978-3-527-41074-3 (cit. on pp. 140, 142).

[18] E. van den Berg and M. P. Friedlander. *SPGL1: A solver for large-scale sparse reconstruction*. http://www.cs.ubc.ca/labs/scl/spgl1. 2007 (cit. on p. 165).

[19] J. W. Bieber, J. Chen, W. H. Matthaeus, C. W. Smith, and M. A. Pomerantz. "Long-term variations of interplanetary magnetic field spectra with implications for cosmic ray modulation." In: *J. Geophys. Res.* 98.A3 (1993), pp. 3585–3603 (cit. on pp. 154, 156).

[20] Dieter Biskamp. *Magnetohydrodynamic turbulence*. Cambridge University Press, 2003. ISBN: 978-0521-0523-5 (cit. on pp. 140, 142, 171).

[21] R. B. Blackman and J. W. Tukey. *The measurement of power spectra*. Dover Publications, 1958 (cit. on pp. 152, 153, 155, 157).

[22] S. Boldyrev, J. Mason, and F. Cattaneo. "Dynamic alignment and exact scaling laws in MHD Turbulence." In: *Astrophysical Journal Letters* 699 (2009), pp. L39–L42 (cit. on p. 186).

[23] J. E. Borovsky and M. H. Denton. "Solar wind turbulence and shear: A superposed epoch analysis of corotating interaction regions at 1 AU." In: *J. Geophys. Res.* 115 (2010). DOI: 10.1029/2009JA014966 (cit. on pp. 142, 155).

[24] B. Breech, W. H. Matthaeus, J. Minnie, S. Oughton, S. Parhi, J. W. Bieber, and B. Bavassano. "Radial evolution of cross helicity at low and high latitudes in the solar wind." In: *Proc. of the Solar Wind 11 - SOHO 16 "Connecting Sun and Heliosphere"*. Ed. by T. Zurbuchen and B. Flek. ESA Special Publication SP-592 592. Whistler, Canada, 2005, pp. 597–600 (cit. on p. 186).

[25] H. S. Bridge, J. W. Belcher, R. J. Butler, A. J. Lazarus, A. M. Mavretic, J. D. Sullivan, G. L. Siscoe, and V. M. Vasyliunas. "The plasma experiment on the 1977 Voyager mission." In: *Space Sci. Rev.* 21 (1977), pp. 259–287 (cit. on p. 144).

[26] R. Bruno, B. Bavassano, V. D'Amicis R.and Carbone, L. Sorriso-Valvo, and E. Pietropaolo. "On the radial evolution of Alfvenic turbulence in the solar wind." In: *Space Sci. Rev.* 122.1-4 (2006), pp. 321–328. DOI: 10.1007/s11214-006-5232-8 (cit. on p. 142).

[27] R. Bruno and V. Carbone. "The The Solar Wind as a Turbulence Laboratory." In: *Living Rev. Solar Phys.* 10.2 (2013) (cit. on p. 140).

[28] L. F. Burlaga. "Merged interaction regions and large-scale magnetic field fluctuations during 1991 - Voyager-2 observations." In: *J. Geophys. Res.* 99 (1994), pp. 19341–19350 (cit. on p. 145).

[29] L. F. Burlaga, W. H. Mish, and D. A. Roberts. "Large-Scale Fluctuations in the Solar wind at 1 AU: 1978–1982." In: *J. Geophys. Res.* 94.A1 (1989), pp. 177–184. DOI: 10.1029/JA094iA01p00177 (cit. on p. 177).

[30] L. F. Burlaga and N. F. Ness. "Compressible "Turbulence" Observed in the Heliosheath by Voyager 2." In: *Astrophys. J.* 703.1 (2009), p. 311. URL: http://stacks.iop.org/0004-637X/703/i=1/a=311 (cit. on p. 201).

[31] L. F. Burlaga and N. F. Ness. "Magnetic field strength fluctuations and the q-Triplet in the Heliosheath: Voyager 2 Observations from 91.0 to 94.2 AU at Latitude 30° s." In: *Astrophys. J.* 765.1 (2013), p. 35 (cit. on p. 198).

[32] L. F. Burlaga, N. F. Ness, and M. H. Acuna. "Magnetic fields in the Heliosheath: Voyager 1 observations." In: *Astrophys. J.* 642.1 (2006), p. 584 (cit. on p. 201).

[33] L. F. Burlaga, N. F. Ness, and M. H. Acuna. "Multiscale structure of magnetic fields in the heliosheath." In: *J. Geophys. Res.-Space Physics* 111.A9 (2006). DOI: 10.1029/2006JA011850 (cit. on p. 216).

[34] L. F. Burlaga, N. F. Ness, and J. D. Richardson. "Heliosheath magnetic field and plasma observed by Voyager 2 during 2011." In: *J. Geophys. Res.* 119.8 (2014). DOI: 10.1002/2014JA020297 (cit. on pp. 201, 204).

[35] L. F. Burlaga, N. F. Ness, Y.-M. Wang, and N. R. Sheeley. "Heliospheric magnetic field strength and polarity from 1 to 81 AU during the ascending phase of solar cycle 23." In: *J. Geophys. Res.* 107 (2002), pp. 1410–19350 (cit. on p. 145).

[36] E. J. Candes, J. K. Romberg, and T. Tao. "Robust uncertainty principles: exact signal reconstruction from highly incomplete frequency information." In: *IEEE T. Inform. Theor.* 52.2 (2006), pp. 489–509. DOI: 10.1109/TIT.2005.862083 (cit. on pp. 154, 164).

[37] E. J. Candes, J. K. Romberg, and T. Tao. "Stable signal recovery from incomplete and inaccurate measurements." In: *Commun. Pure Appl. Math.* 59.8 (2006), pp. 1207–1223. DOI: 10.1002/cpa.20124 (cit. on p. 164).

[38] E. J. Candes and M. B. Wakin. "An introduction to compressive sampling." In: *IEEE Signal. Process. Mag.* 25.2 (2008), pp. 21–30. DOI: 10.1109/MSP.2007.914731 (cit. on p. 164).

[39] B. E. Cannon, C. W. Smith, P. A. Isenberg, B. J. Vasquez, C. J. Joyce, N. Murphy, and R. G. Nuno. "Ulysses observations of magnetic waves due to newborn interstellar pickup ions. I. II. Application of turbulence concepts to limiting wave energy and observability." In: *Astrophys. J.* 787.2 (2014). DOI: 10.1088/0004-637X/787/2/133 (cit. on p. 207).

[40] NASA Goddard Space Flight Center. *Space Physics Data Facility (COHOWeb)*. http://omniweb.gsfc.nasa.gov/coho/. 2016 (cit. on p. 143).

[41] P. Charbonneau and B. Knapp. "A User s Guide to PIKAIA 1.0." In: (1995). URL: http://www.hao.ucar.edu/modeling/pikaia/pikaia.php#sec9 (cit. on p. 171).

[42] F. De Santi, F. Fraternale, and D. Tordella. "Dispersive-to-nondispersive transition and phase-velocity transient for linear waves in plane wake and channel flows." In: *Phys. Rev. E* 93.3 (2016). DOI: 10.1103/PhysRevE.93.033116 (cit. on p. 174).

[43] P. Dmitruk, W. H. Matthaeus, and L. J. Lanzerotti. "Discrete modes and turbulence in a wave-driven strongly magnetized plasma." In: *Geophys. Res. Lett.* 31.21 (2004). ISSN: 0094-8276. DOI: 10.1029/2004GL021119 (cit. on pp. 142, 207).

[44] D. L. Donoho. "Compressed sensing." In: *IEEE T. Inform. Theory* 52.4 (2006), pp. 1289–1306. DOI: 10.1109/TIT.2006.871582 (cit. on pp. 154, 164).

[45] J. F. Drake, M. Opher, M. Swisdak, and J. N. Chamoun. "A magnetic reconnection mechanism for the generation of anomalous cosmic rays." In: *Astrophys. J.* 709.2 (2010), pp. 963–974. DOI: 10.1088/0004-637X/709/2/963 (cit. on p. 196).

[46] M.F. Duarte and Y.C. Eldar. "Structured Compressed Sensing: From Theory to Applications." In: *IEEE T. Signal Proces.* 59.9 (2011), pp. 4053–4085. DOI: 10.1109/TSP.2011.2161982 (cit. on p. 164).

[47] V Florinski. "On the transport of cosmic rays in the distant heliosheath." In: *Adv. Space Res.* 48.2 (2011), pp. 308–313 (cit. on p. 196).

[48] F. Fraternale, L. Gallana, S. M. Fosson, E. Magli, M. Opher, J. D. Richardson, M. Iovieno, and D. Tordella. "Solar wind spectral analysis in heliosheath from Voyager data." In: *Proceedings of the 15th European Turbulence Conference*. Delft, Netherlands, Aug. 2015 (cit. on pp. 191, 195).

[49] F. Fraternale, L. Gallana, M. Iovieno, S. M. Fosson, E. Magli, M. Opher, J. D. Richardson, and D. Tordella. "Turbulence in the Heliosheath: spectral analysis from Voyager 1 and 2 data." In: *Bulletin of the American Physical Society* 55 (2015) (cit. on pp. 154, 164, 191, 195).

[50] F. Fraternale, L. Gallana, M. Iovieno, S. M. Fosson, E. Magli, D. Tordella, M. Opher, and J. D. Richardson. "Spectral Analysis in the Solar Wind and Heliosheath." In: *Proceedings of the 14th Annual International Astrophysics Conference*. Tampa Bay, FL, USA, Apr. 2015 (cit. on p. 191).

[51] F. Fraternale, L. Gallana, M. Iovieno, M. Opher, J. D. Richardson, and D. Tordella. "Magnetic field spectral analysis in the Heliosheath from Voyagers data." In: *Proceedings of the 24th International Congress of Theoretical and Applied Mechanics*. Montrèal, Canada, Aug. 2016 (cit. on pp. 154, 191, 194, 207).

[52] F. Fraternale, L. Gallana, M. Iovieno, M. Opher, J. D. Richardson, and D. Tordella. "Magnetic field spectral analysis in the Heliosheath from Voyagers data." In: *Proceedings of the European Postgraduate Fluid Dynamics Conference*. Warszawa, Poland, July 2016 (cit. on p. 191).

[53] F. Fraternale, L. Gallana, M. Iovieno, M. Opher, J. D. Richardson, and D. Tordella. "Turbulence in the solar wind: spectra from Voyager 2 data at 5 AU." In: *Physica Scripta* 91.2 (2016), pp. 394–401. DOI: 10.1088/0031-8949/91/2/023011 (cit. on pp. 137, 148, 150).

[54] F. Fraternale, M. Iovieno, M. Opher, J. D. Richardson, and D. Tordella. "Magnetic fluctuation spectra comparison inside and outside sectored heliosheath regions." In: *In preparation* () (cit. on p. 191).

[55] Uriel Frisch. *Turbulence: the legacy of A.N. Kolmogorov*. Cambridge university press, 1995. ISBN: 0-521-45713-0 (cit. on p. 216).

[56] Rudi Gaelzer and Luiz F. Ziebell. "The dispersion relations of dispersive Alfven waves in superthermal plasmas." In: *J. Geophys. Res. Space Physics* 119.12 (2014). DOI: 10.1002/2014JA020667 (cit. on p. 174).

[57] L. Gallana, F. Fraternale, M. Iovieno, S. M. Fosson, E. Magli, M. Opher, J. D. Richardson, and D. Tordella. "Voyager 2 solar plasma and magnetic field spectral analysis for intermediate data sparsity." In: *J. Geophys. Res.: Space Physics* 121.5 (2016), pp. 3905–3919. DOI: 10.1002/2015JA021830. URL: http://dx.doi.org/10.1002/2015JA021830 (cit. on pp. 137, 147, 151–153, 155, 164, 165, 168, 178, 182).

[58] S. Galtier, S. V. Nazarenko, N. C. Newell, and A. Pouquet. "A weak turbulence theory for incompressible magnetohydrodynamics." In: *J. Plasma Phys.* 63.5 (2000), pp. 447–488 (cit. on p. 172).

[59] W. Gekelman, S. Vincena, D. Leneman, and J. Maggs. "Laboratory experiments on shear Alfven waves and their relationship to space plasmas." In: *J. Geophys. Res. Space Physics* 102.A4 (1997), pp. 7225–7236. DOI: 10.1029/96JA03683 (cit. on pp. 142, 174).

[60] W. Gekelman, S. Vincena, B. Van Compernolle, G. J. Morales, J. E. Maggs, P. Pribyl, and T. A. Carter. "The many faces of shear Alfven waves." In: *Phys. Plasmas* 18.5 (2011). ISSN: 1070-664X. DOI: 10.1063/1.3592210 (cit. on p. 142).

[61] P. Goldreich and S. Sridhar. "Toward a theory of interstellar turbulence. 2. Strong Alfvénic turbulence." In: *Astrophys. J.* 438.2, 1 (1995), pp. 763–775. DOI: 10.1086/175121 (cit. on p. 173).

[62] M. L. Goldstein, D. A. Roberts, A. E. Deane, S. Ghosh, and H. K. Wong. "Numerical simulation of Alfvenic turbulence in the solar wind." In: *J. Geophys. Res.-Space Physics* 104.A7 (1999), pp. 14437–14451. DOI: {10.1029/1998JA900128} (cit. on p. 207).

[63] MIT Space Plasma Group. *Voyager plasma science experiment. Collection of plasma velocity and magnetic field data*. URL: http://web.mit.edu/space/www/voyager/voyager.html (cit. on p. 143).

[64] M. E. Hill, R. B. Decker, L. E. Brown, J. F. Drake, D. C. Hamilton, S. M. Krimigis, and M. Opher. "Dependence of energetic ion and electron intensities on proximity to the magnetically sectored heliosheath: Voyager 1 and 2 observations." In: *Astrophys. J.* 781.2 (2014). DOI: 10.1088/0004-637X/781/2/94 (cit. on pp. 195, 196, 204).

[65] T. S. Horbury and B. T. Tsurutani. *The heliosphere near solar minimum: the Ulysses perspective*. Springer-Praxis Books in Astrophysics and Astronomy, 2001 (cit. on p. 142).

[66] G. G. Howes, K. G. Klein, and J. M. TenBarge. "Validity of the Taylor hypothesis for linear kinetic waves in the weakly collisional Solar wind." In: *Astrophys. J.* 789 (2 2014), p. 106 (cit. on p. 148).

[67] M. Iovieno, L. Gallana, F. Fraternale, J. D. Richardson, M. Opher, and D. Tordella. "Cross and magnetic helicity in the outer heliosphere from Voyager 2 observations." In: *European Journal of Mechanics B/FluidsS* 55.2 (2016), pp. 394–401. DOI: 10.1016/j.euromechflu.2015.08.009 (cit. on pp. 137, 142, 176, 184–188).

[68] P. S. Iroshnikov. "Turbulence of a conducting fluid in a strong magnetic field." In: *Sov. Astron.* 7 (1964), p. 566 (cit. on p. 172).

[69] C. J. Joyce, C. W. Smith, P. A. Isenberg, S. P. Gary, N. Murphy, P. C. Gray, and L. F. Burlaga. "Observation of Bernstein waves excited by newborn interstellar pickup ions in the solar wind." In: *Astroph. J.* 745 (2012), pp. 112–120 (cit. on pp. 155, 156).

[70] C. J. Joyce, C. W. Smith, P. A. Isenberg, N. Murphy, and N. A. Schwadron. "Observation of Bernstein waves excited by newborn interstellar pickup ions H+ and He+ as seen by Voyager at 4.5 AU." In: *Astroph. J.* 724 (2010), pp. 1256–1261 (cit. on pp. 155, 156).

[71] S. R. Keisler and R. H. Rhyne. "An assesment of prewhitening in estimating power spectra of atmospheric turbulence at long wavelengths." In: *Nasa Technical Note* D-8288 (1976), pp. 1–54 (cit. on pp. 154, 157).

[72] L. W. Klein, W. H. Matthaeus, D. A. Roberts, and M. L. Goldstein. "Evolution of spatial and temporal correlations in the solar-wind - Observations and interpretation." In: *Solar Wind seven*. Vol. 3. COSPAR Colloquia Series. 3rd COSPAR Colloquium on Solar Wind Seven, Goslar, Germany, Sep. 16-20, 1991. 1992, pp. 197–200. ISBN: 0-08-042049-4 (cit. on p. 178).

[73] C. A. Kletzing, S. R. Bounds, J. Martin-Hiner, W. Gekelman, and C. Mitchell. "Measurements of the shear Alfven wave dispersion for finite perpendicular wave number." In: *Phys. Rev. Lett.* 90.3 (2003). DOI: 10.1103/PhysRevLett.90.035004 (cit. on p. 174).

[74] A. N. Kolmogorov. "On the decay of isotropic turbulence in an incompressible viscous fluid." In: *C. R. Acad. Sci. URSS* 31 (1941), pp. 538–540 (cit. on p. 171).

[75] A. N. Kolmogorov. "The local structure of turbulence in an incompressible viscous fluid for very large Reynolds numbers." In: *C. R. Acad. Sci. URSS* 30 (1941), pp. 301–305 (cit. on p. 171).

[76] Leslie S. G. Kovasznay. "The spectrum of locally isotropic turbulence." In: *Phys. Rev.* 73 (9 May 1948), pp. 1115–1116. DOI: 10.1103/PhysRev.73.1115 (cit. on p. 215).

[77] R. H. Kraichnan. "Inertial-range spectrum of hydromagnetic turbulence." In: *Phys. Fluids* 8 (7 1965), pp. 1385–1387 (cit. on p. 172).

[78] RJ Leamon, CW Smith, NF Ness, WH Matthaeus, and HK Wong. "Observational constraints on the dynamics of the interplanetary magnetic field dissipation range." In: *J. Geophys. Res.* 103.A3 (1998), pp. 4775–4787. DOI: 10.1029/97JA03394 (cit. on pp. 155, 156).

[79] J. Li and P. Stoica. "An adaptive filtering approach to spectral estimation and SAR imaging." In: *IEEE Trans. Signal Proc.* 44.6 (1996), pp. 1469–1484. DOI: 10.1109/78.506612 (cit. on p. 163).

[80] Nicholas R Lomb. "Least-squares frequency analysis of unequally spaced data." In: *Astrophysics and Space Science* 39.2 (1976), pp. 447–462 (cit. on pp. 151, 152).

[81] M. Lustig, D.L. Donoho, J.M. Santos, and J.M. Pauly. "Compressed Sensing MRI." In: *Signal Processing Magazine, IEEE* 25.2 (2008), pp. 72–82. DOI: 10.1109/MSP.2007.914728 (cit. on p. 164).

[82] Robert L. Lysak. "On the dispersion relation for the kinetic Alfven wave in an inhomogeneous plasma." In: *Phys. Plasmas* 15.6 (2008). DOI: 10.1063/1.2918742 (cit. on p. 174).

[83] W. M. Macek and A. Wawrzaszek. "Voyager 2 observation of the multifractal spectrum in the heliosphere and the heliosheath." In: *Nonlinear Proc. Geoph.* 20.6 (2013), pp. 1061–1070. DOI: 10.5194/npg-20-1061-2013 (cit. on p. 216).

[84] W. M. Macek, A. Wawrzaszek, and V. Carbone. "Observation of the multifractal spectrum in the heliosphere and the heliosheath by Voyager 1 and 2." In: *J. Geophys. Res.-Space Physics* 117 (2012). DOI: 10.1029/2012JA018129 (cit. on p. 216).

[85] E. Marsch and C.-Y Tu. "On the radial evolution of MHD turbulence in the inner heliosphere." In: *J. Geophys. Res.* 95.A6 (1990), pp. 8211–8229. DOI: 10.1029/JA095iA06p08211 (cit. on pp. 148, 177, 179).

[86] E. Marsch and C.-Y Tu. "Spectral and spatial evolution of MHD turbulence in the inner heliosphere." In: *J. Geophys. Res.* 95.14 (1990), pp. 11945–11956 (cit. on p. 177).

[87] J. Mason, F. Cattaneo, and S. Boldyrev. "Dynamic alignment in driven magnetohydrodynamic turbulence." In: *Phys. Rev. Lett.* 97.25 (2006), p. 255002 (cit. on p. 186).

[88] W. H. Matthaeus and M. L. Goldstein. "Measurement of the rugged invariants of magnetohydrodynamic turbulence in the solar wind." In: *J. Geophys. Res.* 87.NA8 (1982), pp. 6011–6028. DOI: 10.1029/JA087iA08p06011 (cit. on pp. 150, 155, 156, 179, 185).

[89] W. H. Matthaeus, M. L. Goldstein, and C. W. Smith. "Evaluation of magnetic helicity in homogeneous turbulence." In: *Phys. Rev. Letters* 48.18 (1982), pp. 1256–1259. DOI: 10.1103/PhysRevLett.48.1256 (cit. on pp. 177, 178, 185).

[90] W. H. Matthaeus, J. Minnie, B. Breech, S. Parhi, J. W. Bieber, and S. Oughton. "Transport of cross helicity and radial evolution of Alfvénicity in the solar wind." In: *Geophys. Res. Lett.* 31 (2004), p. L12803 (cit. on pp. 142, 186).

[91] W. H. Matthaeus and Y. Zhou. "Extended inertial range phenomenology of magnetohydrodynamic turbulence." In: *Phys. Fluids B* 1 (9 1989), pp. 1929–1931 (cit. on p. 172).

[92] DJ McComas, SJ Bame, BL Barraclough, WC Feldman, HO Funsten, JT Gosling, P Riley, R Skoug, A Balogh, R Forsyth, BE Goldstein, and M Neugebauer. "Ulysses' return to the slow solar wind." In: *Geophys. Res. Lett.* 25.1 (1998), pp. 1–4 (cit. on p. 148).

[93] C Meneveau and K R Sreenivasan. "The multifractal spectrum of the dissipation field in turbulent flows." In: *Nuclear Physics B (Proc. Suppl.)* 2 (1987), pp. 49–79 (cit. on p. 217).

[94] C Meneveau and K R Sreenivasan. "The multifractal nature of turbulent energy-dissipation." In: *J. Fluid Mech.* 224 (1991), pp. 429–484. DOI: 10.1017/S0022112091001830 (cit. on p. 216).

[95] H. K. Moffatt. "The degree of knottedness of tangles vortex lines." In: *J. Fluid Mech.* 36 (1969), pp. 117–129 (cit. on p. 183).

[96] H. K. Moffatt. *Magnetic field generation in electrically conducting fluids*. Cambridge University Press, 1978 (cit. on p. 184).

[97] H. K. Moffatt and A. Tsinober. "Helicity in laminar and turbulent flows." In: *Annu. Rev. Fluid Mech.* 24 (1992), pp. 281–312 (cit. on p. 184).

[98] A. S. Monin and A. M. Yaglom. *Statistical fluid mechanics, Volume 2*. Vol. II. MIT Press, 1971 (cit. on pp. 154, 176, 201).

[99] D Montgomery, MR Brown, and WH Matthaeus. "Density fluctuation spectra in magnetohydrodynamic turbulence." In: *J. Geophys. Res.* 92.A1 (1987), pp. 282–284. DOI: 10.1029/JA092iA01p00282 (cit. on p. 149).

[100] NASA. *Voyager Magnetometer Experiment Data*. https://vgrmag.gsfc.nasa.gov/data.html. 2009 (cit. on p. 143).

[101] S. V. Nazarenko and A. A. Schekochihin. "Critical balance in magnetohydrodynamic, rotating and stratified turbulence: towards a universal scaling conjecture." In: *J. Fluid Mech.* 677 (2011), pp. 134–153. DOI: 10.1017/S002211201100067X (cit. on p. 173).

[102] N. Ness, K. W. Behannon, R. P. Lepping, and K. H. Schatten. "Use of two magnetometers for magnetic field measurements on a spacecraft." In: *J. Geophys. Res.* 76 (1971), p. 3564 (cit. on p. 145).

[103] M. Neugebauer. "Enhancement of solar-wind fluctuations at proton gyroradius." In: *J. Geophys. Res.* 80.7 (1975), pp. 998–1002. DOI: 10.1029/JA080i007p00998 (cit. on p. 149).

[104] M. Opher, J. F. Drake, K. M. Schoeffler, J. D. Richardson, R. B. Decker, and G. Toth. "Is the magnetic field in the heliosheath laminar or a turbulent sea of bubbles?" In: *Astrophys J.* 734.1 (2011). DOI: 10.1088/0004-637X/734/1/71 (cit. on pp. 196, 199, 205).

[105] M. Opher, J. F. Drake, B. Zieger, and T. I. Gombosi. "Magnetized jets driven by the sun: the structure of the heliosphere revisited." In: *Astroph. J. Lett.* 800.2 (2015). DOI: 10.1088/2041-8205/800/2/L28 (cit. on p. 195).

[106] S Orlando, YQ Lou, G Peres, and R Rosner. "Alfvenic fluctuations in fast and slow solar winds." In: *J. Geophys. Res.* 102.A11 (1997), pp. 24139–24149. DOI: 10.1029/97JA01988 (cit. on p. 179).

[107] Edward Ott. *Chaos in dynamical systems*. Cambridge University Press, 2002 (cit. on p. 216).

[108] E. N Parker. "Dynamics of the interplanetary gas and magnetic fields." In: *Astrophys. J.* 128 (1958), p. 664 (cit. on p. 138).

[109] E. N. Parker. "Theoretical studies of the solar wind phenomenon." In: *Space Sci, Rev.* 9.3 (1969), pp. 325–360. DOI: 10.1007/BF00175236 (cit. on p. 138).

[110] J. J. Podesta. "Dependence of solar-wind power spectra on the direction of local mean magnetic field." In: *Astrophys J.* 698.2 (2009), pp. 986–999. DOI: 10.1088/0004-637X/698/2/986 (cit. on p. 173).

[111] J. J. Podesta and A. Bhattacharjee. "Theory of incompressible magnetohydrodynamic turbulence with scale-dependent alignment and cross-helicity." In: *Astrophys. J.* 718.2 (2010), pp. 1151–1157. DOI: 10.1088/0004-637X/718/2/1151 (cit. on p. 173).

[112] J. J. Podesta, D. A. Roberts, and M. L. Goldstein. "Spectral exponents of kinetic and magnetic energy spectra in solar wind turbulence." In: *Astrophys J.* 664 (2007), pp. 543–548. DOI: 10.1086/519211 (cit. on pp. 143, 178).

[113] N. V. Pogorelov, S. N. Borovikov, M. C. Bedford, J. Heerikhuisen, T. K. Kim, I. A. Kryukov, and G. P. Zank. "Modeling solar wind flow with the multi-scale fluid-kinetic simulation suite." In: *Numerical modeling of space plasma flows astronum-2012*. Ed. by NV Pogorelov, E Audit, and GP Zank. Vol. 474. 7th Annual International Conference on Numerical Modeling of Space Plasma Flows, Big Isl, HI, JUN 25-29, 2012. 2013, pp. 165–171 (cit. on p. 205).

[114] N. V. Pogorelov, S. T. Suess, S. N. Borovikov, R. W. Ebert, D. J. McComas, and G. P. Zank. "Three-dimensional features of the outer heliosphere due to coupling between the interstellar magnetic field. IV. Solar cycle model based on Ulysses Observations." In: *Astrophys. J.* 772.1 (2013). DOI: 10.1088/0004-637X/772/1/2 (cit. on pp. 202, 205).

[115] W. H. Press and G. B. Rybicki. "The time delay of gravitational lens 0957+561. I. Methodology and analysis of optical photometric data." In: *Astroph. J.* 385.2, 1 (1992), pp. 404–415. DOI: 10.1086/170951 (cit. on p. 161).

[116] K. Rahbarnia, S. Ullrich, K. Sauer, O. Grulke, and T. Klinger. "Alfvén wave dispersion behavior in single- and multicomponent plasmas." In: *Phys. Plasmas* 17.3 (2010). DOI: 10.1063/1.3322852 (cit. on p. 174).

[117] J. D. Richardson, J. W. Belcher, D. Tordella, F. Fraternale, L. Gallana, and M. Iovieno. "Voyager 2 observations of plasma in the heliosheath." In: *Proceedings of the AGU Fall Meeting*. San Francisco, CA, USA, Dec. 2015 (cit. on p. 191).

[118] J. D. Richardson and L. F. Burlaga. "The solar wind in the outer heliosphere and heliosheath." In: *Space Sci. Rev.* 176.1-4 (2013), pp. 217–235. DOI: 10.1007/s11214-011-9825-5 (cit. on pp. 201, 207).

[119] J. D. Richardson and R. B. Decker. "Voyager 2 observations of plasmas and flows out to 104 AU." In: *Astrophys. J.* 792.2 (2014). DOI: 10.1088/0004-637X/792/2/126 (cit. on pp. 145, 195, 197).

[120] J. D. Richardson, J. C. Kasper, C. Wang, J. W. Belcher, and A. J. Lazarus. "Cool heliosheath plasma and deceleration of the upstream solar wind at the termination shock." In: *Nature* 454.7200 (2008), pp. 63–66. DOI: 10.1038/nature07024 (cit. on p. 195).

[121] D. A. Roberts. "Evolution of the spectrum of solar wind velocity fluctuations from 0.3 to 5 AU." In: *J. Geophys. Res.* 115 (2010). DOI: 10.1029/2009JA015120 (cit. on pp. 143, 177, 178).

[122] D. A. Roberts and M. L. Goldstein. "Spectral signatures of jumps and turbulence in interplanetary speed and magnetic-field data." In: *J. Geophys. Res.* 92.A9 (1987), pp. 10105–10110. DOI: 10.1029/JA092iA09p10105 (cit. on p. 177).

[123] D. A. Roberts, M. L. Goldstein, L. W. Klein, and W. H. Matthaeus. "Origin and evolution of fluctuation in the solar wind: Helios observations and Helios-Voyager comparisions." In: *J. Geophys. Res.* 92.A11 (1987), pp. 12023–12035. DOI: 10.1029/JA092iA11p12023 (cit. on p. 186).

[124] D. A. Roberts, M. L. Goldstein, W. H. Matthaeus, and S. Ghosh. "Velocity shear generation of solar-wind turbulence." In: *J. Geophys. Res* 97.A11 (1992), pp. 17115–17130. DOI: 10.1029/92JA01144 (cit. on p. 142).

[125] B. N. Rogers, R. E. Denton, and M. A. Drake J. F .and Shay. "Role of dispersive waves in collisionless magnetic reconnection." In: *Phys. Rev. Lett.* 87.19 (2001). ISSN: 0031-9007. DOI: 10.1103/PhysRevLett.87.195004 (cit. on p. 174).

[126] H. M. Rosenblatt. "Spectral analysis and parametric methods for seasonal adjustment of economic time series." In: *Working paper - U. S. Bureau of the Census* 23 (1965), pp. 235–257 (cit. on p. 157).

[127] W. Rowe, J. Li, and P. Stoica. "Sparse iterative adaptive approach with application to source localization." In: *2013 IEEE 5th Int. Workshop on Computational Advances in Multi-Sensor Adaptive Processing (CAMPSAP)*. 2013, pp. 196–199 (cit. on p. 164).

[128] M. Rudelson and R. Vershynin. "Sparse reconstruction by convex relaxation: Fourier and Gaussian measurements." In: *40th Annual Conference of Information Sciences and Systems, Vols. 1-4*. Princeton Univ, Dept Elect Engn; IEEE Informat Theory Soc. 2006, pp. 207–212. ISBN: 1-4244-0349-9. DOI: 10.1109/CISS.2006.286463 (cit. on p. 164).

[129] G. B. Rybicki and W. H. Press. "Interpolation, realization, and reconstruction of noisy, irregularly sampled data." In: *Astroph. J.* 398 (1992), pp. 169–176. DOI: 10.1086/171845 (cit. on pp. 154, 161, 162).

[130] J. Šafránková, Z. Němeček, L. Přech, and G. N. Zastenker. "Ion kinetic scale in the solar wind observed." In: *Phys. Rev. Letters* 110.2 (2013), pp. 1–5. DOI: 10.1103/PhysRevLett.110.025004 (cit. on pp. 149, 178).

[131] F. Sahraoui, M. L. Goldstein, P. Robert, and Y. V. Khotyaintsev. "Evidence of a cascade and dissipation of the solar-wind turbulence at the electron gyroscale." In: *Phys. Rev. Letters* 102.23 (2009). DOI: 10.1103/PhysRevLett.102.231102 (cit. on pp. 141, 171).

[132] J. D. Scargle. "Studies in astronomical time series analysis. II-Statistical aspects of spectral analysis of unevenly spaced data." In: *Astrophys. J.* 263 (1982), pp. 835–853 (cit. on p. 151).

[133] A. A. Schekochihin, S. V. Nazarenko, and T. A. Yousef. "Weak Alfven-wave turbulence revisited." In: *Phys. Rev. E* 85 (2012). DOI: 10.1103/PhysRevE.85.036406 (cit. on p. 172).

[134] P. K. Shukla. "Alfvenic tornadoes in a magnetized plasma." In: *J. Geophys. Res.-Space Physics* 118.1 (2013), pp. 1–4. DOI: 10.1029/2012JA018247 (cit. on p. 174).

[135] C. W. Smith, K. Hamilton, B. J. Vasquez, and R. J. Leamon. "Dependence of the dissipation range spectrum of interplanetary magnetic fluctuations upon the rate of energy cascade." In: *Astroph. J. Lett.* 645.1, 2 (2006), pp. L85–L88. DOI: 10.1086/506151 (cit. on pp. 155, 156).

[136] C. W. Smith, W. H. Matthaeus, and N. F. Ness. "Measurement of the dissipation range spectrum of magnetic fluctuations in the solar wind with applications to the diffusion of cosmic rays." In: *Proceedings of the 21st International Cosmic Ray Conference (Adelaide)*. Vol. 5. 1990, pp. 280–283 (cit. on p. 154).

[137] C. W. Smith, B. J. Vasquez, and K. Hamilton. "Interplanetary magnetic fluctuation anisotropy in the inertial range." In: *J. Geophys. Res.* 111.A9 (2006). DOI: 10.1029/2006JA011651 (cit. on pp. 155, 156).

[138] P. Stoica, E. G. Larsson, and J. Li. "Adaptive filter-bank approach to restoration and spectral analysis of gapped data." In: *Astron. J.* 120.4 (2000), p. 2163 (cit. on p. 163).

[139] Petre Stoica, Jian Li, and Jun Ling. "Missing data recovery via a nonparametric iterative adaptive approach." In: *IEEE Signal Process Lett.* 16.4 (2009), pp. 241–244. DOI: 10.1109/LSP.2009.2014114 (cit. on p. 164).

[140] EC Stone, AC Cummings, FB McDonald, BC Heikkila, N Lal, and WR Webber. "Voyager 1 explores the termination shock region and the heliosheath beyond." In: *Science* 309.5743 (2005), pp. 2017–2020 (cit. on p. 195).

[141] W. H. Thomson (Lord Kelvin). "On vortex motion." In: *Trans. Roy. Soc. Edinburg* 25 (1869), pp. 217–260 (cit. on p. 183).

[142] C.-Y Tu and E. Marsch. "MHD structures, waves and turbulence in the solar wind: observations and theories." In: *Space Sci. Rev.* 73.1-2 (1995), pp. 1–210. DOI: 10.1007/BF00748891 (cit. on pp. 140, 142, 179).

[143] Y. W. Wang, P. Stoica, J. Li, and T. L. Marzetta. "Nonparametric spectral analysis with missing data via the EM algorithm." In: *Dig. Signal Proc.* 15.2 (2005), pp. 191–206. DOI: 10.1016/j.dsp.2004.10.004 (cit. on p. 163).

[144] R. T. Wicks, D. A. Roberts, A. Mallet, A. A. Schekochihin, T. S. Horbury, and C. H. K. Chen. "Correlations at large scales and the onset of turbulence in the fast solar wind." In: *Astrophys. J.* 778.2 (2013). DOI: 10.1088/0004-637X/778/2/177 (cit. on p. 143).

[145] L. Woltjer. "A theorem on force-free magnetic fields." In: *Proc. Nat. Acad. Sci.* 44.6 (1958), pp. 489–491 (cit. on p. 183).

[146] Guangwu Xu and Zhiqiang Xu. "Compressed sensing matrices from Fourier matrices." In: *IEEE Trans. Inf. Theory* 61.1 (2015), pp. 469–478. DOI: 10.1109/TIT.2014.2375259 (cit. on p. 164).

[147] T. Yardibi, J. Li, P. Stoica, and A. B. Xue M. and Baggeroer. "Source localization and sensing: a nonparametric iterative adaptive approach based on weighted least squares." In: *IEEE Trans. Aero. Elec. Sys.* 46.1 (2010), pp. 425–443 (cit. on p. 164).

[148] N. Yokoi. "Cross helicity and related dynamo." In: *Geophys. Astrophys. Fluid Dyn.* 107.1-2, SI (2013), pp. 114–184. DOI: {10.1080/03091929.2012.754022} (cit. on pp. 183, 184).

[149] N. Yokoi and G. Balarac. "Cross-helicity effects and turbulent transport in magnetohydrodynamic flow." In: *J. Physics: Conf. Series* 318 (2011), p. 072039 (cit. on p. 183).

[150] G. P. Zank, P. Hunana, P. Mostafavi, and M. L. Goldstein. "Pickup ion mediated plasmas. I. Basic model and linear waves in the solar wind and local interstellar medium." In: *Astrophys. J.* 797.2 (2014). DOI: 10.1088/0004-637X/797/2/87 (cit. on p. 174).

[151] Y. Zhou, W. H. Matthaeus, and P. Dmitruk. "Colloquium: Magnetohydrodynamic turbulence and time scales in astrophysical and space plasmas." In: *Rev. Mod. Phys.* 76.4 (2004), pp. 1015–1035. DOI: 10.1103/RevModPhys.76.1015 (cit. on pp. 140, 171).

FINAL REMARK

As a general conclusion to this thesis, I would like to draw attention to the rich phenomenologies that can be pointed out by the hydrodynamic analogy between the transient propagation of internal waves in sheared flows and in the solar wind. I consider it important to promote future studies on the dispersion of Alfvén MHD waves in the general situation where both velocity and magnetic field fields are nonuniform.

PUBLICATIONS

Most of the present doctoral research has been published in journal papers and conference proceedings as listed below.

Journal papers

[1] F. De Santi, F. Fraternale, and D. Tordella. "Dispersive-to-nondispersive transition and phase-velocity transient for linear waves in plane wake and channel flows." In: *Phys. Rev. E* 93.3 (2016). DOI: 10.1103/PhysRevE.93.033116.

[2] F. Fraternale, L. Gallana, M. Iovieno, M. Opher, J. D. Richardson, and D. Tordella. "Turbulence in the solar wind: spectra from Voyager 2 data at 5 AU." In: *Phys. Scripta (Invited Comment)* 91.2 (2016), pp. 394–401. DOI: 10.1088/0031-8949/91/2/023011. URL: http://iopscience.iop.org/article/10.1088/0031-8949/91/2/023011/meta.

[3] L. Gallana, F. Fraternale, M. Iovieno, S. M. Fosson, E. Magli, M. Opher, J. D. Richardson, and D. Tordella. "Voyager 2 solar plasma and magnetic field spectral analysis for intermediate data sparsity." In: *J. Geophys. Res.: Space Physics* 121.5 (2016), pp. 3905–3919. DOI: 10.1002/2015JA021830. URL: http://dx.doi.org/10.1002/2015JA021830.

[4] M. Iovieno, L. Gallana, J. D. Fraternale F. and Richardson, M. Opher, and D. Tordella. "Cross and magnetic helicity in the outer heliosphere from Voyager 2 observations." In: *Eur. J. Mech. B/Fluids* 55.2 (2016), pp. 394–401. DOI: 10.1016/j.euromechflu.2015.08.009.

Journal papers in preparation

[1] F. Fraternale, L. Domenicale, G. Staffilani, and D. Tordella. "Linear waves in sheared flows. Lower bound of the vorticity growth and propagation discontinuities in the parameters space." In: *Submitted, preprint version on Arxiv* (2017). URL: https://arxiv.org/abs/1611.02964.

[2] F. Fraternale, G. Nastro, and D. Tordella. "Existence of niches of non-dispersion for long perturbation waves in the Poiseuille flow." In: *In preparation* ().

[3] F. Fraternale, M. Iovieno, M. Opher, J. D. Richardson, and D. Tordella. "Magnetic fluctuation spectra comparison inside and outside sectored heliosheath regions." In: *In preparation* ().

Conferences

[1] F. Fraternale, L. Gallana, M. Iovieno, M. Opher, J. D. Richardson, and D. Tordella. "Magnetic field spectral analysis in the Heliosheath from Voyagers data." In: *Proceedings of the 24th International Congress of Theoretical and Applied Mechanics*. Montrèal, Canada, Aug. 2016. URL: `http://areeweb.polito.it/ricerca/philofluid/includes/proceedings/ICTAM2016_Fraternale_131134.pdf`.

[2] F. Fraternale, L. Gallana, M. Iovieno, M. Opher, J. D. Richardson, and D. Tordella. "Magnetic field spectral analysis in the Heliosheath from Voyagers data." In: *Proceedings of the European Postgraduate Fluid Dynamics Conference*. Warszawa, Poland, July 2016.

[3] J. D. Richardson, J. W. Belcher, D. Tordella, F. Fraternale, L. Gallana, and M. Iovieno. "Voyager 2 observations of plasma in the heliosheath." In: *Proceedings of the AGU Fall Meeting*. San Francisco, CA, USA, Dec. 2015.

[4] F. Fraternale, L. Gallana, M. Iovieno, S. M. Fosson, E. Magli, M. Opher, J. D. Richardson, R. Morgan, and D. Tordella. "Turbulence in the heliosheath: spectral analysis from Voyager 1 and 2 data." In: *Bulletin of the American Physical Society - 68th Annual Meeting of the APS Division of Fluid Dynamics*. Vol. 60. 21. Boston, MA, USA, Nov. 2015. URL: `http://meetings.aps.org/link/BAPS.2015.DFD.A8.9`.

[5] L. Domenicale, F. Fraternale, G. Staffilani, and D. Tordella. "Perturbation enstrophy decay in Poiseuille and Couette flows according to synge's method." In: *Bulletin of the American Physical Society - 68th Annual Meeting of the APS Division of Fluid Dynamics*. Vol. 60. 21. Boston, MA, USA, Nov. 2015. URL: `http://meetings.aps.org/link/BAPS.2015.DFD.G16.2`.

[6] F. Fraternale, L. Gallana, M. Iovieno, S. M. Fosson, E. Magli, D. Tordella, M. Opher, and J. D. Richardson. "Spectral Analysis in the Solar Wind and Heliosheath." In: *Proceedings of the 14th Annual International Astrophysics Conference*. Tampa Bay, FL, USA, Apr. 2015.

[7] F. Fraternale, L. Gallana, S. M. Fosson, E. Magli, M. Opher, J. D. Richardson, M. Iovieno, and D. Tordella. "Solar wind spectral analysis in heliosheath from Voyager data." In: *Proceedings of the 15th European Turbulence Conference*.

Delft, Netherlands, Aug. 2015. URL: http://www.etc15.nl/proceedings/proceedings/documents/489.pdf.

[8] F. De Santi, F. Fraternale, and D. Tordella. "Dispersive to nondispersive transition in the plane wake and channel flows." In: *Proceedings of the 15th European Turbulence Conference*. Delft, Netherlands, Aug. 2015. URL: http://www.etc15.nl/proceedings/proceedings/documents/492.pdf.

[9] L. Gallana, F. Fraternale, M. Iovieno, S. M. Fosson, E. Magli, M. Opher, J.D. Richardson, and D. Tordella. "Spectra and correlations in the solar wind from Voyager 2 around 5AU." In: *Bulletin of the American Physical Society - 67th Annual Meeting of the APS Division of Fluid Dynamics*. Vol. 59. 20. San Francisco, CA, USA, Nov. 2014. URL: http://meetings.aps.org/link/BAPS.2014.DFD.A36.5.

[10] F. Fraternale, L. Gallana, M. Iovieno, J. D. Richardson, and D. Tordella. "Solar wind plasma: turbulence signature in Voyager 2 1979 spectra." In: *Proceedings of the Vortical Structures and Wall Turbulence Conference*. Rome, Italy, Sept. 2014.

[11] F. Fraternale, L. Gallana, M. Iovieno, J.D. Richardson, and D. Tordella. "Turbulence in the solar wind, spectra from Voyager 2 data." In: *Proceedings of the international Turbulent Mixing and Beyond Workshop*. Trieste, Italy, Aug. 2014. ISBN: 9789295003552.

Part III

Appendix

A

A CHANDRASEKHAR EIGENFUNCTION EXPANSION METHOD TO SOLVE THE LINEARIZED 3D INITIAL VALUE PROBLEM

This appendix reports the numerical method used to solve the Orr-Sommerfeld and Squire initial value problem. The solution is based on the Galërkin variational minimization method and on an eigenfunctions expansion in terms of the Chandrasekhar functions [1]. The technique can be applied to any parallel basic flow with homogeneous boundary conditions and represents an extension, specific to 3D *non-modal* analysis, of the method by Gallagher & Mercer [6]. This was based on the use of Chandrasekhar's functions to solve the two-dimensional modal problem for the Couette flow. The original version of the numerical Matlab® code was developed by me in the Master's thesis period [2013, 5]. Successively, during the first year of Ph.D, the software was extended to unbounded flows as the wake and the Blasius boundary layer. A detailed software manual and flow chart can be found in our website[1].

As a starting point, the IVP in the wall-normal velocity and vorticity formulation is recalled (see 11-12)

$$\partial_t \partial_y^2 \hat{v} - k^2 \partial_t \hat{v} + i\alpha U(y) \partial_y^2 \hat{v} - i\alpha k^2 U(y) \hat{v} - i\alpha U''(y) \hat{v} - \frac{1}{Re}\left(\partial_y^4 \hat{v} - 2k^2 \partial_y^2 \hat{v} + k^4 \hat{v}\right) = 0, \tag{175}$$

$$\partial_t \hat{\omega}_y + i\alpha U(y) \hat{\omega}_y - \frac{1}{Re}\left(\partial_y^2 \hat{\omega}_y - k^2 \hat{\omega}_y\right) = -i \;\; U(y)' \hat{v}, \tag{176}$$

$$\hat{v}(y = \pm 1, t) = \partial_y \hat{v}(y = \pm 1, t) = \hat{\omega}_y(y = \pm 1, t) = 0, \tag{177}$$

$$\hat{v}(y, t = 0) = \hat{v}_0(y) \quad \hat{\omega}_y(y, t = 0) = 0. \tag{178}$$

A.1 Solution to the $\hat{v}$ equation

The solution of Eq. 175 can be expressed as a generalized Fourier expansion with time-dependent coefficients:

$$\hat{v}(y, t) = \sum_{n=1}^{\infty} c_n(t) X_n(y) \quad y \in [-1, 1], \tag{179}$$

1 http://areeweb.polito.it/ricerca/philofluid/software/249-hydro-chandraskhar.html

where $X_n(y)$ are orthogonal functions, and the following inverse transform applies:

$$c_n(t) = \frac{\int_{-1}^{1} \hat{v}(y,t) X_n(y)\,\mathrm{d}y}{\int_{-1}^{1} X_n(y) X_n(y)\,\mathrm{d}y}. \tag{180}$$

Since in the initial value problem both the initial condition and the boundary conditions need to be imposed, it is worthwhile to consider functions that satisfy the boundary conditions. Moreover, note that the coefficients c_n of the series are in general complex, since $\hat{v}$ is complex-valued and the spatial modes are considered as real. The particular orthogonal functions which we use are those defined by the following fourth order eigenvalue problem

$$\frac{\mathrm{d}^4}{\mathrm{d}y^4} X(y) = \lambda^4 X(y) \qquad y \in [-1,1] \tag{181}$$

$$X(y=\pm 1) = 0 \qquad \frac{\mathrm{d}}{\mathrm{d}y} X(y=\pm 1) = 0. \tag{182}$$

Two different sets of eigenvalues and the corresponding eigenfunctions are found, respectively odd and even, by numerically solving the following transcendental equations

$$tan(\lambda_n) - tanh(\lambda_n) = 0 \quad (odd\ set) \tag{183}$$

$$tan(\lambda_n) + tanh(\lambda_n) = 0 \quad (even\ set). \tag{184}$$

The corresponding normalized eigenfunctions (figure 79) are

$$X_n = \frac{1}{\sqrt{2}} \left[\frac{sinh(\lambda_n y)}{sinh(\lambda_n)} - \frac{sin(\lambda_n y)}{sin(\lambda_n)} \right] \qquad n = 1,3,5..,N-1$$

$$(odd\ set) \tag{185}$$

$$X_n = \frac{1}{\sqrt{2}} \left[\frac{cosh(\lambda_n y)}{cosh(\lambda_n)} - \frac{cos(\lambda_n y)}{cos(\lambda_n)} \right] \qquad n = 2,4,6..,N$$

$$(even\ set). \tag{186}$$

Similar functions, in a different domain, have been used in the study of the circular Couette flow between coaxial cylinders [1, appendix V].

Since the imaginary and the real part of the solution $\hat{v}$ usually have opposite parity, independently on the initial condition, both the odd and the even sets are necessary to completely describe the problem and obtain the correct result.
In the following paragraphs a compact notation for the space derivatives is introduced. In order to simplify the reading, the y-derivatives will be indicated with a subscript. The temporal derivatives will be indicated explicitly or with a dot.

The numerical solution to the $\hat{v}$ equation 175 is obtained by applying the variational Galërkin method. Truncating the series 179 at N functions and substituting yields

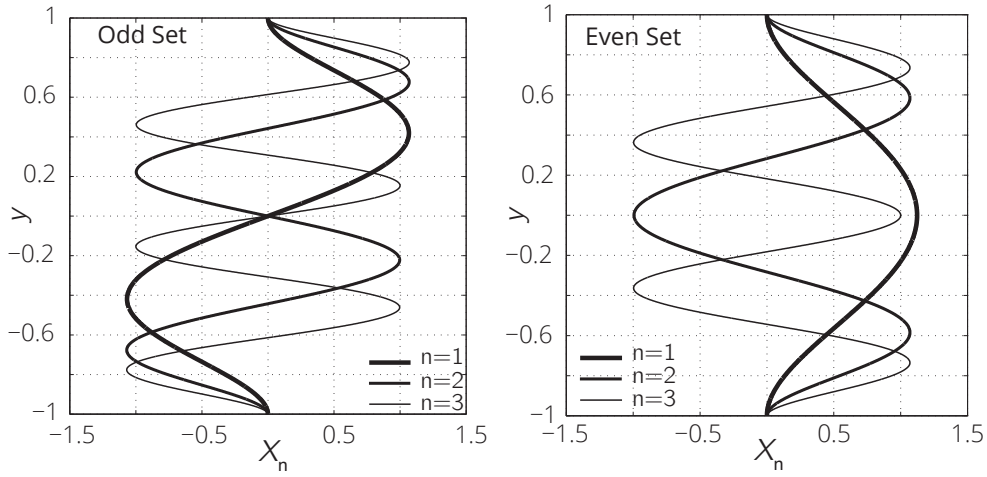

Figure 79: The Chandrasekhar eigenfunctions.

$$\begin{aligned}\epsilon(y,t;\ \alpha,\quad) = &\sum_{n=1}^{N}\frac{\mathrm{d}}{\mathrm{d}t}c_n(t)X_{n_{yy}} - k^2\sum_{n=1}^{N}\frac{\mathrm{d}}{\mathrm{d}t}c_n(t)X_n\\ &+ i\alpha U(y)\sum_{n=1}^{N}c_n(t)X_{n_{yy}} - i\alpha k^2 U(y)\sum_{n=1}^{N}c_n(t)X_n\\ &- i\alpha\frac{\mathrm{d}^2U(y)}{\mathrm{d}y^2}\sum_{n=1}^{N}c_n(t)X_n - \frac{1}{Re}\sum_{n=1}^{N}c_n(t)X_{n_{yyyy}}\\ &+ \frac{2k^2}{Re}\sum_{n=1}^{N}c_n(t)X_{n_{yy}} - \frac{k^4}{Re}\sum_{n=1}^{N}c_n(t)X_n. \end{aligned} \tag{187}$$

The error functional ϵ is minimized when it is orthogonal to the space of the linearly independent trial functions X_n with $n = 1, 2, ..N$. In this context, given two functions $u(y)$ and $v(y)$ with $y \in\ \Omega = [-1,\ 1]$, the following definition of scalar product applies

$$\langle u, v\rangle = \int_\Omega u\cdot v\,\mathrm{d}y. \tag{188}$$

With above notation the Galerkin orthogonality condition is expressed as

$$\langle \epsilon, X_m\rangle = 0 \qquad\qquad m = 1, 2, ..., N. \tag{189}$$

The Orr-Sommerfeld PDE is now reduced to a system of N ODEs of the first order, where the time dependent coefficients $c_n(t)$ are the only unknowns.

$$
\begin{aligned}
0 = & \sum_{n=1}^{N} \frac{\mathrm{d}}{\mathrm{d}t} c_n(t) \langle X_{n_{yy}}, X_m \rangle - k^2 \sum_{n=1}^{N} \frac{\mathrm{d}}{\mathrm{d}t} c_n(t) \langle X_n, X_m \rangle \\
& + i\alpha \sum_{n=1}^{N} c_n(t) \langle U(y) X_{n_{yy}}, X_m \rangle - i\alpha k^2 \sum_{n=1}^{N} c_n(t) \langle U(y) X_n, X_m \rangle \\
& - i\alpha \sum_{n=1}^{N} c_n(t) \langle \frac{\mathrm{d}^2 U(y)}{\mathrm{d}y^2} X_n X_m \rangle - \frac{1}{Re} \sum_{n=1}^{N} c_n(t) \langle X_{n_{yyyy}}, X_m \rangle \\
& + \frac{2k^2}{Re} \sum_{n=1}^{N} c_n(t) \langle X_{n_{yy}}, X_m \rangle - \frac{k^4}{Re} \sum_{n=1}^{N} c_n(t) \langle X_n, X_m \rangle \\
& n, \ m = 1, 2, 3, ..., N. \qquad (190)
\end{aligned}
$$

The scalar products can be evaluated analytically or computed by numerical integration:

$$D_{m,n} = \langle X_n, X_m \rangle = \delta_{m,n} \qquad (191)$$

$$S_{m,n} = \langle X_{n_{yy}}, X_m \rangle = \qquad (192)$$

$$
= \begin{cases} +4 \frac{\lambda_n^2 \lambda_m^2}{\lambda_n^4 - \lambda_m^4} (\lambda_n \mu_n - \lambda_m \mu_m) & \text{if } (n+m) \text{ is even, } n \neq m \\ 0 & \text{if } (n+m) \text{ is odd} \\ -\lambda_n^2 \mu_n^2 + \lambda_m \mu_m & \text{if } n = m \end{cases}
$$

$$F_{m,n} = \langle X_{n_{yyyy}}, X_m \rangle = \lambda_n^4 \delta_{m,n} \qquad (193)$$

$$U^{(1)}_{m,n} = \langle U(y) X_{n_{yy}}, X_m \rangle \qquad (194)$$

$$U^{(2)}_{m,n} = \langle U(y) X_n, X_m \rangle \qquad (195)$$

$$U^{(3)}_{m,n} = \langle \frac{\mathrm{d}^2 U(y)}{\mathrm{d}y^2} X_n X_m \rangle, \qquad (196)$$

where

$$\mu_n = \frac{cosh(2\lambda_n) - cos(2\lambda_n)}{sinh(2\lambda_n) - sin(2\lambda_n)} \qquad \lim_{n \to \infty} \mu_n = 1. \qquad (197)$$

It is convenient to express the ODE system 190 in a compact notation: in the following, vectors will be indicated either explicitly using braces or with bold lower case letters; matrices will be indicated with bold capital letters; constants with roman capital letters and physical parameters in italic. The system can be written as

$$\mathbf{H}\dot{\mathbf{c}} - \mathbf{G}\mathbf{c} = 0, \qquad (198)$$

where

$$\mathbf{H} = \mathbf{S} - k^2\mathbf{D} \tag{199}$$

$$\mathbf{G} = -i\alpha\mathbf{U^{(1)}} + i\alpha k^2\mathbf{U^{(2)}} + i\alpha\mathbf{U^{(3)}} + \frac{1}{Re}\mathbf{F} - \frac{2k^2}{Re}\mathbf{S} + \frac{k^4}{Re}\mathbf{D}, \tag{200}$$

where $\mathbf{D} = [D_{m,n}]$ etc., i.e. the element $D_{m,n}$ is placed at the n^{th} column and at the m^{th} row of the matrix. $\mathbf{H}$ is invertible, so denoting $\mathbf{A} = \mathbf{H}^{-1}\mathbf{G}$ yields

$$\dot{\mathbf{c}} - \mathbf{A}\mathbf{c} = 0. \tag{201}$$

The complex eigenvalues σ_i of $\mathbf{A}$ constitute the spectrum of the Orr-Sommerfeld equation, and the analytic solution to eq. 201 can be easily implemented and computed numerically (the QR method is used to compute the eigenvalues, in the Matlab environment).

A.2 Solution to the non-homogeneous equation for $\hat{\omega}_y$

In order to solve the Squire IVP, a set of normal functions different from the one adopted for the velocity is needed, since the second order PDE only requires $\hat{\omega}_y$ to vanish at the boundaries, but not its first derivative. A simple choice for the basis functions, here adopted, is the following

$$Y_n = sin(\xi_n y) \qquad n = 1, 3, 5, ...N-1 \qquad (odd\ set) \tag{202}$$

$$Y_n = cos(\xi_n y) \qquad n = 2, 4, 6, ...N \qquad (even\ set), \tag{203}$$

where

$$\xi_n = \frac{(n+1)\pi}{2} \qquad n = 1, 3, 5, ...N-1 \qquad (odd\ set) \tag{204}$$

$$\xi_n = \frac{(n-1)\pi}{2} \qquad n = 2, 4, 6, ...N \qquad (even\ set). \tag{205}$$

Also in this case, note that two sets of eigenfunctions are put together to form a unique set, since both are necessary to completely describe the complex-valued normal vorticity. The general solution is then obtained as the sum of a particular solution $\hat{\omega}_{y_p}$ and the solution to the corresponding homogeneous equation, $\hat{\omega}_{y_h}$:

$$\hat{\omega}_y(y,t) = \hat{\omega}_{y_h}(y,t) + \hat{\omega}_{y_p}(y,t) \tag{206}$$

$$\hat{\omega}_y(y,t) = \sum_{n=1}^{\infty}(b_{h_n} + b_{p_n})(t)Y_n(y). \tag{207}$$

The application of the Galërkin method yields to the following forced ODE set

$$\dot{\mathbf{b}} - \underbrace{\left(-i\alpha\mathbf{U}^* + \frac{1}{Re}\mathbf{S}^* - \frac{2k^2}{Re}\mathbf{D}^* \right)}_{\mathbf{G}^*} \mathbf{b} = \underbrace{-i}_{\mathbf{B}} \mathbf{F}^* \mathbf{c} \tag{208}$$

$$\dot{\mathbf{b}} - \mathbf{G}^*\mathbf{b} = \mathbf{B}\mathbf{c}, \tag{209}$$

where the eigenvalues of $\mathbf{G}^*$ constitute the spectrum of the Squire equation and

$$D^*_{m,n} = \langle Y_n, Y_m \rangle = \delta_{m,n} \tag{210}$$

$$S^*_{m,n} = \langle Y_{n_{yy}}, Y_m \rangle = -\xi_n^2 \delta_{m,n} \tag{211}$$

$$U^*_{m,n} = \langle U(y) Y_n, Y_m \rangle \tag{212}$$

$$F^*_{m,n} = \langle \frac{\mathrm{d}U(y)}{\mathrm{d}y} X_n, Y_m \rangle. \tag{213}$$

The homogeneous solution $\mathbf{b_h}$ of Eq. 209 is analytically known, while a particular solution $\mathbf{b_p}$ of the following form is sought

$$b_{p_n}(t) = \sum_{j=1}^{N} a_{nj} e^{\sigma_j t}, \tag{214}$$

where a_{nj} are constants and σ_j are the eigenvalues of $\mathbf{G}$, in such a way the forced solution has the same spectral content of forcing term. The coefficients are obtained through the solution of N algebraic sets, after the computation of $\mathbf{c}(0)$.

The Galërkin method was first applied to the Orr-Sommerfeld modal equation by Dolph&Lewis [1958, 4]. They used normal functions that guarantee a $1/N^4$ convergence ratio. Gallagher&Mercer [6] used, for the modal problem, the Chandrasekhar-Reid functions and the error decreased as $1/N^5$ with $N \to \infty$ as shown by Orszag [1971 9]. The fifth order of accuracy is ensured for the present formulation as well, as shown in figure 80.

The method results to be fast and accurate in time and space. Since the time evolution is analytically represented, the complete wave transient, up to the asymptote, can be simulated without typical drawbacks of time-marching techniques. Arbitrary initial conditions can be specified for bounded flows. The limits of the method are related to the non-normality of the Orr-Sommerfeld and Squire operators. The non-normal effects act on the numerical procedure by worsening the condition number of the eigenvector matrices. Anyway, the sensibility of the spectrum (especially at high Re and k values) is a property of the stability operator and it is thus independent on the numerical scheme.

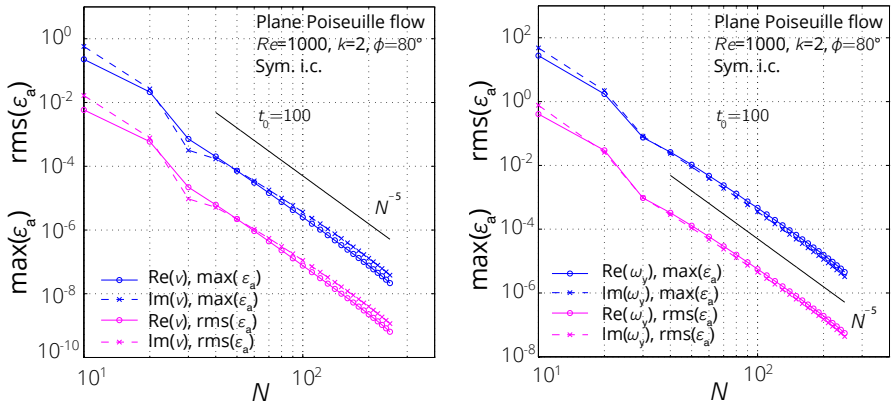

Figure 80: Maximum and rms of the absolute error on the computation of $\hat{v}$ (left panel) and $\hat{\omega}_y$ (right panel) as a function of the number of modes N for channel flow with $t_0 = 100$, $Re = 1000$, $k = 2$, $\phi = 80^\circ$ and symmetrical initial condition. Continuous line: real part. Dashed line: imaginary part. Magenta line: maximum absolute error. Blue line: rms of the absolute error. Black line: accuracy trend N^{-5} [9]. Since the exact solution is not known, the residuals are defined as the difference between the solution and an accurate solution computed with 350 modes. $\epsilon_a(y,t) = |\hat{v}_N(y,t) - \hat{v}_{N=350}(y,t)|$, $rms(\epsilon_a)(t) = \frac{1}{N_y}\sqrt{\sum_{i=1}^{N_y} \epsilon_a^2(y,t)}$, $max(\epsilon_a)(t) = \max_{y_i}(\epsilon_a(y,t))$

A.3 **Spectra computation**

In order to compute the spectra of the Orr-Sommerfeld equation we used two different numerical methods: (i) a fourth order finite differences collocation scheme and (ii) the present non modal three dimensional version of the Gallagher&Mercer (1962) method which is described above. Here, we report a comparison with literature results as a validation of our spectral calculations, see figure 81. For unbounded flows it has been shown by Grosch&Salwen [7, pp. 1978,] that a continuous spectrum can be analytically found, if the boundary conditions are relaxed to $\hat{v}$ *bounded* as $y \to \infty$. If finite-norm boundary conditions are imposed and therefore only the class of decaying solutions as $|y| \to \infty$ is considered, the continuous part of the spectrum is approximated in a discrete way. If the boundary conditions are imposed far from the wake, the approximation is very good. The Galërkin method with Chandrasekhar functions described above was successfully adapted to the wake flow and to the boundary layer flow. Since no spectra with our wake basic flow (see [12]) have been found in literature, the schemes have been validated with the Blasius boundary layer flow (see figure 81, panel **a**). Eventually, for the channel flow, the comparison with a hybrid spectral collocation method based on Chebyshev polynomials [11, A.6] is shown in figure 81, panel **b**.

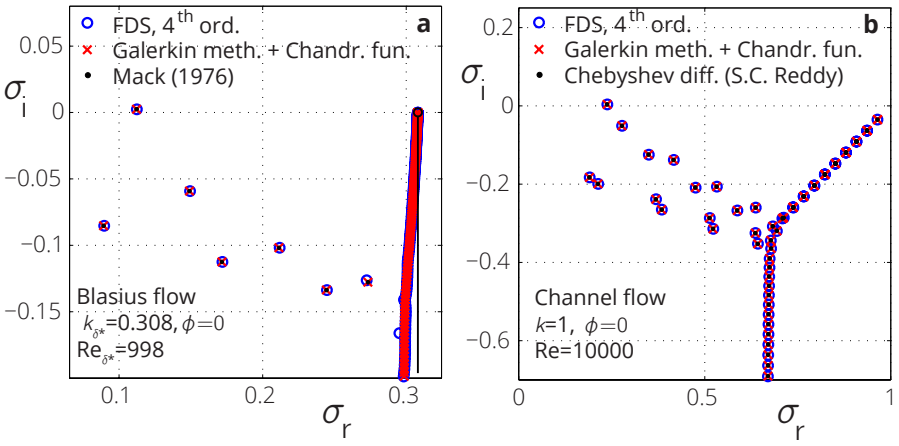

Figure 81: Computation of eigenvalues spectra ($\sigma = \sigma_r + i\sigma_i$) of the Orr-Sommerfeld equation. Different numerical methods are compared: a 4^{th} order finite-differences scheme on uniform grid (blue circles); a 5^{th} order Galërkin method on nonuniform grid (red x); a Chebyshev spectral collocation method (code by S.C. Reddy, black points on panel **(b)**; results by Mack [8] (black points on panel **a**). **(a)** Blasius boundary layer flow, $Re_{\delta^*} = 998$, $k_{\delta^*} = 0.308$, $\phi = 0$. The continuous part of the spectrum is discretely approximated. The black line represents the analytic solution, obtainable only if the boundary condition at $y \to \infty$ is relaxed to $\hat{v}_{y\to\infty} bounded$. As Re_{δ^*} and k_{δ^*} increase, particular attention was paid in order to avoid spurious eigenvalues due to the spectrum intrinsic sensibility. **(b)** Channel flow, $Re = 10000$, $k = 1$, $\phi = 0$.

B

MONOTONIC STABILITY ANALYSIS OF THE 2D PLANE POISEUILLE AND BLASIUS BOUNDARY LAYER FLOWS, VIA GENETIC ALGORITHMS

The genetic algorithm PIKAIA is used to search the monotonic stability limit Re_E, for two archetypal shear flows, the plane Poiseuille and the Blasius boundary layer flows. Re_E is defined as the minimum value of Reynolds number ($Re = \rho UL/\nu$) below which any perturbation introduced in the basic flow decays monotonically over time. As shown in the following, this stability problem can be formulated in terms of a kinetic energy functional maximization. The "chromosomal" representation adopted here consists of the N coefficients of the perturbation velocity expansion. The lower bound for transient kinetic energy growth $Re_E(k)$ is found and compared to the solution given by the Euler-Lagrange equations associated to this problem. The functional to be optimized for this problem is convex, so a comparison with the variational technique is possible: the discrepancy resulted below 3.5% for all the cases.
The advantage of the genetic code allows to analyze non-convex functionals. An extension to the three-dimensional problem is straightforward, since considering the wall-normal vorticity terms of Eq. 218, just leads to a doubling of the parameters. The wall-normal vorticity $\widehat{\omega}_y$ vanishes at the walls and can be therefore expressed by a Fourier series.

B.1 **Physical problem and formulation**

The monotonic stability problem is investigated for two shear flows: the plane Poiseuille flow and the Blasius boundary layer. The steady laminar solution $U(y)$ is perturbed so that the complete velocity field is $(U(y) + \widetilde{u}(x,y,t),\ \widetilde{v}(x,y,t),\ \widetilde{w}(x,y,t))$, where $\widetilde{u}$, $\widetilde{v}$ and $\widetilde{w}$ are the longitudinal (x) and wall-normal (y) components of the perturbation velocity. The linearized 3D Navier-Stokes equations (see Eqs. 1-4 in Chapter 1) in non-dimensional form are derived. The reference length for the channel flow is the half-width h, while for the Blasius flow we use the displacement thickness $\delta*$. The reference velocity for the channel flow is the centerline velocity U_{CL}, while in the boundary layer case the free-stream velocity U_∞, is considered. The reference time is the convective one. About the base flow, the analytical expression $U(y) = 1 - y^2$ represents the Poiseuille exact solution, while Blasius flow is numerically computed from the Falkner-

Scan equation. An accurate solution is obtained by means of the Matlab routine *FSCprof*, which uses Chebyshev polynomials. Homogeneous boundary conditions are imposed to the perturbation.

Let's consider the kinetic energy equation for a single wave disturbance. In the physical space the equation is

$$\frac{\mathrm{d}E}{\mathrm{d}t} = \underbrace{-\int \frac{\mathrm{d}U}{\mathrm{d}y}\widetilde{u}\widetilde{v}\,\mathrm{d}\mathcal{V}}_{Production} \underbrace{-\frac{1}{Re}\int |\nabla\widetilde{u}|^2 + |\nabla\widetilde{v}|^2 + |\nabla\widetilde{w}|^2\,\mathrm{d}\mathcal{V}}_{Dissipation}. \tag{215}$$

while in the Fourier space we have:

$$\begin{aligned}\frac{\mathrm{d}E}{\mathrm{d}t} = &\underbrace{\frac{1}{k^2} Imag \int U'\left(\alpha\bar{v}\partial_y\widehat{v} - \beta\bar{v}\widehat{\omega}_y\right)\,\mathrm{d}y}_{Production} \\ &\underbrace{-\frac{1}{Re\ k^2}\int \left(|\partial_y^2\widehat{v}|^2 + 2k^2|\partial_y\widehat{v}|^2 + k^4|\widehat{v}|^2 + |\partial_y\widehat{\omega}_y| + k^2|\widehat{\omega}_y|^2\right)\mathrm{d}y}_{Dissipation},\end{aligned} \tag{216}$$

where the prime indicates the total y-derivative, and α, β are the streamwise and spanwise wavenumber components. Note that the first term is called *production* since it can have positive sign, so the condition $U'\widetilde{u}\widetilde{v} < 0$ occurring somewhere in the domain is a necessary condition for (algebraic or asymptotic exponential) instability. If we are looking for stable perturbations, the condition

$$\mathrm{d}E/\,\mathrm{d}t \leq 0 \quad \forall t \geq 0$$

becomes a bound on the Reynolds number:

$$\frac{1}{Re} \leq \frac{Imag \int U'\left(\alpha\bar{v}\partial_y\widehat{v} - \beta\bar{v}\widehat{\omega}_y\right)\,\mathrm{d}y}{\int \left(|\partial_y^2\widehat{v}|^2 + 2k^2|\partial_y\widehat{v}|^2 + k^4|\widehat{v}|^2 + |\partial_y\widehat{\omega}_y| + k^2|\widehat{\omega}_y|^2\right)\mathrm{d}y}. \tag{217}$$

The *monotonic* (or *unconditional*) *stability threshold* $Re_{\mathrm{E}}(\alpha,\beta)$ is the Reynolds number below which any initial perturbation decays monotonically. For values of Re above this threshold, one can always find a perturbation experiencing kinetic energy growth for some $t \geq 0$. This limit results in the following optimization problem:

$$\frac{1}{Re_{\mathrm{E}}} = \sup_{\widehat{v}(y),\widehat{\omega}_y(y)} \frac{Imag \int U'\left(\alpha\bar{v}\partial_y\widehat{v} - \beta\bar{v}\widehat{\omega}_y\right)\,\mathrm{d}y}{\int \left(|\partial_y^2\widehat{v}|^2 + 2k^2|\partial_y\widehat{v}|^2 + k^4|\widehat{v}|^2 + |\partial_y\widehat{\omega}_y| + k^2|\widehat{\omega}_y|^2\right)\mathrm{d}y}, \tag{218}$$

under the divergence-free constraint.

In the following, the solution to this optimization problem is computed for two-dimensional perturbations ($\beta = 0$) by means of a Fortran90 software, built starting from the genetic open-source algorithm PIKAIA [2, 3]. The results are compared to those obtained via the variational approach [see e.g. 10].

B.2 Chromosomal representation and parameters

The general perturbation $\widehat{v}(y)$ can be expressed as a generalized Fourier expansion as shown in Appendix A:

$$\hat{v}(y,t) = \sum_{n=1}^{\infty} c_n X_n(y) \quad y \in [-1,1], \tag{219}$$

where $X_n(y)$ are orthogonal functions, and the following inverse transform applies

$$c_n = \frac{\int_{-1}^{1} \hat{v}(y) X_n(y)\,\mathrm{d}y}{\int_{-1}^{1} X_n(y) X_n(y)\,\mathrm{d}y}, \tag{220}$$

where $c_n = a_n + i b_n$ are complex-valued coefficients.

The orthogonal functions used are the Chandrasekhar-Reid functions, which satisfy the homogeneous boundary condition of the problem. Two sets of eigenfunctions are needed for a complete description of the problem, the symmetric and the antisymmetric sets, respectively (see figure 79)

This decomposition naturally yields to a chromosomal representation of the optimization problem, where a finite number N of coefficients of the truncated series constitute the chromosomes.
PIKAIA is a GA-based Fortran90 subroutine, and incorporates the two basic genetic operators: uniform one-point crossover, and uniform one-point mutation. The encoding within PIKAIA is based on a decimal alphabet made of the 10 simple integers (0 through 9). Three reproduction plans are available: Full generational replacement, Steady-State-Delete-Random, and Steady-State-Delete-Worst. Elitism is available and is a default option. The mutation rate can be dynamically controlled by monitoring the difference in fitness between the current best and median in the population (also a default option). Selection is rank-based and stochastic, making use of the Roulette Wheel Algorithm (from `http://www.hao.ucar.edu/modeling/pikaia/pikaia.php`).
Since the parameters need to be real numbers, the following representation is considered for the stability problem:

$$chromosome = [a_{1o}, a_{1e}, b_{1o}, b_{1e}, a_{2o}, a_{2e}, \ldots\ldots\ldots, a_{No}, a_{Ne}, b_{No}, b_{Ne}] \tag{221}$$

where "o" stands for "odd" and "e" stands for "even". This genotype corresponds to a particular admissible perturbation $\widehat{v}$, so the total number of parameters to be optimized is $2N$. Since all the parameters within the code should take values in $[0,1]$, the genotype is rescaled to the range $[-1,1]$ before the evaluation of the fitness function. In fact, the coefficients a_n, b_n can also take negative values.
The fitness function in terms of this representation is derived from Eq. 218 for 2D perturbations. The divergence-free constraint is already included in the expression, while the boundary conditions are satisfied by the series 179, which can be differentiated termwise up to the third derivative:

$$fitness = \frac{1}{Re} = \frac{\int U'\alpha\left(\widehat{v}_r\partial_y\widehat{v}_i - \widehat{v}_i\partial_y\widehat{v}_r\right)}{\int\left(\partial_y^2(\widehat{v}_r^2+\widehat{v}_i^2) + 2k^2\partial_y(\widehat{v}_r^2+\widehat{v}_i^2) + k^4(\widehat{v}_r^2+\widehat{v}_i^2)\right)}, \qquad (222)$$

where $\widehat{v}_r$ and $\widehat{v}_i$ are the real and the imaginary part of the velocity, respectively. They are computed in a pre-processing step as follows, in matrix notation:

$$\begin{aligned}
\{\widehat{v}_r\} &= [X]\{chr(i)\} \qquad i\ odd\\
\{\widehat{v}_i\} &= [X]\{chr(i)\} \qquad i\ even\\
\{\partial_y\widehat{v}_r\} &= [\partial_y X]\{chr(i)\} \qquad i\ odd\\
\{\partial_y\widehat{v}_i\} &= [\partial_y X]\{chr(i)\} \qquad i\ even\\
\{\partial_y^2\widehat{v}_r\} &= [\partial_y^2 X]\{chr(i)\} \qquad i\ odd\\
\{\partial_y^2\widehat{v}_i\} &= [\partial_y^2 X]\{chr(i)\} \qquad i\ even
\end{aligned}$$

where all the eigenmode matrices are sized $N \times N_y$ and have been previously computed and loaded by the program, as well as the spatial grid of size N_y and the base flow ($N = 100$ and $N_y = 400$ for the channel case, $N = 100$ and $N_y = 200$ for the boundary layer). In the Blasius case, a Chebyshev grid was used. The domain size is $y \in [-1,1]$ for the channel flow, while $y \in [0,10]$ for Blasius, in the latter case a proper scaling of the derivatives is needed in order to use the expansion 179 (remind that X_i are defined in $[-1,1]$). In order to find the lowest threshold among all wavenumbers (the red point in figure 83), two further simulations have been performed, where also the wavenumber α was included as part of the genotype.

B.3 **Results**

The convergence of the computation is shown in figure 82, for several values of the wavenumber. The results are shown with black triangles in figure 83, where the blue profiles represent the velocity perturbation at the boundary of the monotonic energy decay region.

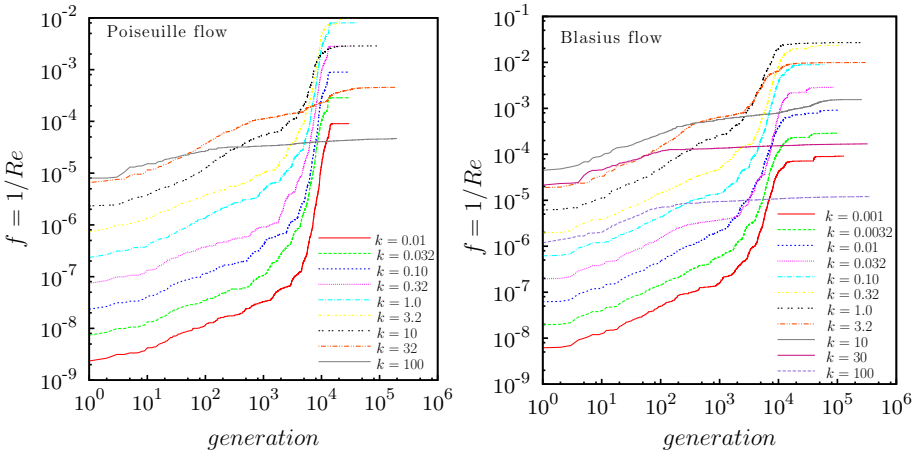

Figure 82: Genetic algorithm convergence to the maximal value of the functional $1/Re$. *Top*: Poiseuille flow; *bottom*: Blasius boundary layer flow.

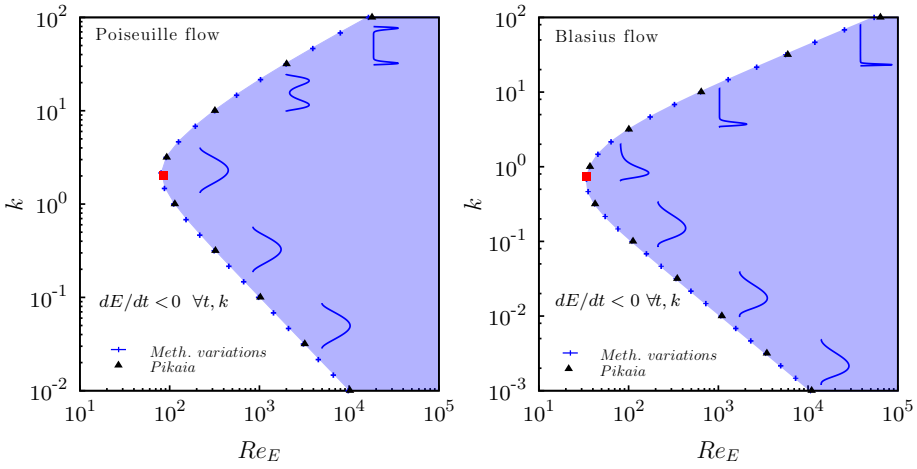

Figure 83: Monotonic stability threshold for the plane Poiseuille flow (top) and the Blasius boundary layer (bottom). The blue symbols represent the result of the variational optimization problem associated with 218, while the black triangles indicate the solutions given by the genetic algorithm. In the white region, no energy growth is possible, whatever the shape of the initial condition. Velocity profiles at the threshold are also shown (blue curves) for some (k, Re_E) combinations. The smallest value of Re_E is indicated with a red square; the computed values are $k^* = 2.1$, $Re_E^* = 88.1$ for the channel case, and $k^* = 0.8$, $Re_E^* = 35.4$ for Blasius.

APPENDIX BIBLIOGRAPHY

[1] S. Chandrasekhar. *Hydrodynamic and Hydromagnetic Stability*. Oxford University Press, 1961 (cit. on pp. 245, 246).

[2] P. Charbonneau. "Genetic algorithms in astronomy and astrophysics." In: *Astrophys. J. Suppl. S.* 101.2 (1995), pp. 309–334. DOI: 10.1086/192242 (cit. on p. 255).

[3] P. Charbonneau and B. Knapp. "A User s Guide to PIKAIA 1.0." In: (1995). URL: http://www.hao.ucar.edu/modeling/pikaia/pikaia.php#sec9 (cit. on p. 255).

[4] C. L. Dolph and D. C. Lewis. "On the application of infinite systems of ordinary differential equations to perturbations of plane Poiseuille flow." In: *Quart. Appl. Math* 16 (1958), pp. 97–110 (cit. on p. 250).

[5] F. Fraternale. "Frequency transient of three-dimensional perturbations in shear flows. Similarity properties and wave packets linear formation." MA thesis. Politecnico di Torino, 2013 (cit. on p. 245).

[6] A. P. Gallagher and A. McD. Mercer. "On the behaviour of small disturbances in plane Couette flow." In: *J. Fluid Mech.* 13.1 (1962), pp. 91–100. DOI: 10.1017/S0022112062000531 (cit. on pp. 245, 250).

[7] C. E. Grosch and H. Salwen. "The continuous spectrum of the Orr-Sommerfeld equation. Part 1. The spectrum and the eigenfunctions." In: *J. Fluid Mech.* 87.01 (1978), pp. 33–54 (cit. on p. 251).

[8] Leslie M. Mack. "A numerical study of the temporal eigenvalue spectrum of the Blasius boundary layer." In: *J. Fluid Mech.* 73 (1976), pp. 497–520 (cit. on p. 252).

[9] S. A. Orszag. "Accurate solution of the Orr-Sommerfeld stability equation." In: *J. Fluid Mech.* 50.4 (1971), pp. 689–703 (cit. on pp. 250, 251).

[10] S. C. Reddy and D. S. Henningson. "Energy growth in viscous channel flows." In: *J. Fluid Mech.* 252 (1993), pp. 209–238. DOI: 10.1017/S0022112093003738 (cit. on p. 255).

[11] P. J. Schmid and D. S. Henningson. *Stability and Transition in Shear Flows*. Springer, 2001 (cit. on p. 251).

[12] D. Tordella and M. Belan. "A new matched asymptotic expansion for the intermediate and far flow behind a finite body." In: *Phys. Fluids* 15.7 (2003), pp. 1897–1906. DOI: 10.1063/1.1580482 (cit. on p. 251).